THE UNIVERSITY *of* EDINBURGH

This thesis has been submitted in fulfilment of the requirements for a postgraduate degree (e.g. PhD, MPhil, DClinPsychol) at the University of Edinburgh. Please note the following terms and conditions of use:

This work is protected by copyright and other intellectual property rights, which are retained by the thesis author, unless otherwise stated.
A copy can be downloaded for personal non-commercial research or study, without prior permission or charge.
This thesis cannot be reproduced or quoted extensively from without first obtaining permission in writing from the author.
The content must not be changed in any way or sold commercially in any format or medium without the formal permission of the author.
When referring to this work, full bibliographic details including the author, title, awarding institution and date of the thesis must be given.

Saturation Tracking and Identification of Residual Oil Saturation

Tannaz Pak

Doctorate of Philosophy
The University of Edinburgh

2014

Abstract

Carbonate rocks are of global importance as they contain about 50% of the world's remaining hydrocarbon reserves and are also a major host to the world's groundwater resources. Therefore, understanding and modelling the fluid flow processes in carbonates are of great importance. A critical problem is that, unlike homogenous media (such as sandstones), carbonates often show features, including porosity, that span across a wide spatial range, from sub-micron porosity to fractures of meters length-scale.

In this study X-ray computed micro-tomography (μCT) has been utilised as a tool to monitor two phase (oil-brine) flow in porous carbonate (dolomite) plugs at ambient temperature and pressures smaller than 690 kPa. A simple, low-cost and highly X-ray transparent core-holder was utilised for which the design is introduced. Capillary end effects were recognised and avoided in data analysis. Displacement processes that occur in the dolomite under water-wet, oil-wet, and partially mixed-wet states were investigated. The experiments consisted of a series of drainage and imbibition processes occurring under capillary and viscous dominated flow regimes. Pore-scale mechanisms of piston-like displacement and snap-off (or at least clear results of them), that were previously observed in sandstones and 2D micro-models, were observed in the dolomite under study. In addition, a new pore-scale mechanism was identified which occurred at high capillary numbers, referred to as droplet-fragmentation. This new pore-scale mechanism may provide an explanation to the capillary-desaturation process for heterogeneous media.

In the experiments performed on the oil-wet plug formation of a stable water in oil emulsion was observed which appears to be the first 3D observation of in situ emulsion formation made using μCT.

Direct visualisation of the oil-brine-rock configurations and measurement of the contact angles are presented. A comparison was made for the contact angle distributions measured for the water-wet and oil-wet conditions. Observation of fluid displacement processes as well as oil-brine-rock contact angle distributions demonstrate that pore-scale imaging provides a promising tool for wettability

characterisation on both pore and core scales. Such detailed wettability data can also be used in pore-scale flow models.

For the dolomite under study multiple-scale pore network models were constructed by integrating single-scale networks extracted from μCT images acquired at different length-scales. Mercury injection capillary pressure laboratory measurements were used to evaluate the capillary pressure (vs. saturation) curves calculated using single, two-scale, and three-scale network models of this dolomite. The integrated networks displayed an improved match to the laboratory measurements in comparison with the single-scale network model. The three-scale network provided the closest simulated curve, this result confirms that a more representative model displays closer properties. While simulated capillary pressure curves are close (converging) for the integrated networks the calculated relative permeability curves show variability for different multiple-scale networks.

The present work demonstrates that the pore-scale fluid displacement processes occurring in heterogeneous porous media are more complex than those occurring in homogeneous media. In addition, successful fluid flow simulations require construction of multiple-scale models as well as consideration of the pore-scale processes (such as droplet-fragmentation) that are specific to such complex pore systems.

Declaration

I declare that the presented thesis is all my own work, except where otherwise acknowledged, and that it has not been submitted, either in whole or in part, in any previous application for a degree.

Tannaz Pak
October 2014

Acknowledgement

The past three years have been an unforgettable and indeed rewarding journey for me. Looking back to the first day I arrived in Edinburgh and warmly welcomed by Ian, I feel I have gained far more than I had imagined coming to this country.

My sincere appreciation goes to my God, who gave me wisdom, and health to come this far. I would like to express my deepest gratitude to my supervisors, Ian Butler, Sebastian Geiger and Rink van Dijke for their constant support, and invaluable discussions that shaped the present work. I will always remain grateful to Ian's patience in the lab and all the effort he put in guiding me to become an experimentalist of some sort!

During this PhD I had the privilege of working as part of the ICCR team. The international centre for carbonate reservoirs gave me the chance to practise team work, as well as to improve my individual networking and communication skills. I enjoyed every moment of our ICCR meetings, trips and conferences, all around the world. I learned a lot from all the collaborative works with Brazilian universities and research centres. For all these I am grateful to Rachel Wood, Patrick Corbett, and all my fellow ICCR colleagues. I thank Petrobras and BG Group for their financial support. I am grateful to Petrobras Research Centre (CENPES) for permitting me to use their laboratories. My appreciation goes to Rodrigo Surmas not only for providing rock samples, but also for his constant support and scientific input during the course of this project. I also thank Ken Sorbie and Zeyun Jiang for the time and enthusiasm they devoted to this project.

I thank Robert Brown and Alex Hart for manufacturing the core flooding cell, Mike Hall for preparing thin sections of my rock samples, and the Centre of Environmental Scanning Microscopy at Heriot-Watt University for SEM images.

A big thanks to my dear friends: Robyn, Hanna, Claudia, Adele, Temy, Maddy, Ola, Alice, Sophie, Zeinab and Morteza with whom I shared memorable moments during my three years of stay in Edinburgh.

My whole heart appreciation goes to my mum, dad and sisters, Nazi and Bahar, for all their trust, support, encouragement and love during my entire life, nearly three decades now!

Last but not least, a special thanks to my husband Majid, who gave me endless motivation, and love. Without his support and help this work would have never been completed.

Chapter 1

Introduction

1. Research Questions

1.1. Study of the Pore-scale Fluid Displacement Processes in Complex Carbonates

Multiphase fluid displacement processes in porous media are important for a broad range of natural and engineering applications such as transport of non-aqueous phase liquid contaminants in aquifers, oil and gas production from hydrocarbon reservoirs, subsurface CO_2 storage, or gas transport in fuel cells.

Surface wettability (see chapter 2, section 6 for wettability definition) is one major parameter that controls the fluid distributions in porous materials. In addition to viscous and gravity forces, wettability causes the capillary forces to come into play in a multiphase fluid displacement process. In many industrial applications the objective is to remove (or recover) a non-wetting phase from the porous media by means of injecting the wetting phase. An example is the removal of a trapped non-aqueous liquid contaminant (NAPL) from aquifers or oil and gas from hydrocarbon reservoirs. Herein, capillary trapping is a fundamental mechanism that causes immobilization of a portion of the resident non-wetting phase when it is displaced by an invading wetting phase. As a result, production of the non-wetting phase is always less than 100%. Understanding the amount and structure of this remaining fluid phase is essential for designing and modelling effective and improved recovery processes.

Direct visualisation of multiphase fluid displacement in porous media has been possible using transparent micro-models (in 2D) and more recently using X-ray computed micro-tomography (μCT) technique (in 3D). Most micro-models are made of pores with idealised geometries. Likewise, the focus of most of the previous μCT studies has been mainly on homogeneous pore structures such as those of the bead packs, sand packs or sandstones. Whereas, little attention has paid to more complex porous material such as carbonate rocks. However, the ability to correctly understand and reliably model the fluid displacement processes in carbonate rocks is of particular economic and environmental importance. Carbonates host more than 50% of worldwide oil and gas reserves (Burchette, 2012). Moreover, carbonate aquifers supply water wholly or partially to one quarter of the global population (Hartmann et al., 2014).

This study is aimed at establishing a better understanding of the pore-scale processes responsible for bulk oil and brine redistribution in porous carbonate rocks. To achieve this two-phase core-flood experiments are combined with μCT visualisation of oil-brine distributions. More specifically this research is focused on characterising the residual oil saturation (S_{or}) distribution in carbonate media during water flooding for different wetting systems. In a two phase (water-oil) system the residual oil saturation is defined as the amount of oil (fraction of the pore volume) that remains in the swept zone of a water-flooded reservoir when the produced ratio of water to oil has reached its economic limit (Morrow, 1985). The residual oil (non-wetting) saturation S_{or} ranges from 5% to 60% (Morrow (1985).

$$S_{or} = \frac{remaining\ oil\ volume}{pore\ volume} \times 100\% \quad (1.1)$$

The amount and structure of residual non-wetting phase in a porous material is controlled by the multiphase petrophysical properties of the porous medium such as capillary pressure, relative permeability and wettability. These properties are highly influenced by pore geometry, pore-size distribution, pore connectivity, and the mineralogy of the porous media.

1.2. Porous Media Wettability Characterisation

Surface wettability of the rock is considered as an essential piece of data in all hydrocarbon field development studies. Traditional wettability characterisation methods such as USBM and Amott can only measure an average wetting index for a core plug. In addition, these conventional measurements methods are lengthy and costly. A faster and less expensive approach for wettability characterisation is desirable. Pore-scale imaging allows in-situ observation of fluid phases that saturate a porous sample and provides a means to directly visualise the fluid-fluid-rock configurations. Hence, pore-scale imaging can indicate not only the surface wetting preference, but any spatial variation in wettability across the sample. Wettability characterisation using μCT imaging are addressed in many recent studies (Turner et al., 2004, Iglauer et al., 2011, Wildenschild et al., 2011, Andrew et al., 2014). These studies look at analysing the wetting and non-wetting fluid phase structures (their shape and connectivity) in porous samples. However, to the author's knowledge, there

has been no report on the fluid-fluid-rock configurations in a porous medium under different wetting conditions that can demonstrate the capacity of pore-scale imaging as a wettability analysis alternative approach. This research looks into compares the in-situ contact angles that the oil-water interface makes with the carbonate surface under water-wet and oil-wet conditions. The wetting preference of a carbonate plug before and after wettability alteration is investigated.

1.3. Informing Pore Network Models of the Pore-scale Fluid Displacement Physics for Heterogeneous Media

Another objective of this research is to inform pore-scale network models of the displacement processes that occur in complex carbonate pore systems. Simulation of fluid displacement processes using pore networks has received much attention in the previous decades (Fatt, 1956, Wilkinson and Willemsen, 1983, Reeves and Celia, 1996, Valvatne and Blunt, 2004, Joekar-Niasar and Hassanizadeh, 2012, Ryazanov et al., 2009). Pore-scale flow simulations have proven to be a successful approach in modelling a wide range of processes including: (a) prediction of macro-scale properties of the porous media, e.g. absolute and relative permeability, (b) study of the effectiveness of different improved oil recovery (IOR) methods such as water flooding, as well as enhanced oil recovery (EOR) methods such as chemical flooding, and miscible gas injection, and (c) study of the non-wetting phase fluid trapping and structure.

Reservoir simulation studies cannot take pore-scale processes into consideration. It is computationally impossible to simulate the micro-scale fluid-fluid-rock configurations in reservoir scale calculations. However, developing pore-scale models with correct implementation of fluid displacement physics provides a means to calculate the macroscopic flow properties of rocks, such as relative permeability, capillary pressure, residual oil saturation and structure, etc., which are in turn used in reservoir-scale models. (Blunt and Scher, 1995, Blunt and King, 1991, Blunt, 2001, Valvatne and Blunt, 2004, Patzek, 2000, S. R. McDougall 1997, Meakin and Tartakovsky, 2009, Ryazanov et al., 2009, Joekar-Niasar et al., 2008). Pore-scale imaging using μCT has enabled 3D validation of the a number of displacement processes (such as piston-like displacement and snap-off, see chapter 2, section 5) that were previously observed only in 2D, using micro-models. So far, investigations have been confined to pore-

scale mechanisms that happen in homogeneous samples, leaving the question of the possibility of having other naturally occurring processes in more heterogeneous pore systems unanswered. This research investigates the existence of other possible pore-scale mechanisms that can be imposed by complex structures of heterogeneous porous media.

2. Overall Work-flow of This Study

Figure 1.1 illustrates the overall work-flow of this study which is composed of experimental and modelling approaches.

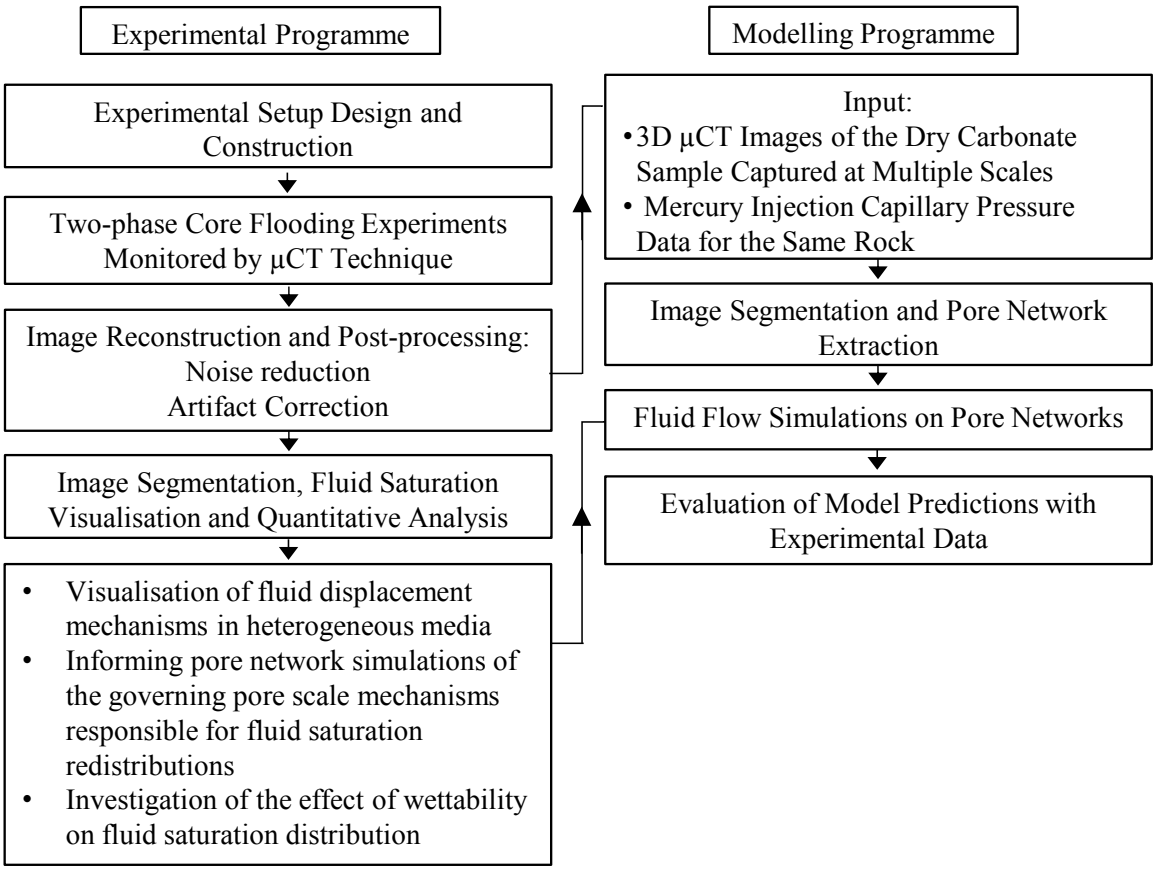

Figure 1.1: Overall work-flow used in this study. The study is composed of two parallel experimental and modelling approaches.

3. Tools Available to This Study

In the experimentation phase the following facilities were used:

- ECOSSE X-ray μCT instrument, University of Edinburgh (chapter 3, section 1)

- A simple X-ray transparent, low pressure core flooding system that was developed during this project (chapter 3, section 1)
- Scanning Electron Microscope (SEM) facilities at Heriot-Watt University and the University of Edinburgh.
- Optical microscopy laboratory, University of Edinburgh
- Petrobras Research Centre (CENPES) for the mercury injection capillary pressure tests

To process the μCT data sets three software packages were utilised:

- Octopus (v.8.5-8.7): used for image reconstruction from raw μCT outputs (described in chapter 2 section 3)
- Avizo (v.6-8): used for image quantification and analysis.
- Matlab (Image processing toolbox) and ImageJ software.

On the modelling side of this project the following pore network modelling packages developed at Heriot-Watt University were utilised:

- Pore analysis tools (PATs), (Jiang, 2008)
- Pore-scale fluid flow simulation code, (Ryazanov, 2012)

References:

ANDREW, M., BIJELJIC, B. & BLUNT, M. J. 2014. Pore-scale contact angle measurements at reservoir conditions using X-ray microtomography. *Advances in Water Resources,* 68**,** 24-31.

BLUNT, M. & KING, P. 1991. Relative permeabilities from two- and three-dimensional pore-scale network modelling. *Transport in Porous Media,* 6**,** 407-433.

BLUNT, M. J. 2001. Flow in porous media — pore-network models and multiphase flow. *Current Opinion in Colloid & Interface Science,* 6**,** 197-207.

BLUNT, M. J. & SCHER, H. 1995. Pore-level modeling of wetting. *Physical Review E,* 52**,** 6387-6403.

BURCHETTE, T. P. 2012. Carbonate rocks and petroleum reservoirs: a geological perspective from the industry. *Advances in Carbonate Exploration and Reservoir Analysis. Geological Society, London, Special Publications,* 370**,** 17-37.

FATT, I. 1956. The Network Model of Porous Media. Society of Petroleum Engineers.

HARTMANN, A., GOLDSCHEIDER, N., WAGENER, T., LANGE, J. & WEILER, M. 2014. Karst water resources in a changing world: Review of hydrological modeling approaches. *Reviews of Geophysics,* 52**,** 218-242.

IGLAUER, S., PALUSZNY, A., PENTLAND, C. H. & BLUNT, M. J. 2011. Residual CO_2 imaged with X-ray micro-tomography. *Geophysical Research Letters,* 38**,** L21403.

JIANG, Z. 2008. *Quantitative characterisation of the geometry and topology of pore space in 3D rock images.*

JOEKAR-NIASAR, V. & HASSANIZADEH, S. 2012. Analysis of fundamentals of two-phase flow in porous media using dynamic pore-network models: A review. *Critical Reviews in Environmental Science and Technology,* 42**,** 1895-1976.

JOEKAR-NIASAR, V., HASSANIZADEH, S. M. & LEIJNSE, A. 2008. Insights into the Relationships Among Capillary Pressure, Saturation, Interfacial Area and Relative Permeability Using Pore-Network Modeling. *Transport in Porous Media,* 74**,** 201-219.

MEAKIN, P. & TARTAKOVSKY, A. M. 2009. Modeling and simulation of pore-scale multiphase fluid flow and reactive transport in fractured and porous media. *Reviews of Geophysics,* 47**,** RG3002.

MORROW, N. R. A Review of the Effects of Initial Saturation, Pore Structure and Wettability on Oil Recovery by Waterflooding. North Sea Oil and Gas Reservoirs Seminar, 1987 1985 Trondheim. Graham and Trotman, Ltd., London, pp 179-191.

PATZEK, T. W. 2000. Verification of a Complete Pore Network Simulator of Drainage and Imbibition.

REEVES, P. C. & CELIA, M. A. 1996. A functional relationship between capillary pressure, saturation, and interfacial area as revealed by a pore-scale network model. *Water Resources Research,* 32**,** 2345-2358.

RYAZANOV, A. 2012. *Pore scale network modelling of residual oil saturation in mixed-wet systems.* PhD, Heriot-Watt University.

RYAZANOV, A. V., VAN DIJKE, M. I. J. & SORBIE, K. S. 2009. Two-Phase Pore-Network Modelling: Existence of Oil Layers During Water Invasion. *Transport in Porous Media,* 80**,** 79-99.

S. R. MCDOUGALL , K. S. S. 1997. The application of network modelling techniques to multiphase flow in porous media. *Petroleum Geoscience* 3**,** 161 - 169

TURNER, M. L., KNÜFING, L., ARNS, C. H., SAKELLARIOU, A., SENDEN, T. J., SHEPPARD, A. P., SOK, R. M., LIMAYE, A., PINCZEWSKI, W. V. & KNACKSTEDT, M. A. 2004. Three-dimensional imaging of multiphase flow in porous media. *Physica A: Statistical Mechanics and its Applications,* 339**,** 166-172.

VALVATNE, P. H. & BLUNT, M. J. 2004. Predictive pore-scale modeling of two-phase flow in mixed wet media. *Water Resources Research,* 40**,** W07406.

WILDENSCHILD, D., ARMSTRONG, R. T., HERRING, A. L., YOUNG, I. M. & WILLIAM CAREY, J. 2011. Exploring capillary trapping efficiency as a function of interfacial tension, viscosity, and flow rate. *Energy Procedia,* 4**,** 4945-4952.

WILKINSON, D. & WILLEMSEN, J. F. 1983. Invasion percolation: a new form of percolation theory. *Journal of Physics A: Mathematical and General,* 16**,** 3365.

Chapter 2

Literature Review

1. Carbonate rocks

1.1. Introduction

Significant amounts of water, oil and gas are contained and recovered from carbonate rocks (see chapter 1). It is, therefore, economically important to develop an understanding of carbonate mineralogy, formation, petrology and digenesis. This assists understanding of the fluid flow related characteristics of carbonates, such as porosity and pore connectivity. Carbonate rocks have complex 3D pore structure since they are composed of features of widely differing scale (from *nm* to *cm*), including lime muds, crystals, ooids and fossil fragments. Therefore, generating a model for their pore structure that is capable of simulating multiphase fluid flow reliably is not necessarily a straightforward task.

1.2. Carbonate Pore System Classification

The pore systems of sedimentary carbonate rocks are generally complex in terms of geometry and genesis, and commonly differ markedly from those of sandstones (Choquette and Pray, 1970). The most noticeable characteristic of carbonate reservoirs is their heterogeneity in pore structure which can result in complex fluid flow behaviour as well as uncertainty in reservoir performance predictions. Thus, classification of carbonate rocks based on petrophysical properties such as porosity and permeability is a practical approach used in reservoir characterization. To date, attempts to classify carbonate rocks have been based either on their lithological texture and composition or their pore types. Since the petrology of carbonate rocks is not the major concern of this study, carbonate classification based on lithological texture will be summarized only briefly. Carbonate classifications based on pore types are discussed in greater detail.

1.2.1. Origin of Carbonate Rocks

Carbonates differ from clastics in their origin, their formation process and their depositional area. A large proportion of carbonate materials can be produced either by inorganic (e.g. lime muds, ooids, sparry cements) or by biological processes (e.g. shells, corals, pellets). Both biological and inorganic materials can be mixed, often

reflecting different stages of development of the rock. They can be produced locally or transported into the depositional environment. Diagenetic processes are responsible for considerable alteration of carbonates, sometimes completely obliterating the primary texture of the rock.

Clastic rocks, by their nature, contain less biological material. They are mainly produced by physical processes, particularly the transport and deposition of materials eroded from older rocks and sediments. Clastic materials are usually sourced from beyond the local deposition environment.

1.2.2. Mineralogy

There are three main minerals in carbonate rocks: calcite, aragonite and dolomite. Calcite (rhombohedral system) and aragonite (orthorhombic system) are naturally occurring crystalline forms of calcium carbonate, $CaCO_3$. The third mineral, dolomite $CaMg(CO_3)_2$ also has rhombohedral symmetry.

1.2.3. Carbonate Classification based on Lithological Texture

Two of the most widely used classifications in this area have been proposed by Folk (1959) and Dunham (1962). As illustrated in Figure 2.1 Folk (1962) recognized four diagenetic materials: the allochems (particles), microcrystalline ooze, called micrite; crystalline calcite, called spar or sparite; and inter-grown fossiliferous reef rock, called biolithite. His scheme consists of five classes of carbonate rocks which were designated in geologic shorthand by the Roman numerals I, II, III, IV, V. Rocks with meso-crystalline spar between the allochems belong to class I. The Class II rocks have micrite filling the space between the allochems. Class III rocks have less than 10% by volume carbonate allochems. Class IV rocks are all "undisturbed bioherm rocks" which are almost synonymous with boundstone rocks defined by Dunham (1962).

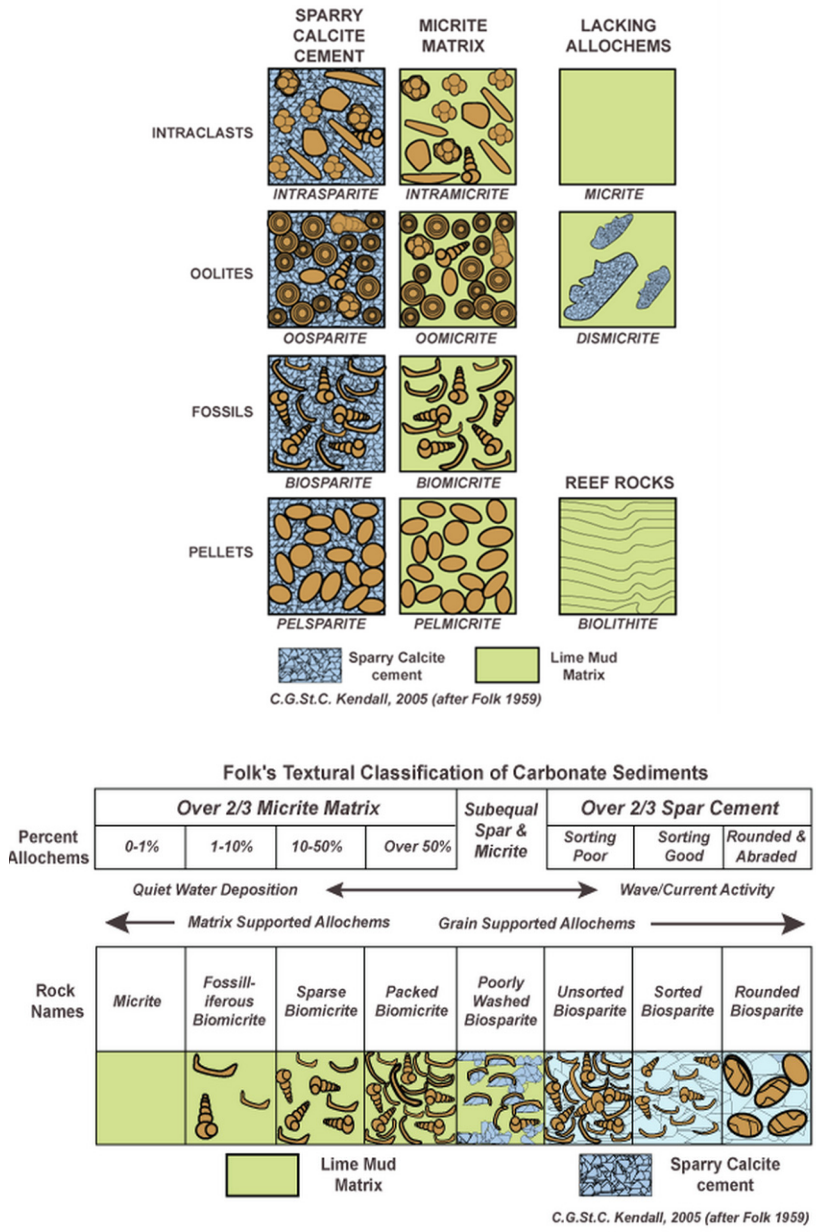

Figure 2.1: Classification of carbonate rocks and carbonate textures by Folk (1959), image from (http://www.sepmstrata.org/page.aspx?pageid=89).

Dunham (1962) used the relative amount of mud (equivalent to the term micrite used by Folk (1959)) to carbonate grains to define his four major allochemical limestone types of: mudstone, wackestone, packstone, and grainstone (Figure 2.2).

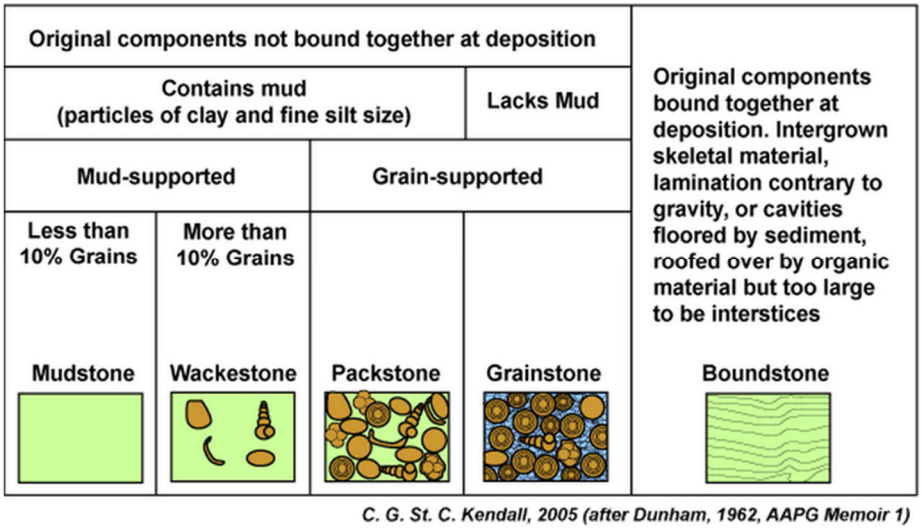

Figure 2.2: Classification of carbonate rocks and carbonate textures by Dunham (1962), image from (http://www.sepmstrata.org/page.aspx?pageid=89).

1.2.4. Carbonate Rock Classification based on Pore Types

Before 1952 porosity was not included in carbonate classifications, therefore these classifications are of limited application for reservoir engineers. At this time Archie (1952) pioneered the inclusion of porosity information in carbonate classification according to his observations of carbonate rocks under the microscope. He classified the pore space into matrix and visible porosity. Moreover, he introduced three matrix texture types (compact crystalline, chalky and granular) based on visible pore space between constituent's crystals. He also classified visible pores in four groups of A to D based on their size. Archie's classification was the first attempt to include petrophysical properties in rock typing and it forms the basis of later more advanced carbonate classifications.

Choquette and Pray (1970) proposed another pore system classification in which they divided the porosity types into two main classes of fabric selective and non-fabric selective, as shown in Figure 2.3. This model is widely used by geologists in geological modelling studies.

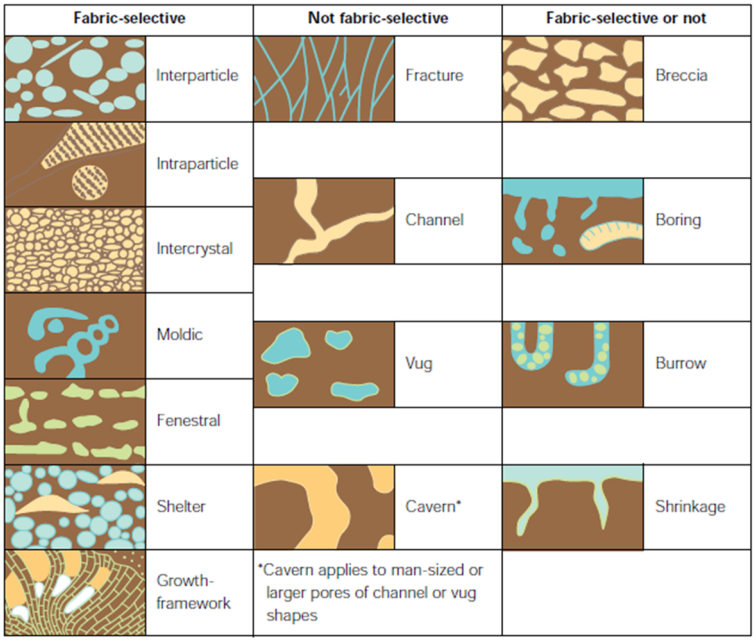

Figure 2.3: Classification of carbonate rocks and carbonate textures by Choquette and Pray (1970), image from Akbar et al. (1995).

However, since this model is more focused on the genesis of pore space and not petrophysical properties of pore system it is of limited application for dynamic studies.

Lucia (1983) made an attempt to develop Archie's pore system classification based on the idea of classifying carbonate rocks in terms of both rock fabrics and petrophysical properties. In order to link the pore classification to fluid flow properties more directly Lucia focused on correlating the porosity and permeability of carbonate rocks. He showed that, unlike sandstones, there is no particular correlation between porosity and permeability of carbonate rocks unless the pore-size distribution is taken into account. He used Dunham's carbonate texture classes in his proposed pore system and similar to Archie, Lucia (1995) divided the carbonate pore space into inter-particle and vuggy porosity groups. As shown in Figures 2.4 and 2.5 the inter-particle pore space is sub-sectioned into three classes based on particle size and sorting.

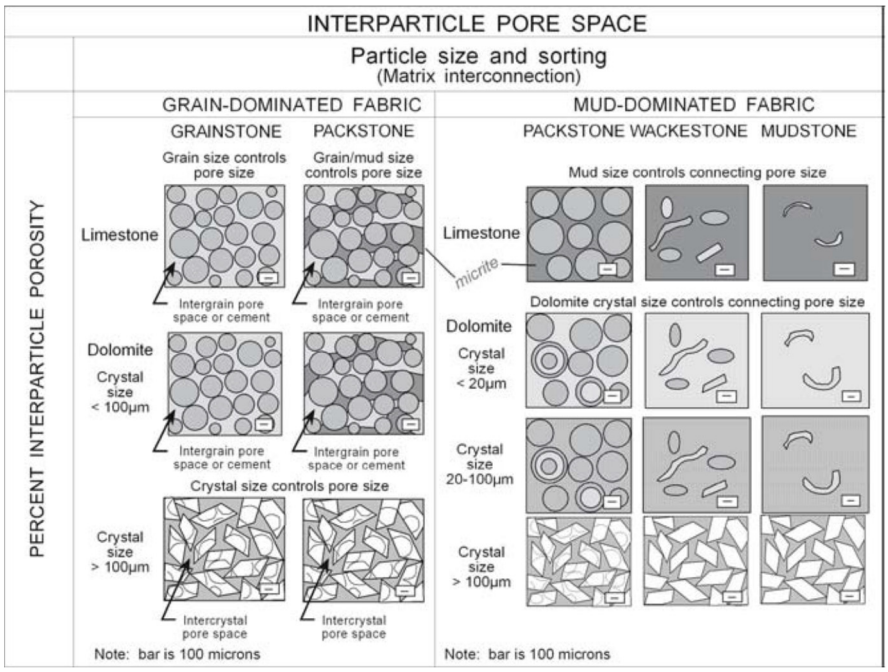

Figure 4: Inter-particle pore space sub-classification, image from Lucia (1995).

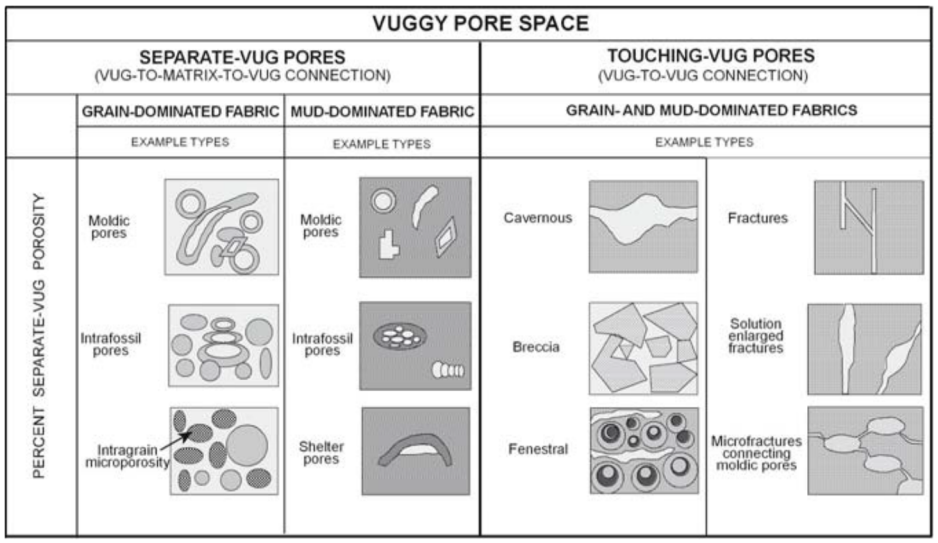

Figure 2.5: Vuggy pore space sub-classification, image from Lucia (1995).

Lønøy (2006) realized that Lucia's pore classification has some weaknesses while trying to apply Lucia's classification system to a Norsk Hydro database. Lønøy found that there is a significant difference in permeability trends between interparticle and intercrystalline porosity, the two pore types that are grouped

together in Lucia's classification. Lønøy argued that Lucia had neglected the effect of cement and grain sorting on pore-size. To improve Lucia's classification, Lønøy proposed a new pore classification system including 20 pore type classes based on pore type, pore-size and pore distribution (Figure 2.6).

In this pore classification system, porosity distribution was a new element that had not been previously considered by Lucia. Lønøy classified pores either as uniform or patchy porosity and reported that for similar porosities the samples with patchy porosity distributions have more permeability compared with uniformly distributed porosity rocks. This is because of the concentration of pores in a smaller volumes and thereby better connectivity of the patchy distributed porosity rocks. Consequently Lønøy presented 20 different permeability-porosity cross plots based on his classification. The trend line coefficients of determination (R^2) assigned to each pore class were significantly improved compared to other classifications.

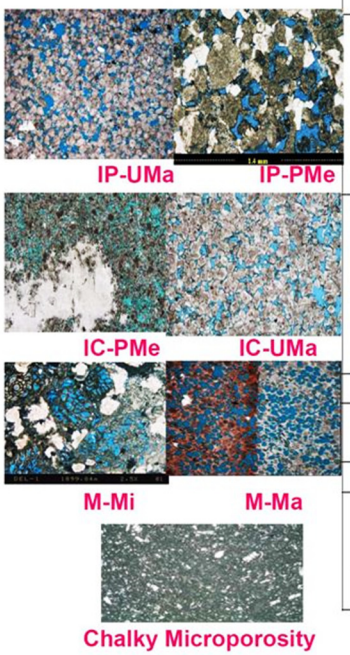

Pore Type	Pore Size	Pore Distribution	Pore Fabric
Interparticle	Micropores (10-50 μm)	Uniform	Interparticle, uniform micropores
		Patchy	Interparticle, patchy micropores
	Mesopores (50-100 μm)	Uniform	Interparticle, uniform mesopores
		Patchy	Interparticle, patchy mesopores
	Macropores (>100 μm)	Uniform	Interparticle, uniform macropores
		Patchy	Interparticle, patchy macropores
Intercrystalline	Micropores (10-20 μm)	Uniform	Intercrystalline, uniform micropores
		Patchy	Intercrystalline, patchy micropores
	Mesopores (20-60 μm)	Uniform	Intercrystalline, uniform mesopores
		Patchy	Intercrystalline, patchy mesopores
	Macropores (>60 μm)	Uniform	Intercrystalline, uniform macropores
		Patchy	Intercrystalline, patchy macropores
Intraparticle			Intraparticle
Moldic	Micropores*		Moldic micropores
	Macropores*		Moldic macropores
Vuggy			Vuggy
Mudstone microporosity	Micropores (<10 μm)		Tertiary chalk
			Cretaceous chalk
		Uniform	Chalky micropores, uniform
		Patchy	Chalky micropores, patchy

Figure 2.6: Lønøy (2006) pore system classification associated with thin section images of some classes, image from Lønøy (2006).

Among the presented carbonate classification systems the pore based systems of classification (i.e. Archie, Lucia and Lønøy classifications) are more relevant for studies of fluid flow in pore space of carbonates.

Diverse materials and origins of carbonate rock creates complexity in their pore structure. A robust characterization tool is therefore required to study the carbonate's porosity in 3D. Computed tomography techniques are a good candidate for such studies. However, due to their structural complexity compared to idealised systems (e.g. bead packs) and many clastic rocks, there are relatively few publications that deal with the characterization of carbonate rocks by means of μCT, and especially where fluid flow experiments are included.

2. X-ray Computed Tomography as a Characterization Tool

X-ray Computed tomography (CT) was first introduced in medical science as a non-destructive technique to investigate internal parts of human body in 1971. Sir Godfrey Newbold Hounsfield, an English electrical engineer, is known for the invention of the first CT scanning device. He shared the 1979 Nobel Prize for Physiology or Medicine with Allan McLeod Cormack for his part in developing the diagnostic technique of X-ray computed tomography. CT then found its way to industrial sectors. A brief overview of the physics of CT technique and its applications is presented here, for more details the reader is referred to: (Akin and Kovscek, 2003, Wildenschild and Sheppard, 2013, Ketcham and Carlson, 2001), Akin and Kovscek, 2003, Wildenschild and Sheppard, 2013.

2.1. X-ray Physics

2.2.1. X-ray Generation

X-ray photons are generated when accelerated charged particles strike the surface of a target material. Two types of interactions occur during the electron bombarding process, first and more applicable is the Bremsstrahlung interaction which takes place while accelerated electrons are affected by the presence of an electric field near the nucleus. Attractive forces change the electron path and deceleration occurs. The

produced Bremsstrahlung radiation energy is equal to the electron's energy loss. Second interaction is called K-shell interaction. It happens when an accelerated electron displaces an electron from an inner shell of a target atom. The displaced electron will be replaced by an electron from an outer shell level with a higher energy. The falling electron emits a characteristic photon during the replacement process (Figure 2.7). The photon energy is equal to the energy difference of the two shells.

$$E_i - E_f = h \times f \tag{2.1}$$

where E_i and E_f are initial and final energy states respectively, h is Planck's constant and f is the frequency of emitted radiation.

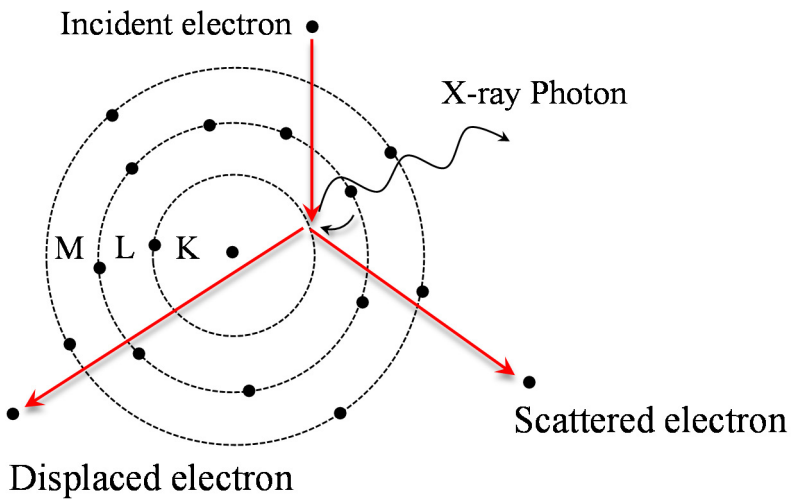

Figure 2.7: X-ray generation by electron bombarding a Si atom. Image from (http://li155-94.members.linode.com/myscope/analysis/eds/xraygeneration/characteristic/).

2.2.2. Interaction of X-radiation with Matter:

X-rays are attenuated as they pass through an object by interactions of the X-ray photons with the atoms in the object. As depicted in Figure 2.8, there are two main interactions between X-ray photons and the electrons of the object's atoms. First is the photoelectric interaction which happens whenever the incident photon gives its entire energy to remove a deep shell electron out of its place. Consequently, an outer shell electron falls into the inner shell and emits a characteristic photon. Second is

the Compton interaction which happens when the interacting photon has much more energy than is required to liberate an electron from its shell level. As a result the incident photon will experience an energy loss and will be deflected out of the atom. The deflected X-ray photon is able to further interact with other atoms.

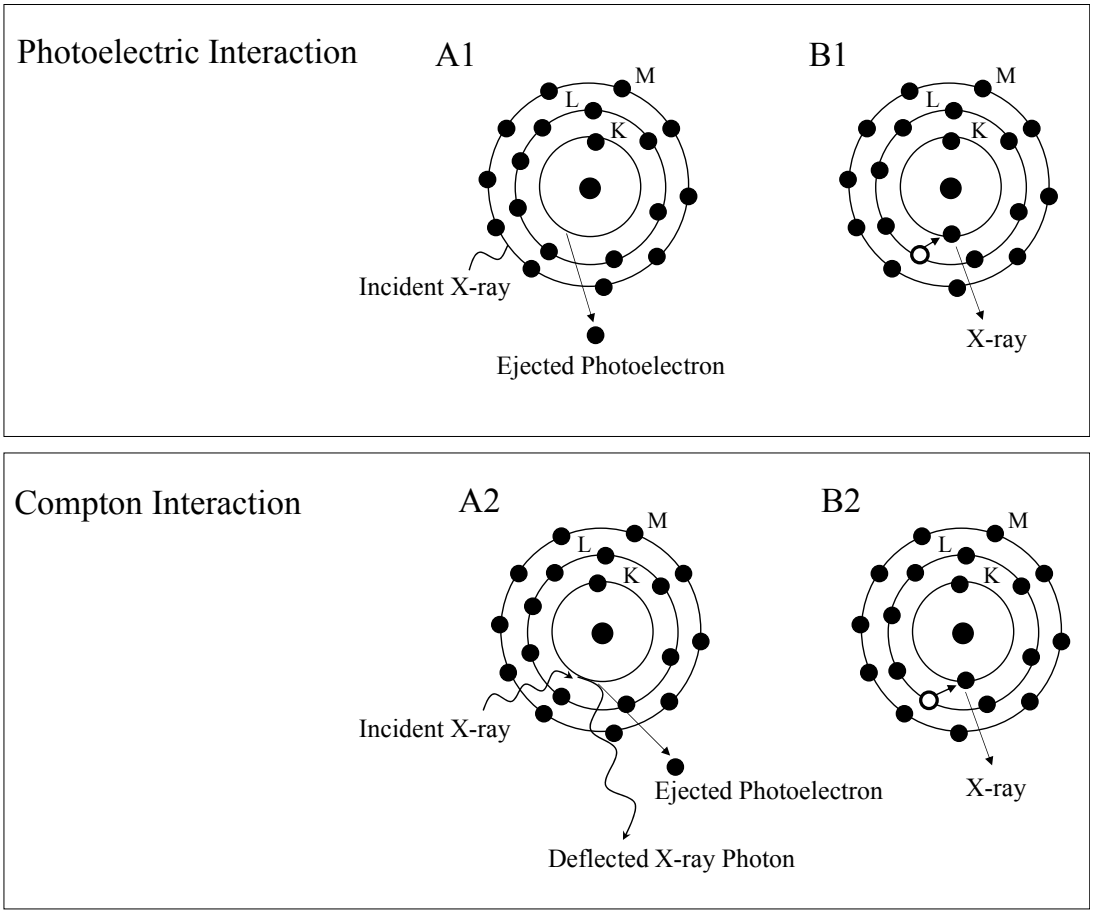

Figure 2.8: Main interactions between X-ray photons and object's electrons. (A1 and B1) show the photoelectric interaction and (A2 and B2) show Compton interactions.

The Beer-Lambert law (eq. 2.2) provides an exponential relationship between the incident and transmitted X-ray intensities. This simple relationship is applicable in a wide range of applications in which light interacts with matter (e.g. colourimetry). In this correlation it is assumed that the incident photon is monochromatic and the object is homogeneous.

$$I = I_0 \, e^{-\mu L} \tag{2.2}$$

where I_0 is the incident radiation intensity, I is the exit radiation intensity, μ is the attenuation coefficient and L is the object thickness. The attenuation coefficient is expressed as:

$$\mu = \tau + \sigma \tag{2.3}$$

where τ and σ are photoelectric and Compton attenuation coefficients, respectively. The photoelectric absorption coefficient (τ) is dependent on the atomic number while the Compton attenuation coefficient (σ) is a function of bulk density of the material. The energy of the X-ray photons governs the relative importance of the photoelectric and Compton effects. As shown in Figure 2.9 at low photon energies the photoelectric interaction is dominant while the effect of the Compton interaction is more pronounced at higher photon energies. Photoelectric attenuation is in proportion to a power of the atomic number of the interacting atoms while Compton scattering is proportional to the electron density, which approximates to the bulk density.

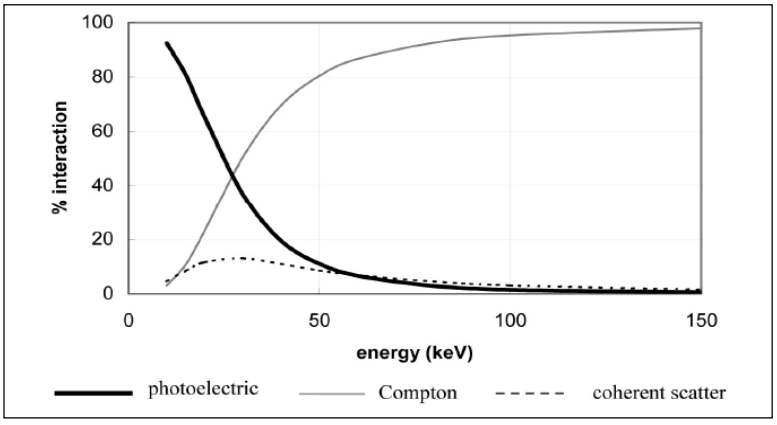

Figure 2.9: Effect of X-ray energy on the type of interaction happens with material, image from Hsieh (2009). The photoelectric interaction is predominant at X-ray energies below 100 keV, while Compton scattering becomes progressively more important for X-ray energies above 100 keV.

The attenuation coefficient is subject both to the material and X-ray energy. The simple form of the Beer-Lambert law (eq. 2.2) is only valid for a single material interacting with monochromatic X-rays. However, in reality the object under

investigation may be a complex mixture of two or more different materials, and in the case of industrial scanners X-ray beams comprising a range of energies are used. To apply the Beer-Lambert's law for a complex object, the object is assumed to be subdivided into several smaller divisions which are uniform (Figure 2.10). Hence, for a non-uniform object interacting with monochromatic X-rays the Beer-Lambert's law is formulated as:

$$\frac{I}{I_0} = \exp\left(\sum_i^n (-\mu_i x_i)\right) \tag{2.4}$$

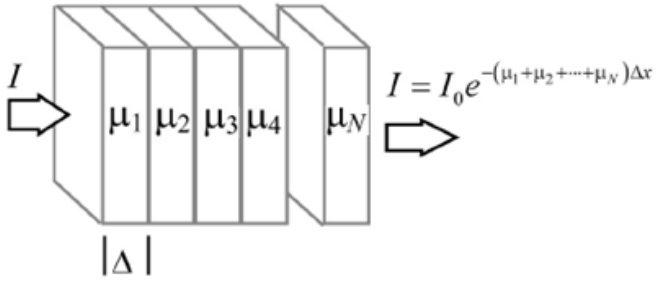

Figure 2.10: Any non-uniform object can be subdivided into multiple elements. Within each element, a uniform attenuation coefficient can be assumed. The Beer–Lambert law can then be applied in a cascade fashion, image from Hsieh (2009).

A further modification to the Beer-Lambert law is required for polychromatic X-rays, and so for a non-uniform object interacting with a range of X-ray energies:

$$I = \int I_0(E) \exp\left(\sum_i^n (-\mu_i(E) x_i)\right) dE \tag{2.5}$$

Using these equations a different attenuation coefficient could be assigned to each voxel (3D unit) of the object under inspection. In practice, when a polychromatic beam is used, the attenuation coefficients that are assigned to the object's voxels are the effective attenuation coefficients rather than the absolute attenuation coefficients. The effective attenuation coefficient depends on both the properties of the object under inspection and the range of X-ray energies of the beam. On this basis an object displays different effective attenuation coefficient when scanned using polychromatic beams with different spectrum. The practical consequence is that

calibration of greyscales to absolute attenuation coefficient of a sample that is scanned by a polychromatic beam is complex.

2.2. X-ray CT Scanners

2.2.1. Medical CT Scanners

The main components of any X-ray tomography instrument are: (a) an X-ray source, (b) an X-ray detector, and (c) a means to rotate either the object under inspection, or the source and detector concentrically around the object. In medical scanners the images are captured during a translation-rotation movement of the source-detector components around the patient. In industrial CT scanners, however, the source and detector are fixed and the sample is rotated by means of a rotary table.

Figure 2.11 illustrates the geometry of medical scanners classified into four generations according to the geometry of their source-detector components and their movement method during the scanning process (Ketcham and Carlson, 2001). Scanning time is of particular importance for medical scanners since the investigated object is a human body, therefore minimisation of the exposure time is crucial. Advances in the design of medical scanners resulted in reduction of the acquisition times to less than 100 ms (Flohr et al., 2009). The spatial resolution of medical scanners, however, remained limited to several hundreds of micro-meters (Cnudde and Boone, 2013).

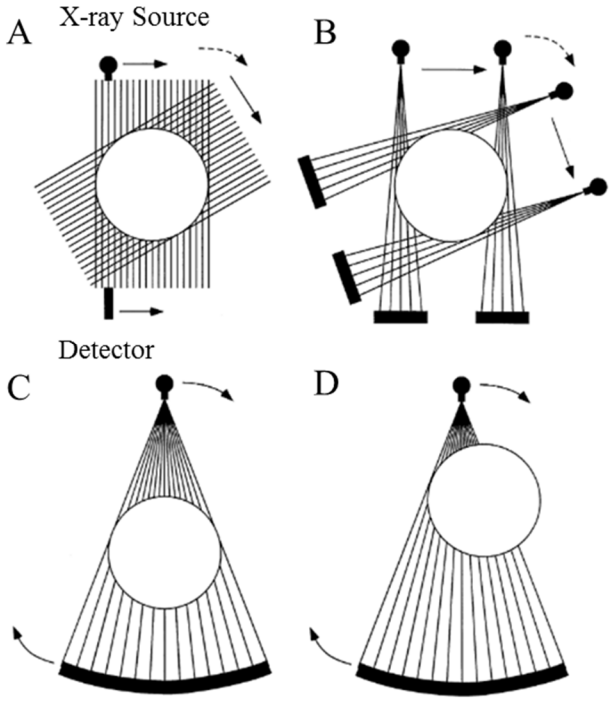

Figure 2.11: Different generations of medical CT scanners, image from Ketcham and Carlson (2001), A-D: First-fourth generation CT scanners respectively. The scanning time was shorter in the later generations.

Many early 3D imaging studies of geological samples utilized medical CT instruments, see the reviews by Akin and Kovscek (2003) and Cnudde and Boone (2013). However, the coarse resolution of the images acquired by medical scanners limited their application for studies of pore-scale processes. Core analysis laboratories utilise medical scanners in core screening process, during which reservoir cores are scanned upon their arrival to the laboratory and prior to any subsampling practices. Core screening provides broad information on the lithological structures such as fractures, beddings and heterogeneities of the cores. In addition, the materials that constitute the rock can be derived based on the calculated X-ray attenuation coefficient of the sample.

Scanning Geometry

Figure 2.12 depicts different scanning geometries. First and second generation medical scanners used parallel beam geometry to collect data while third and fourth

generation scanners used the fan beam pattern. The other scanning mode is referred to as cone beam (Figure 2.12C), which allows geometric magnification. The design covers a volume section of an object in a single shot. The relative distances of (sample-source) to (sample-detector) and the camera pixel dimensions determine the degree of magnification and the ultimate resolution of the image. Therefore, the smaller the sample, the closer it can be to the X-ray source and the higher the resolution of the acquired image becomes. The trade-off between the sample size and the achievable image resolution is one of the primary parameters considered in designing the experiments which involve μCT imaging.

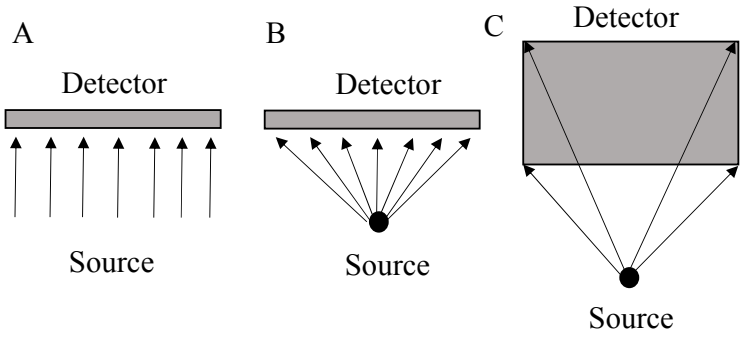

Figure 2.12: Different scanning geometries of parallel beam (A), fan beam (B), and cone beam (C).

2.2.2. Industrial CT Scanners (μCT)

The ability to analyse the internal parts of an object without destroying it led to computed tomography being used in industrial sectors. Computed tomography is considered as a practical tool for characterization of fluid flow in porous media (Akin and Kovscek, 2003, Wildenschild and Sheppard, 2013, Ketcham and Carlson, 2001). Micro-scale resolution tomography data (μCT) can be acquired using laboratory based μCT scanners as well as synchrotron facilities. Industrial μCT units differ from medical scanners in scanning time, X-ray energy, device configuration, and the ultimate image resolution. Industrial scanners work with the cone beam X-ray beam configuration which improves the acquisition time as well as the image resolution compared to medical scanners. To achieve resolutions down to micro-meters

industrial scanners benefit from micro focus X-ray sources. The electron beam footprint of a micro focus tube is only a few microns in size, and can yield up to 100 times better resolution compared to medical scanners.

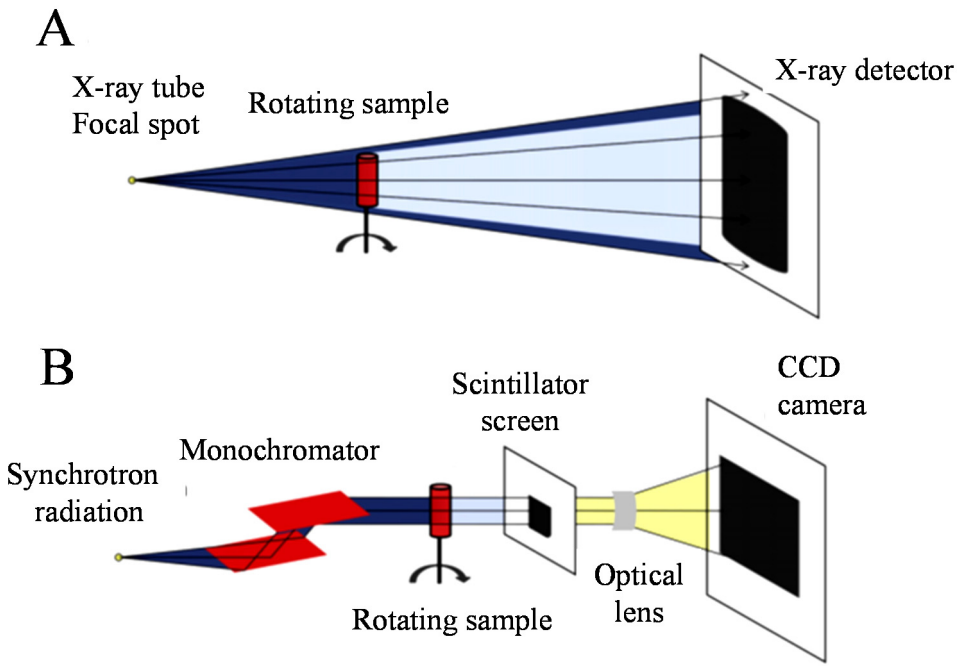

Figure 2.13: Schematic drawings of laboratory based (A) and synchrotron (B) µCT scanners. Synchrotron scanners benefit from mono-chromatic beams which improves the image quality by minimising the beam hardening artifact. Image from Cnudde and Boone (2013).

Figure 2.13A and 2.13B shows schematic drawings of laboratory based µCT and synchrotron scanners, respectively. The main difference between these two scanning devices is the X-ray source. Laboratory based scanners use X-ray tubes which generates X-ray beams with a range of energies (referred to as poly-chromatic beam). In contrast, synchrotron facilities benefit from X-ray beams with a narrow range of energies, (referred to as mono-chromatic beam) filtered by the monochromator Figure 2.13B. Monochromatic beams improve the quality of the acquired data by minimising beam hardening artifact, for more details refer to section 5.2. For detailed information about synchrotron imaging techniques and applications the reader is referred to a recent review paper by Fusseis et al. (2014).

The main advantages of synchrotron facilities over the laboratory based μCT scanners are (a) the shorter data acquisition time (due to higher photon flux), (b) the monochromatic X-ray beam, and (c) the parallel X-ray beam (that reduces the blur). However, access to synchrotron facilities can be limited and sporadic. Laboratory based scanners are useful for performing long experiments which may extend over several days or weeks on dedicated instruments.

2.3. Image Resolution

Image resolution is mainly dependent on (a) the X-ray source spot size (b) the detector's pixel size, and (c) the geometric magnification (Feser et al., 2008). The X-ray source spot size is dependent on the X-ray energy generated by the source, this information is available in the X-ray source user manual in form of a spot-size vs. X-ray energy plots. Any X-ray detector has a specific resolution which is its physical pixel size (r_D). The geometric magnification can, however, be different depending on how close to the X-ray source the sample is placed. Geometric magnification, M, is defined as:

$$M = \frac{a+b}{a} \tag{2.6}$$

Where a and b are the source to object and object to detector distances, respectively (see Figure 2.14). The closer the sample is placed to the X-ray source the more magnified the projections become. X-ray spot size introduces a blurring effect in the image as shown in Figure 2.14. The extent of blurring is controlled by the X-ray spot size (S) which can be calculated as:

$$r_S = S\left(\frac{b}{a}\right) \tag{2.7}$$

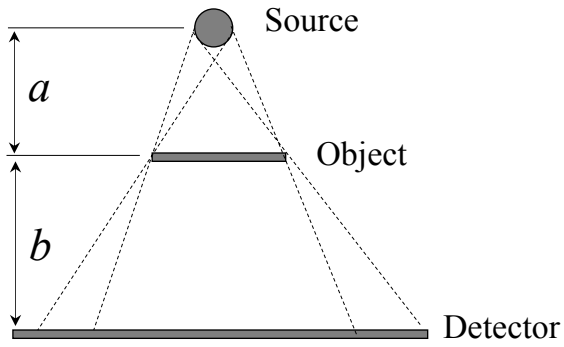

Figure 2.14: The extended size of X-ray source controls the blurring of the images.

The higher the magnification the more pronounced the image blurring becomes. Taking all these three above mentioned factors into account the total image resolution is defined as:

$$r_{total} = \frac{\sqrt{r_S^2 + r_D^2}}{M} \tag{2.8}$$

where r_S is the blurring and r_D is the detector resolution (pixel size). The spot size of the ECOSSE scanner's X-ray source is12 ± 1 μm. This data is obtained from the source manual for the X-ray energy of 120 keV. The source to detector distance is 416 mm. The camera pixel size is 48 μm. The total image resolution for the different experiments performed in this research are presented in chapter 3, section 4.

3. Image Processing

3.1. Image Reconstruction

The output of the data acquisition process is a set of raw data, called projections, which represents the X-ray image of the object collected through a full 360º rotation. Figure 2.15A illustrates a single projection of a carbonate sample recorded in the plane normal to the axis of the X-ray cone. During the acquisition process the sample is rotated and a few hundred to a few thousand 2D images are captured from different views (i.e. different scanning angles). A projection at a given angle is the integral of the X-ray attenuation in the direction specified by that angle. Figure 2.15B

illustrates multiple projections throughout an entire rotation presented in another space called sinogram space, in which the vertical axis represents the projection angle while the horizontal axis represents the detector row. The mathematical concept behind building the sinograms and their application is described in appendix.

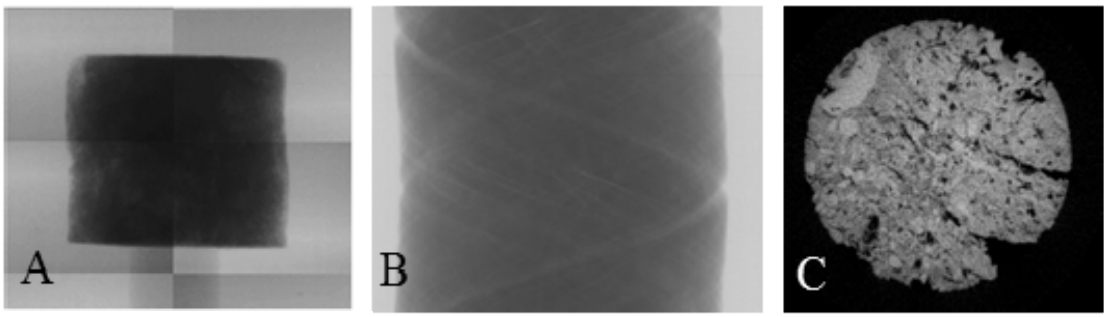

Figure 2.15: A single projection of a carbonate rock sample in the XY plane (A), the same projection presented in Sinogram space (B), a reconstructed slice using Octopus software (C).

In practice, reproducing a set of 2D images (slices) normal to the axis of rotation of the object (and later a 3D image of the sample) from a set of projections is an inverse problem in which the desired information is not directly available. The measured data are a transformed form of the image, therefore to recover the image the measured data should be inversely transformed. The final goal is to assign a 3D attenuation distribution map to the object based on the projections. In this study Octopus (v8.5-8.7) software (Vlassenbroeck et al., 2010) was used to reconstruct images from raw projections. The reconstruction method implemented in Octopus (v8.5-8.7) software is the filtered back projection (FBP) method. It is an improved version of the simple back projection (SBP) method. In SBP method the image is reconstructed by taking each projection and smearing the data along the acquired path and adding up all the projections as illustrated in Figure 2.16. The result gives a blurry image of the object. FBP method was introduced by Feldkamp et al. (1984) to correct the blurring associated with the simple back projection technique. It is the most common technique of image reconstruction in computed tomography. As depicted in Figure 2.17 in filtered back projection method each view is first filtered before the back projection, this corrects the blurring and delivers a sharper image.

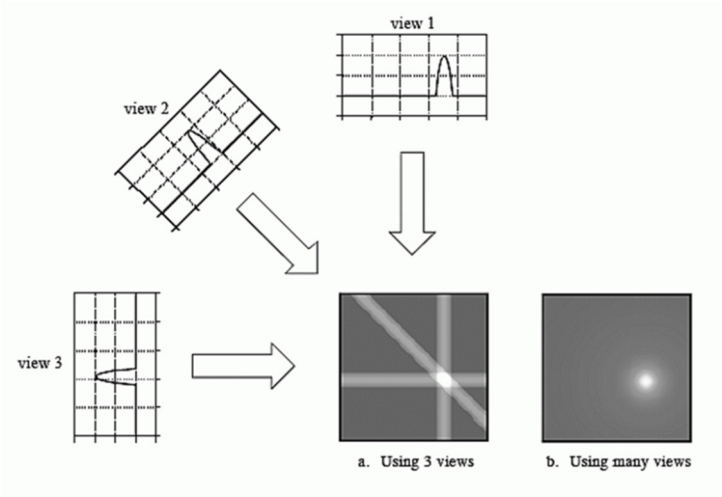

Figure 2.16: Simple back projection method for image reconstruction, image from (Smith, 1997).

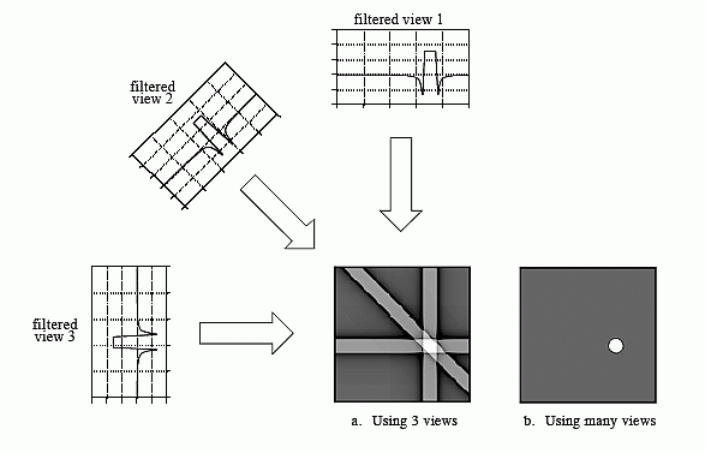

Figure 2.17: Filtered back projection - Image reconstruction, image from (Smith, 1997).

3.2. Image Artifacts

An image artifact is referred to any discrepancy between the reconstructed values in an image and the true attenuation coefficients of the object (Hsieh, 2009). Based on this broad definition, any CT image is associated with artifacts. These include: beam hardening, ring artifacts, and partial volume effects.

3.2.1. Beam hardening

According to Beer's law when a monochromatic X-ray beam travels through a homogeneous object, the total X-ray attenuation displays an exponential relationship with the thickness of the object along the incident X-ray path. However, the X-ray beams generated by laboratory CT sources are polychromatic. When a polychromatic beam passes through a homogeneous object (i.e. an object that is made of a single material), the X-ray photons with lower energy levels are absorbed firstly. As a result the X-ray beam becomes harder (with higher mean photon energy). Therefore, although the scanned object is made of a uniform material, the voxels close to the object boundary display higher attenuation coefficient and hence appear as brighter. This is referred to as beam hardening. A line profile drawn on a reconstructed beam-hardened CT slice displays a "cupping" of image brightness (and hence the calculated attenuation coefficient), as it is depicted in Figure 2.18.

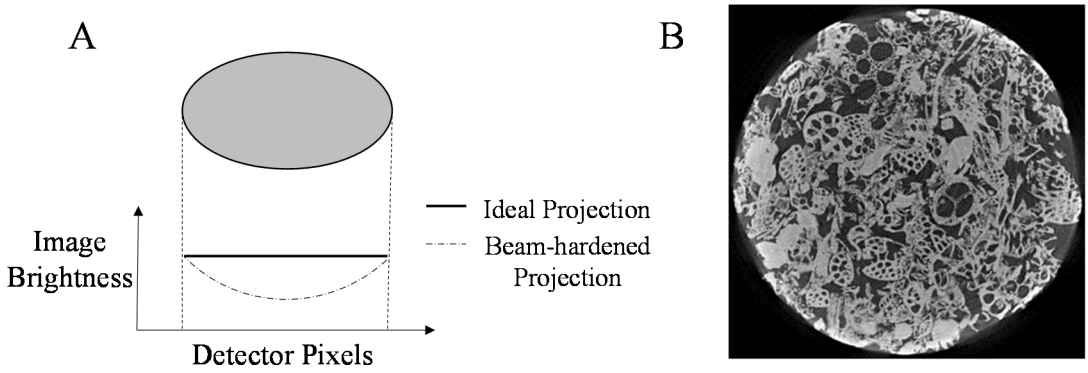

Figure 2.18: Beam hardening artifact manifests as a cupping of the intensity line profile. (A) Although the sample is made of a uniform material, the beam-hardened image is brighter on the edges and darker in the middle (Barrett and Keat, 2004), (B) Example µCT image of Mt Gambier limestone (made of pure calcite, sample diameter: 5 mm) with an overlying beam hardening artifact, image from Wildenschild and Sheppard (2013).

Removing this artifact is essential for effective image analysis and reliable data quantification. The impact of beam hardening can be limited during data acquisition by narrowing the broad X-ray source spectrum by introduction of a hardware filter such as a thin metal plate between the source and the object or between the object and the camera. The lower energy photons are absorbed by the metal plate and do not

interact with the detector. Although hardware filters reduce beam hardening, filtering out the photons results in a decrease of the signal to noise ratio, which may be undesirable. Alternatively, it is possible to reduce the beam hardening effect by post-processing the reconstructed images to correct for the effect. In this study both hardware filtering and a beam hardening correction implemented in octopus software is used. The method uses an adjustable four parameter polynomial correction to modify the greyscale values across the reconstructed slice.

3.2.2. Ring Artifacts

Ring artifacts are caused by non-linear drift of detector pixels. As a result complete or partial rings (centred on the rotational axis of the object) appear on the reconstructed images (Figure 2.19). For example a dead pixel on the detector can cause a full ring to overlap the reconstructed data. Anomalies in the detector response stem from several factors such as a change in the temperature or beam strength. For instance when the detector response is calibrated through air, relative response of the detector can change if the beam hardness is affected by passing through the object. In addition, the heterogeneity of the object affects the degree of beam hardening in different views. Ring artifacts could be partly suppressed using a filtered or sufficiently high-energy X-ray beam during the scanning stage. It can also be remedied by deliberate movement of the camera in the plane of data acquisition. Ring artifacts can be corrected during the reconstruction process. In sinogram space the ring artifacts appear as vertical lines, the software can detect and remove these vertical lines during the reconstruction process. However, this may become problematic if the object has different features tangent to circles centred on the rotational axis. Therefore, ring filters should be applied wisely to prevent significant blurring of the original ring shaped features.

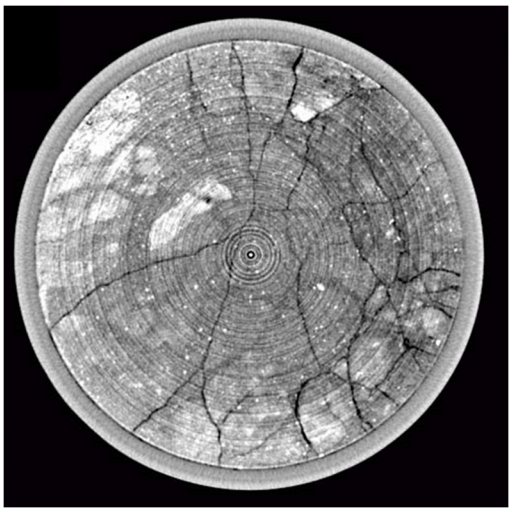

Figure 2.19: Ring artifact on a CT scan of a rock sample, diameter: 15.24 cm, image from Ketcham and Carlson (2001).

3.2.3. Partial Volume Effect

This artifact is commonly observed in CT images of heterogeneous material such as human organs or carbonate rocks. When the resolution of an image is not enough to capture all the fine heterogeneities in separate voxels some voxels represent a combination of the response of multiple phases. Having heterogeneities smaller than the image resolution makes the scanner unable to differentiate between a small amount of high-density material and a larger amount of lower density material. The processor tries to average out the two densities or structures, and a part of the information is lost. One example is the partial volume artifact that appears in voxels composed of both porosity and solid phases as indicated in Figure 2.20. In such boundary voxels the software will return a value by averaging attenuation coefficients of two phases. This can be partially overcome by scanning using thinner slices to enhance the image resolution.

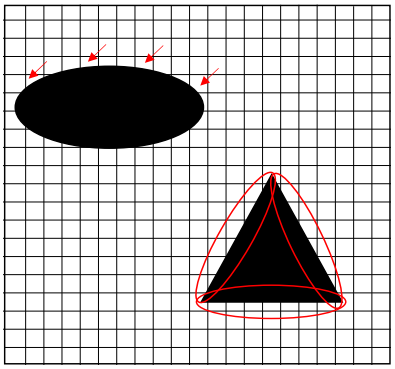

Figure 2.20: Partial volume effect. Pixels around the boundary of the objects (shown by the red arrows and ellipses) are composed of both phases appear, they appear as blurry on the reconstructed images.

Partial volume effects appear as "blurring" over sharp edges. This is quite apparent in rock images captured by medical scanners in the early studies of rocks using computed tomography (Wellington and Vinegar, 1987, Withjack, 1988). The interpretation of CT values in voxels containing multiple components is not straightforward. One approach is to approximate the CT value (attenuation coefficient) of a voxel containing multiple phases by a linear combination of the CT values (attenuation coefficients) of the pure phases according to their volumetric proportions (Wellington and Vinegar, 1987). This provides a reasonable solution if the attenuation values of the different phases are fairly close.

Subsequent to reconstruction, images undergo a series of post-processing steps to (a) suppress digital noise, (b) separate discrete components of the object, and (c) perform quantitative analysis on the images. Noise filtering, segmentation and object identification steps are discussed in detail in chapter 3, section 3.

4. Core Flooding Experiments

In petroleum engineering the conventional method to experimentally investigate fluid flow in porous rocks is core flooding experiments whereby one or more fluids are injected in a rock core. Flow rate, pressure, and composition of the injection and production fluid streams, as well as the temperature of the system are among the parameters which can be monitored during the flooding tests. Properties of the rock

(such as absolute permeability), or the rock–fluid system (such as relative permeability curves) are derived based on the data acquired in core flooding experiments.

Depending on the wettability (see section 8) of the media the process of displacing oil with water is referred to as a drainage or imbibition process. Drainage is the process of displacing the wetting phase by injection of the non-wetting phase (Figure 2.21). During a drainage process the saturation of the wetting phase progressively decreases until it reaches its minimum saturation value referred to as "irreducible wetting phase saturation". Imbibition happens when the wetting phase displaces a non-wetting phase out of a porous media (Figure 2.21). The saturation of the non-wetting phase decreases in an imbibition process until it reaches a minimum value, the "residual non-wetting phase saturation, $S_{nw\text{-}r}$".

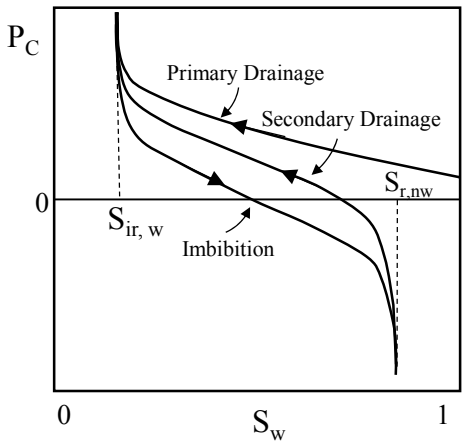

Figure 2.21: Example capillary pressure curves as a function of the wetting phase saturation in different displacement cycles of drainage and imbibition. The arrows show the direction of fluid displacement. $S_{r,nw}$: shows the point at which the non-wetting phase is at its residual saturation state and $S_{ir,w}$ shows the point at which the wetting phase is at its irreducible saturation state.

Three different core flooding techniques are commonly used in special core analysis laboratories (SCAL): (a) steady state, (b) unsteady state and (c) centrifuge. The centrifuge method is incompatible with in-situ CT scanning and is not considered herein.

4.1. Steady state flooding

The two fluid phases are injected simultaneously (co-injection) into the core plug at a fixed flow-rate ratios in a number of steps. At each step the injections are carried out until the fluid saturations and the injection and production pressures reach an equilibrium state. The pressure drop across the core is then measured. It is also possible to scan the core at the equilibrium state. The experiment can be continued by application of a new injection ratio and scanning under a new set of equilibrium conditions. Although this technique is compatible with CT scanning techniques, it is time consuming.

4.2. Unsteady state method

This method was developed by Buckley and Leverett (1942) and extended by Welge (1952). In the unsteady-state technique the core is first saturated with water to S_w=100%. Subsequently, the plug is de-saturated by oil (representing primary drainage) until the water production is stopped. The displacement can be continued

sequentially to model imbibition and secondary drainage. The method is relatively simple and rapid but requires more sophisticated data analysis. In this study the unsteady-state method was used. More details about the experimental procedure is presented in chapter 3, section 4.

4.3. Monitoring of Core Floods using μCT– A Literature Report

In the geoscience context, many studies have utilised μCT as a rock characterisation tool (Sakellariou et al., 2004, Lindquist et al., 2000, Arns et al., 2005, Okabe and Blunt, 2007, Taud et al., 2005, Ketcham and Iturrino, 2005). In this class of studies a dry piece of rock is scanned using either a laboratory-based μCT scanner or a synchrotron imaging facility. The 3D data obtained can also serve as an input to pore network models (Valvatne and Blunt, 2004, Jiang, 2008, Dong and Blunt, 2009). On the other hand, over the past three decades there have been numerous attempts to monitor fluid flow in porous media using X-ray CT. Relevant studies can be classified into two groups by means of the type of CT scanner utilized, i.e. medical CT scanners, μCT scanners (including laboratory-based μCT units, and synchrotron μCT facilities). Due to the resolution limitations the application of the medical scanners are limited to the whole core processes rather than the detailed pore-scale processes. The introduction of industrial μCT scanners provided higher image resolution (down to sub-micron); this made the μCT technique a promising tool for quantitative study of the fluid flow processes in porous media.

Laboratory-based μCT scanners have become an essential part of modern core analysis laboratories. They offer high resolution images at the cost of smaller sample sizes, typically few μm resolution for few mm sample size. Data acquisition for such scanners is typically in the region of a few 10s of minutes to several hours. As a consequence, laboratory-based μCT scanners have limited application for the study of fast, dynamic processes. In contrast, time resolution down to a fraction of second is achievable in synchrotron imaging facilities. Moreover, μCT scanners rotate the sample a full 360 degrees for image acquisition, whereas using synchrotron imaging a sample is scanned only by 180 degree rotation. Full rotation requires flexibility of the experimental set-up, such as the fluid flow connection lines, which can prove technically challenging for high-pressure experiments.

Table 2.1 reviews some of the previous studies that have utilised μCT techniques to investigate fluid flow in porous media. The list includes studies conducted using laboratory-based as well as synchrotron scanners. It includes qualitative as well as quantitative studies. Here special attention is paid to the sample type and size, core holder design and resolution of the reconstructed images. Reviewing the list shows there were only a few studies that have examined carbonate samples and no study has focused on oil-water processes.

Table 2.1: Previous studies that have utilised µCT technique to investigate fluid flow in porous media, with special attention to the sample type and size, core holder design and resolution of the reconstructed images

	Scanner	Sample	Fluid Phases	Sample size, mm	Image resolution, µm	Core Holder	Study of
Coles et al. (1998)	Synchrotron	Sandstone	Oil-water	D=25.4, L=31.8	30	Plastic flow cell	3D visualisation of oil-water distributions in sandstone, Earliest published µCT study
Turner et al. (2004)	Laboratory-based µCT	Bead pack Berea sandstone	Air-Oil Air-Fluorocarbon	D=25, L= 38 D= 8, L: -	33.6 9	Resin	The shape of wetting phase films
Wildenschild et al. (2005)	Synchrotron	Sand pack	Air–water	D=6, L=38.8 D=1.5, L=20	17 6.7	Lucite (Perspex)	Pore-scale fluid flow processes and the residual wetting phase under various flow conditions
Brusseau et al. (2006)	Synchrotron	Sand pack	Oil-water	D=4.6 or 5.8 L= 44	not mentioned	Aluminium	Immiscible organic fluid saturation in natural porous media
Culligan et al. (2006)	Synchrotron	Glass bead	Air–water Oil–water	D=7, L=7	17	Acrylic tube	NAPL dissolution in porous media
Kumar et al. (2009)	Laboratory-based µCT	Fontainebleau sandstone Sucrosic dolomite Reservoir carbonate	Air-oil	D=5, L> 20	3.1	Carbon fibre	The effect of wettability on trapped oil blob size distribution
Zhou et al. (2010)	Laboratory-based µCT	Sandstone	Nitrogen-water	D=8, L=15	23	Teflon heat shrink wrapped core, removed from high pressure vessel for scans	Gas trapping in porous media
Porter and Wildenschild (2010)	Synchrotron	Glass beads	Oil-water	D= 7, L= 25	13	Glass column	The relationship between capillary pressure, saturation, and interfacial area
Silin et al. (2011)	Synchrotron	Sandstone	CO_2 - water	D=5.5, L=20.16	4.48	Aluminium	The pore-scale mechanisms of CO2 injection in aquifers
Wildenschild et al. (2011)	Laboratory-based µCT	Sintered glass core	CO_2 - water	D=6.35, L=35	14.9	Aluminium	The capillary trapping efficiency as a function of interfacial tension, viscosity, and flow rate
Iglauer et al. (2011)	Laboratory-based µCT	Doddington Sandstone	CO_2 - water	D=4.95, L= 9	13.16	Carbon fibre	Structure of the trapped residual CO_2 saturation
Georgiadis et al. (2012)	Laboratory-based µCT	Sintered glass core	Oil-water	D=10, L=20	11.5	Polycarbonate	Distribution of trapped clusters during drainage and imbibition processes
Youssef et al. (2013)	Synchrotron	Fontainebleau sandstone	Air–water	D=5.8, L=8	5.5	PEEK (Polyether ether ketone)	Dynamic fluid flow in porous media
Berg et al. (2013)	Synchrotron	Sandstone	Oil-water	D=4, L=10	3	Polycarbonate cylinder	Haines jumps and snap-off mechanisms
Ghosh and Tick (2013)	Synchrotron	Sand Pack	Oil-water	D=5, L=44	≤10 µm	Aluminium	The effect of surfactant flooding on oil distribution
Andrew et al. (2014)	Laboratory-based µCT	Carbonate: Ketton, Mount Gambier, Estaillades Sandstone: Bentheimer, Doddington	CO_2 - water	D=6.5, L=30-50	6.6	Carbon fibre	Clusters of supercritical carbon dioxide trapped under capillary forces

The present research required a custom built core holder with good X–ray transparency since (a) the material under inspection (carbonate) is of high X–ray attenuation, (b) the selected core plug was of larger size compared to the similar studies, which in turn, increased the total X-ray attenuation. The sample size was constrained by the heterogeneity of the studied carbonate, for more discussions over the sample size selection refer to chapter 7, section 3.

A variety of flow cells (in terms of design and material) have been utilised in the previous pore-scale imaging studies. In some studies a conventional pressure vessel (mostly made of stainless steel) was used for the fluid injections. Subsequent to fluid injections the sample (often wrapped in heat shrink sleeve to seal its outer surface) had to be removed from the flow cell for imaging, see for example Zhou et al. (2010). This approach creates the possibility of fluid redistribution at the pore-scale due to the pressure drop on the core. One example of pore level fluid redistribution is presented in chapter 4, section 4. An X-ray transparent core holder provides the chance to scan the fluid saturations in-situ keeping the sample in the same position on the instrument during sequential fluid injections.

According to Table 2.1, the most common materials used for X-ray transparent flow cells are aluminium and carbon fibre. The development of a new carbon fibre wound pressure vessel was beyond the scope and finances of the project. Machining of carbon fibre tubes have proven challenging. For this study a simple core holder was designed and constructed in-house. The design is easy to prepare and use and suitable for low pressure and low temperature experiments.

5. Pore Network Modelling

In early modelling studies of fluid transport in porous media the porous media was represented by a set of parallel cylindrical capillary tubes. (Scheidegger, 1954, Yuster, 1951). It was first proposed by Fatt (1956) to represent the porous media using a regular lattice rather than bundle of capillary tubes. Fatt found that the lattice model's predictions were in better agreement with experimental results than those from the capillary tube bundle models. In subsequent pore-scale network modelling studies the porous media (such as porous rocks or soil) was represented by a system

of interconnected pores and throats in a way that the geometry and topology of the porous media was preserved. In this context geometry refers to the pore shape and size distribution and topology refers to the spatial location and connectivity of the pores (Vogel and Roth, 2001). Published modelling studies commonly used one or a combination of the following approaches to construct a pore network model:

(a) Idealized networks in form of a 3D regular lattice (Fatt, 1956, Wilkinson and Willemsen, 1983, McDougall and Sorbie, 1995a). These networks mostly have a constant coordination number, Z (for definition of Z see section 7.2.2), and were used in preliminary fluid displacement studies.

(a) Networks extracted from process based reconstructed pore space (Øren and Bakke, 2002). The approach included generating a digital representation of the rock by modelling the grain sedimentation, compaction and diagenesis processes. The grain size distributions were measured from thin section images. The method successfully represents homogeneous sandstones, but fails to generate carbonate rock models because of the extensive diagenetic modification of real carbonate pore structures.

(b) Stochastic network generation based on information directly derived from 2D thin section (or SEM) images or mercury injection data (Adler and Thovert, 1998, Vogel and Roth, 1998, Okabe, 2004, Arns et al., 2004, Wu et al., 2006). The high resolution of SEM images (down to nm) are specifically useful for inclusion of the very fine porosity in the constructed pore network models. Such fine structures are smaller than the achievable resolution of μCT images with the existing facilities.

(c) Realistic network extraction directly from 3D μCT images (Lindquist et al., 1996, Al-Raoush and Willson, 2005, Al-Kharusi and Blunt, 2007, Jiang, 2008, Raoof and Hassanizadeh, 2010, Bakke and Øren, 1997). This approach is capable of considering the three dimensional geometry and topology of the pore space, hence the method offers improved models of the 3D pore structure.

5.1. Pore Network Models - Basic Concepts

Using a pore network representation of a porous medium the static (e.g. porosity) and dynamic (e.g. conductivity) properties of the medium can be computed. This is achieved by analysing the geometry and topology of the network elements, respectively. In this study realistic pore networks are extracted from μCT images (Jiang, 2008). The starting point is the acquisition and reconstruction of μCT images. Reconstructed images are filtered to suppress the noise prior to image segmentation step. More details on noise filtering and image segmentation can be found in chapter 3, section 3. The outcome is a binary image of the pore space of the rock. The first step in network extraction is to partition this binary image into pores and throats. The geometry of the pore space is defined by the following parameters: pore and throat cross-sectional shape and area, the length and volume of the pores and throats, and their shape factor. The topology of the network is then assessed by determining the coordination number, Euler number, and connectivity function of the pore network.

5.1.1. Geometry of Network Elements

Network elements with a variety geometries have been used in the literature. In early network modelling studies it was common to use network elements with circular cross-section (Fatt, 1956, Wilkinson and Willemsen, 1983, Koplik and Lasseter, 1985, Dias and Payatakes, 1986). One major restriction associated with circular cross sections is they are not capable of transmitting or retaining more than one fluid simultaneously. To enable modelling of corner films researchers used network elements with angular cross sections. Figure 2.22 shows the variety of pore-throat cross sections reported in the literature,

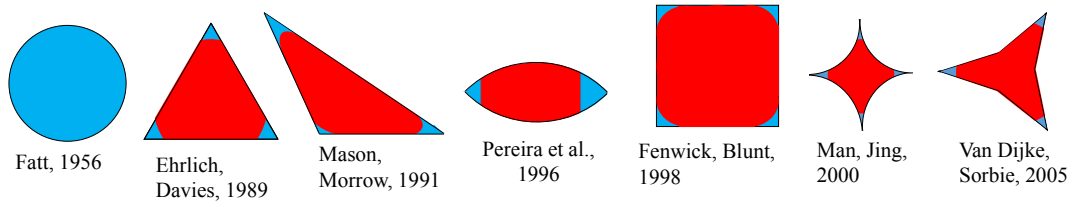

Figure 2.22: Various cross-sectional shapes used for pore throats in pore-network models, image adapted from Joekar-Niasar and Hassanizadeh (2012).

For example, Mason and Morrow (1991) published their studies on networks with triangular pore-throat shapes. Angular shaped network elements permit retention of

the wetting phase in their corners, which maintains the bulk continuity of the wetting phase throughout the network. They introduced a dimensionless term referred to as the "shape factor" (eq.1.9) and suggested that capillaries with the same shape factors have the same capillary behaviour even if they are geometrically different.

$$G = \frac{A}{P^2} \tag{2.9}$$

where A is the cross sectional area and P is the perimeter of network element. The concept of the shape factor is used to replace irregular, complex cross sections commonly found in naturally deposited structures by regular network elements with the same shape factor.

5.1.2. Topology of the network

Coordination Number (Z): The coordination number is a local topology descriptor, defined as the number of neighbouring pore-throats connected to each pore. Z was fixed in the pioneering studies (networks with regular lattice) and was regarded as the measure of connectivity of the pore network. However, it has proven to be inadequate as an indication of network connectivity since it is only a local topological descriptor (Nagel et al., 2000, Ohser et al., 2002). Coordination number can range between $2<Z<5$ for naturally deposited porous media (Vogel and Roth, 2001), with average Z of 2.8 and 4.3 for Berea sandstone and random bead packs, respectively. Z can be substantially variable for heterogeneous carbonate rocks.

Euler Number (x): the Euler number is a measure of global connectivity of a structure, and defined as:

$$x = h_0 - h_1 + h_2 \tag{2.10}$$

where: h_0 is the number of isolated components, h_1 is the number of redundant connections (the connections that can be removed without disconnecting the remaining elements), and h_2 is the number of completely enclosed cavities (in this context solid objects floating in the pore space). Positive Euler numbers indicate poor connectivity whereas negative values indicate more connected structures. The

specific Euler number is defined as the Euler number divided by the volume of the image (V):

$$x_v = \frac{N_N - N_B}{V} \tag{2.11}$$

where N_N is the number of nodes (pores) and N_B the number of bonds (throats). In practice, Euler number based modelling approaches are faced with two major limitations in describing the topology of a pore structure. Firstly, the Euler number is very sensitive to the digital noise present in the input image. Secondly, the algorithms used for computation of the Euler number are sophisticated and computationally expensive (Jiang, 2008).

Connectivity Function: Vogel (1997) introduced the concept of the connectivity function based on the specific Euler number. The connectivity function is the specific Euler number for a reduced version of an input network. The reduction refers to removing all the network elements with radius smaller than r. Therefore, the connectivity function is expressed as a function of r, as formulated in eq. 2.12 and shown in Figure 2.23.

$$x_v(r) = \frac{N_N(r) - N_B(r)}{V} \tag{2.12}$$

where N_N is the number of nodes (pores) and N_B the number of bonds (throats) with radii larger than or equal to r. The highest connectivity corresponds to the entire network (the most negative value). By removing smaller network elements the network becomes locally disconnected in places. Hence, the network connectivity decreases with progressively increasing Euler number. At some value of r the specific Euler number becomes positive and this is the point where the network becomes globally disconnected.

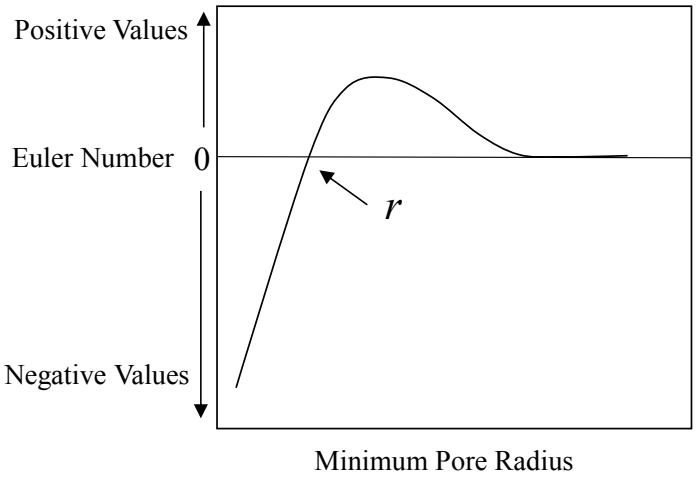

Figure 2.23: Connectivity function expressed as a function of *r*. The input network is the most connected form of it, by reducing the network through removing elements with radius smaller than *r* the network becomes progressively less connected until at some radius it becomes globally disconnected.

The Euler number is used in chapter 5, section 2 to compare the connectivity of fluid phase structures extracted from μCT images.

5.2. Pore-scale Fluid Flow Simulations

5.2.1. Model Classification

The problem of simulating fluid displacement process in porous media has been approached using various models. One approach is to perform calculations directly on 3D images of the pore space. The flow simulations can be done by solving the Navier–Stokes equation, the method is known as Lattice Boltzmann, (LB) (Pan et al., 2004). However the application of LB models are limited by their intensive computational expenses and memory usage (Porter et al., 2009). To address this issue pore network models can be used which are simplified representations of the pore space of rocks. Such networks of interconnected pores and throats should ideally preserve the geometry as well as the connectivity of the pore space.

As simplified models, pore networks reduce the amount of information about the pore structure of the rock by several orders of magnitudes, at least three orders (Patzek and Silin, 2001). This is favourable from the point of view of computational costs. Fluid flow simulations are significantly faster using a pore network modelling

approach. The compromise enables simulating fluid displacements in larger samples with sizes approaching the representative elementary volume (REV) of the rock.

Simulation of fluid displacement processes in pore networks has received much attention in the previous decades (Fatt, 1956, Wilkinson and Willemsen, 1983, Reeves and Celia, 1996, Valvatne and Blunt, 2004, Joekar-Niasar and Hassanizadeh, 2012, Ryazanov et al., 2009). Two groups of pore-scale flow simulation approaches were developed: quasi-static and dynamic models.

Quasi-static models

Percolation models were used to simulate the displacement processes with infinitesimally slow flow rates where the process is strictly controlled by capillary forces and hence all other forces including viscous and gravity forces are ignored (Sahimi, 1994). In such models the displacement happens through a sequence of discrete pore-scale events at which the fluid/fluid interface configuration jumps from one static configuration to another updated static configuration as a result of the displacement event. The transient phase between the two static steps is not modelled.

At each step the fluid displacement is carried out by invading the network elements with the least resistance to flow, this is controlled by the size of network elements and the wettability assigned to them. The easiest elements to invade are the largest and smallest pores (throats) for the drainage and imbibition processes, respectively. For example, in simulating a drainage process the pressure of the invading fluid phase increases stepwise (while the pressure of the defending phase is kept constant). Therefore, progressively smaller pores (throats) are intruded as the invasion pressure increases. The displacement happens based on a series of simple rules, for example:

- The pressure of the invading phase should exceed the capillary entry pressure (i.e. $P_i > P_{entry}$) before it can invade a pore.
- At each time step only the accessible network elements are invaded.
- The invading phase should be connected to the injection face and the defending phase should have a connected path to the production face.

Fluid trapping is an important feature included in this class of models (Wilkinson and Willemsen, 1983). Trapping of the non-wetting phase is physically observed in

micro-models (e.g. Lenormand et al. (1983)) and 3D μCT studies (see the review by Wildenschild and Sheppard (2013)). In pore network simulations trapping is modelled using: (a) snap-off: when the oil is trapped in one single pore, (b) a bypassing mechanism: when a cluster of oil saturating a number of connected pores becomes surrounded by the water phase, and hence trapped (Wilkinson, 1984).

The development, collapse and regeneration of wetting films is another essential feature of fluid-displacement processes. In order to achieve reliable predictions of the macroscopic properties such as relative permeability, residual saturations, and the electrical properties of a porous media the existence and connectivity of the wetting films must be considered in the model.

Dynamic models

In this class of pore-scale models viscous forces are taken into account as well as capillary forces. Similar to the quasi-static models for any network element to become invaded the capillary entry pressure has to be exceeded, but in addition the dynamic models calculate the pressure field in the pore network continuously. This enables modelling of the configuration of the dynamic fluid-fluid interface between any two equilibrium states before and after an invasion event. Dynamic models are therefore more complex and computationally time-consuming (Hughes and Blunt, 2000, Singh and Mohanty, 2003, Al-Gharbi and Blunt, 2005, Joekar-Niasar and Hassanizadeh, 2012). Dynamic modelling is of particular importance in modelling the forced imbibition processes during which the displacement is no longer dominated by flow through the smaller pores, as it is for the spontaneous imbibition. In a forced imbibition, the high rate of wetting phase influx forces the microscopic fluid interfaces to select the easiest paths available to flow, i.e. the largest accessible pores. At the same time smaller pores become imbibed locally as a result of wetting forces. This causes the fluid displacement to happen simultaneously in pores of different sizes. The structure of the saturating fluids after a forced imbibition is therefore different from a capillary dominated imbibition (Sahimi, 1994).

In this study μCT images of carbonate rock samples were used as the starting point, pore analysis tools (PATs) developed by Jiang (2008) were used to extract realistic

pore network models from the μCT images. Fluid flow simulations performed using a quasi-static code developed by Ryazanov et al. (2009).

5.2.2. Pore-scale Fluid Displacement Mechanisms

In a multiphase fluid displacement process happening in a porous media it is the micro-scale events that ultimately control the distribution of fluid phases in the macro-scale. In a porous medium less than 100% of the resident saturating phase (the "defending" phase) can be produced upon injection of an immiscible displacing ("invading") phase.

Micro-models were used in early experimental attempts to visually observe the fluid displacement processes in porous media. Micro-models are 2D networks of interconnected capillaries made of transparent material such as glass or resin (Lenormand et al., 1983, Mohanty et al., 1994, Lenormand and Zacone, 1988, Vizika et al., 1994). Lenormand et al. (1983) used capillaries with rectangular cross section in their micro-model, in which they performed two-phase drainage and imbibition tests. They observed simultaneous existence and flow of the two fluid phases in a capillary. The wetting phase occupied the capillary corners, while the non-wetting phase occupied the capillary centre. According to their results there are three major mechanisms for two immiscible fluids displacing each other in a network of capillaries: (1) piston-like displacement, (2) snap-off and (3) pore-body filling (Figure 2.24).

In the reminder of this chapter the wetting and non-wetting phases are assumed to be water and oil, respectively.

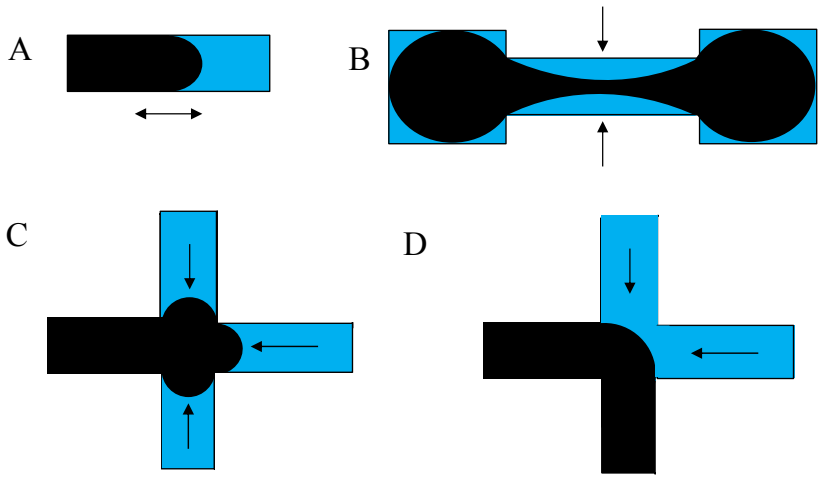

Figure 2.24: The possible pore-scale mechanisms during immiscible fluid displacement in non-circular pores are the piston-like displacement (A), snap-off (B), and pore-body filling (C, D). Blue and black indicate wetting and non-wetting phases, respectively. After Lenormand et al. (1983).

Piston-like Displacement: In this mechanism, the invading phase displaces the defending phase in a piston-like fashion (Figure 2.24A). The event may happen during drainage or imbibition. For example, during drainage, oil displaces water only from the centre of the pores while water remains in the corners and crevices of the pore in form of corner films. The water corner films only exist in pores with non-circular cross sections. Such pores are common in most natural pore systems such as rocks and soil samples. Moreover, in case of stronger wetting preferences (contact angles close to zero), water maintains its contact with the pore surface by forming thin fluid films that coat the rock surface. The development of such thin films assist the water phase to remain connected throughout the pore network of the rock. During drainage the flow of water films permits continuous water production and hence low residual water saturations.

Pore-body Filling: Figure 2.24C and 2.24D shows imbibition in a pore (pore coordination number of $Z = 4$) which have connecting throats saturated with both water and oil phases. The oil-water meniscus can have a number of possible configurations, depending on the pore coordination number and the saturation state of its pore throats. Two of the possible oil-water configurations are shown in Figure

2.24C and 2.24D for this pore. These are referred to as pore-body filling mechanism. When all throats but one are saturated with the wetting phase, the process is similar to piston-like displacement.

Snap-off: This mechanism occurs when water is injected into a pore that contains oil but also has water films in its corners and crevices (Figure 2.24B). During imbibition the pre-existing water films start to swell and become progressively thicker until at some point the films meet, the water-oil interface becomes unstable, and eventually the oil phase connection collapses, i.e. the oil "snaps off" and becomes disconnected from the oil cluster. Note that snap-off can only occur if there are no accessible pores that have already been saturated with water. Snap-off is one of the main mechanisms responsible for oil entrapment inside single pores. Another mechanism that traps larger oil clusters due to the non-uniform frontal displacement is referred to as oil bypassing (Wilkinson, 1984).

Traditionally, pore-scale displacement processes were observed in 2D micro-model experiments. Pore-network models that simulate these displacement processes hence had to assume that the same displacement processes that have been observed in idealised 2D pores also occur in the complex 3D pore geometries inherent to real reservoir rocks. Experiments in 3D are therefore required to observe pore-scale displacement processes in real reservoir rocks, to quantify the pore-scale events, and ultimately, to implement them in pore-network models.

Such experimental advances have recently become possible using synchrotron X-ray μCT techniques, which enable the imaging of dynamic pore-scale displacement processes in real-time. In a pioneering study, Berg et al. (2013) used synchrotron X-ray μCT to visualise the dynamic evolution of fluid-fluid configurations in sandstones during drainage and imbibition. For the first time, they observed Haines jumps, pore-body filling, and snap-off events and were able to calculate the pore-scale energy dissipation by measuring the fluid-fluid interfacial areas from the images. In a similar study, Youssef et al. (2013) also visualised the snap-off events in sandstones using real-time synchrotron imaging. Some of the observed processes have been readily implemented in quasi-static invasion-percolation based pore-

network models. For example, thermodynamic arguments enabled prediction of oil layer collapse in pores with non-uniform wettability (Van Dijke and Sorbie, 2006). Other pore-scale displacement events such as Haines jumps, although well-known, cannot be simulated with quasi-static pore-network models and require dynamic pore-network simulations instead.

Although synchrotron μCT is a powerful tool to visualise pore-scale displacement processes in real time, there are also a number of technical challenges involved in such experiments. These challenges include, but may not necessarily be limited to, (a) the design and construction of an experimental set-up suitable for sufficiently small rock samples that are needed to achieve the required spatial resolutions (sub-μm-scale), and (b) the handling, processing and analysing of extensive amounts of μCT data, which can comprise hundreds of datasets (each containing thousands of 2D μCT slices). High-performance computing is therefore required for efficient analysis of such heavy datasets. These challenges have limited the number of studies that use real-time imaging of pore-scale multiphase flow processes in porous media.

6. Wettability

6.1. Wettability Concept

By definition wettability is the tendency of one fluid to spread over a solid surface in presence of another fluid (Craig, 1971). When a fluid is exposed to a solid surface there is a competition between the capillary forces acting over the fluid/fluid interface and the adhesive forces acting over the fluid-solid contact surfaces. The force balance governs the contact angle the fluid-fluid interface makes with the solid surface (Figure 2.25). This contact angle is used as an indication of surface wettability, this is discussed in further detail in chapter 6.

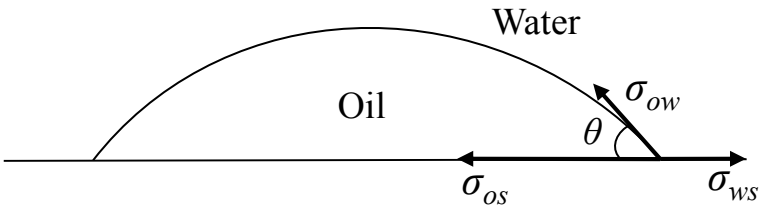

Figure 2.25: Force balance for an oil droplet placed on a surface in presence of water phase. The contact angle can be used as a wettability indicator.

$$\sigma_{os} - \sigma_{ws} = \sigma_{ow} \cos\theta \tag{2.13}$$

where σ_{os} and σ_{ws} (N/m) are the oil-solid, water-solid surface tensions, respectively. σ_{ow} is the oil/water interfacial tension. Wettability is considered to be a key parameter which controls the distribution of fluids in a porous medium. In multiphase flow in a heterogeneous media (composed of variety of pore-sizes from micro pores to millimetre fractures), the rock surface's wetting preference controls the fluid flow paths. According to McDougall and Sorbie (1995b) a porous rock can be considered to have uniform or non-uniform wettability. In a uniform-wettability system the wettability of the entire porous media is considered to be the same (oil-wet, water-wet or intermediate-wet) which means the fluid-rock contact angles remain constant throughout the system. In the real world wettability is not uniform in the entire pore space and may change from pore to pore or even inside a single pore. Figure 2.26 shows the two main classes of non-uniform wettability systems: Fractionally wet and Mixed wet. A fractionally wet system could have oil wet pores of all sizes, while in a mixed wet system small pores are considered as water wet and large pores as oil wet.

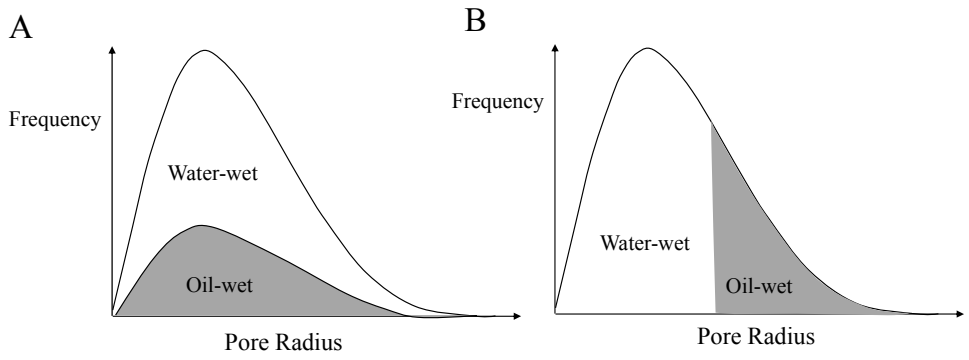

Figure 2.26: Classification of non-uniform wetting systems. (A and B) show the pore-size distribution of the pores wetted by oil and water in a fractionally-wet system (A), and a mixed-wet system (B). After McDougall and Sorbie (1995b).

6.2. Wettability Alteration

Wettability alteration (restoration) of rock samples by aging of the sample in crude oil from the same reservoir is considered to be a vital step in core analysis studies (Anderson, 1986a). In core analysis laboratories, core flooding experiments are performed at reservoir pressure and temperature to closely mimic the reservoir conditions. It is of particular importance to restore the wettability state of the rock, since wettability is one of the parameters controlling the fluid saturation distributions in porous media.

The mechanism of wettability alteration is by deposition of heavier and polar components of the crude oil including asphaltenes and resins onto the surface of the rock. A number of studies (Buckley and Liu, 1998, Morrow et al., 1986, Cuiec, 1984, Graue et al., 1999, Tang and Morrow, 1999, Tong et al., 2003, Buckley and Morrow, 1992) have identified the main parameters controlling the effectiveness of the aging process:

- Crude oil chemical composition
- Mineralogy (surface charge) of the rock
- Salinity and composition of the brine
- Aging time and temperature

Polar components of crude oil, found to be either acidic or basic charged groups (Benner and Bartel, 1941), can cause wettability alterations through interaction with surface minerals of the rock (Crocker and Marchin, 1988). For carbonate rocks,

having isoelectric points around 8<pH< 10, the rock surface is positively charged at pH < 8 (Hirasaki and Zhang, 2004, Buckley and Liu, 1998). Therefore, negatively charged groups, i.e. the *acidic* compounds, are attracted to the carbonate surface. For sandstones, however, the surface is negatively charged at natural pH and hence the positively charged groups, i.e. basic groups are mostly adsorbed to it (Cuiec, 1984, Buckley and Liu, 1998).

Asphaltene and resins are heavy polar components of crude oil. Figure 2.27 shows a typical molecular structure of asphaltene and resin compounds (Hunt, 1996). Asphaltenes (Figure 2.27A and 2.27B) are the heaviest components of the crude oil which display polycyclic aromatic structure with aliphatic branches attached to their planar molecules. The existence of polar sites in the molecular structure of asphaltene causes them to actively interact with other polar components of crude oil (such as resins), as well as with charged sites on the rock surface.

According to petroleum industry standards (e.g. ASTM 650, BS 2000-143) asphaltenes are defined as a class of heavy hydrocarbon fractions of crude oil which are soluble in aromatic solvents such as toluene and insoluble in saturated solvents such as n-C_7 .This solubility criteria is used in laboratory for separating asphaltene from the crude oil.

Resins (Figure 2.27C and 2.27D) are a further heavy polar component of crude oil. Being polar, resins can act as solvents which adsorb to the aromatic cores of asphaltene molecules from their polar ends while actively interacting with the non-polar components of the crude oil from their aliphatic end as shown in Figure 2.28. Higher resin to asphaltene ratios enhance the solubility of asphaltene aggregates in crude oil (Spiecker et al., 2003).

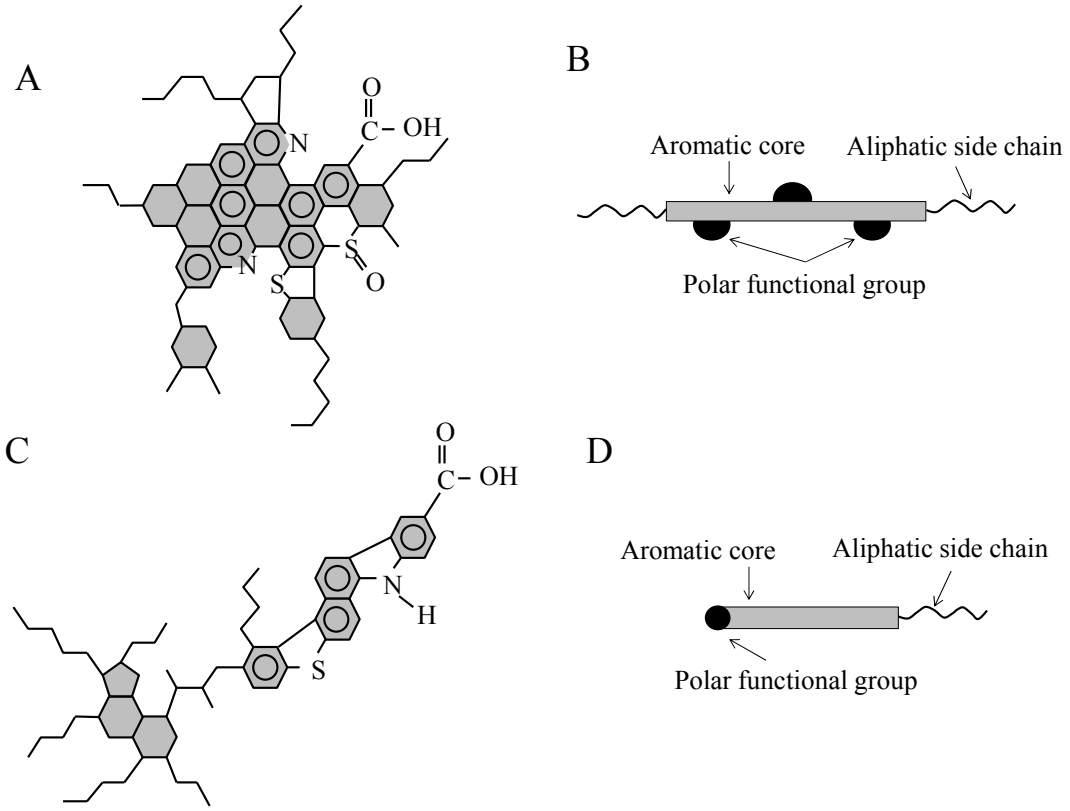

Figure 2.27: Molecular structure of asphaltene (A and B) and resin (C and D) compounds of crude oil. (A and C) show the top view and (B and D) show the side view, after Hunt (1996).

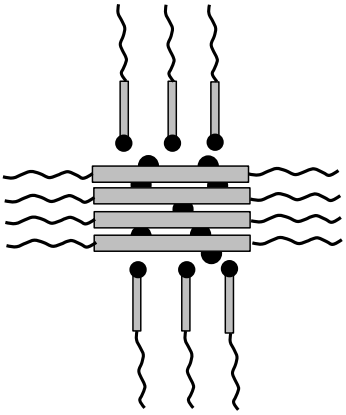

Figure 2.28: Resin solubilised asphaltene aggregates, after McLean and Kilpatrick (1997).

Prior to oil migration most reservoirs are saturated with an aqueous phase (reservoir brine) and the rocks are predominantly water-wet. Oil migration leaves behind an irreducible water saturation in form of thin layers of brine coating the surface of the rock. Wettability alteration happens if the heavy polar components of the crude oil

reach the rock surface and deposit onto it. To achieve this there are two possible mechanisms:

(a) Diffusion through the brine film: During the aging time (geological time for real reservoirs) low solubility polar components of the crude may diffuse through the brine layer and deposit on the rock surface (Cuiec, 1984, Anderson, 1986b). The pre-requisite of this mechanism is that the polar components of the crude have some miscibility in the brine phase. The mechanism is shown schematically in Figure 2.29.

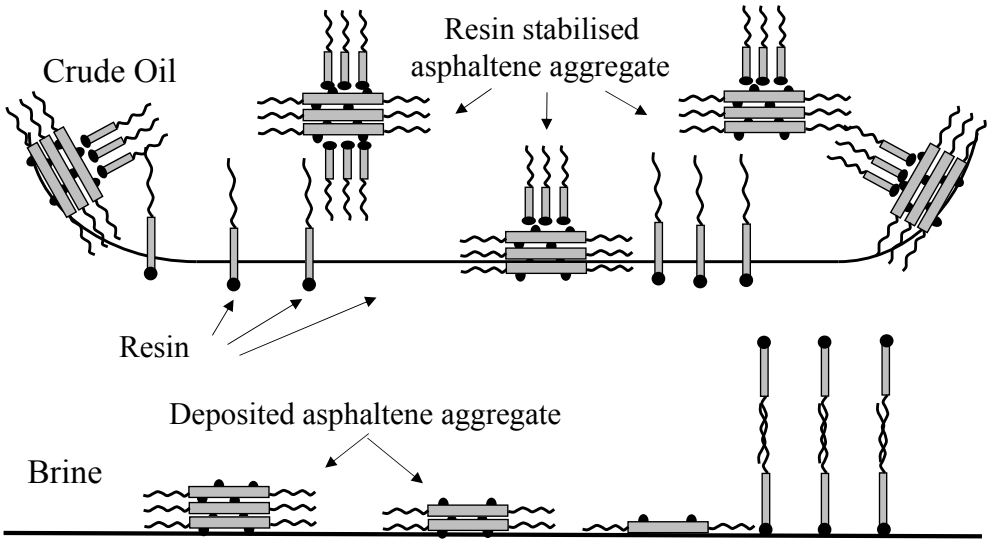

Figure 2.29: Diffusion of crude oil polar components through the brine film and deposition on the rock surface causes oil-wetness, after Kaminsky and Radke (1997).

(b) Brine film collapse: For immiscible fluid pairs the brine film may collapse as a result of attractive-repulsive forces acting across this thin layer. If the two oil-brine and brine-rock interfaces have opposite charges, an electrostatic attraction causes the sandwiched brine film to collapse and hence the rock becomes exposed to the crude oil (HirasakL, 1988, Buckley, 1996). Figure 2.30 shows schematically the adsorption mechanism of the polar components of crude oil onto the oil-brine interface followed by brine film rupture which renders the rock surface oil-wet (Buckley and Liu, 1998).

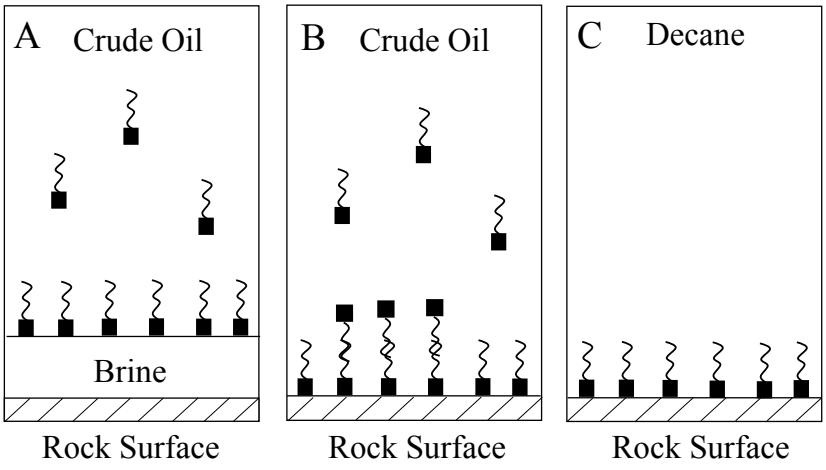

Figure 2.30: Schematic model of development of an oil-wet surface as a result of deposition of crude oil polar components on the rock surface. A water layer is initially covering the rock surface (A). The water films is collapsed, and the polar components of crude oil are adsorbed to the rock surface (B). The attached polar components are stable after the crude is displaced with a lighter oil (C), after Buckley and Liu (1998).

For carbonate systems the concentration of carboxylic compounds present in crude oil, measured by "Acid Number" (AN in mg KOH/g), is an influential parameter on wetting alteration (Buckley and Liu, 1998). Carboxylic acid anions (carboxylates, $RCOO^-$) absorbed to a positively charged carbonate surface can assist the adsorption of other crude oil polar compounds (such as resins and asphaltenes) to the surface.

The existence of brine films on the carbonate surface before the rock is exposed to crude oil has been shown to assist the aging process (Buckley, 1996). In particular, existence of multi-valent ions in the brine phase can increase the chance of brine film collapse leading to the surface becoming oil-wet (Buckley, 1996).

Aging in crude oil was used in this research to alter the wetting preference of a dolomite core plug (which was original water-wet) towards a reduced water-wet state. More discussions on the wettability alteration process is presented in chapter 3, section 4.

7. Summary

This chapter provides an overview of the literature related to tracking of fluid saturations in porous media using combined core flooding and computed tomography techniques. Basic concepts behind carbonate rock classifications, X-ray physics, core analysis techniques, pore network modelling, and surface wettability are introduced.

A comprehensive review of the previously published studies that have utilised μCT techniques to investigate fluid flow in porous media is presented with a special attention to the sample type and size, core holder design and resolution of the reconstructed images. The review suggested that only a few studies have examined carbonate samples among which no study has focused on oil-water processes. One primary challenge in the study of heterogeneous pore systems is selecting a representative sample. Small samples (few mms in diameter) can represent the pore structure of homogeneous material. A representative sample of a heterogeneous material, however, can be significantly larger (e.g. few cm vs few mm). This is mainly due to the broad range of pore-sizes present in heterogeneous material. The consequence of working with large samples is the lower achievable image resolutions, which may prove insufficient for capturing the finer pores that contribute to the fluid flow. This research investigates the trade-off between the sample size and image resolution using pore network models extracted from different size samples of a carbonate rock. Details are presented in chapter 7.

References

ADLER, P. & THOVERT, J.-F. 1998. Real porous media: Local geometry and macroscopic properties. *Applied Mechanics Reviews,* 51**,** 537-585.

AKBAR, M., PETRICOLA, M., WATFA, M., BADRI, M., CHARARA, M., BOYD, A., CASSELL, B., NURMI, R., DELHOMME, J.-P. & GRACE, M. 1995. Classic interpretation problems: evaluating carbonates. *Oilfield Review,* 7**,** 38-57.

AKIN, S. & KOVSCEK, A. 2003. Computed tomography in petroleum engineering research. *Geological Society, London, Special Publications,* 215**,** 23-38.

AL-GHARBI, M. S. & BLUNT, M. J. 2005. Dynamic network modeling of two-phase drainage in porous media. *Physical Review E,* 71**,** 016308.

AL-KHARUSI, A. S. & BLUNT, M. J. 2007. Network extraction from sandstone and carbonate pore space images. *Journal of Petroleum Science and Engineering,* 56**,** 219-231.

AL-RAOUSH, R. & WILLSON, C. 2005. Extraction of physically realistic pore network properties from three-dimensional synchrotron X-ray microtomography images of unconsolidated porous media systems. *Journal of Hydrology,* 300**,** 44-64.

ANDERSON, W. 1986a. Wettability literature survey-part 2: Wettability measurement. *Journal of Petroleum Technology,* 38**,** 1,246-1,262.

ANDERSON, W. G. 1986b. Wettability literature survey-Part 1: Rock/oil/brine interactions and the effects of core handling on wettability. *J. Pet. Technol.;(United States),* 38.

ANDREW, M., BIJELJIC, B. & BLUNT, M. J. 2014. Pore-scale imaging of trapped supercritical carbon dioxide in sandstones and carbonates. *International Journal of Greenhouse Gas Control,* 22**,** 1-14.

ARCHIE, G. E. 1952. Classification of carbonate reservoir rocks and petrophysical considerations. *AAPG Bulletin,* 36**,** 278-298.

ARNS, C. H., BAUGET, F., LIMAYE, A., SAKELLARIOU, A., SENDEN, T., SHEPPARD, A., SOK, R. M., PINCZEWSKI, W., BAKKE, S. & BERGE, L. I. 2005. Pore-scale characterization of carbonates using X-ray microtomography. *SPE JOURNAL-RICHARDSON-,* 10**,** 475.

ARNS, C. H., KNACKSTEDT, M. A. & MECKE, K. 2004. Characterisation of irregular spatial structures by parallel sets and integral geometric measures. *Colloids and Surfaces A: Physicochemical and Engineering Aspects,* 241**,** 351-372.

BAKKE, S. & ØREN, P.-E. 1997. 3-D pore-scale modelling of sandstones and flow simulations in the pore networks. *SPE JOURNAL-RICHARDSON-,* 2**,** 136-149.

BARRETT, J. F. & KEAT, N. 2004. Artifacts in CT: Recognition and Avoidance. *RadioGraphics,* 24**,** 1679-1691.

BENNER, F. & BARTEL, F. 1941. The effect of polar impurities upon capillary and surface phenomena in petroleum production. *Drilling and Production Practice*.

BERG, S., OTT, H., KLAPP, S. A., SCHWING, A., NEITELER, R., BRUSSEE, N., MAKURAT, A., LEU, L., ENZMANN, F., SCHWARZ, J. O., KERSTEN,

M., IRVINE, S. & STAMPANONI, M. 2013. Real-time 3D imaging of Haines jumps in porous media flow. *Proc Natl Acad Sci U S A,* 110**,** 3755-9.

BRUSSEAU, M. L., PENG, S., SCHNAAR, G. & COSTANZA-ROBINSON, M. S. 2006. Relationships among air-water interfacial area, capillary pressure, and water saturation for a sandy porous medium. *Water resources research,* 42.

BUCKLEY, J. & LIU, Y. 1998. Some mechanisms of crude oil/brine/solid interactions. *Journal of Petroleum Science and Engineering,* 20**,** 155-160.

BUCKLEY, J. & MORROW, N. 1992. An overview of crude oil adhesion phenomena. *Physical chemistry of colloids and interfaces in oil production***,** 39-45.

BUCKLEY, J. S. 1996. Mechanisms and consequences of wettability alteration by crude oils.

BUCKLEY, S. E. & LEVERETT, M. C. 1942. Mechanism of Fluid Displacement in Sands.

CHOQUETTE, P. W. & PRAY, L. C. 1970. Geologic nomenclature and classification of porosity in sedimentary carbonates. *AAPG bulletin,* 54**,** 207-250.

CNUDDE, V. & BOONE, M. 2013. High-resolution X-ray computed tomography in geosciences: A review of the current technology and applications. *Earth-Science Reviews,* 123**,** 1-17.

COLES, M. E., HAZLETT, R. D., SPANNE, P., SOLL, W. E., MUEGGE, E. L. & JONES, K. W. 1998. Pore level imaging of fluid transport using synchrotron X-ray microtomography. *Journal of Petroleum Science and Engineering,* 19**,** 55-63.

CRAIG, F. F. 1971. *The Reservoir Engineering Aspects of Waterflooding*, Society of Petroleum Engineers of AIME, Monograph.

CROCKER, M. & MARCHIN, L. 1988. Wettability and adsorption characteristics of crude-oil asphaltene and polar fractions. *Journal of Petroleum Technology,* 40**,** 470-474.

CUIEC, L. 1984. Rock/crude-oil interactions and wettability: An attempt to understand their interrelation. *paper SPE,* 13211**,** 16-19.

CULLIGAN, K. A., WILDENSCHILD, D., CHRISTENSEN, B. S. B., GRAY, W. G. & RIVERS, M. L. 2006. Pore-scale characteristics of multiphase flow in porous media: A comparison of air–water and oil–water experiments. *Advances in Water Resources,* 29**,** 227-238.

DIAS, M. M. & PAYATAKES, A. C. 1986. Network models for two-phase flow in porous media Part 1. Immiscible microdisplacement of non-wetting fluids. *Journal of Fluid Mechanics,* 164**,** 305-336.

DONG, H. & BLUNT, M. J. 2009. Pore-network extraction from micro-computerized-tomography images. *Physical review E,* 80**,** 036307.

DUNHAM, R. J. 1962. Classification of carbonate rocks according to depositional textures.

FATT, I. 1956. The Network Model of Porous Media. Society of Petroleum Engineers.

FELDKAMP, L. A., DAVIS, L. C. & KRESS, J. W. 1984. Practical cone-beam algorithm. *Journal of the Optical Society of America A,* 1**,** 612-619.

FESER, M., GELB, J., CHANG, H., CUI, H., DUEWER, F., LAU, S., TKACHUK, A. & YUN, W. 2008. Sub-micron resolution CT for failure analysis and process development. *Measurement science and technology,* 19**,** 094001.

FLOHR, T. G., RAUPACH, R. & BRUDER, H. 2009. Cardiac CT: how much can temporal resolution, spatial resolution, and volume coverage be improved? *Journal of cardiovascular computed tomography,* 3**,** 143-152.

FOLK, R. L. 1959. Practical petrographic classification of limestones. *AAPG Bulletin,* 43**,** 1-38.

FUSSEIS, F., XIAO, X., SCHRANK, C. & DE CARLO, F. 2014. A brief guide to synchrotron radiation-based microtomography in (structural) geology and rock mechanics. *Journal of Structural Geology,* 65**,** 1-16.

GEORGIADIS, A., BERG, S., MAITLAND, G. & OTT, H. 2012. Pore-Scale Micro-CT Imaging: Cluster Size Distribution During Drainage and Imbibition. *Energy Procedia,* 23**,** 521-526.

GHOSH, J. & TICK, G. R. 2013. A pore scale investigation of crude oil distribution and removal from homogeneous porous media during surfactant-induced remediation. *Journal of contaminant hydrology,* 155**,** 20-30.

GRAUE, A., VIKSUND, B. G., EILERTSEN, T. & MOE, R. 1999. Systematic wettability alteration by aging sandstone and carbonate rock in crude oil. *Journal of Petroleum Science and Engineering,* 24**,** 85-97.

HIRASAKI, G. & ZHANG, D. L. 2004. Surface Chemistry of Oil Recovery From Fractured Oil-Wet Carbonate Formations. *SPE Journal,* 9**,** 151-162.

HIRASAKL, G. 1988. Wettability: fundamentals and surface forces. *Spe/Doe,* 17367.

HSIEH, J. 2009. *Computed Tomography Principles, Design, Artifacts, and Recent Advances*, Wiley.

HUGHES, R. G. & BLUNT, M. J. 2000. Pore scale modeling of rate effects in imbibition. *Transport in Porous Media,* 40**,** 295-322.

HUNT, A. 1996. Uncertainties remain in predicting paraffin deposition. *Oil and Gas Journal,* 94**,** 96-103.

IGLAUER, S., PALUSZNY, A., PENTLAND, C. H. & BLUNT, M. J. 2011. Residual CO_2 imaged with X-ray micro-tomography. *Geophysical Research Letters,* 38**,** L21403.

JIANG, Z. 2008. *Quantitative characterisation of the geometry and topology of pore space in 3D rock images.*

JOEKAR-NIASAR, V. & HASSANIZADEH, S. 2012. Analysis of fundamentals of two-phase flow in porous media using dynamic pore-network models: A review. *Critical Reviews in Environmental Science and Technology,* 42**,** 1895-1976.

KAMINSKY, R. & RADKE, C. 1997. Asphaltenes Water Films and Wettability Reversal. *SPE Journal,* 2**,** 485-493.

KETCHAM, R. A. & CARLSON, W. D. 2001. Acquisition, optimization and interpretation of X-ray computed tomographic imagery: applications to the geosciences. *Computers & Geosciences,* 27**,** 381-400.

KETCHAM, R. A. & ITURRINO, G. J. 2005. Nondestructive high-resolution visualization and measurement of anisotropic effective porosity in complex

lithologies using high-resolution X-ray computed tomography. *Journal of Hydrology,* 302**,** 92-106.

KOPLIK, J. & LASSETER, T. 1985. Two-phase flow in random network models of porous media. *Society of Petroleum Engineers Journal,* 25**,** 89-100.

KUMAR, M., SENDEN, T., KNACKSTEDT, M. A., LATHAM, S. J., PINCZEWSKI, V., SOK, R. M., SHEPPARD, A. P. & TURNER, M. L. 2009. Imaging of pore scale distribution of fluids and wettability. *Petrophysics,* 50**,** 311.

LENORMAND, R. & ZACONE, C. 1988. Physics of Blob Displacement in a Two-Dimensional Porous Medium.

LENORMAND, R., ZARCONE, C. & SARR, A. 1983. Mechanisms of the displacement of one fluid by another in a network of capillary ducts. *Journal of Fluid Mechanics,* 135**,** 337-353.

LINDQUIST, W. B., LEE, S.-M., COKER, D. A., JONES, K. W. & SPANNE, P. 1996. Medial axis analysis of void structure in three-dimensional tomographic images of porous media. *Journal of Geophysical Research: Solid Earth,* 101**,** 8297-8310.

LINDQUIST, W. B., VENKATARANGAN, A., DUNSMUIR, J. & WONG, T.-F. 2000. Pore and throat size distributions measured from synchrotron X-ray tomographic images of Fontainebleau sandstones. *Journal of Geophysical Research: Solid Earth,* 105**,** 21509-21527.

LØNØY, A. 2006. Making sense of carbonate pore systems. *AAPG bulletin,* 90**,** 1381-1405.

LUCIA, F. 1983. Petrophysical parameters estimated from visual descriptions of carbonate rocks: a field classification of carbonate pore space. *Journal of Petroleum Technology,* 35**,** 629-637.

LUCIA, F. J. 1995. Rock-fabric/petrophysical classification of carbonate pore space for reservoir characterization. *AAPG bulletin,* 79**,** 1275-1300.

MCDOUGALL, S. & SORBIE, K. 1995a. The impact of wettability on waterflooding: pore-scale simulation. *SPE Reservoir Engineering,* 10**,** 208-213.

MCDOUGALL, S. R. & SORBIE, K. S. 1995b. The Impact of Wettability on Waterflooding: Pore-Scale Simulation.

MCLEAN, J. D. & KILPATRICK, P. K. 1997. Effects of asphaltene aggregation in model heptane–toluene mixtures on stability of water-in-oil emulsions. *Journal of Colloid and Interface Science,* 196**,** 23-34.

MOHANTY, K. K., GUPTA, A. & DERUITER, R. A. 1994. Pore-Level Mechanisms of Residual Oil Formation during Miscible Displacement. *Journal of Colloid and Interface Science,* 163**,** 199-216.

MORROW, N. R., LIM, H. T. & WARD, J. S. 1986. Effect of crude-oil-induced wettability changes on oil recovery. *SPE Formation Evaluation,* 1**,** 89-103.

NAGEL, W., OHSER, J. & PISCHANG, K. 2000. An integral-geometric approach for the Euler-Poincaré characteristic of spatial images. *Journal of microscopy,* 198**,** 54-62.

OHSER, J., NAGEL, W. & SCHLADITZ, K. 2002. *The Euler number of discretized sets—on the choice of adjacency in homogeneous lattices*, Springer.

OKABE, H. 2004. *Pore-scale modelling of carbonates.* Imperial College London.

OKABE, H. & BLUNT, M. J. 2007. Pore space reconstruction of vuggy carbonates using microtomography and multiple-point statistics. *Water Resources Research,* 43.

ØREN, P.-E. & BAKKE, S. 2002. Process based reconstruction of sandstones and prediction of transport properties. *Transport in Porous Media,* 46**,** 311-343.

PAN, C., HILPERT, M. & MILLER, C. 2004. Lattice-Boltzmann simulation of two-phase flow in porous media. *Water Resources Research,* 40.

PATZEK, T. & SILIN, D. 2001. Shape factor and hydraulic conductance in noncircular capillaries: I. One-phase creeping flow. *Journal of colloid and interface science,* 236**,** 295-304.

PORTER, M. & WILDENSCHILD, D. 2010. Image analysis algorithms for estimating porous media multiphase flow variables from computed microtomography data: a validation study. *Computational Geosciences,* 14**,** 15-30.

PORTER, M. L., SCHAAP, M. G. & WILDENSCHILD, D. 2009. Lattice-Boltzmann simulations of the capillary pressure–saturation–interfacial area relationship for porous media. *Advances in Water Resources,* 32**,** 1632-1640.

RAOOF, A. & HASSANIZADEH, S. M. 2010. A new method for generating pore-network models of porous media. *Transport in porous media,* 81**,** 391-407.

REEVES, P. C. & CELIA, M. A. 1996. A functional relationship between capillary pressure, saturation, and interfacial area as revealed by a pore-scale network model. *Water Resources Research,* 32**,** 2345-2358.

RYAZANOV, A. V., VAN DIJKE, M. I. J. & SORBIE, K. S. 2009. Two-Phase Pore-Network Modelling: Existence of Oil Layers During Water Invasion. *Transport in Porous Media,* 80**,** 79-99.

SAHIMI, M. 1994. *Applications of percolation theory*, CRC Press.

SAKELLARIOU, A., SAWKINS, T. J., SENDEN, T. J. & LIMAYE, A. 2004. X-ray tomography for mesoscale physics applications. *Physica A: Statistical Mechanics and its Applications,* 339**,** 152-158.

SCHEIDEGGER, A. E. 1954. Statistical Hydrodynamics in Porous Media. *Journal of Applied Physics,* 25**,** 994-1001.

SILIN, D., TOMUTSA, L., BENSON, S. M. & PATZEK, T. W. 2011. Microtomography and pore-scale modeling of two-phase fluid distribution. *Transport in porous media,* 86**,** 495-515.

SINGH, M. & MOHANTY, K. K. 2003. Dynamic modeling of drainage through three-dimensional porous materials. *Chemical Engineering Science,* 58**,** 1-18.

SMITH, S. W. 1997. The scientist and engineer's guide to digital signal processing.

SPIECKER, P. M., GAWRYS, K. L., TRAIL, C. B. & KILPATRICK, P. K. 2003. Effects of petroleum resins on asphaltene aggregation and water-in-oil emulsion formation. *Colloids and Surfaces A: Physicochemical and Engineering Aspects,* 220**,** 9-27.

TANG, G.-Q. & MORROW, N. R. 1999. Influence of brine composition and fines migration on crude oil/brine/rock interactions and oil recovery. *Journal of Petroleum Science and Engineering,* 24**,** 99-111.

TAUD, H., MARTINEZ-ANGELES, R., PARROT, J. F. & HERNANDEZ-ESCOBEDO, L. 2005. Porosity estimation method by X-ray computed tomography. *Journal of Petroleum Science and Engineering,* 47**,** 209-217.

TONG, Z., MORROW, N. & XIE, X. 2003. Spontaneous imbibition for mixed-wettability states in sandstones induced by adsorption from crude oil. *Journal of Petroleum Science and Engineering,* 39**,** 351-361.

TURNER, M. L., KNÜFING, L., ARNS, C. H., SAKELLARIOU, A., SENDEN, T. J., SHEPPARD, A. P., SOK, R. M., LIMAYE, A., PINCZEWSKI, W. V. & KNACKSTEDT, M. A. 2004. Three-dimensional imaging of multiphase flow in porous media. *Physica A: Statistical Mechanics and its Applications,* 339**,** 166-172.

VALVATNE, P. H. & BLUNT, M. J. 2004. Predictive pore-scale modeling of two-phase flow in mixed wet media. *Water Resources Research,* 40**,** W07406.

VAN DIJKE, M. & SORBIE, K. 2006. Existence of fluid layers in the corners of a capillary with non-uniform wettability. *Journal of Colloid and Interface Science,* 293**,** 455-463.

VIZIKA, O., AVRAAM, D. G. & PAYATAKES, A. C. 1994. On the Role of the Viscosity Ratio during Low-Capillary-Number Forced Imbibition in Porous Media. *Journal of Colloid and Interface Science,* 165**,** 386-401.

VLASSENBROECK, J., MASSCHAELE, B., CNUDDE, V., DIERICK, M., PIETERS, K., VAN HOOREBEKE, L. & JACOBS, P. 2010. Octopus 8: A High Performance Tomographic Reconstruction Package for X-ray Tube and Synchrotron micro-CT. *In:* DESRUES, J., VIGGIANI, G. & BÉSUELLE, P. (eds.) *Advances in X-ray Tomography for Geomaterials.* ISTE.

VOGEL, H. J. 1997. Morphological determination of pore connectivity as a function of pore size using serial sections. *European Journal of Soil Science,* 48**,** 365-377.

VOGEL, H. J. & ROTH, K. 1998. A new approach for determining effective soil hydraulic functions. *European Journal of Soil Science,* 49**,** 547-556.

VOGEL, H. J. & ROTH, K. 2001. Quantitative morphology and network representation of soil pore structure. *Advances in Water Resources,* 24**,** 233-242.

WELGE, H. J. 1952. A Simplified Method for Computing Oil Recovery by Gas or Water Drive.

WELLINGTON, S. L. & VINEGAR, H. J. 1987. X-ray computerized tomography. *Journal of petroleum technology* 39**,** 885-898

WILDENSCHILD, D., ARMSTRONG, R. T., HERRING, A. L., YOUNG, I. M. & WILLIAM CAREY, J. 2011. Exploring capillary trapping efficiency as a function of interfacial tension, viscosity, and flow rate. *Energy Procedia,* 4**,** 4945-4952.

WILDENSCHILD, D., HOPMANS, J. W., RIVERS, M. L., KENT, A. J. R., WILDENSCHILD, D., HOPMANS, J. W., RIVERS, M. L. & KENT, A. J. R. 2005. Quantitative analysis of flow processes in a sand using synchrotron-based X-ray microtomography. *Vadose Zone Journal,* 4**,** 112-126.

WILDENSCHILD, D. & SHEPPARD, A. P. 2013. X-ray imaging and analysis techniques for quantifying pore-scale structure and processes in subsurface porous medium systems. *Advances in Water Resources,* 51**,** 217-246.

WILKINSON, D. 1984. Percolation model of immiscible displacement in the presence of buoyancy forces. *Physical Review A,* 30**,** 520.

WILKINSON, D. & WILLEMSEN, J. F. 1983. Invasion percolation: a new form of percolation theory. *Journal of Physics A: Mathematical and General,* 16**,** 3365.

WITHJACK, E. M. 1988. Computed tomography for rock-property determination andfluid-flow visualization. . *SPE Formation Evaluation* 696–704.

WU, K., VAN DIJKE, M. I., COUPLES, G. D., JIANG, Z., MA, J., SORBIE, K. S., CRAWFORD, J., YOUNG, I. & ZHANG, X. 2006. 3D stochastic modelling of heterogeneous porous media–applications to reservoir rocks. *Transport in Porous Media,* 65**,** 443-467.

YOUSSEF, S., DESCHAMPS, H., DAUTRIAT, J., ROSENBERG, E., OUGHANEM, R., MAIRE, E. & MOKSO, R. 2013. 4D IMAGING OF FLUID FLOW DYNAMICS IN NATURAL POROUS MEDIA WITH ULTRA-FAST X-RAY MICROTOMOGRAPHY.

YUSTER, S. T. 1951. Theoretical Considerations of Multiphase Flow in Idealized Capillary Systems. World Petroleum Congress.

ZHOU, N., MATSUMOTO, T., HOSOKAWA, T. & SUEKANE, T. 2010. Pore-scale visualization of gas trapping in porous media by X-ray CT scanning. *Flow Measurement and Instrumentation,* 21**,** 262-267.

Chapter 3

Methods, Material and Experimental Techniques

In this chapter the main techniques used in this research are listed and briefly explained. The chapter outlines the instruments, experimental techniques and workflows specifically used in this study. Detailed description of the instruments designed and constructed in-house at the University of Edinburgh as well as the pore-scale network modeling software package developed at Heriot-Watt University is presented.

1. Experimental Techniques

1.1. Mercury Intrusion Capillary Pressure

1.1.1. Theory

A fluid does not spontaneously imbibe into a porous media to which it is non-wet. For instance, in order to inject a non-wetting fluid such as mercury into a bundle of capillary tubes with a range of diameters, external pressure needs to be applied. Mercury starts penetrating into the capillary tubes with the largest diameters. As the injection pressure increases mercury intrudes into capillaries with increasingly smaller diameters. The Young-Laplace equation relates the applied pressure to the diameter of the capillaries (Young, 1805):

$$P_c = \frac{-2\,\sigma\cos\theta}{r}, \tag{3.1}$$

where σ is the interfacial tension of mercury and air (484 dynes/cm), r is the radius of the capillary tube, and θ is the contact angle between mercury-air interface and the capillary tube surface (typical advancing contact angle for mercury-air-quartz reported in the literature is 140° degrees, $\cos 140° = -0.77$). Mercury intrusion capillary pressure (MICP) tests are designed to: (a) generate *(Pc-Sat)* curves, and (b) analyse the pore-throat size distribution of the porous medium. Although MICP is a destructive test it can be performed on samples of any shape and size including drilling operation cuttings. In addition, it is a relatively quick and low-cost test which can be completed in less than one hour.

1.1.2. Test Procedure and Output Data

Figure 3.1 shows the steps involved in a MICP test. The sample is placed into a glass cell known as penetrometer which is then pumped to a vacuum. Mercury is then injected into the vessel with progressively increasing pressures. Depending on the type of penetrometer the pressure can increase up to 4×10^5 kPa (~60,000 psi). At each pressure step the volume of the penetrated mercury is recorded. It is the narrowest parts of the pore space which control the amount of mercury intrusion, in other words the pore-throats are resisting the mercury intrusion. Therefore, the translated pore-size distribution obtained from the pressure data corresponds to the pore-throats.

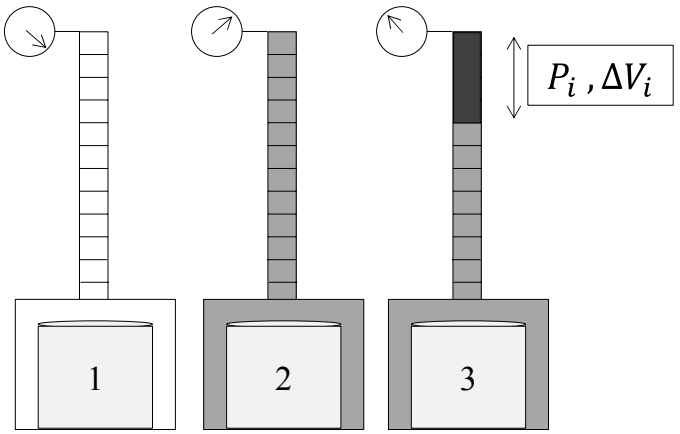

Figure 3.1: Mercury injection capillary pressure test procedure. The penetrometer is first pumped to a vacuum (1), mercury is then introduced into the cell (2). Increase in the pressure of the system (3) results in the mercury to invade the pore space of the rock sample.

For a pore to be invaded by mercury it is essential that the pore is accessible through a connected path of pores and throats to the outer surface of the sample. This is referred to as the accessibility of the pores and is considered as a tuning parameter in some pore network modelling approaches. The raw output of the MICP test is the pressure vs. injected mercury volume plot. The *(Pc-Sat)* curve is then plotted by calculating the mercury saturation at each pressure step based on the following equation:

$$S_{Hg\ at\ P_i} = \frac{Total\ volume\ of\ injected\ Hg\ \ at\ \ P_i}{Total\ \ volume\ injected\ Hg\ at\ the\ end} = \frac{\int_{r_i}^{\infty} f_{(r)} V_p(r) dr}{\int_{0}^{\infty} f_{(r)} V_p(r) dr}, \qquad (3.2)$$

where $f_{(r)}$ is the distribution function of the accessible pores and $V_p(r)$ is the volume of the pores with pore-throat radius r (Sahimi, 1994). It should be noted that the pore-throat size distributions calculated from MICP data should not be directly compared to the pore-size distributions calculated for instance from 3D image analysis of the pore space.

MICP measurements for a dolomite sample were used in a pore-network modelling study which is discussed in chapter 7. The data provided assistance in fine-tuning the multiple-scale pore network models of the complex pore systems of the dolomite, prior to using those models in further fluid flow simulations.

1.2. X-ray Computed micro-Tomography (μCT)

The μCT scanner used in this research (located at the university of Edinburgh, School of Geosciences) was constructed in-house with a cone-beam configuration (refer to chapter 2, section 2) and main components as shown in Figure 3.2:

- X-ray source (Feinfocus FXT-160.48-2, dual head transmission/directional nano/microfocus tube), with spot size of 12 ± 1 μm for X-ray energy of 120 keV.
- X-ray camera (4 MP Gadox Rad-icon Shad-O-Box 4K, 12bit). The camera pixel size is 48 μm.
- Air-bearing rotary table (Micos UPR-160F SMC pegasus with taurus motion controller)

The data collection was performed via a suit of C++ codes written in-house and operated via a Testpoint (v.6) Shell program to coordinate the table movement with image acquisition. The microfocus X-ray source can generate an electron beam with a cross-section of only a few microns, this is essential for achieving image resolutions of few micrometers. The μCT scanner was designed at the University of Edinburgh specifically for the purpose of running in-situ experiments. The best obtainable voxel resolution typically equates to 1/1500 of the sample diameter.

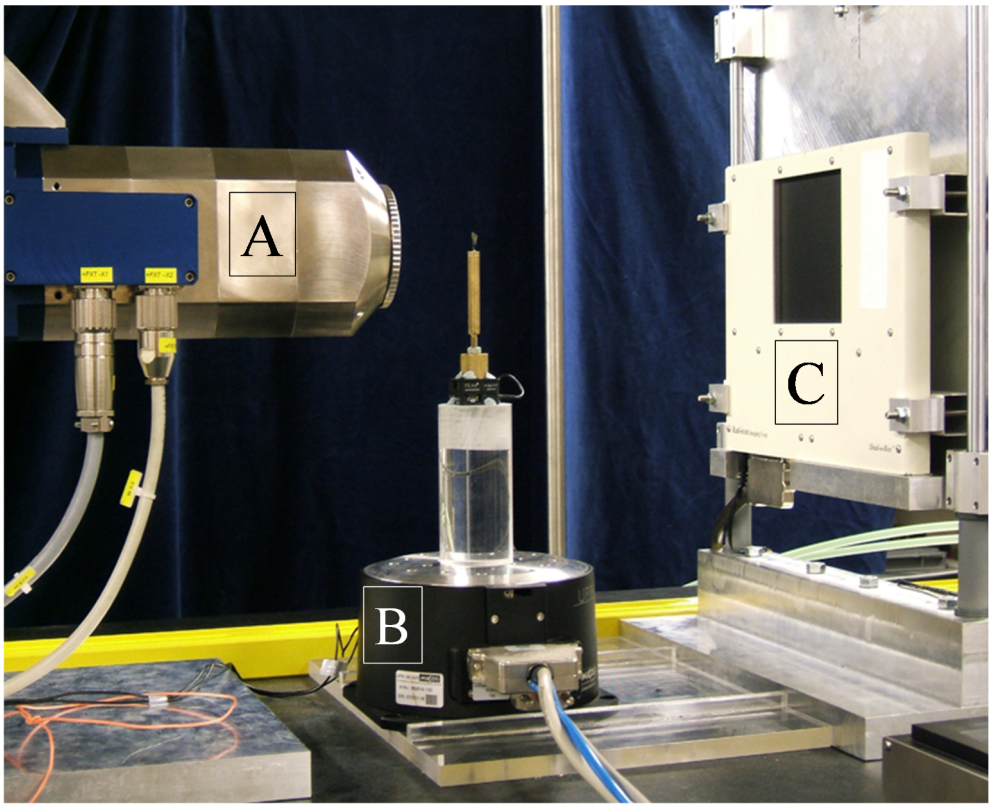

Figure 3.2: ECOSSE X-ray µCT scanner components: (A) X-ray source (Feinfocus dual head transmission/directional nano/microfocus tube), (B) Air-bearing rotary table (Micos UPR-160F SMC pegasus with taurus motion controller), and (C) 4 MP Gadox X-ray camera (Rad-icon Shad-O-Box).

Subsequent to data acquisition images were reconstructed using Octopus (v 8.5 - v 8.7) (Vlassenbroeck et al., 2010). In order to perform mathematic operations on images such as subtraction, masking and averaging it is essential that the input images are of the exact same dimensions. Therefore, to make images captured at different stages of each experiment consistent the reconstructions were done on the exact same window, in addition to that the same normalization window, ring filtering and beam hardening correction factors were used.

1.3. Core Flooding: A Simple Low-cost X-ray Transparent Core Holder

For in-situ monitoring of the fluid saturation distributions inside the pore space of a rock an X-ray transparent core holder is required. Commercially available X-ray transparent core holders are commonly made of carbon fibre wrapped tubes, PEEK (Polyether Ether Ketone, an organic polymer), aluminium or a combination of these

materials (refer to Table 2.1). The flow cell used in this study was designed in-house and constructed in Edinburgh university workshop (Pak et al., 2013).The flow cell operates under modest pressures (not more than 100 Psi = 690 kPa) and temperatures (up to 50°C). It has a simple, low-cost design with a very high level of X-ray transparency. It is composed of four main components:

- Epoxy encased core plug (Epoxy ID number: 20-8130-032)
- 2 x Delrin® (Polyoxymethylene) end pieces
- 2 x 12 mm ID x 1.8mm Nitrile o-rings, Shore hardness 70
- 3 x M4 Nylon threaded rods located through two aluminium thrust plates

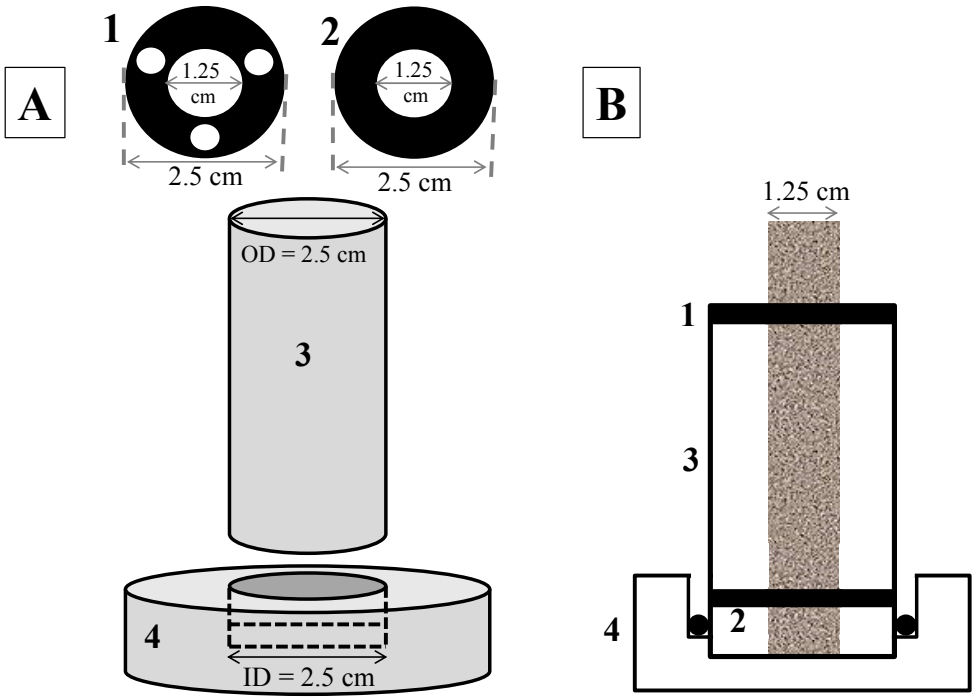

Figure 3.3: Preparation kit used to encapsulate the core plug in epoxy. (A1 and A2) aluminium pieces, (A3) acrylic tube, (A4) Delrin stand, (B) side view of the core in the moulding system.

Before the cell is assembled, the core plug is encapsulated in epoxy using a simple moulding system shown in Figure 3.3. In order to keep the core centered in the cast two washer-shape aluminum pieces are used. Once the epoxy has set the tube should be turned down to a precise outside diameter on a lathe making a slip fit into the end

caps as shown in Figure 3.4. A lathe is a machining tool which is used to rotate the sample around its central axis for performing machining operations.

Finally, the epoxy wrapped plug is placed between the two end caps before all parts are clamped together tightly using 3 nylon threaded rods. This way a fluid-tight seal is made between the o-rings of the end pieces and the epoxy jacket of the core plug. Figure 3.4 shows a schematic drawing of the core holder.

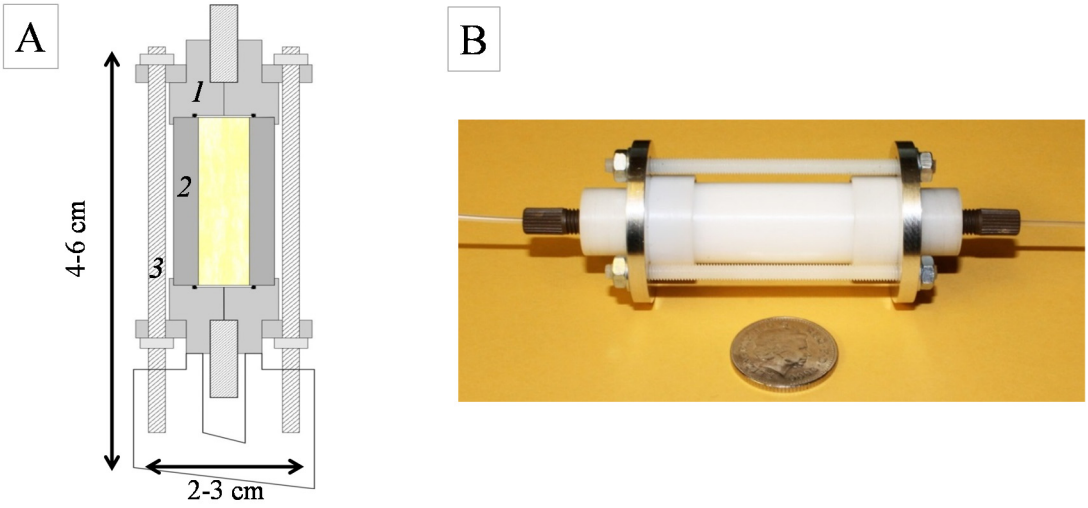

Figure 3.4: X-ray transparent core holder design composed of (A1) Derlin end cap, (A2) epoxy encased core plug, and (A3) M4 Nylon threaded rods. (B) Photo of the constructed core-holder.

All fluid connections within the system were made using standard low pressure liquid chromatography (LPLC) flangeless fittings. A list of the LPLC fittings used in this set-up is presented in Appendix D. Fluid injections utilised a Milligat MG-1 LF pump which offers pulseless, continuous flow over a range of 6 orders of magnitude of flow rates (nL/min – mL/min). Figure 3.5 shows the cross-section of this pump. There are four equal syringes of 25 µl volume inside the pump which are driven by a stepper motor coupled to a swash plate. The flow rate and direction are controlled by the stepper motor's rotation rate and direction. The stepper motor is of micro-step accuracy.

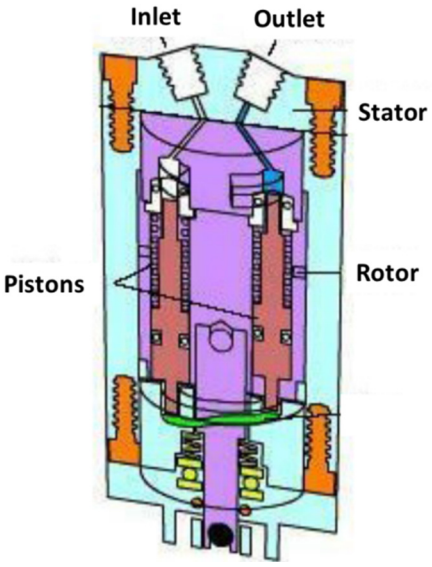

Figure 3.5: Cross section of the milliGAT pump taken from the milliGAT manual.

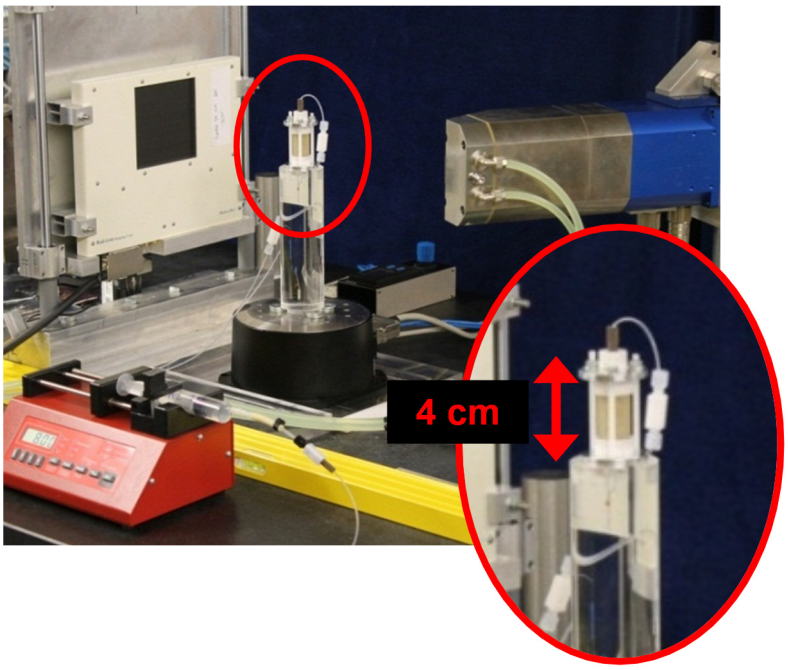

Figure 3.6: X-ray transparent core holder placed on the rotary table of the µCT scanner.

One of the advantages of the presented simple core holder design is that it works with plugs of different sizes from few millimeters up to few centimeters. Once the cell is assembled it is positioned on the rotary table of the µCT scanner (Figure 3.6). In order to keep the tomographic data collected throughout the flooding cycle in

alignment the flooding cell was kept in the same position during the entire experimental duration.

2. Material

2.1. Rock Sample

A Silurian Dolomite (SD) from an outcrop (Thornton formation, located near Chicago, Illinois, in US) was used in this study for all core flooding experiments. The samples were supplied by Petrobras. This carbonate was selected on the basis of its reasonable porosity (17 %) and well-connected pore network (approximate permeability ~50 mD) which makes it suitable for low pressure experiments. The rock is a recrystallized dolomite with a range of pore-sizes from large millimetre scale pores to pores of less than 1 µm. Multiple-scale porosity is an inherent characteristic of many carbonate rocks, for this reason, a representative sample of such a heterogeneous carbonate rock is much larger than representative samples of more homogeneous rocks such as sandstones.

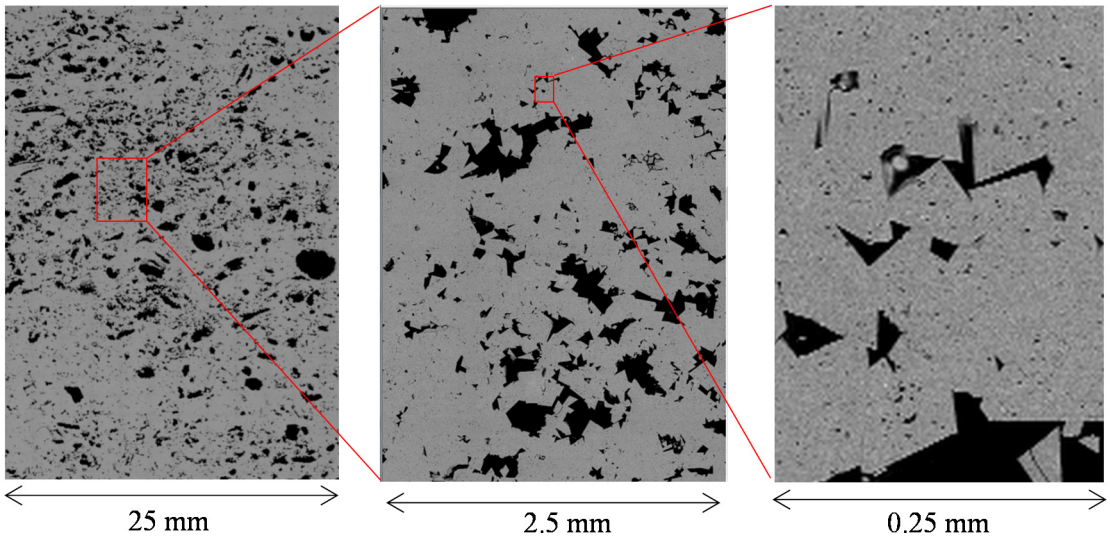

Figure 3.7: Backscattered SEM image of a polished thin section of SD in three different magnifications, acquired at SEM facility at Heriot-Watt University.

Figure 3.7 shows a scanning electron microscope (SEM) image of a polished thin section of SD acquired in backscattered mode at three different magnifications. The images were acquired at the SEM facility at Heriot-Watt University. The left hand

side image represents a tessellated image constructed from 400 fields of view stitched together. The multiple-scale porosity of the rock is characterised by pores spanning 3 orders of magnitude in dimension.

From the mineralogical point of view SD is a very simple rock composed of more than 99% dolomite mineral based on X-ray diffraction (XRD) test performed at University of Edinburgh. The presence of highly X-ray absorbent minerals such as pyrite may introduce artifacts such as strike artifacts on the acquired X-ray images. For SD, the uniform mineralogy provided a uniform greyscale on the images. Figures 3.8 and 3.9 show mercury injection capillary pressure (MICP) data for three SD plugs (1", 2.54cm diameter). MICP tests were carried out at the Petrobras Research Centre (CENPES) in Brazil.

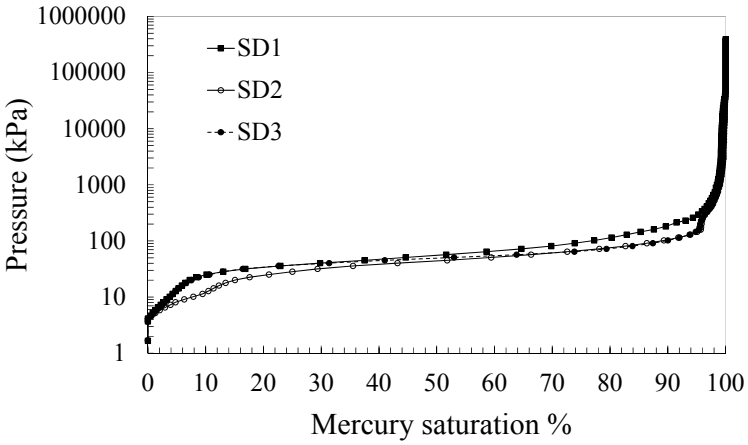

Figure 3.8: Capillary pressure vs mercury saturation curves for 3 SD plugs (1", 2.54cm diameter), based on mercury injection capillary pressure (MICP) tests. SD shows a well-connected porosity by having 98% of its pore space invaded at pressures less than 690 kPa (100 psi).

(Pc-Sat) curves show 98 % of the accessible pore space of SD plugs was invaded by mercury with injection pressures less than 690 kPa (100 psi). Therefore, the injection pressures needed for fluid flow experiments in this rock are well within the operating pressure of the core flooding cell (100 psi).

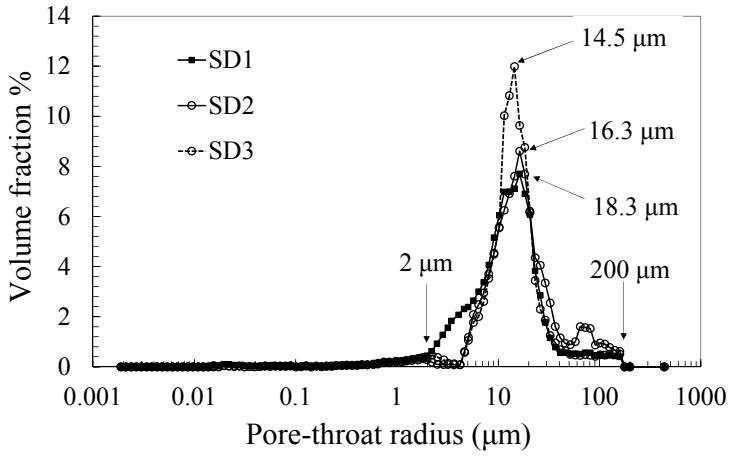

Figure 3.9: Pore-throat size distribution for 3 SD plugs (1", 2.54cm diameter) based on MICP tests. The curves shows peak values at 14.5, 16.3, and 18.3 µm. The image resolution of the acquired µCT images used in this study are smaller than these peak values, this enables imaging of most pore-throats.

2.2. Fluid Phases

The purpose of the experiments was to record fluid displacement processes for an immiscible fluid pair in porous carbonate rock. Dodecane and water were chosen to be used as the aqueous and organic phases based on their negligible solubility. The solubility of dodecane in water at 25 °C is reported in the literature to be 8.9×10^{-10} in mole fraction (Shaw et al., 2006). Apart from the solubility other factors were taken into consideration in order to select a suitable pair of organic and aqueous fluids for these experiments. These include: (a) the X-ray attenuation coefficient of each fluid phase and the phase contrast on the resulting µCT images, and (b) the density difference between the two fluid phases which results in gravity driven forces to come into play.

The X-ray source used generates bremsstrahlung, with a continuous spectrum below the peak energy used (120kV). Consequently, at the X-ray energies used in this study the influence of the iodine k-edge ensures that the mass attenuation coefficients for all three phases result in strong differences in X-ray attenuation. Figure 3.10 plots the mass X-ray attenuation coefficient (chapter 2, section 2) of water, dodecane, and the two main minerals forming the carbonate rocks (calcite and dolomite). The mass X-ray attenuation coefficients of water and dodecane are very similar. In order to be

able to distinguish these two fluid phases on X-ray images low X-ray energies (10 to 30 keV) should be used. However, in this application the fluid phases are saturating pore space of a rock comprising significantly more attenuating minerals. As shown in Figure 3.10 the difference in mass X-ray attenuation coefficient of the rock and fluid phases is even more pronounced in the lower energies. Therefore, a low energy X-ray beam is completely absorbed by the rock resulting in not enough low energy X-ray photons to reach the camera.

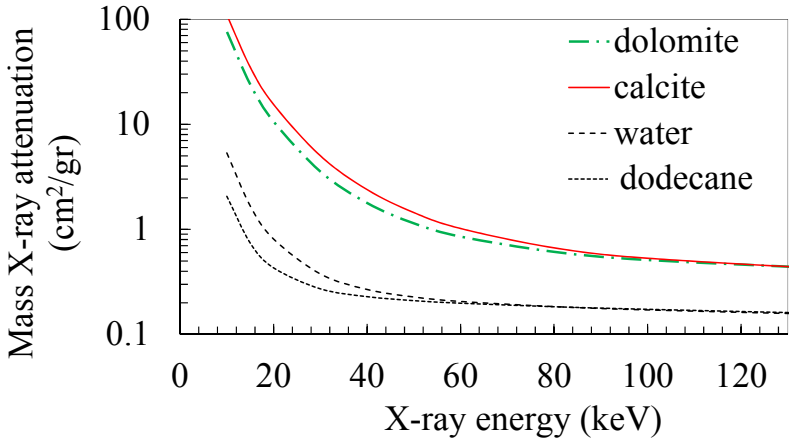

Figure 3.10: Mass X-ray attenuation coefficient plotted against X-ray energy (MuCalc Tool, University of Texas, XCOM: Photon Cross Sections Database).

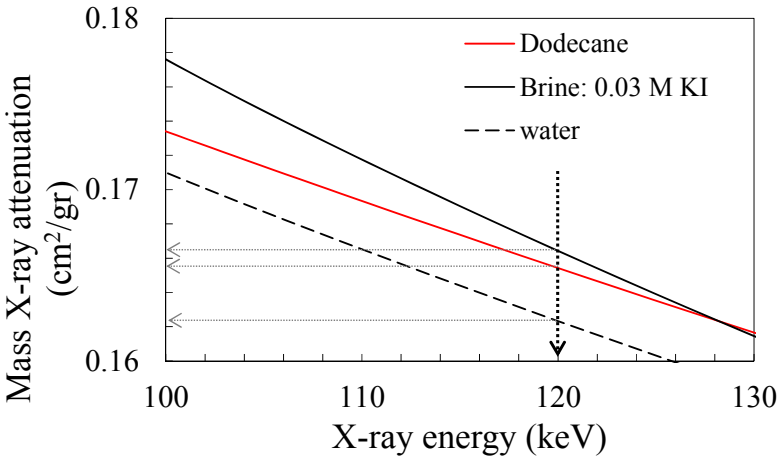

Figure 3.11: Mass X-ray attenuation coefficient of dodecane, water and 0.03 M KI brine plotted against X-ray energy (MuCalc Tool, University of Texas, XCOM: Photon Cross Sections Database). These three fluids display close mass X-ray attenuation coefficients.

The size of the core plug determines how much carbonate is on the way of the X-ray beam, the larger the plug the higher the energy of the X-ray beam should be to have reasonable X-ray transmission. For the 12.5 mm diameter plugs used in this study X-ray energy of 120keV was selected. At this X-ray energy the mass X-ray attenuation coefficients of dodecane and water are very close, 0. 162, and 0.165 (cm^2/gr), respectively, see Figure 3.11.

Therefore, a doping agent is required to enhance contrast between the two fluid phases and the rock. A doping agent is an impurity element that is mixed with a fluid phase in order to increase the X-ray attenuation property of the fluid. Application of iodated hydrocarbons or iodide brines is common in μCT studies (Iglauer et al., 2011, Culligan et al., 2006, Porter and Wildenschild, 2010, Youssef et al., 2009). Doping amplifies the produced signal and hence enhances the signal to noise ratio. On this basis, the two following fluid pairs were considered:

- Organic phase: Dodecane, and aqueous phase: 0.5 M KI brine
- Organic phase: 50%v/v iododecane in dodecane, and aqueous phase: 0.03 M KI brine

Figure 3.12 shows both pairs provided a reasonably good contrast between the two fluid phases and the rock at 120 keV. The density difference between the two phases was considered to be potentially a significant factor which might drive fluid redistribution during data acquisition. With the available instrument the data acquisition time for each single scan of 1000 to 1500 projections (each comprising of the summation of 3 one second exposure projections) was 150 to 250 minutes, respectively. In addition, a time delay of 12-48 hours between any two injection steps in the test procedure was inevitable. Therefore, in order to avoid saturation redistributions governed by gravity-driven forces during data collection, the density of the two fluid phases was closely matched. The 50%v/v iododecane in dodecane and 0.03M KI solution were chosen which display equal density at room temperature (1.005 gr/cm^3) as well as an excellent contrast between the three oil-brine-rock phases.

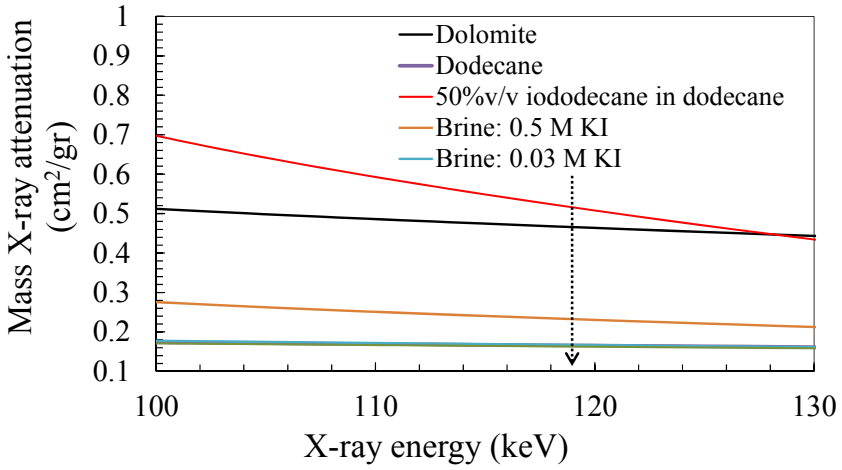

Figure 3.12: Mass X-ray attenuation coefficient plotted against x-ray energy (MuCalc Tool, University of Texas, XCOM: Photon Cross Sections Database)

3. Image Processing and Quantification Techniques

3.1. Noise Analysis

One crucial question that needs to be addressed in any tomographic study is “how much the original signal is corrupted by measurement noise?”. Overlapping noise can cause errors in the subsequent segmentation and quantitative analysis of the images. As explained in chapter 2, section 2, the CT technique involves physical measurement of the X-ray beam intensity that is transmitted through a sample at the detector plane. Therefore, the measurements are subject to noise. Noise is the uncertainty in a signal due to random fluctuations in that signal. The causes of these fluctuations come from source, sample and sensor. An X-ray beam produced by an X-ray tube is inherently statistical in nature and the number of photons emitted per unit time varies as a Poisson distribution. Other sources of random fluctuation result from attenuation and X-ray scattering by the sample, sample holder and X-ray filters. The sensor can also introduce noise not because the absorption of radiation by the detector is a random process, but because the detectors can generate currents from thermal sources that introduce random fluctuations into the signal. Such noise is most readily recognised in "dark images" where a random sensor response is recorded without X-ray illumination of the sensor.

In addition to these sources of measurement noise the images are subject to numerical noise introduced during the reconstruction process. To illustrate the problem a 12.5 mm (half inch) diameter core plug of a limestone was scanned 3 times under the same scanning conditions. The image reconstructions performed using the same reconstruction parameters such as normalisation window, beam hardening and ring filter correction factors. Figure 3.13 illustrates the same slice from these three identical scans. It is noticed, visually and considering the pixel values, that the results of these three identical scans are not exactly the same meaning that each pixel does not necessarily display the same grey value on these 3 images.

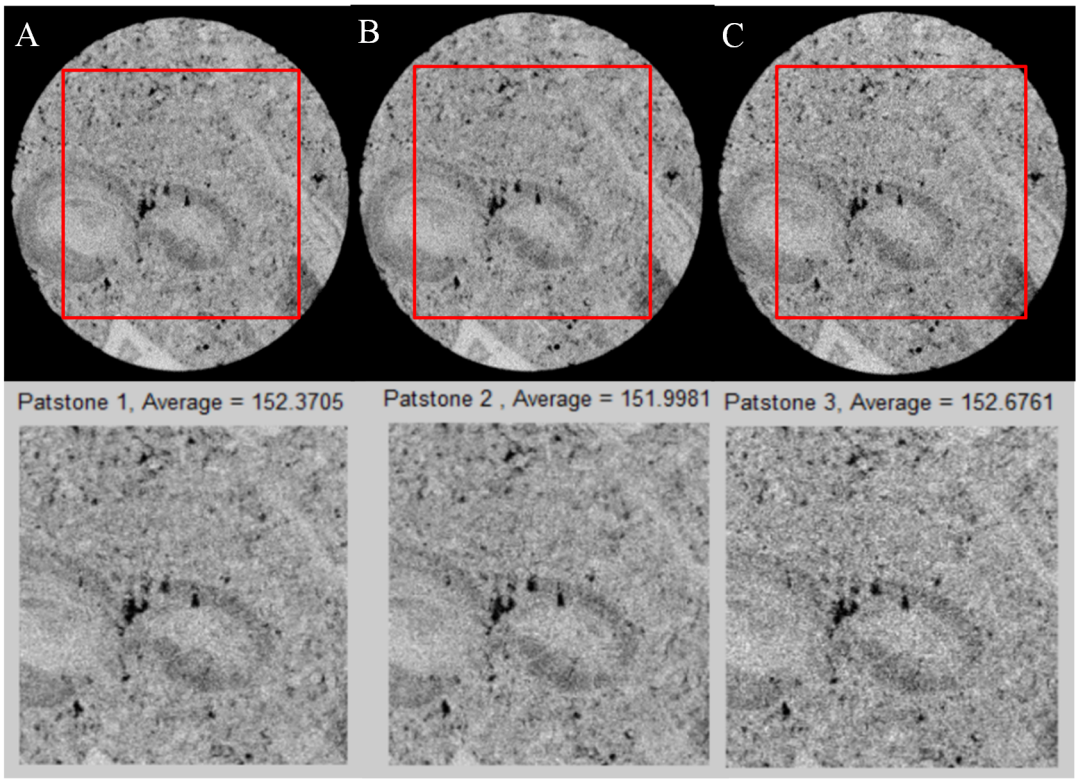

Figure 3.13: Corresponding µCT slices from 3 identical scans of a carbonate rock. Core diameter is 12.5 mm.

To obtain an idea of how different are the two images (acquired at identical scanning conditions) on a pixel by pixel level one image was subtracted from the other, results are illustrated in Figure 3.14.

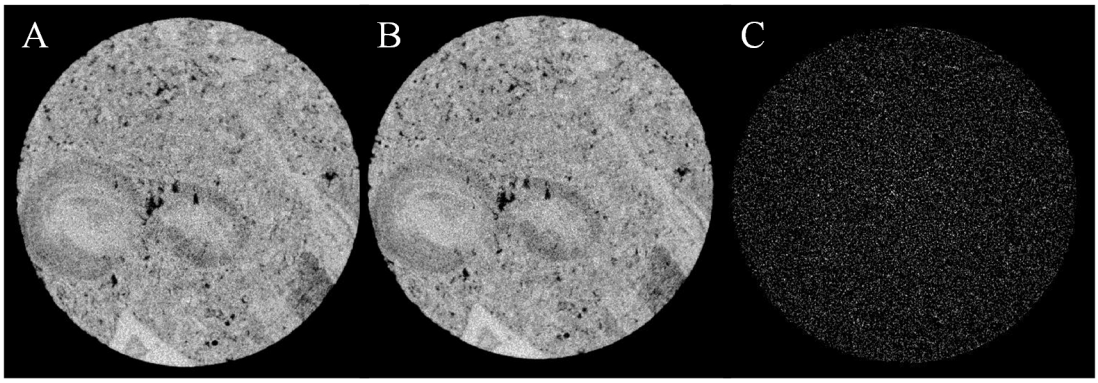

Figure 3.14: Corresponding µCT slices from two identical scans (A and B) and their subtraction image (C).

By reviewing the subtracted images no specific pattern is observed, instead the noise pattern seems to be a random (white) noise, this suggests that there is no systematic error in the measurement exercise such as a systematic defect in any of the scanners components. On this basis, to suppress the noise the following solution was implemented.

3.1.1. Averaging Identical Scans of a Sample to Effectively Suppress the Noise

Benson et al. (2011) assessed the error of the CT measurements on a pixel-by-pixel level for medical CT images of sandstone rock samples. They demonstrated that averaging multiple scans taken at identical positions can suppress the random noise corrupting the CT images. Their analysis also suggests that using contrast enhancing agents (i.e. doping agents) can limit the uncertainty. Such image enhancement techniques assisted them to obtain closer estimations of the rock porosity and fluid saturations.

Figure 3.15 illustrates the signal profile along the line for the three images shown in Figure 3.13 and their average image (Figure 3.15A). The line profile is drawn in a way that it touches one large pore in the centre of the image to see the effect of averaging on the edges of the pores. The signal of the averaged image exhibits a cleaner profile with significantly lower fluctuations compared to the individual scans. The averaging exercises has made the edges sharper and cleaner, this is especially

favourable in quantitative analysis since sharper edges are better detected in the segmentation step.

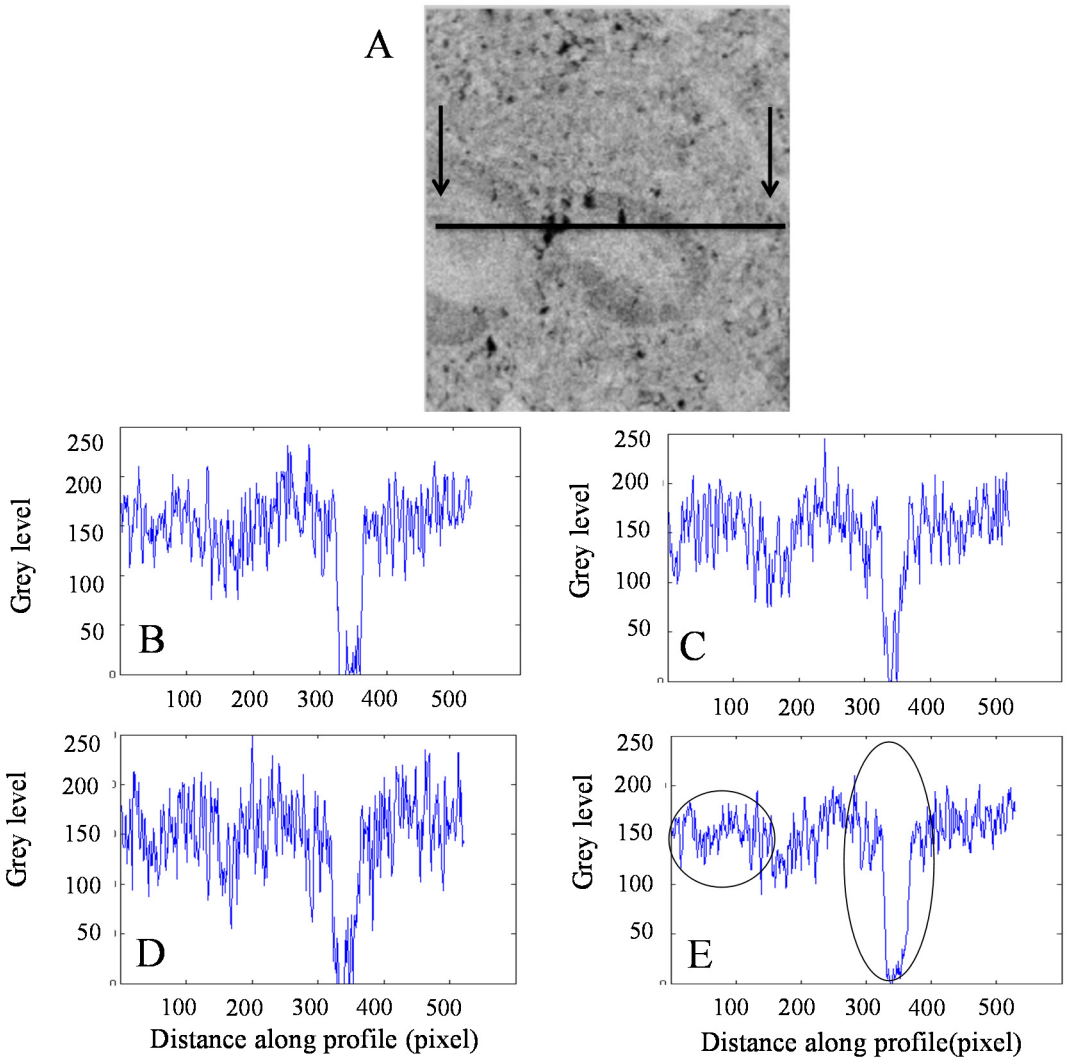

Figure 3.15: (B to E) Line profile for the three slices shown in Figure 3.13 and their average image (A), along the line shown in (A). The average image displays a less noisy profile (E). The ellipses show the lower degree of fluctuation as well as the sharper edges for the large pore.

Scanning the sample several times and averaging the reconstructed images is an applicable method as long as the state of the sample is not changing with time (such as a dry core plug), however this is not necessarily the case for a saturated core plug since there might be some saturation redistributions (for instance due to gravity). In addition the imaging instrument used in this study was relatively slow compared to

similar laboratory-based μCT scanners, therefor multiple acquisitions at each step of the fluid flow cycle was not practical. The averaging method was applied to obtain the most accurate and least noisy image of the dry rock, this was helpful in two ways: firstly, a clean image of the rock could be used as a mask to subtract the rock from the saturated rock images, secondly and more importantly the dry rock images were subsequently used as the input for the pore-scale network modelling package. A less noisy image assists extraction of a more realistic pore network model of the rock.

Avizo-Fire (v.6-v.8) is an image processing software package used in this study for visualization and quantification of μCT images. The package provides a range of image processing tools including: (a) 2D and 3D visualisation of data for exploring the acquired as well as processed images, and (b) image filtering, segmentation, labelling and quantitative analysis of individual labels. Avizo-Fire is equipped with a broad selection of image filters and quantitative measurement tools, however at the time of writing this thesis there is a limited selection of image segmentation algorithms implemented in Avizo-Fire (v.8). The development of a more robust segmentation method or writing codes for more sophisticated segmentation algorithms that already exist in the literature such as indicator kriging (Oh and Lindquist, 1999) was beyond the scope of this study, therefore the currently available segmentation tools in Avizo-Fire (v.8) were used.

3.1.2. Noise Filters

The optimal way of removing random noise is to minimize it during data acquisition. For instance using physical filters placed in front of the camera can absorb scattered low energy photons before they can reach the camera. On this basis a 0.8 mm aluminum plate was placed in front of the camera for the fluid flow experiments reported in this thesis. In addition averaging identical scans as well as summing multiple projections at each position during sample rotation are two other methods that were utilized to suppress the measurement noise.

Subsequent to acquisition and reconstruction image processing tools such as noise filters can assist the enhancement of the image quality and signal to noise ratio. A filter can be considered as a transformation operator which is information-reducing and smoothing, but which should not create any artifacts which were not present in

the original data (Gonzalez et al., 2004). Of particular importance to noise filtering is the preservation of the essential features of the image such as phase boundaries and edges which are important for the subsequent segmentation and quantification. Among the filters implemented in Avizo-Fire (v.8) the median, anisotropic diffusion, and non-local means filters were used in this study.

3.1.2.1. Median Filter

This filter replaces the value of each pixel on an input image with the median value of its neighbouring pixels (Gonzalez et al., 2004). The size of the neighbourhood window (kernel) that the algorithm considers can be adjusted by the user. Median filter is applied globally on the input image. The larger the kernel size the smoother the resulting image becomes. This filter is specifically useful for removing pixels with outlier values (values far from the range of neighbouring pixels, e.g. salt and pepper noise). These outlier values could be: (a) random noise, or (b) realistic features of the image such as phase boundaries and edges. Figure 3.16 illustrates the concept behind the median filter.

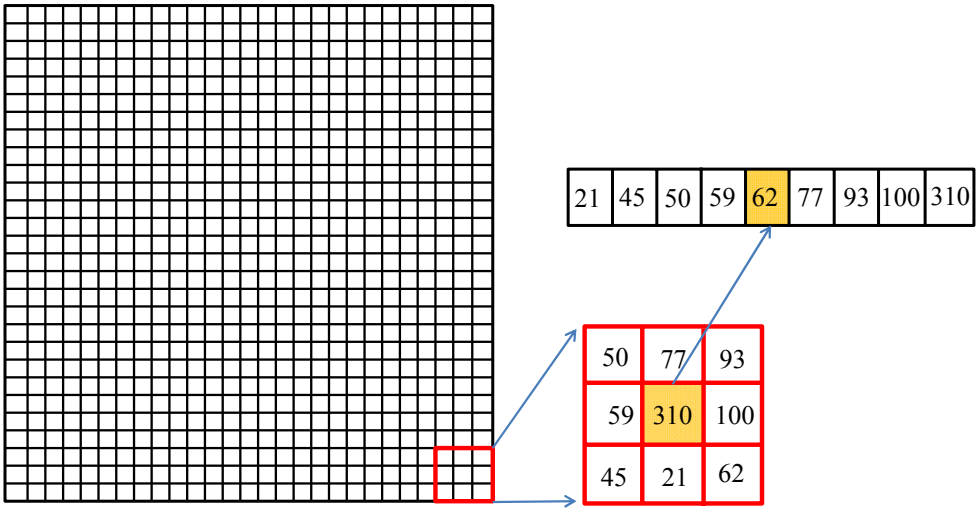

Figure 3.16: Application of median filter on a 2D image. The red matrix shows the kernel or the neighbourhood window.

Figure 3.17A shows an example µCT slice of a two-phase (oil and brine) saturated carbonate core. The results of the median filtering with four different kernel sizes of 2, 3, 4, and 5 are shown respectively in Figure 3.17B to 3.17E. Figure 3.17F

compares the image histogram before and after the denoising exercise. As shown the histogram of the filtered images display narrower grey value distributions.

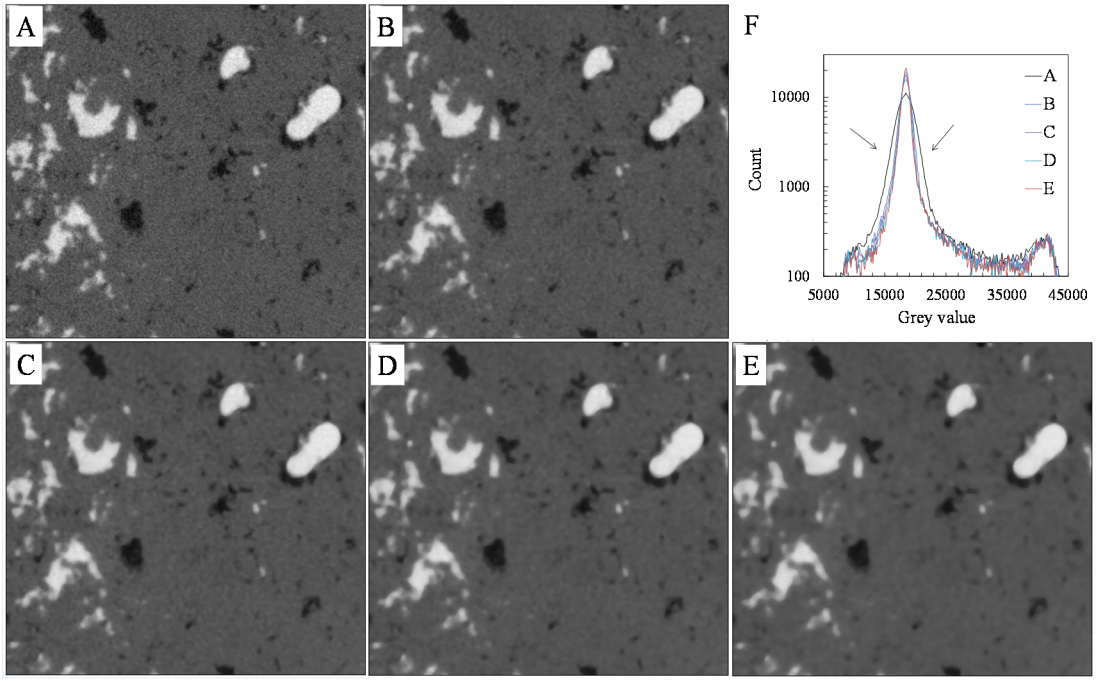

Figure 3.17: Median filtering of a µCT image of a two-phase saturated carbonate core. (A) shows the original image. (B to E) are the filtered images with kernel sizes of 2, 3, 4, and 5, respectively. The filtered images display narrower histograms (F). White: oil, black: water, and grey: rock.

It is also visually clear that the filtered image is smoother with fewer outlier pixels; however, the images appears to be blurry over the edges (and smaller structures), the lack of sharpness becomes more pronounced as the kernel size increases.

3.1.2.2. Anisotropic Diffusion Filter

This filter provides intra-region smoothing while phase boundaries (feature edges) and smaller details are preserved. Originally proposed by Perona and Malik (1990) the filter assumes the original image is the solution of a partial differential equation such as diffusion equation. The method utilises the first derivative of the image (image gradient) to control the diffusion process in the areas which are more likely to be the feature edges. The diffusion-type model can be mathematically formulated as:

$$\frac{\partial}{\partial t} I(\bar{x}, t) = div\left(C(\bar{x}, t) \nabla I(\bar{x}, t) \right), \tag{3.3}$$

where $\bar{x}$ is the spatial coordinates, $I(\bar{x},t)$ is the image intensity, and $C(\bar{x},t)$ is the diffusion function which in turn is a function of the image gradient magnitude,

$$C(\bar{x},t) = f(|\nabla I(\bar{x},t)|^2). \quad (3.4)$$

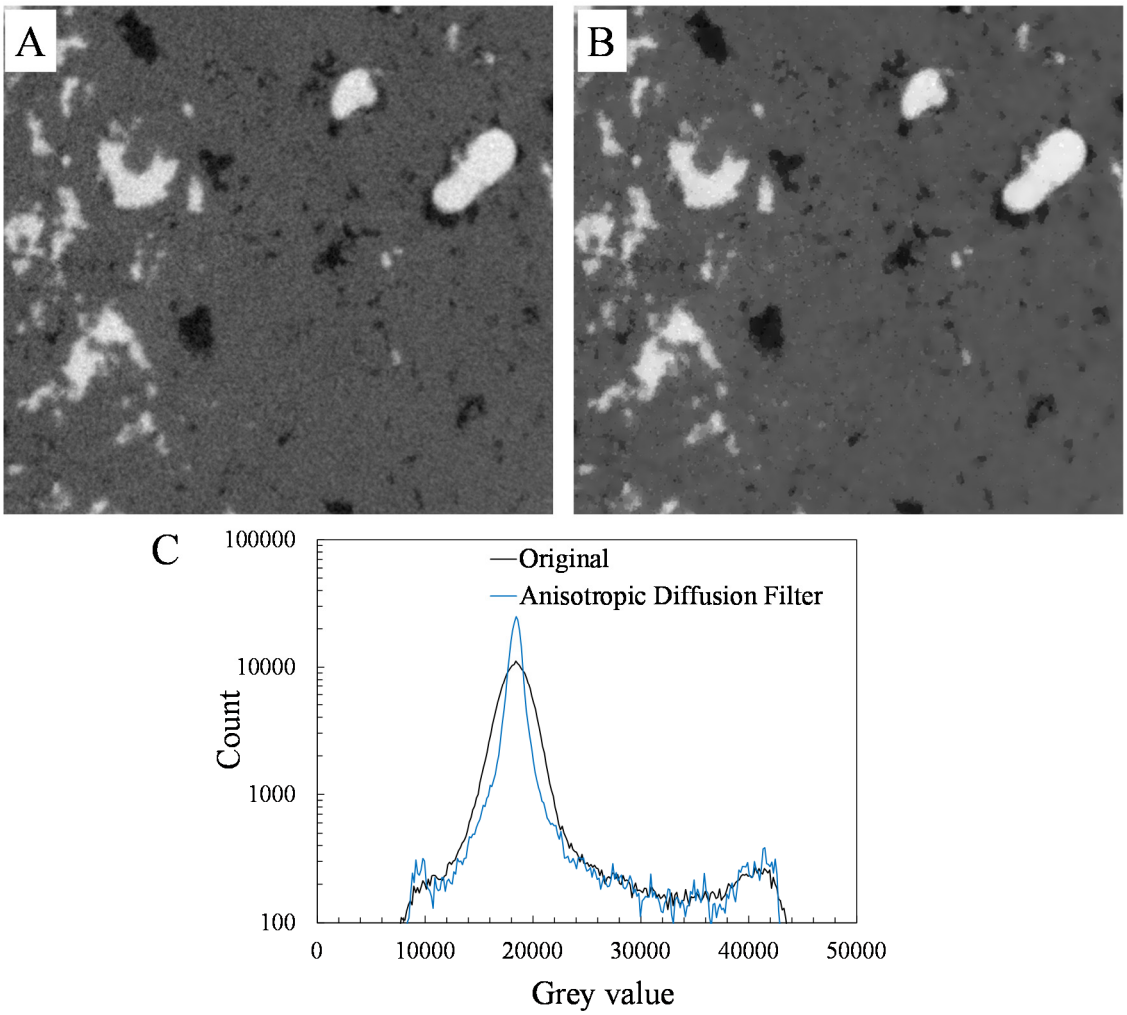

Figure 3.18: Application of anisotropic-diffusion filter on the same µCT image shown in Figure 3.17A. (A and B) indicate the image before and after filtering. The histogram of the filtered image displays a narrower distribution compared to that of the original image (C). White: oil, black: water, and grey: rock.

The filter takes two parameters as inputs: (a) the diffusion threshold, and (b) the number of iterations. The diffusion threshold controls the level of smoothing by allowing the diffusion process to happen if the difference between the values of any two neighbouring pixels is smaller than the selected threshold. In case the difference

is larger than the diffusion threshold the diffusion process is stopped and the pixels are considered to be part of a phase boundary. The filter is an iterative process, hence a larger number of iterations results in a smoother image.

Figure 3.18A and 3.18B compares the results of anisotropic-diffusion filter applied on the same μCT image as Figure 3.18A. Similar to the median filter the image histogram shows the filtered image has a narrower grey value distribution for the rock phase. Although this filter preserves the sharpness over the phase boundaries a significant number of small structures (outliers) remain on the filtered image. This happens where the gradient of the noise with its neighbouring pixels is larger than the diffusion threshold value. The remained noise may be assigned to a wrong class during the segmentation step. For the analysis performed in this study, wherever this filter is used, an assumption was made to ignore all structures with volumes smaller than 10 voxels in 3D (on the segmented images). This assumption allowed removal of the remaining noise that has survived the anisotropic-diffusion filtering.

3.1.2.3. Non-Local Means Filter

Mean filter is a basic filter which simply replaces the value of each pixel by the average value of its neighboring pixels. One major drawback for this filter is pixels with outlier values (e.g. salt and pepper noise) significantly affect the mean value. Moreover, simple averaging blurs the phase boundaries significantly, causing less certainty in the subsequent image segmentation and analysis results.

Non-local means filter (Buades et al., 2005) is a more sophisticated version of the mean filter. Instead of simple averaging the non-local means filter performs a weighted average by comparing each pixel's neighborhood with a larger window in the image (possibly the entire image). The weight (w) by which each pixel (j) in the image influence the updated value of the current pixel (i) is determined by the similarity of their neighborhoods.

$$NLM\big(I(i)\big) = \sum_{j \epsilon I} w(i,j) I(j) \tag{3.5}$$

Where I is the input noisy image and $w(i,j)$ are the weights which depend on the similarity between the neighborhood of pixels i and j. Figure 3.19 compares the

output of three different filters of: median, anisotropic diffusion filter and non-local means with the original image.

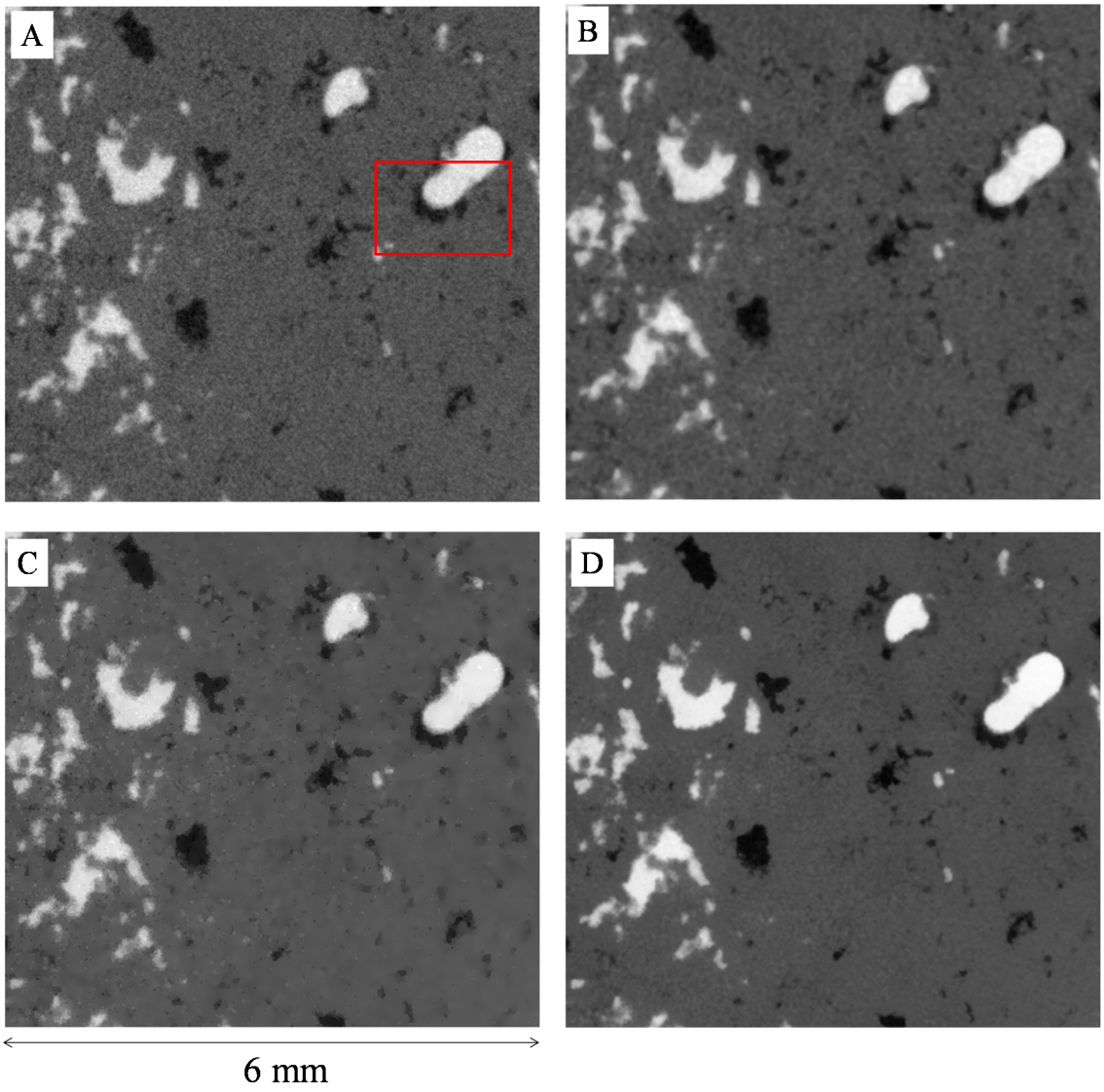

Figure 3.19: Comparison between different filters applied on a µCT slice of a two-phase saturated carbonate core. (A) shows the original image, (B, C, and D) show the slice filtered by median, anisotropic-diffusion and non-local means filters. The non-local means filter appears to be the best of these three filters. It has removed the noise while preserving the edges. White: oil, black: water, and grey: rock.

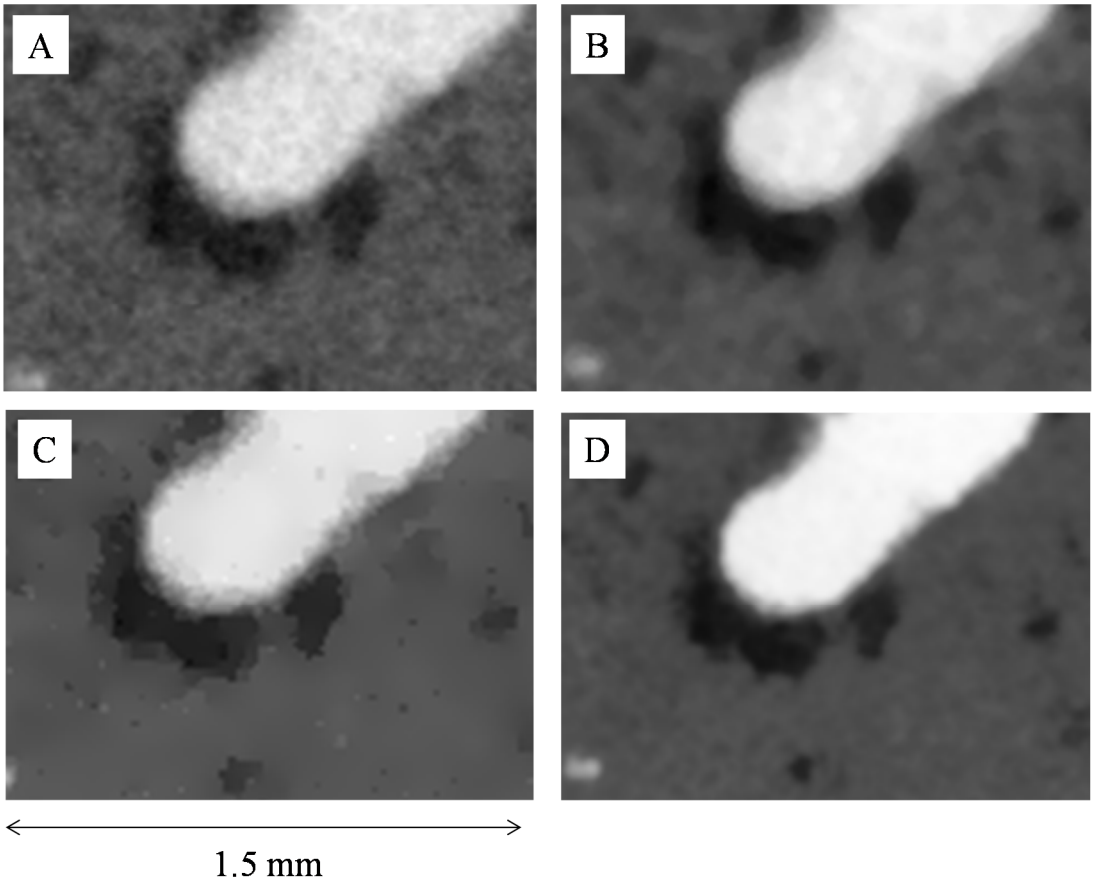

Figure 3.20: Magnified view of the highlighted window on Figure 3.19. White: oil, black: water, and grey: rock.

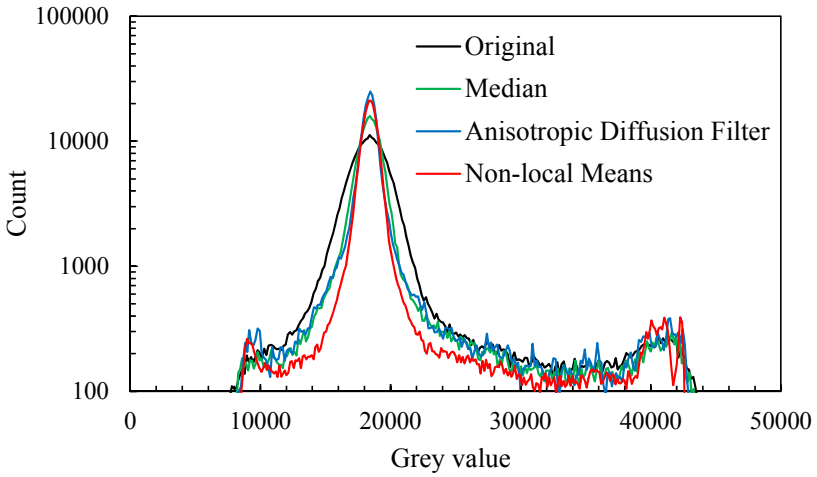

Figure 3.21: Comparison between the image histogram of the µCT slices shown in Figure 3.19. The non-local means filtered image shows a narrower distribution.

Table 3.1: Standard deviation of the distributions of the filtered images shown in Figure 3.19. The non-local means filtered image shows the smallest value.

Image	Standard Deviation
Original	12246.95
Median	10999.02
Anisotropic Diffusion	11833.86
Non-local means	10209.21

Visual comparison of the three filtered images and the original one suggests that the nonlocal means filter is the best of the three presented filters in terms of removing the noise while preserving the phase boundaries as well as the image sharpness. This is also confirmed by comparing the histograms of the images (Figure 3.21) and their standard deviation values, listed in Table 3.1. The grey value distribution of the non-local means filtered image appears to be the narrowest with the smallest standard deviation.

For an image of (800×800×1600) which is the typical size of images used in this study the run time is 0.16, 0.8 and 4 hours respectively for median, anisotropic diffusion filter and non-local means filters with the available workstation (96 GB RAM). Despite the fact that the non-local means provides the best filtering results its computational expense can be a major drawback when dealing with a sequence of large μCT datasets. In this study these three filters were used depending on the quality of the input image. The non-local means filter was used where there was a significant amount of noise on the data, in cases of less noisy images anisotropic diffusion filter or median filter were used for a faster result.

3.2. Image Segmentation

The prerequisite of performing any quantitative analysis on an input image is identification of the voxels which belong to each existing phase. Segmentation is the process of classifying the voxels of an input (here greyscale) image into a number of non-intersecting regions or phases. If only two phases make up an image, such as pores and grains in an image of a rock, then image segmentation is also known as

binerisation. Binerisation converts a greyscale image to a binary image with pixel values of 0 and 1. Although there are several advanced image segmentation methods outlined in the literature, the current versions of Avizo-Fire (v6-v8) have only implemented the global thresholding and watershed methods.

3.2.1. Thresholding

Thresholding is one of the most common and simplest methods of image segmentation. The goal of thresholding is to mark each pixel of a given image as a foreground or a background pixel. According to Sezgin and Sankur (2001) thresholding methods can be categorized in six classes of: histogram-shape based methods, clustering-based methods, entropy-based methods, object attribute-based methods, spatial methods and local methods; based on the information they use to assign pixels to foreground or background. Within this study the histogram-based approach was applied.

In histogram-based binerisation the goal is to distinguish two peaks on the image histogram, so that the threshold can be placed in the valley between those two peaks. However, not all images display distinguishable peaks on their histograms, and as a consequence visual thresholding is an uncertain method.

A typical histogram of a μCT image of porous materials shows a bimodal population distribution, consistent with two phases of pores and solid. However for complex pore structures with multiple-scale porosity (such as carbonate rocks) the two populations overlap over a range of grey values. It is not a straightforward task to classify the overlapped grey values while preserving the two distributions including their tail distributions. The pixels associated with the grey values of the overlapped area are mainly: (a) the smaller pores or porosities beyond the image resolution, and (b) the edges of the larger pores. Both related to partial volume effect.

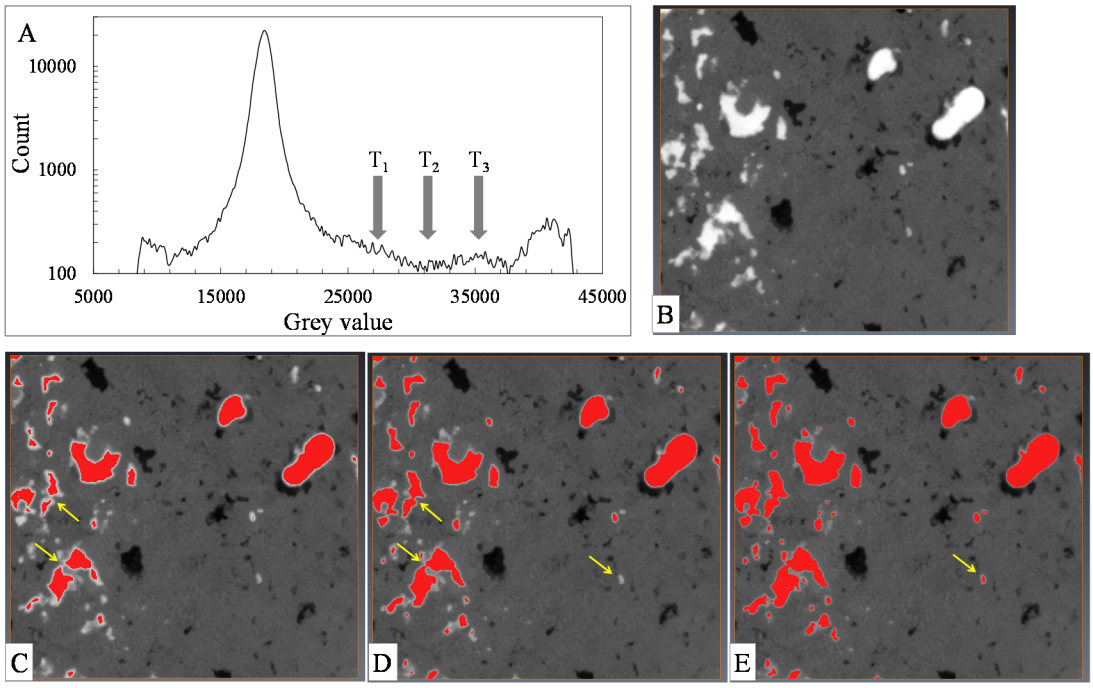

Figure 3.22: Selecting different threshold values affect the resulting segmented phases. The red pixels on (C, D, and E) indicate the pixels that are assigned to the oil phase as a result of thresholding with T_3, T_2, and T_1 values, respectively. The yellow arrows show examples where selecting different thresholds can cause the oil phase to get disconnected over the narrower connections. Inclusion of the smaller features is specifically sensitive to the threshold value.

The smaller structures are more sensitive to small changes in the threshold values as they are subject to not being selected at all. The larger structures, however, experience a dilation or erosion of a number voxels around their boundaries where different thresholds are selected. Figure 3.22 shows the effect of selecting different threshold values on the segmented oil phase. Highlighted by the yellow arrows on the image are two of the main uncertainties associated with simple thresholding method: (a) changes in selected threshold values affect the connectivity of the segmented structures, (b) smaller structures, here pores saturated with oil, may be lost. These uncertainties introduce a systematic error into subsequent quantifications as well as simulations made using information extracted from such segmentations. Taking the method one step forward, Prewitt and Mendelsohn (1966) proposed a method in which the algorithm looks for the modes on the histogram and picks the threshold value from the minima between them. In statistics the mode is the value that appears most often in a dataset. Another method that uses the smoothed

histogram to obtain a peak-valley representation is discussed in Guo and Pandit (1998).

The success of thresholding attempts is highly dependent on the type of the input image. μCT images of natural materials (such as carbonate rock used in this research) are restricted in terms of the range of the bulk attenuation coefficients of their constituting minerals. However, in an experimental design careful selection of compositionally modified synthetic fluids can enhance the contrast between the phases that appear on the captured images. This can assist the segmentation exercise.

In general thresholding (visual or automatic) is considered as an uncertain method of image segmentation.

3.2.2. Watershed Segmentation

Segmentation becomes a more complicated task when the phase boundaries on the input image are not sharp, or in the case of having a complex structure with a broad range of feature sizes. For example consider a carbonate rock with multiple-scale porosity (from sub-micron to mm pore-sizes). Depending on the resolution of an acquired μCT image a range of small pores would be underrepresented. In addition, insufficient resolution can result in blurred or indistinct phase boundaries (i.e. features edges). Under such circumstances thresholding based on the intensity histogram alone may introduce significant errors in the segmented images, this can cause errors in the results of any subsequent quantitative analysis. Thus more sophisticated segmentation methods capable of extracting more information from the input image (such as building the image gradient to investigate the edges and phase boundaries) are required.

Watershed segmentation is a long established method (Beucher and Lantuéjoul, 1979, Vincent and Soille, 1991, Roerdink and Meijster, 2000) which is implemented in Avizo-Fire (v.6-v.8). The method constructs a gradient map for the input greyscale image. The map reveals the phase boundaries and feature edges. Image gradient is the first derivative of the intensity values of an image (Gonzalez et al., 2004). The

phase transition parts on the image gradient is then thresholded, these are the part of the image which are subject to mislabeling in a simple thresholding approach.

The user is then asked to mark regions on the input image which certainly belong to each phase (Figure 3.23), this is done using simple thresholding. These regions will be used as seeds to grow the regions assigned to each phase. In the final step the algorithm grows the seed regions until they meet, the meeting boundaries are referred to as watershed lines. The algorithm stops when the boundaries touch.

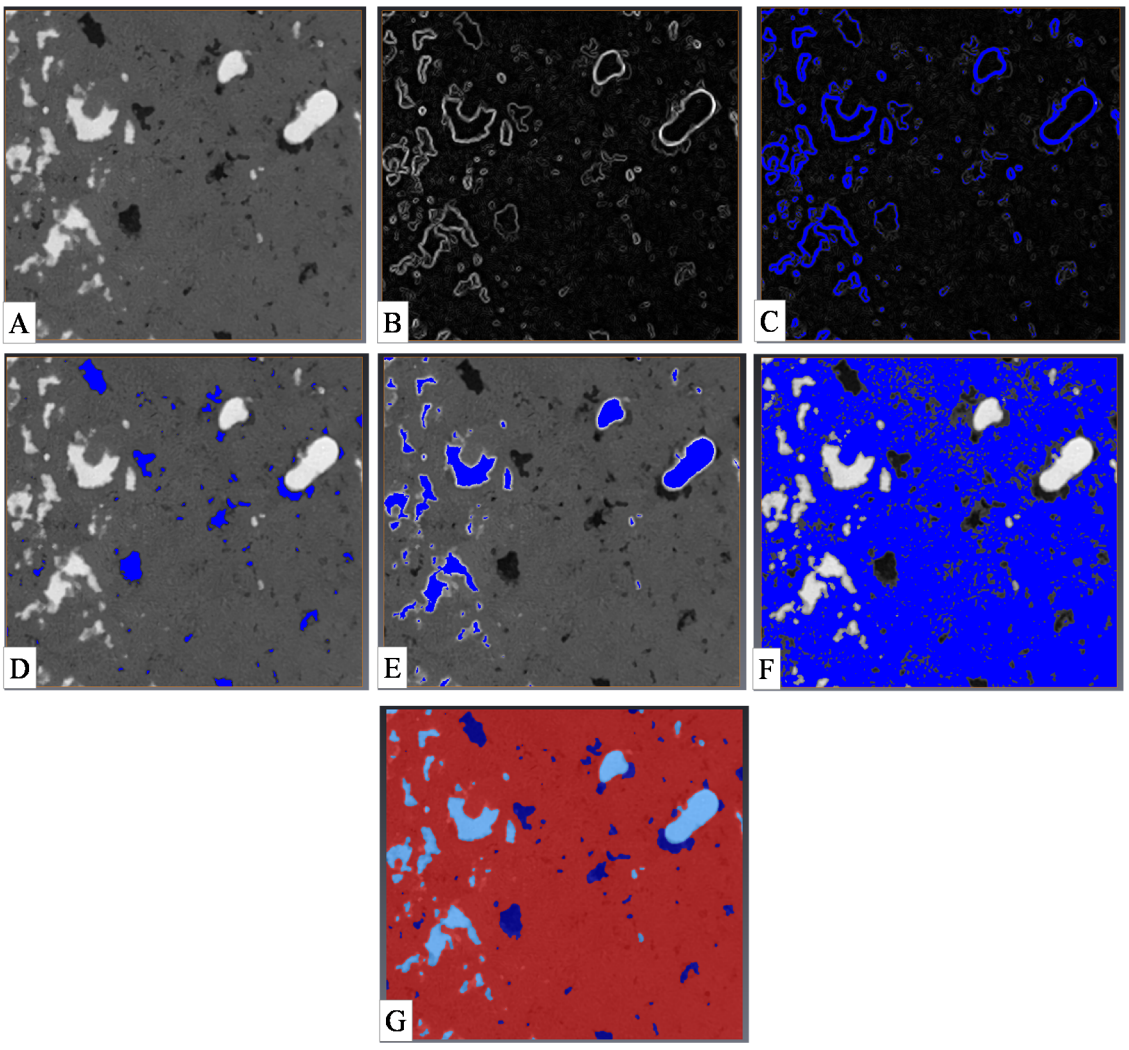

Figure 3.23: Watershed segmentation steps including, constructing image gradient (B), thresholding it to mask the phase boundaries (C), selecting areas which certainly belong to each phase (D to E), and the segmeted image obtained from running the region growing algoritm (G).

3.3. Labelling – Individual Analysis of Labels

The simplest quantification of a binarised image of a porous rock is calculating the porosity (φ) of the rock by voxel counting as following:

$$\varphi = \frac{Number\ of\ pore\ space\ voxels}{Total\ number\ of\ voxels\ in\ the\ image} \tag{3.6}$$

Porosity is a global measure calculated based on the entire image. However, in most applications more detailed information about the individual objects appearing on the image is desired, for example grain size distribution, grain shapes and orientations are among the common measures of interest in geological studies of reservoir rocks. Starting from a binary image it is possible to identify the individual objects of an image by searching for groups of connected voxels and assigning each group a unique label. Any group of connected voxels is referred to as a cluster. Connected component labelling (Dillencourt et al., 1992) or in short labelling enables clusters to be identified individually, for both visualisation and quantification purposes. Figure 3.24 illustrates the concept behind identifying and labelling clusters on a 2D binary image.

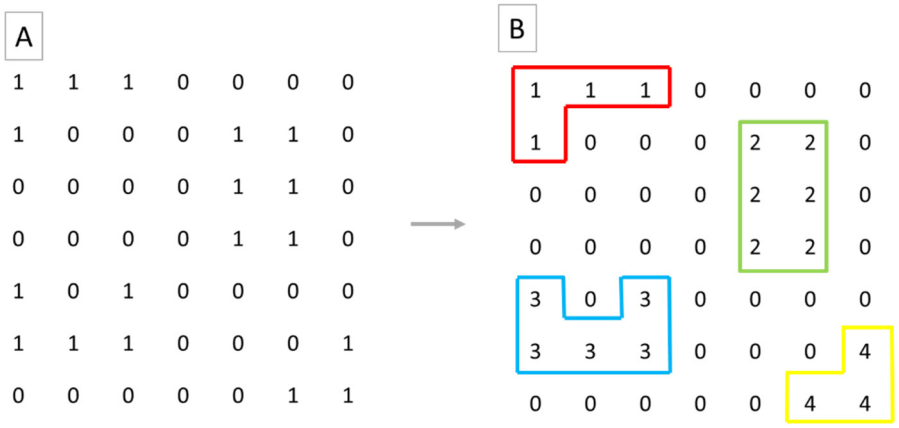

Figure 3.24: Identification and labelling of clusters on a 2D binary image.

In 3D the labelling can be controlled by defining the connectivity criterion for every two adjacent voxels. In the labelling algorithm available in Avizo-fire there are three labelling criteria: 6, 18, and 26 referring to connectivity with common face, common edge and common vertex, respectively.

Once the clusters are labelled individually performing quantitative analysis on them is straightforward since each label is identified and can be selected individually. As an example a basic analysis could include: measuring the 3D volume and 3D surface area of each cluster. In this study a number of more sophisticated measures such as sphericity (chapter 5, section 2) and Euler number (which is a measure of connectivity, chapter 5, section 2) are used.

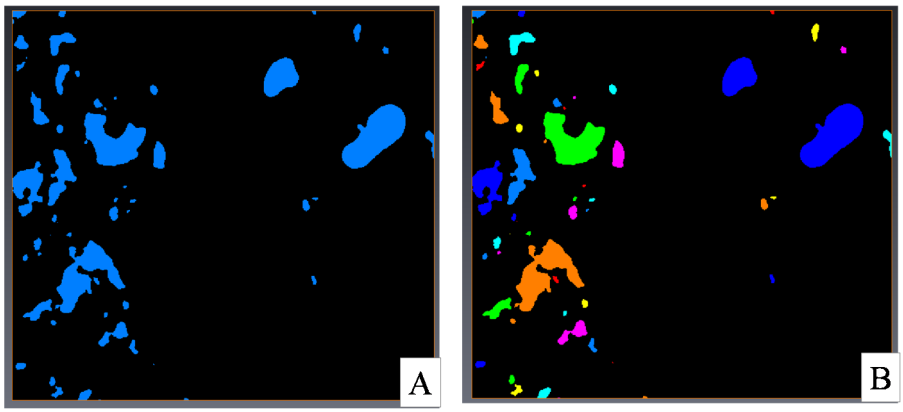

Figure 3.25: Labelling of a binary image (A) of the oil phase shown in Figure 3.22. (B) shows the labelled image on which clusters are shown with different colours.

4. Experimental Procedures

4.1. Introduction

The experimental cycle consisted of a series of fluid injections followed by static (zero flow) in-situ μCT scans of the core. In the present experiments, the static points refer to the stages at which no non-injected (displaced) fluid is produced. More than 10 pore volumes of the displacing phase were injected at each stage. The fluid injections were performed using two constant rates of "low" and "high" which were chosen such that the displacements occur in capillary-dominated as well as viscous-dominated regimes. The exact flow rates are listed in Tables 3.2 and 3.3. The flow regimes are defined using the capillary number which is a dimensionless ratio of viscous to capillary forces (Bear, 1988):

$$N_c = \frac{V\,\mu}{\sigma}, \tag{3.7}$$

where V (m/s) is the linear velocity and μ (Pa.S) is viscosity of the displacing fluid phase and σ (N/m) is the interfacial tension between the two fluid phases. In oil reservoirs natural flow occurs at capillary numbers of approximately ~10^{-7} (Ng et al., 1978, Sheng, 2010). In displacement of a fluid with another immiscible one the capillary, viscous, and gravity forces act. The interplay between these forces has been extensively discussed in the literature, for example see (Løvoll et al., 2005, Méheust et al., 2002, Or, 2008). It is the competition between these three forces that determines the shape of the displacement front and the ultimate recovery of oil. Here, the gravity forces do not act since the density of oil and brine phases are closely matched. The capillary numbers corresponding to the fluid injections with the "low", and "high" flow rates were of the order of 10^{-7} and 10^{-5}, respectively. The transition between capillary-dominated and viscous-dominated flow regimes does not occur at a single threshold capillary number for different porous media and fluid pairs (Sheng, 2010). The core-scale and pore-scale evidences presented in chapters 4 to 6 demonstrate that the displacements have happened under the capillary-dominated as well as viscous-dominated flow regimes using the two selected "low" and "high" injections rates. These evidences briefly include the observation of fluid redistributions, capillary end effect, and the pore-scale displacement events.

4.2. Experimental Set-up

The rock under inspection, a recrystallized dolomite (SD), was originally water-wet. A core plug of SD (D=12.5 mm, and L=44 mm) was used for the experiments under water-wet state. The wettability of the core was then altered using aging in crude oil. A shorter piece of the same core with altered wettability (L=28 mm) was used for a second, similar experiment. This allowed investigation of the effect of rock wettability on the pore-scale fluid saturation distributions. The test procedures of these two set of experiments are explained in sections 5.3 and 5.4, respectively. The aqueous and organic fluid phases used were 0.03 M KI brine and 50%v/v iododecane in dodecane, respectively. More details about the fluid phases and the rock sample can be found in section 3. Figure 3.26 shows a schematic drawing of the combined core flooding-μCT experimental set-up used in this study.

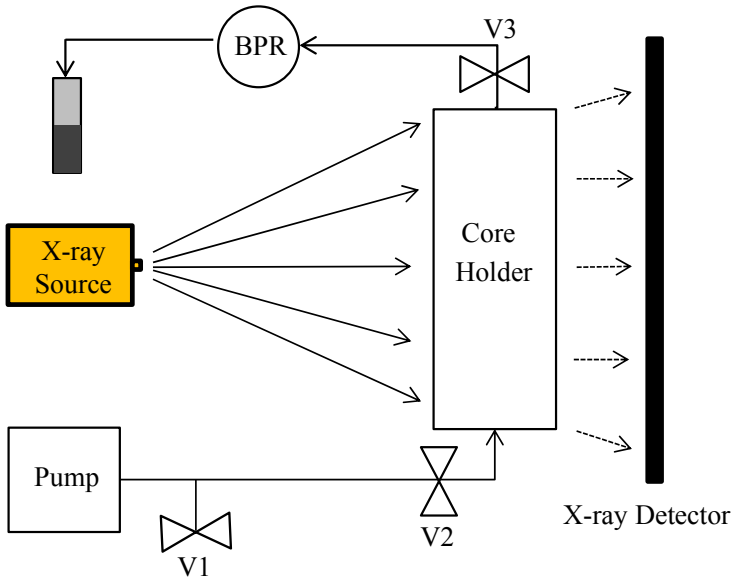

Figure 3.26: Schematic drawing of the combined core flooding-μCT experimental set-up. To avoid over pressuring the pump a pressure relief value of ~690 kPa (100 psi) was used (V1). V2 and V3 are the valves used to lock the cell after each injection step. BPR: Back pressure regulator.

SD rock has a multiple-scale porosity (see Figure 3.7) with pores ranging from sub-micron to mm scale. Therefore, to achieve sufficient resolution that captures all pores and pore-throats a sample with a diameter smaller than the dimensions of some pores present in the sample was required. Thus, incomplete capture of the existing pores and pore-throats was an inevitable consequence of working with a sample with such a multiple-scale porosity. Figure 3.27 shows the pore-throat size distribution of SD carbonate measured by MICP test (same as Figure 3.9). The highest resolutions of the μCT images acquired during water-wet and oil-wet experiments are marked on this plot (11.25 μm and 10 μm, respectively). Having voxel sizes smaller than the peak values (~14.5, 16.3, 18.3 μm) of the pore-throat size distribution indicates that the higher magnification scans could capture most of the pore-throats and fluid connections (more discussions can be found in chapter 7, section 5).

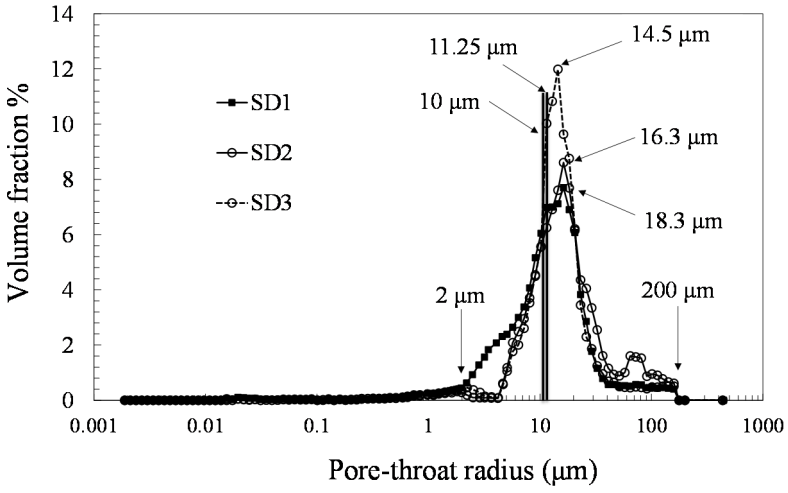

Figure 3.27: Pore-throat size distributions for three SD core plugs measured using MICP. The two black lines are showing the image resolutions for the high and low magnification µCT scans, respectively. Incomplete capture of the existing pores and pore-throats is an inevitable consequence of working with a larger core plug.

Helium sparging was used to degas all the aqueous fluids prior to their injection to limit bubble nucleation in the aqueous phase during the vacuum saturation or injection steps. Sparging is a technique which involves bubbling a chemically inert gas, such as helium, nitrogen, or argon through a liquid to remove dissolved gases (e.g. oxygen) from the liquid.

Fluid samples were collected from the production line after each pore volume of fluid injection using an automated fraction collector. Due to small volumes of the collected samples (~1 ml, and ~0.6 ml for the water-wet and oil-wet experiments, respectively) physical separation of the two fluid phases and analysing them may involve significant measurement errors. An alternative approach is to image the collected fluid samples. Due to the significant contrast between the X–ray attenuation of the oil and brine phases collecting single projections permits calculation of their relative volume using image analysis. This can provide a quantitative production profile for oil and brine phases which can be correlated to the fluid saturations calculated based on image analysis, for different stages of the experiment. Figure 3.28 shows a 2D projection of a set of produced samples from a

similar experiment of drainage and imbibition. The darker and brighter phases represent oil and brine, respectively.

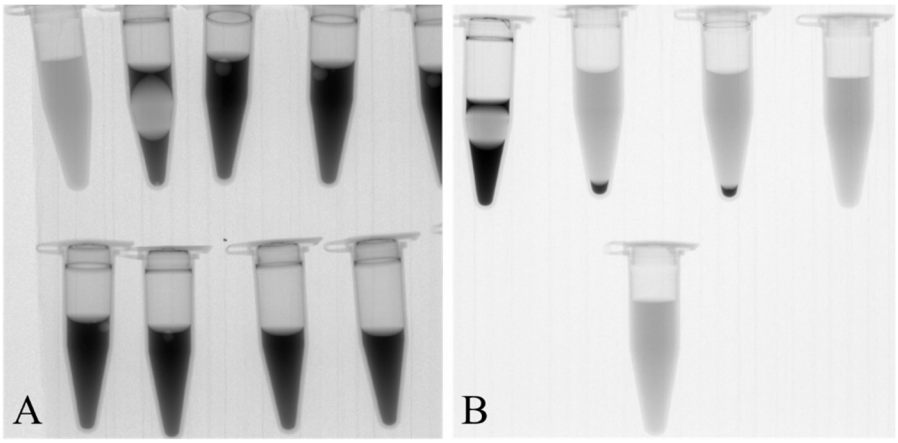

Figure 3.28: Exemplary 2D µCT projections of the produced samples from a similar experiment after oil injection into a brine saturated core at 100 µl/min (A) and a subsequent brine injection at 100 µl/min (B). The darker and brighter phases represent oil and brine, respectively. The sample volumes are ~ 1 ml. For small fluid samples imaging can be used as an alternative method to physical separation of the fluid samples.

However, during the fluid collection, it was noticed that the back-pressure regulator allowed oil to accumulate. Hence, the quantitative assessment of the produced fluid volumes is not reliable for these experiments.

The image reconstructions were performed using a filtered back projection method implemented in Octopus (v.8.5, v 8.6) software package. Beam hardening effects and ring artefacts were corrected during the reconstruction step by routines implemented in Octopus. Detailed information on these artefacts can be found in chapter 2, section 3.

Reconstructed data were filtered using the anisotropic diffusion and non-local means filters for the water-wet and oil-wet experiments, respectively. These filters are implemented in Avizo-Fire software (v8), and explained in section 4.3. The reconstructed volumes were segmented into three binary volumes, each representing the discrete oil, water, or rock component using a watershed segmentation algorithm, (section 4.4.2). To quantitatively analyse fluid distributions, binary images of each

fluid phase were labelled assuming any two voxel with a common face as connected, i.e. the labelling criterion was set to 6 in Avizo. More information about the labelling algorithms can be found in section 4.5. In this thesis the fluid "clusters" are assumed to be equivalent to the "labels" that are obtained by labelling the binary images of fluid phases, captured at the higher resolutions (voxel size: 11.25 µm and 10 µm, for the water-wet and oil-wet experiments, respectively).

4.3.Water-wet Experiment

A back pressure of ~517 kPa (75) psi was applied to the production end of the plug. The pore volume of the core plug was 957 µl. At each stage two different magnification µCT images were collected (Figure 3.29). For the lower magnification scans the sample-X-ray source distance was 236 mm. The collected images captured almost the entire length of the core plug (41.5 mm, voxel size: 24 µm). This permitted analysing the overall saturation profiles of the two fluid phases along the entire core length as well as the boundary effects. The magnification is 1.76 (416 mm/236 mm, see chapter 2, section 2). The blurring is 9.15 µm (12 µm × 180 mm/236 mm). The camera pixel size is 48 µm. The total resolution is 27.76 µm (i.e. $\frac{\sqrt{9.15^2+48^2}}{1.76}$).

For the higher magnification scans the sample-X-ray source distance was 104 mm. A central section of the core plug (20.5 mm, voxel size: 11.25 µm) was captured on the images (i.e. from 8 to 28.5 mm from the injection face). The magnification is 4 (416 mm /104 mm, see chapter 2, section 2). The blurring is 36 µm (12 µm × 312 mm/104 mm). The total resolution is 15 µm (i.e. $\frac{\sqrt{36^2+48^2}}{4}$). These higher resolution data provided more detailed observation of fluid distributions.

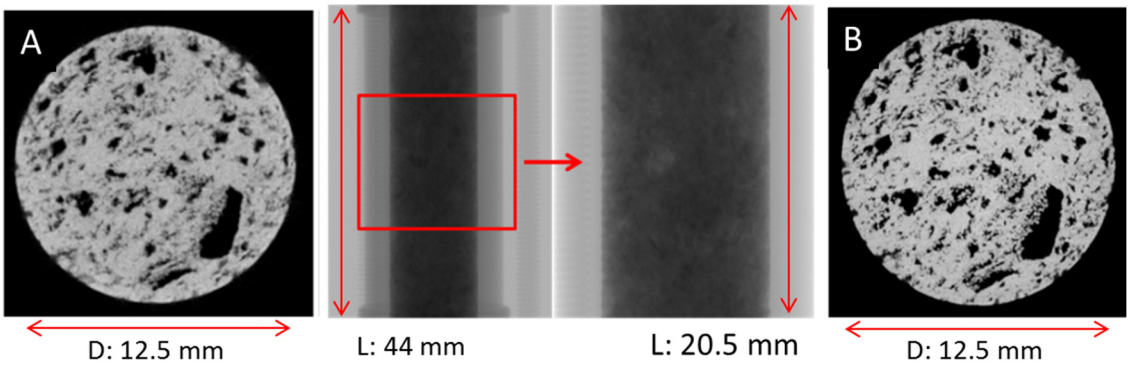

Figure 3.29: Exemplary 2D µCT projections and reconstructed slices in the two different magnifications (total resolutions) of (A) 1.76 (27.76 µm) and (B) 4 (15 µm).

The experiment started with vacuum saturation of the rock with degassed water followed by injection of 0.5 M KI brine into the plug. A scan was acquired to check the saturation state and to map the accessible porosity of the core at the applied pressure ranges. The well-connected porosity of this rock allowed close to complete saturation of the visible pore space of the plug with the low pressure ranges applied. Once the saturation state was satisfactory (meaning that most pores were saturated with the brine phase and no air bubbles were trapped in the pore space) the core was flushed with 0.03 KI brine. This represents the start of the experiment.

Table 3.2: Fluid injection test cycle for the water-wet experiment.

Injection step (shown on Figure 3.30)	Flow Rate (µl/min)	Capillary Number	Linear Velocity (µm/s)	Injection Period (hrs)	Pore Volumes Injected
Capillary dominated oil injection Figure 3.30 (1-2)	10	3.95×10^{-7}	7.68	18	10
Viscous dominated oil injection Figure 3.30 (2-3)	700	2.77×10^{-5}	538	0.23	10
Capillary dominated brine injection Figure 3.30 (3-4)	10	1.95×10^{-7}	7.68	18	10
Viscous dominated brine injection Figure 3.30 (4-5)	700	1.37×10^{-5}	538	0.23	10

Table 3.2 and Figure 3.30 present the fluid injection-µCT scanning test cycle used in these experiments. Injections were done using two constant flow-rates to replicate spontaneous and forced fluid displacement processes. These two injection rates were q=10 µl/min (corresponds to $Nc \sim 10^{-7}$) and q=700 µl /min (corresponds to $Nc \sim 10^{-5}$).

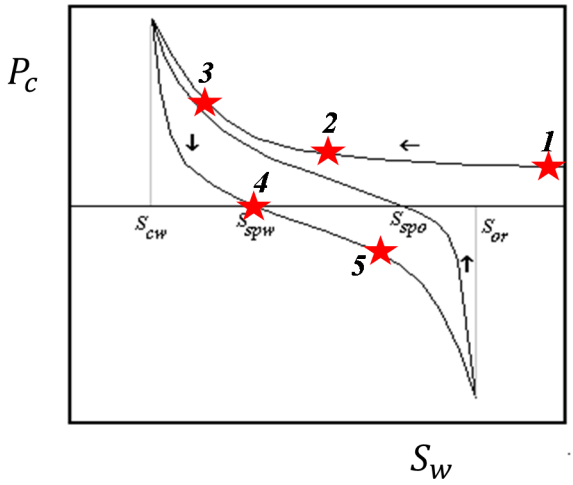

Figure 3.30: Test procedure for the core flood experiments (in terms of the appropriate capillary pressure describing the process). Red stars show the points of µCT scans.

The test cycle includes 4 injection steps and 20 scans comprising a total of 60,000 projections throughout the experiment. Each scan comprised 1000 projections each of which was a summation of 3 acquisitions (1.1 second exposure times) to reduce digital noise and artifacts due to sensor non-linearity. To suppress the noise further two scans were made at each static point and averaged. Collecting two independent scans at each point also allows the assessment of the stability of the fluid distributions.

4.4. Oil-wet Experiment

Subsequent to the water-wet experiments the core plug was flushed with ethanol followed by air in order to displace all the trapped residual oil out of its pore space. The plug was subsequently scanned and only trace oil was observed to be present in the core. The wettability of the rock was then altered by aging in crude oil. The crude oil used contained measured asphaltene contents ranging from 3 to 6%. Measured acid number of samples of this crude oil range between 1.5 to 3.0%, which is at the high end of the spectrum of the AN values reported in the literature (Buckley, 1996).

It is beyond the scope of this study to investigate the effect of crude oil and brine chemical composition on the wettability alteration process. Therefore, one anonymous oil sample, known to be effective in wettability alteration, was used to alter the wetting preference of SD core plug (which was original water-wet) towards a reduced water-wet state. Characteristics of this crude oil are presented in Appendix E. The aging procedure is explained in the following.

4.4.1. Wettability Alteration Procedure

1 M $CaCl_2$ brine was injected into the core plug before it was placed in an oven (temperature =75°C) overnight. Subsequently the brine was displaced out of the core by dodecane injection. The injections were done using four different constant flow rates (q = 100, 300, 500, 700 µl/min) to achieve a small amount of remaining brine in the plug. Toluene was injected into the plug as an intermediate solvent to avoid precipitation of the heavy components of crude oil in contact with dodecane. Finally, three pore volumes of crude oil were injected into the plug at a slow flow rate (q = 50 µl/min) with no back pressure (Figure 3.31). The measured viscosity of samples taken from this crude oil (at 25°C) range between 12 to 18 cP. Such high viscosity made it impossible to inject the crude with higher flow rates using the available low pressure core-flooding set-up, i.e. $P_{injection}$<690 kPa (100 psi). Starting from q = 100 µl/min the injection rates were reduced until the pressure relief valve stopped bleeding. Therefore the injection pressure was smaller but close to 690 kPa (100 psi). However, simple calculations based on Young-Laplace equation (eq. 3.1) suggest that the 690 kPa pressure is sufficient to penetrate in pore-throats of ~0.06 µm radius. This can be obtained by assuming the IFT equal to 0.03 N/m which is a typical value for the oil-brine IFT, and contact angle of 48.6 degrees, (as suggested by measurements chapter 6). MICP test results show ~ 99 % of the pore space of SD core plugs was connected to throats of radius larger than 0.07 µm, therefore it is expected that the majority of the pore volume of the core plug was exposed to crude oil during aging.

After the crude oil injection the core holder was locked and placed in an oven (temperature 75°C) for 2 months. According to Anderson (1986) the wettability alteration process requires ~ 1000 hours (40 days).

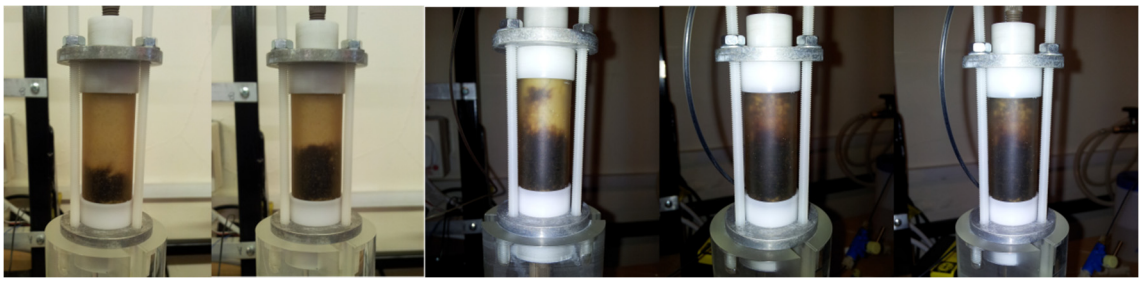

Figure 3.31: Injection of crude oil (q = 50 µl/min) in SD core plug primarily saturated with toluene/brine. The injection performed from bottom to the top. The injection front is clearly visible due to the transparency of the epoxy coating.

In order to avoid a sudden temperature drop which can cause asphaltene precipitation and deposition, and hence clogging of the pore space the temperature of the oven was gradually decreased from 75°C to room temperature. The core holder was then taken out of the oven and scanned. The images revealed that during the aging period a gap had formed between the epoxy jacket and the rock. This indicates that the temperatures used for the aging process, and potentially interactions of the crude oil with the epoxy caused the epoxy to swell and separate from the core plug, see Figure 3.32.

A gap between the core surface and the epoxy sleeve is a highly permeable path that causes the fluids to bypass the core during the injections. To address this the epoxy jacket was shaved off of the plug, and the plug wrapped in a thin aluminium film, cast in a new epoxy sleeve and trimmed to size. The thin aluminium foil was used to avoid epoxy penetrating the core plug.

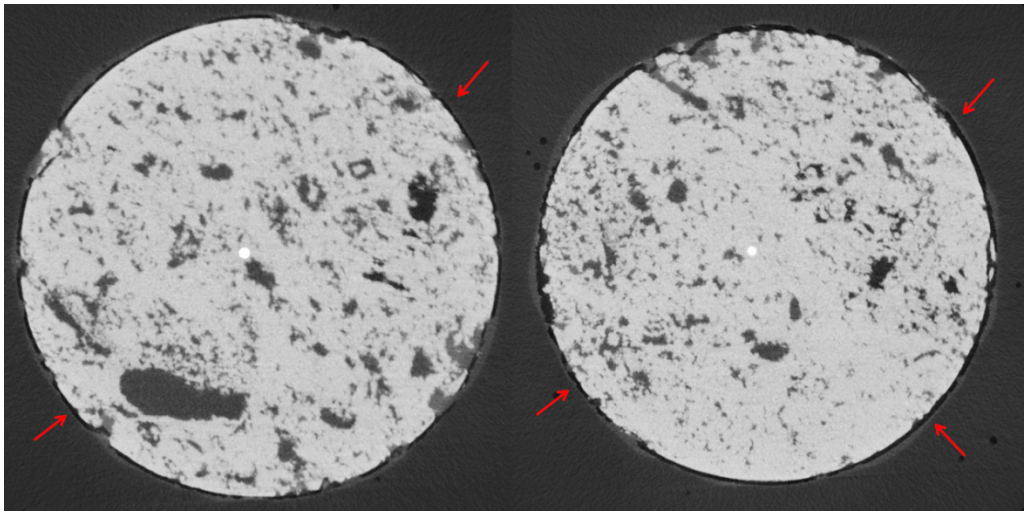

Figure 3.32: Exemplary 2D µCT slices from the crude oil saturated plug after aging for two months. The red arrows show the separation of the epoxy jacket from the core plug.

The remaining crude oil was flushed from the core plug using a mixture of toluene in dodecane (1:4 volumetric) with q = 10 µl/min overnight. The effluent showed residues of crude oil, therefore, the injection rate increased to q = 300 µl/min with no back pressure. Further crude oil was produced, and flushing was continued until the effluent was almost colourless.

4.4.2. Experimental Procedure

The same organic and aqueous phases that were used in the water-wet experiments were used for the oil-wet drainage and imbibition cycle. Prior to starting the two phase fluid displacements 50%v/v iododecane in dodecane mixture was injected into the core plug to check the saturation state of the plug. Figure 3.33 shows six example µCT slices from the oil saturated core plug. Most of the pore space of the rock was saturated with oil (white in Figure 3.33), while some pores (black in Figure 3.33) were not saturated. It is probable that these pores are connected to narrow throats that have been clogged as a result of asphaltene deposition during wettability alteration. Asphaltene deposition on the surface of the rock happens anywhere the surface is exposed to crude oil; this includes pore walls inside the pore bodies as well as the pore-throats. The thin layer of asphaltene coating the pore wall surfaces may not alter the size distribution of the pore bodies, however it can narrow down or completely

plug those pore-throats with only a submicron to micron scale apertures. This was discussed by Wojtanowicz et al. (1987), as shown in Figure 3.34.

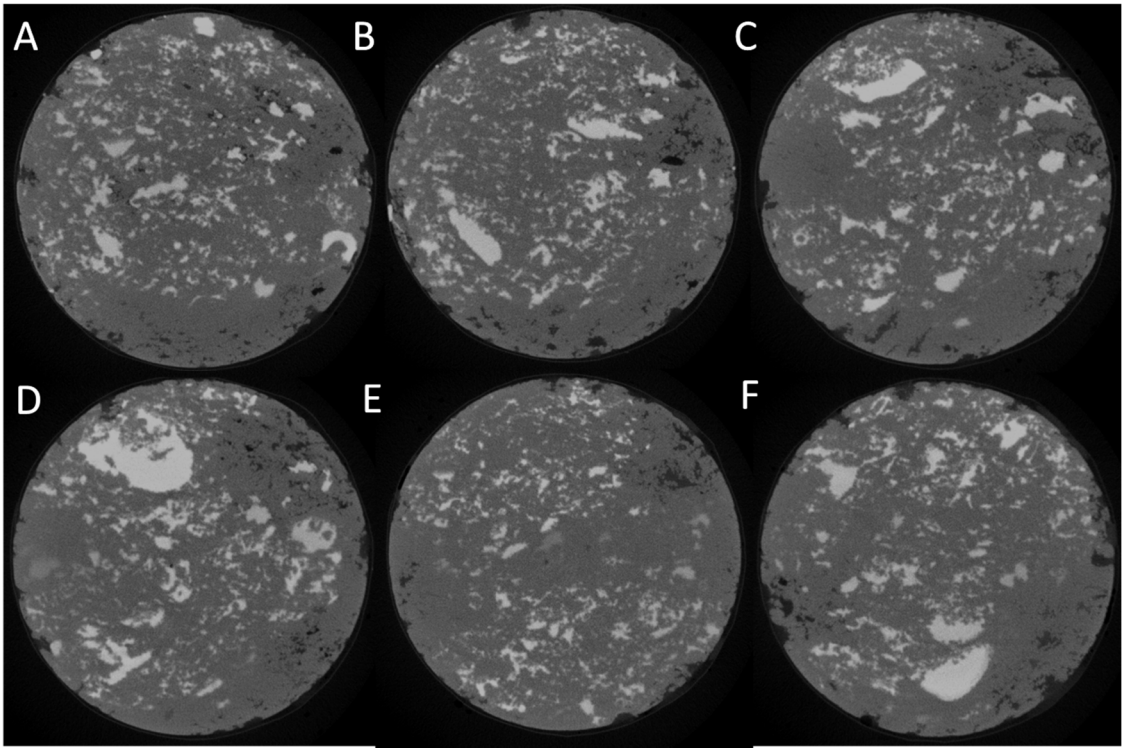

Figure 3.33: Exemplary 2D µCT slices of the doped oil saturated core plug after the aging. The slices (A to F) are from distances of 1, 2, 4.35, 5.35, 7.35, 10.95 mm from the injection face, respectively. This is the initial saturation state of this experiment. The pore space is mostly saturated displaying some unsaturated (black) pores probably due to clogging of some pore-throats as a result of asphaltene deposition.

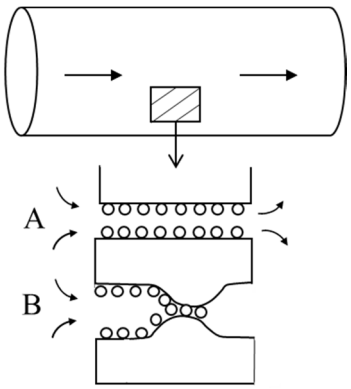

Figure 3.34: Schematic model of asphaltene deposition and its effect on narrowing down (A) or plugging (B) the pore space, after Wojtanowicz et al. (1987).

A further indication of asphaltene deposition was reduction in the permeability of the core plug. Permeability measurements were not performed on the plug since no differential pressure gauge was implemented in the experimental set-up. However, a pressure relief valve connected to the pump leaked if the injection pressure exceeded 690 kPa (100 psi). In the water-wet experiment a back pressure of ~570 kPa (75 psi) was used, however after the aging process the back pressure had to be reduced to ~138 kPa (20 psi), and at some stages removed to avoid leakage of the pressure relief valve. This indicates a significantly greater pressure drop over the core and hence tighter pore space as suggested above.

The pore volume of the core plug was 600 µl. The injections were performed under two constant flow rates. Figure 3.35 shows the conceptual test procedure followed in this experiment. Table 3.3 summarises the injection steps. The capillary dominated drainage and imbibition were performed at a constant injection rate of q = 5 µl/min. Different flow rates were used for the viscous dominated drainage and imbibition due to the higher viscosity of the oil phase compared to the brine phase (section 3.2). The viscous dominated injection rates used in the oil-wet experiments were smaller than the ones used for the water-wet core (see Tables 3.2 and 3.3). This was due to lower relative permeability of the core plug after the aging process. Using lower injection rates has the advantage of avoiding fluid auto-redistributions observed during the fast drainage step in the water-wet core (chapter 4, section 4).

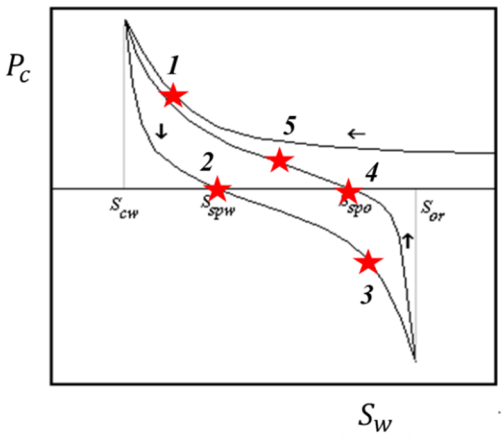

Figure 3.35: The test cycle used in the oil-wet experiment consisted of drainage and imbibition processes. The experiment started from oil saturated plug (point 1).

Table 3.3: Details of experimental test cycle for the oil-wet experiment.

Injection step	Flow Rate (µl/min)	Capillary Number	Linear Velocity (m/s)	Injection Period (hrs)	Pore Volumes Injected
Brine injection Figure 3.35 (1-2)	5	9.77×10^{-8}	3.84×10^{-6}	40	20
Brine injection Figure 3.35 (2-3)	250	4.88×10^{-6}	1.92×10^{-4}	0.8	20
Oil injection Figure 3.35 (3-4)	5	1.98×10^{-7}	3.84×10^{-6}	40	20
Oil injection Figure 3.35 (4-5)	150	5.93×10^{-6}	1.15×10^{-4}	1.34	20

In total the procedure included 4 injection steps and 10 scans, each consisting of 1500 projections. Each projection was a summation of 3 acquisitions (with one second exposure time) to reduce digital noise and reduce the effect of detector non-linearity. The scans were done at two magnifications. In all steps a high magnification scan of a section of 15 mm length of the core plug was collected at 10 µm voxel size. The magnification is 3.35 (466 mm/139 mm, see chapter 2, section 2). The blurring is 28.23 µm (12 µm × 327 mm/139 mm). The camera pixel size is 48 µm. The total resolution is 16.62 µm (i.e. $\frac{\sqrt{28.23^2+48^2}}{3.35}$).

Additionally, in some steps lower magnification scans of ~14 µm voxel size were collected from the entire length of the plug to determine the overall saturation profile. The magnification is 4.8 (466 mm/97 mm, see chapter 2, section 2). The blurring is 45.65 µm (12 µm × 369 mm/97 mm). The camera pixel size is 48 µm. The total resolution is 13.8 µm (i.e. $\frac{\sqrt{45.65^2+48^2}}{4.8}$).

In this round of experiments more than 20 pore volumes (as opposed to 10 pore volumes used in the water-wet experiment) of the displacing phase was injected into the core plug at each injection step. This was due to the fact that some extra oil was

produced after the first 10 pore volumes of brine injection. Figure 3.36 shows the production of extra oil after 12 pore volumes of capillary-dominated brine injection. Continuation of the oil production indicates that the oil phase is connected through oil films, and that the rock is oil-wet.

Although the injected oil used for initial saturation of the plug was a colourless fluid (50%v/v iododecane in dodecane) the produced oil had a brown colour as seen in Figure 3.36. This was due to continuous production of some remaining residues of the crude oil. Crude oil components were probably diffusing into the oil phase from the deposited layers coating the rock surface. The colour contrast between the two brine and oil phases made the oil phase readily observable in the production line.

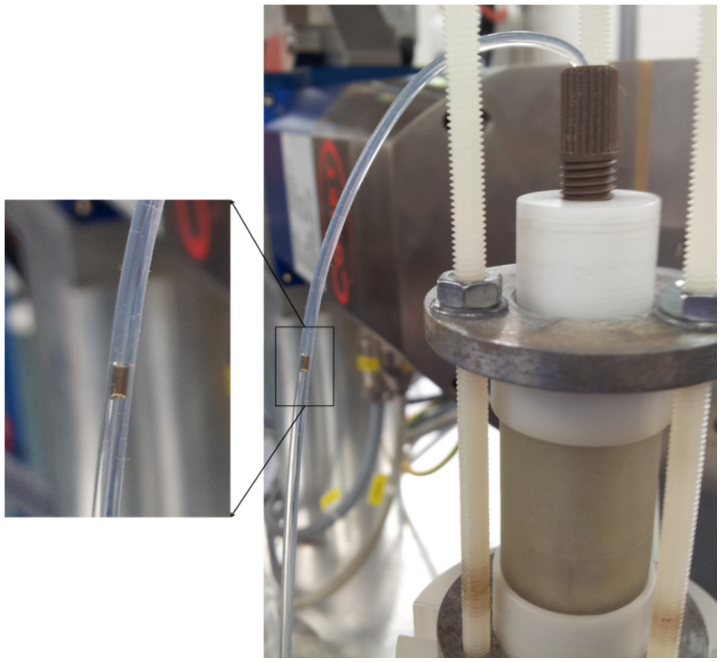

Figure 3.36: Continuation of oil production from the oil-wet core after 12 pore volumes of brine injection. This indicates established wetting oil films throughout the core which connect the oil phase and facilitate its ongoing production.

5. Summary

This chapter describes the experimental methods along with image analysis techniques used in this research. The image processing steps including image filtering, segmentation, and quantitative analysis are overviewed. The design of an in-house built X-ray transparent core holder is presented. The carbonate rock used in this study is introduced. The experimental set-up design and test procedures are described. Fluid displacements were performed using two constant injection flow rates to study the fluid distributions under capillary-dominated and viscous-dominated flow regimes. The fluid injection-μCT test cycle included drainage and imbibition steps. The experiments performed on the same core plug under water-wet and oil-wet states. The oil wet-plug was obtained by aging the water-wet plug in crude oil. The results of these experiments are presented in chapters 4 to 6.

References

ANDERSON, W. 1986. Wettability literature survey-part 2: Wettability measurement. *Journal of Petroleum Technology,* 38**,** 1,246-1,262.

BEAR, J. 1988. *Dynamics of Fluids in Porous Media*, Dover Publication.

BENSON, S. M., LI, B., KRAUSE, M., KREVOR, S., KUO, C.-W. & PINI, R. 2011. Investigations in Geologic Carbon Sequestration: Multiphase Flow of CO2 and water in reservoir rocks. Stanford University: Department of Energy Resources Engineering, School of Earth Sciences

BEUCHER, S. & LANTUÉJOUL, C. 1979. Use of watersheds in contour detection.

BUADES, A., COLL, B. & MOREL, J.-M. A non-local algorithm for image denoising. Computer Vision and Pattern Recognition, 2005. CVPR 2005. IEEE Computer Society Conference on, 2005. IEEE, 60-65.

BUCKLEY, J. S. 1996. Mechanisms and consequences of wettability alteration by crude oils.

CULLIGAN, K. A., WILDENSCHILD, D., CHRISTENSEN, B. S. B., GRAY, W. G. & RIVERS, M. L. 2006. Pore-scale characteristics of multiphase flow in porous media: A comparison of air–water and oil–water experiments. *Advances in Water Resources,* 29**,** 227-238.

DILLENCOURT, M. B., SAMET, H. & TAMMINEN, M. 1992. A general approach to connected-component labeling for arbitrary image representations. *Journal of the ACM (JACM),* 39**,** 253-280.

GONZALEZ, R. C., WOODS, R. E. & EDDINS, S. L. 2004. Digital image processing using MATLAB. *Upper Saddle River, N. J: Pearson Prentice Hall*.

GUO, R. & PANDIT, S. 1998. Automatic threshold selection based on histogram modes and a discriminant criterion. *Machine Vision and Applications,* 10**,** 331-338.

IGLAUER, S., PALUSZNY, A., PENTLAND, C. H. & BLUNT, M. J. 2011. Residual CO2 imaged with X-ray micro-tomography. *Geophysical Research Letters,* 38**,** L21403.

LØVOLL, G., MÉHEUST, Y., MÅLØY, K. J., AKER, E. & SCHMITTBUHL, J. 2005. Competition of gravity, capillary and viscous forces during drainage in a two-dimensional porous medium, a pore scale study. *Energy,* 30**,** 861-872.

MÉHEUST, Y., LØVOLL, G., MÅLØY, K. J. & SCHMITTBUHL, J. 2002. Interface scaling in a two-dimensional porous medium under combined viscous, gravity, and capillary effects. *Physical Review E,* 66**,** 051603.

NG, K., DAVIS, H. & SCRIVEN, L. 1978. Visualization of blob mechanics in flow through porous media. *Chemical Engineering Science,* 33**,** 1009-1017.

OH, W. & LINDQUIST, W. B. 1999. Image thresholding by indicator kriging. *Pattern Analysis and Machine Intelligence, IEEE Transactions on,* 21**,** 590-602.

OR, D. 2008. Scaling of capillary, gravity and viscous forces affecting flow morphology in unsaturated porous media. *Advances in Water Resources,* 31**,** 1129-1136.

PAK, T., GEIGER, S., JIANG, Z., SORBIE, K. S., ELPHICK, S., VAN DIJKE, M. I. J. & BUTLER, I. 2013. Pore-Scale Visualisation of Two-Phase Fluid

Displacement Processes in a Carbonate Rock using X-ray micro-TomographyTechnique. Society of Petroleum Engineers.

PERONA, P. & MALIK, J. 1990. Scale-space and edge detection using anisotropic diffusion. *Pattern Analysis and Machine Intelligence, IEEE Transactions on,* 12**,** 629-639.

PORTER, M. & WILDENSCHILD, D. 2010. Image analysis algorithms for estimating porous media multiphase flow variables from computed microtomography data: a validation study. *Computational Geosciences,* 14**,** 15-30.

PREWITT, J. M. S. & MENDELSOHN, M. L. 1966. The analysis of cell images. *Ann. New York Acad. Sci.,* 128**,** 1035–1053.

ROERDINK, J. B. & MEIJSTER, A. 2000. The watershed transform: Definitions, algorithms and parallelization strategies. *Fundamenta Informaticae,* 41**,** 187-228.

SAHIMI, M. 1994. *Applications of percolation theory*, CRC Press.

SEZGIN, M. & SANKUR, B. Selection of thresholding methods for nondestructive testing applications. Image Processing, 2001. Proceedings. 2001 International Conference on, 2001. IEEE, 764-767.

SHAW, D. G., MACZYNSKI, A., HEFTER, G., KLEINSCHMIDT, M., MACKAY, D., MEYERS, P., MIYAMOTO, H. & SHIU, W. 2006. IUPAC-NIST solubility data series. 81. Hydrocarbons with water and seawater-Revised and updated part 12. C 5-C 26 hydrocarbons with seawater. *Journal of physical and chemical reference data,* 35**,** 785-838.

SHENG, J. 2010. *Modern chemical enhanced oil recovery: theory and practice*, Gulf Professional Publishing.

VINCENT, L. & SOILLE, P. 1991. Watersheds in digital spaces: an efficient algorithm based on immersion simulations. *IEEE transactions on pattern analysis and machine intelligence,* 13**,** 583-598.

VLASSENBROECK, J., MASSCHAELE, B., CNUDDE, V., DIERICK, M., PIETERS, K., VAN HOOREBEKE, L. & JACOBS, P. 2010. Octopus 8: A High Performance Tomographic Reconstruction Package for X-ray Tube and Synchrotron micro-CT. *Advances in X-ray Tomography for Geomaterials.* ISTE.

WOJTANOWICZ, A., KRILOV, Z. & LANGLINAIS, J. Study on the effect of pore blocking mechanisms on formation damage. SPE Production Operations Symposium, 1987. Society of Petroleum Engineers.

YOUNG, T. 1805. An essay on the cohesion of fluids. *Philosophical Transactions of the Royal Society of London***,** 65-87.

YOUSSEF, S., BAUER, D., BEKRI, S., ROSENBERG, E. & VIZIKA, O. Towards a better understanding of multiphase flow in porous media: 3D in-situ fluid distribution imaging at the pore scale. International Symposium of the Society of Core Analysts, Noordwijk, The Netherlands 27–30 September, 2009. 1-12.

Chapter 4

Core-scale Analysis of Fluid Saturation Distributions in a Water-wet Carbonate

Drainage and imbibition processes in a water-wet carbonate rock (SD) were monitored using μCT technique based on the experimental procedures described in chapter 3, section 4. Two constant flow rates were used for fluid injections, q =10 μl/min and q =700 μl/min. The corresponding capillary numbers are of the order of 10^{-7} and 10^{-5}, respectively. It is shown later in sections 3 and 4 that during the slow drainage the capillary end effect has caused brine accumulation close the core outlet, in addition to this a fluid saturation redistribution was recorded as a result of the fast drainage. Based on these observation it can be concluded that the slow and fast injections have happened within the capillary-dominated and viscous-dominated flow regimes, respectively. This chapter presents the observations and analysis of the fluid saturation distributions at core-scale.

1. Wettability Assessment using Direct Observation of Pore-sizes Occupied by the Fluid Phases

μCT imaging enables in-situ visualisation of fluid clusters occupying porous media. Image analysis allows extraction of the cluster size (volume) distributions for each fluid phase. Al-Raoush (2009) studied the structure of the residual NALP phase in sand packs under different wetting states. The porous media were made by mixing different ratios of oil-wet and water-wet sands (0, 25, 50, and 100%). The findings demonstrate that the residual NALP clusters are larger for the sand-packs with more water-wet fractions. In a similar study Landry et al. (2011) imaged trapped oil clusters in pore space of acrylic bead packs (oil-wet). They compared their findings with the results of a similar experiment (Karpyn et al., 2010) conducted in glass bead packs (water-wet). Trapped oil clusters were found to be smaller in the oil-wet system compared to the water-wet system. Iglauer et al. (2012) compared the oil cluster size distribution in water-wet and oil-wet sandstone samples. They reported the observation of fewer large oil clusters in the oil-wet core, which is in agreement with the findings of Al-Raoush (2009) and Landry et al. (2011). These studies analysed the trapped oil phase in porous media after the imbibition process. They demonstrated variability in the trapped oil cluster size distributions as a function of the wetting state of the porous media. However, the reported trends are not distinct enough to provide sufficient ground for wettability assessment based solely on cluster size distributions.

All the above mentioned studies have used the "cluster size (volume) distribution" as the basis of their comparisons. They used simple and self-similar pore systems (bead packs and sandstones) with narrow pore-size distributions. In such cases the simplicity of the pore structure does not assist in gaining a clearer understanding of the underlying processes that control the fluid saturation distributions. The simple structure diminishes the variability of capillary forces in the pore system. More precisely, pores (and pore-throats) of similar sizes allow limited number of possible oil-water curvatures (and hence capillary forces) throughout the pore system. Moreover, the pore entry pressure (eq. 3.1) covers a narrow range for majority of the pores. The capillary entry pressure of a tube (pore) correlates inversely with the tube (pore) size (Young, 1805). In a more heterogeneous pore structure, however, a broad range of pore (and pore-throat) sizes translates into widely variable pore entry pressures as well as oil-water interface curvatures. Therefore, in such complex pore systems the size distribution of the pores occupied by fluid clusters can communicate valuable information about the wettability of the porous media.

Consider an oil-water displacement in a water-wet rock. During drainage, oil (with help of external force) enters the largest accessible pores (pore-throats) leaving the smaller pores (pore-throats) occupied by water (Sahimi, 1994). By increasing the injection rates (injection pressures) oil invades into progressively smaller pores. During this process the capillary pressure increases. Here the oil and water clusters occupying the SD plug after the "drainage" cycle are considered. Taking the image-based cluster size analysis discussed above one step forward, the "pore-size distributions occupied by each fluid phase" have been extracted from μCT images. The pore-size distribution, however, should not be mistaken for the cluster size distribution mainly because a fluid cluster may span over several connected neighbouring pores. To calculate the pore-size distributions based on μCT images, a sphere fitting method (Jiang et al., 2012) was used. Binary images of each fluid phase were used as input. It should be mentioned that this approach is valid where the pores are occupied only by a single fluid phase. Pores that are partially occupied by the two fluid phases (or in cases where the water film is captured in the corners of the pores) introduce errors in the calculated pore-size distributions. More details about partial

pore occupancies and wetting film development is presented in chapter 5. In the images captured after the primary drainage steps no pore was observed to be partially occupied by oil and brine phases.

Based on the 24 μm resolution data (low magnification) that covered the entire length of the core the oil saturation after the capillary-dominated and viscous-dominated drainage cycles are measured to be 0.86 and 0.91, respectively. Here the calculations are based on a volume of 370×360×1100 voxels (8.8×8.64×26.4 mm^3). This region corresponds to the entire length of the core plug excluding a zone close to the core exit (~15 mm length) which observed to have experienced capillary boundary effects. More details are discussed in section 4. It should also be mentioned that after the viscous-dominated drainage an auto-redistribution was observed in the fluid saturations between the duplicate scans, this is discussed in section 5. The data discussed in this section were acquired before the rearrangements in fluid saturations occurred.

Figure 4.1 shows 3D renderings of the labelled brine and oil phases after the capillary-dominated drainage. It is clear that the defending brine phase has remained saturated within the smaller pores while the larger pores and intermediate size pores are occupied by the invading oil phase. This behaviour is an indication of a water-wet system. Figure 4.2 shows the labelled brine and oil phases after the viscous-dominated drainage, rendered in 3D. Increasing the oil injection flow rate has forced more of the brine phase out of increasingly smaller pores during this step.

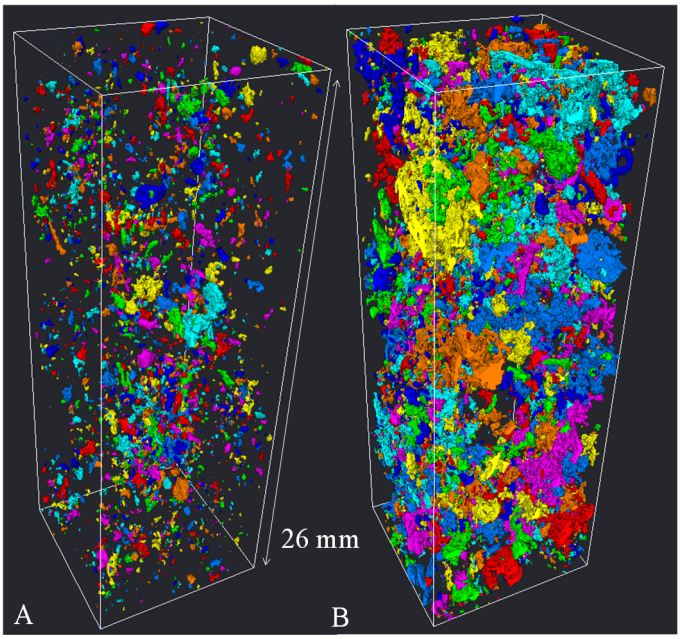

Figure 4.1: 3D rendering of labelled brine (A) and oil (B) phases after the capillary-dominated drainage. The images show a volume of 370×360×1100 voxels (8.8×8.64×26.4 mm^3). The remaining brine phase occupies the smaller pores which may be an indication of the water-wetness of the rock.

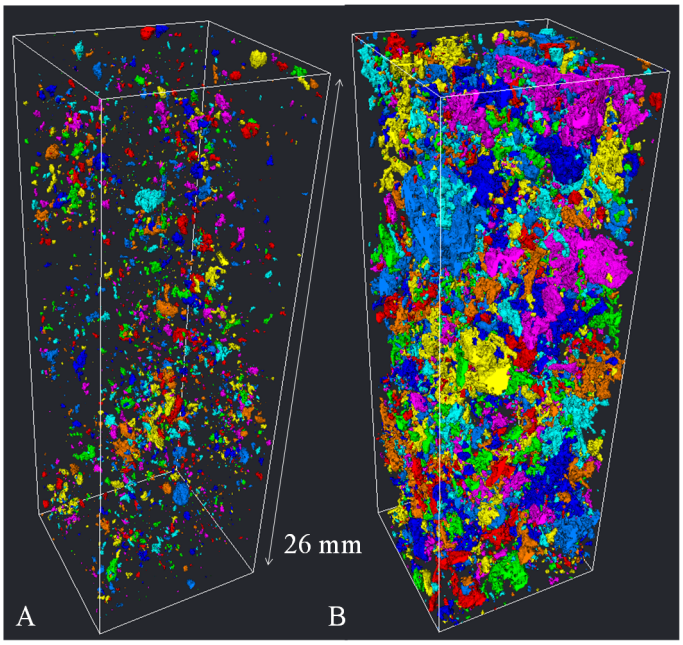

Figure 4.2: 3D rendering of labelled brine (A) and oil (B) phases after the viscous-dominated drainage. The images show a volume of 370×360×1100 voxels (8.8×8.64×26.4 mm^3). The remaining brine phase occupies the smaller pores which may be an indication of the water-wetness of the rock.

Figure 4.3 shows the distribution of the "pore-sizes" occupied by each fluid phase after the two drainage processes. It is clear that the brine phase has remained in the smaller pores while the larger pores are occupied with the oil phase. The distributions of pore-sizes occupied by oil and brine after the viscous-dominated drainage indicate that more brine has been displaced form these smaller pores as a result of higher injection rates (and hence pressures). This extra brine production is measured to be 5% of the porosity.

A comparison between the oil cluster size distributions for this core plug at water-wet and oil-wet states is presented in chapter 6, section 1. The comparison displays a distinct difference between the cluster size distributions as a result of wettability alteration.

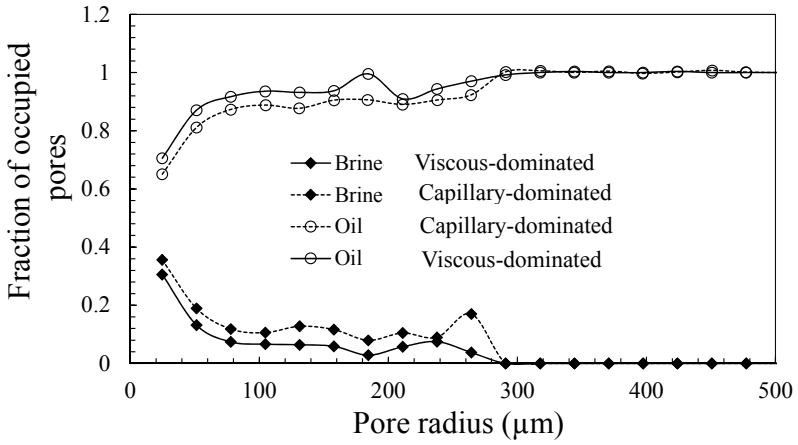

Figure 4.3: Distribution of the pore-sizes occupied by the two fluid phase after two drainage steps. The brine phase has remained in the smaller pores while the larger pores were occupied by the oil phase. This behaviour can be an indication of a water-wet system.

2. Cluster size Analysis – Percolation Theory

Percolation theory suggests that size distribution of the trapped non-wetting phase clusters in a porous medium after imbibition at infinitesimal flow rates should scale as a power-law $N(s) \sim s^{-\tau}$ (Stauffer, 1979, Lorenz and Ziff, 1998), where s is the number of pores that contain a trapped non-wetting cluster and τ is the power-law exponent. For three dimensional structures the τ exponent has been shown to be larger than 2 using numerical simulations (Wilkinson and Willemsen, 1983, Strenski et al., 1991,

Lorenz and Ziff, 1998, Blunt and Scher, 1995). This value has also been measured using pore-scale imaging of the trapped cluster distributions in clastic and carbonate rocks as well as some synthetic porous media (Iglauer et al., 2010, Iglauer et al., 2011, Andrew et al., 2014).

Fundamentally, percolation theory can only be applied to capillary-dominated flow with infinitesimal slow displacement rates. In the fast injections of our experiments the displacement happened in a mix of viscous and capillary flow regimes. This resulted in a large number of droplets with $s \ll 1$ to be trapped in the pore space for which the power-law relation is not valid.

The distribution of the trapped cluster volumes after the capillary dominated imbibition does not follow a simple power-law. It is possible to fit portions of the trapped oil "volume" distribution with a number of power-law functions such that $\tau \geq 2$. However, the entire range of the data does not fit a single power-law function. Figure 4.4 shows the probability of the clusters larger than size *s* (*M(s)*) plotted against *s*. The power-law fitting was performed using a maximum likelihood estimator developed by Clauset et al. (2009). *M(s)* is defined as:

$$M(s) = \frac{\int_s^\infty N(s)\, ds}{\int_0^\infty N(s) ds} \sim s^{1-\tau}. \quad (4.1)$$

The two lines show two distinct power-law functions which were fitted to different ranges of the cluster size data, measured in volume (voxels).

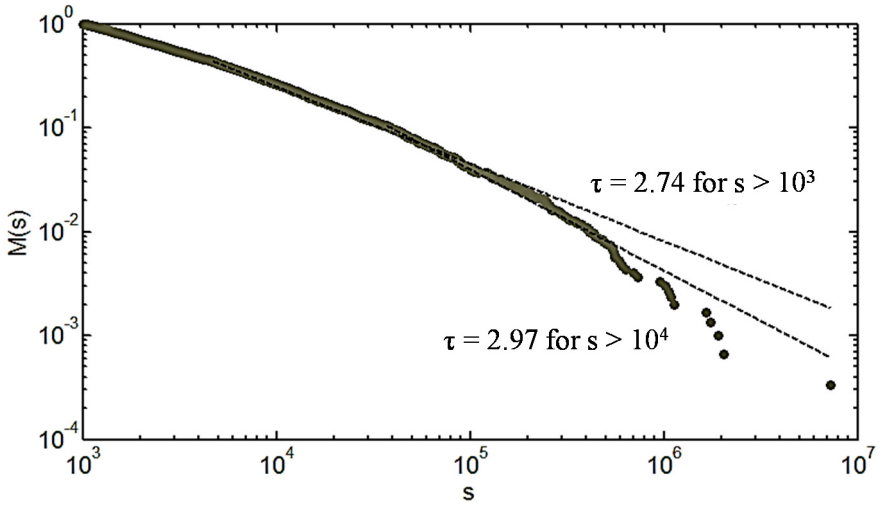

Figure 4.4: Cumulative cluster size probability distributions calculated using a maximum likelihood estimator developed by Clauset et al. (2009). It is possible to fit portions of the trapped oil "volume" distribution with a number of power-law functions such that $\tau \geq 2$. However, the entire range of the data does not fit a single power-law function.

In percolation theory, a power-law behaviour is only applicable if the cluster sizes are defined as the number of pores occupied by each cluster, and not the cluster volumes (Wilkinson, 1986). Further, the power-law scaling is valid only for clusters with $s > 1$ (i.e. the by passed oil clusters and not the clusters trapped in single pores as a result of snap-off). For this reason clusters smaller than an average pore-size were excluded by Iglauer et al. (2010) and Andrew et al. (2014) prior to fitting power-law functions to clusters size distributions (derived from μCT imaging).

In homogeneous pore structures, such that the ones studied by Iglauer et al. (2010) and Andrew et al. (2014), the pore-size distributions are narrow. Therefore, the pore number-to-volume scaling approaches 1:1. Hence, the cluster sizes measured in volume using X-ray μCT imaging can reflect the number of pores occupied by the clusters. For heterogeneous pore systems with a wide pore-size distribution, however, the pore number-to-volume scaling is no longer 1:1. Therefore, the number of pores occupied by a cluster cannot be deduced from the volume of the cluster. On this basis, for heterogeneous rocks the cluster volume distributions measured directly on X-ray μCT images are not the applicable to percolation theory. The low values of tau

measured by Andrew et al. (2014) for Mt Gambier Limestone may be in part related to this problem.

3. Capillary End Effect

In core flooding experiments a capillary end effect is known to occur when the wetting phase is displaced with a non-wetting phase within the capillary dominated flow regime (Bear, 1972). Due to the capillary discontinuity at the production end of the core plug the wetting phase accumulates in a zone close to the production face of the plug, and hence establishes higher saturations compared to the zones that are not influenced by this effect. The capillary end effect is considered as a serious source of error in calculation of fluid saturations in core flooding tests, in particular for end point fluid saturations, and hence for relative permeability curves. To correct for this effect a number of methods are practised in core analysis laboratories: (a) using long cores in the core flood experiments (b) placing an end piece at the end of the core plug to displace the end effect out of the core plug (O'Meara Jr and Vinegar, 1990), and (c) correcting the saturation profile in subsequent calculations (Chang et al., 1997).

In core analysis laboratories longer core plugs are used, where possible, as the simplest remedy. However, in the studies where μCT technique is used to monitor the pore-scale processes smaller (not necessarily shorter) core plugs are essential to achieve high resolutions required to visualise the pore-scale events. Depending on the range of pore-sizes the required resolution is variable. Small plugs of D~5 mm and L~10 are commonly used in combined porous media flow-μCT studies. This is an acceptable sample size for many homogeneous pore systems, such as bead packs, sand packs and some sandstone rocks. However for heterogeneous rocks the issue of representativity comes into play. This is discussed in further details in chapter 7. As a result of selecting a small sample from a heterogeneous rock the network of larger-pores may not be statistically well-represented, i.e. only a few larger pores are included. Studies performed on such a sample may not be extended to the rock type. In this study a larger core plug was used (D=12.5mm, L=44 mm) with the aim of having a more representative sample of the heterogeneous dolomite under study. This allowed

observation of the capillary-driven brine accumulation close to the core production face during the capillary dominated drainage.

Figure 4.5A and 4.5B shows a 3D rendering of oil (white) and brine (blue) phases on almost entire length of the core plug after the 10 µl/min and 700 µl/min primary drainage steps. Here the images show a volume of 370×360×1730 voxels (8.8×8.64×41.52 mm^3). The injections were performed from bottom to the top of the plug. More than 10 pore volumes of oil were injected at each step. Due to practical limitations of the laboratory-based µCT scanner used here (such as long data acquisition time) the core was not scanned during the injection period. There was no single highly-connected channel of pores in the plug, therefore the breakthrough (of the injecting phase) was observed within the first 3 to 4 pore volumes of injection at all stages. Figure 4.5A and 4.5C demonstrates a significant brine accumulation in a zone subjacent to the production face of the plug after the capillary-dominated drainage. The images captured after the viscous-dominated drainage show the accumulated brine was no longer present in the corresponding volume.

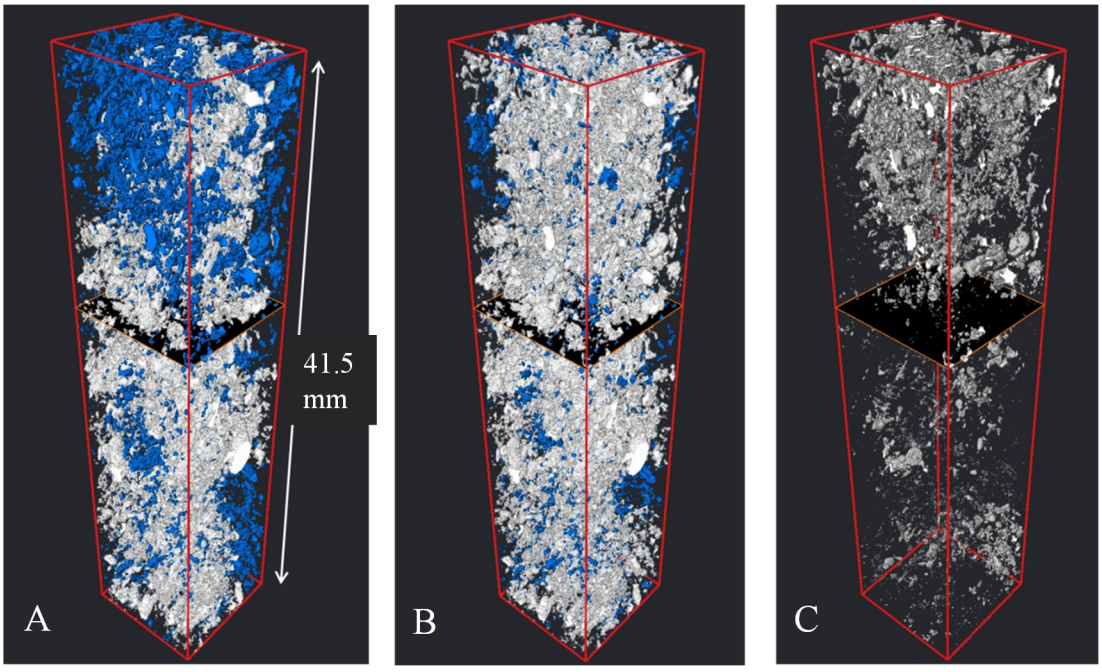

Figure 4.5: 3D rendering of oil (white) and brine (blue) phases after the capillary-dominated (A), and viscous-dominated (B) drainage steps. Brine phase that has been present in the core after the capillary-dominated drainage, but was produced as a result of the viscous-dominated

drainage is shown in (C). The images are from the 24 μm resolution images of the entire length of the core plug. Here the images show a volume of 370×360×1730 voxels (8.8×8.64×41.52 mm^3).

Extra brine production was observed immediately after the flow rate was increased, presumably coming from the accumulated brine near the core exit. In order to visualise the extra brine production during the viscous-dominated drainage the brine phase on Figure 4.5B can be subtracted from the brine phase on Figure 4.5A. Figure 4.5C shows the subtracted image, which corresponds to the brine phase that has been present in the core after the capillary-dominated drainage, but was produced as a result of the viscous-dominated drainage.

Figure 4.6 shows oil and brine saturation profiles after the capillary-dominated drainage, along with example μCT image re-sliced parallel to the direction of fluid flow. Significantly higher saturations of brine were measured over a zone of almost 15 mm (almost one third of the core plug length) close to the production face.

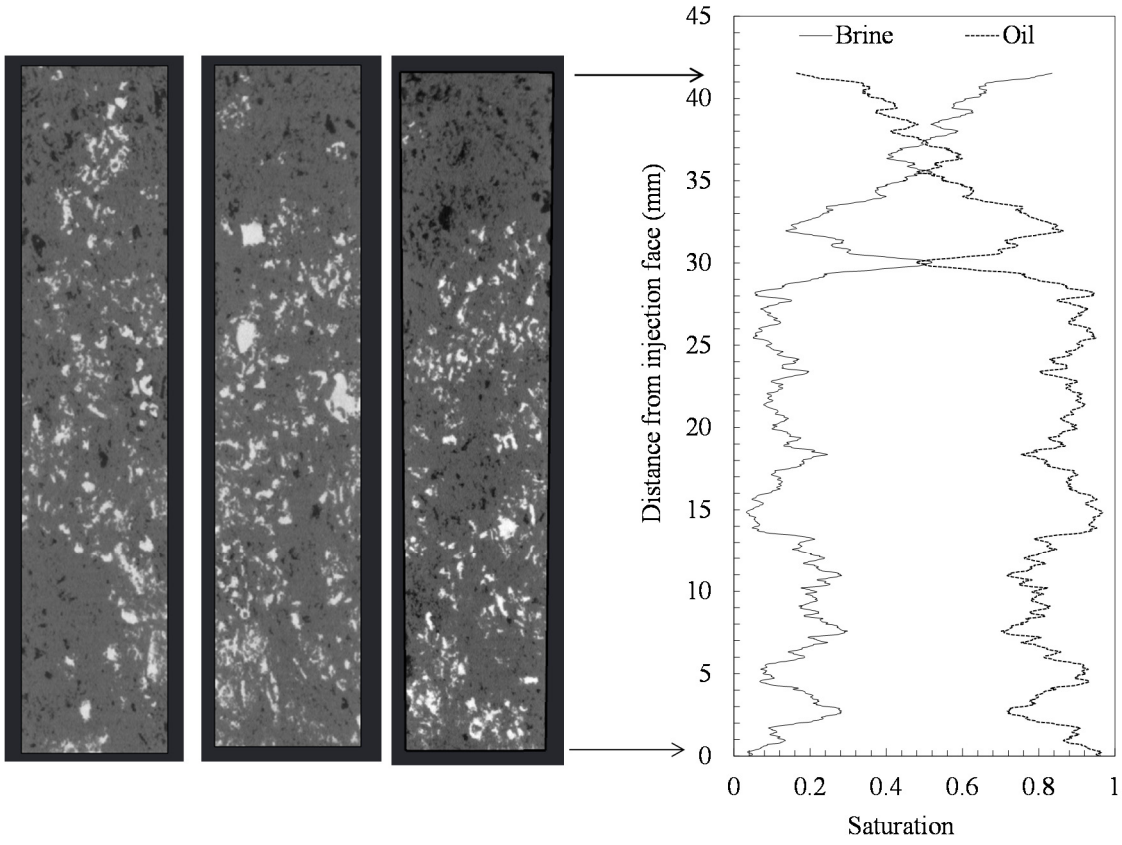

Figure 4.6: Example µCT images re-sliced parallel to the direction of fluid flow, after the capillary-dominated drainage. White and black phases indicate oil and brine, respectively. The plot shows the oil and brine saturation profiles along the core plug length.

The saturation gradient in this zone displays to be much larger than that of the rest of the core plug. This zone is referred to as the "capillary affected zone" (CAZ). The brine saturation varies in the range of 0.2 to 0.9 within the CAZ, compared to a mean of 0.12±0.07 in the rest of the core.

Figure 4.7 shows the oil and brine saturation profiles after the viscous-dominated drainage, along with three example µCT images re-sliced parallel to the direction of fluid flow. The viscous flow displaced the brine accumulated in the CAZ. At this stage, the two phases display more uniform saturation profiles throughout the length of the core plug. The average brine saturation in the zone previously influenced by the capillary end effect and the rest of the core plug are much more comparable, 0.06±0.03 compared to 0.08±0.05, respectively.

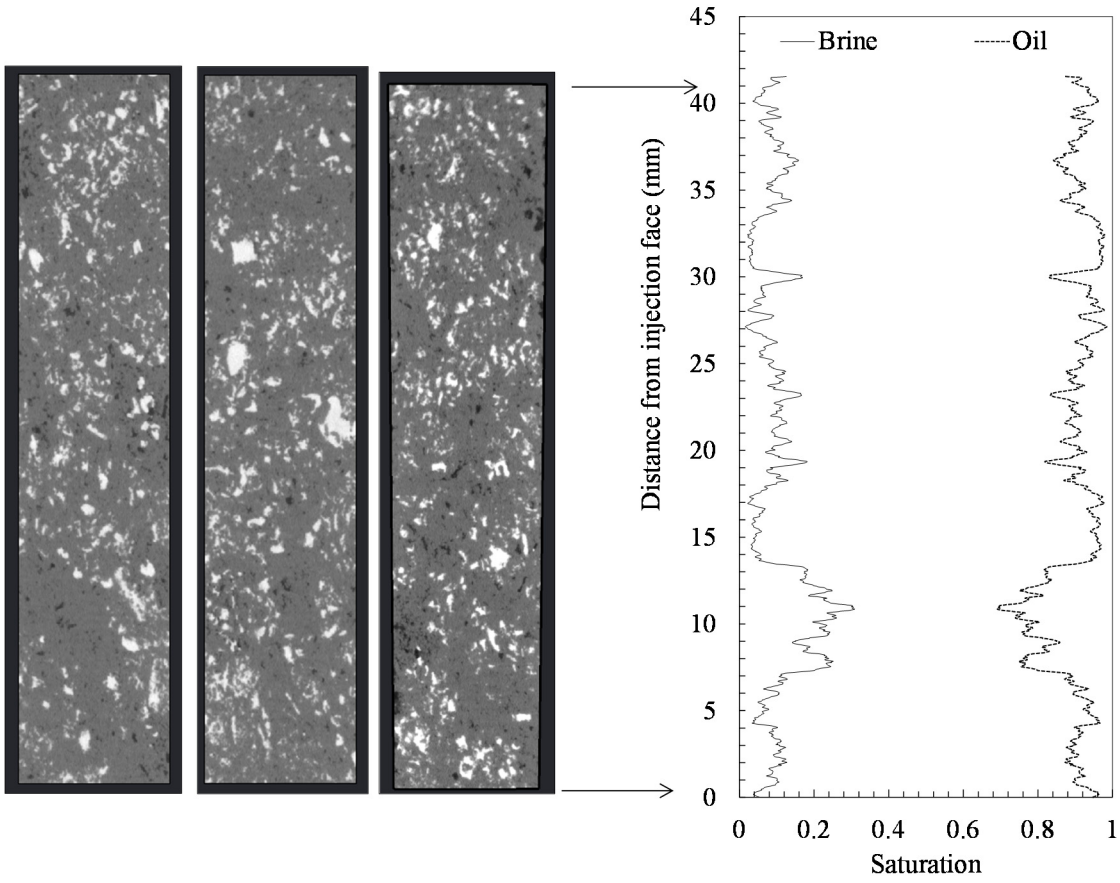

Figure 4.7: Example µCT images re-sliced parallel to the direction of fluid flow, after the viscous-dominated drainage. White and black phases indicate oil and brine, respectively. The plot shows the oil and brine saturation profiles along the core plug length.

Figure 4.8 illustrates a comparison between the pore-sizes occupied by oil and brine in the CAZ after the two drainage steps. To obtain this a sphere fitting method (Jiang et al., 2012) was used taking binary volumes of each fluid phase as input data. The volumetric fraction occupied by each pore-size is normalised against the volumetric pore-size distribution of the "pore space" in the CAZ. For each phase,

$$Normalised\ volume\ fraction\ of\ phase\ i\ occupying\ pores\ of\ radius\ r = \frac{total\ volume\ ccupied\ by\ phase\ i\ in\ pores\ with\ radius\ r}{total\ volume\ of\ the\ pores\ of\ radius\ r\ in\ the\ CAZ} \quad (4.2)$$

The pore space image was obtained by subtracting an image of the water saturated core from a brine (1M KI) saturated core image.

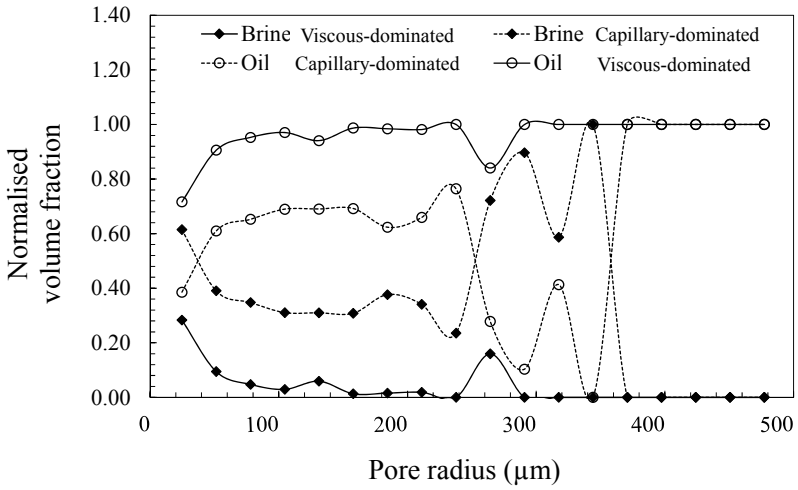

Figure 4.8: Comparison between the pore-size distributions occupied by the two fluid phases in the CAZ after drainage steps.

After the capillary-dominated drainage the brine phase occupied pores with a broad range of radius (24 μm < r < 344μm). After the viscous-dominated drainage, however, the brine phase remained only in smaller pores (24 μm < r < 264 μm). This trend is expected from a water-wet rock.

Figure 4.9 shows the labelled brine phase after the two drainage steps rendered in 3D. It is visually apparent that the volume of the brine labels spans a broader range in the CAZ compared to the rest of the core plug after the capillary-dominated oil injection step, this is mainly due to brine accumulation in the CAZ which resulted in brine saturating some larger pores as well as the smaller pores as shown in Figure 4.7A. However, after the viscous-dominated oil injection step the remaining brine clusters are comparable in the CAZ with the rest of the core plug.

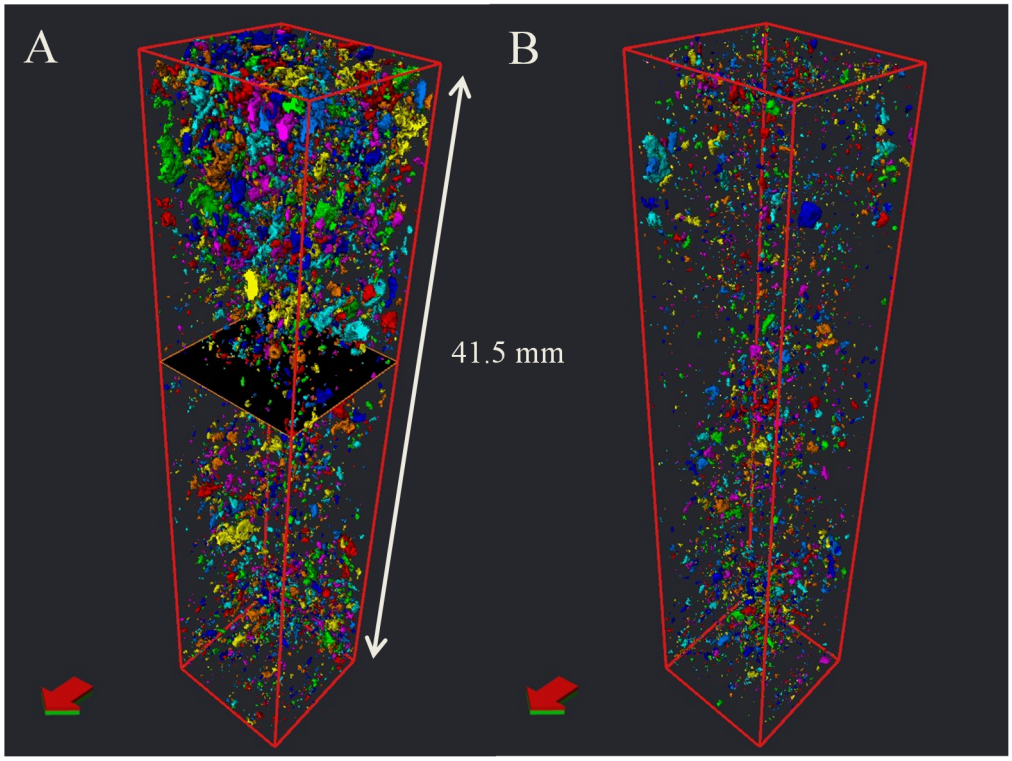

Figure 4.9: Labelled brine clusters after capillary-dominated and viscous dominated drainage cycles (A and B), respectively. It is visually apparent that the brine phase occupies a broader range of pore-sizes in the CAZ compared to the rest of the core plug.

Figure 4.10 compares pore-size distributions (normalised volumetric) for the *brine* phase in the CAZ and the rest of the plug after the two drainage steps. The volume fraction occupied by each pore-size is normalised against the volume fraction of the pore-sizes in the pore space for the relevant section of the plug (CAZ or Rest).

$$Normalised\ volume\ fraction\ of\ phase\ i\ occupying\ pores\ of\ radius\ r = \frac{total\ volume\ ccupied\ by\ phase\ i\ in\ pores\ with\ radius\ r}{volume\ of\ the\ pores\ with\ radius\ r\ in\ the\ corresponding\ section\ of\ the\ rock} \quad (4.3)$$

The pore-size distribution curve for the slow drainage in CAZ is significantly higher than the 3 other distributions. The brine distribution away from the CAZ (bottom 26.5 mm) is very similar after the two drainage steps.

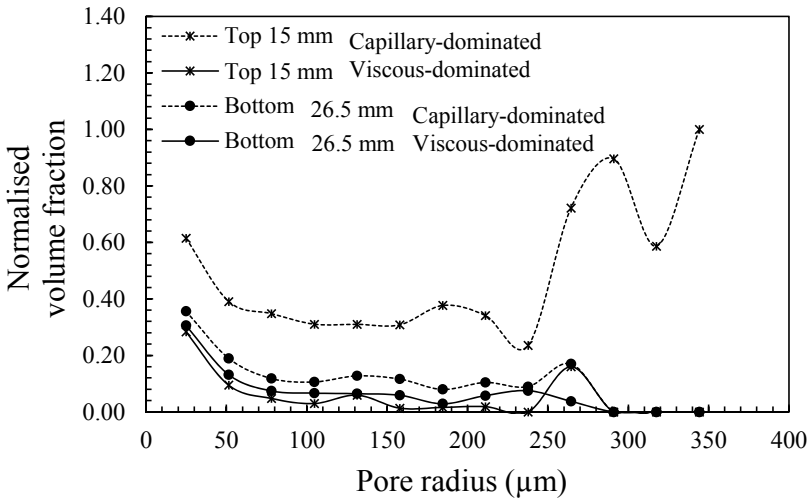

Figure 4.10: Distribution of the pore-sizes occupied by the brine phase after the two drainage steps, comparison between the CAZ and the rest of the plug. The brine phase occupies a broad range of pore-sizes under the influence of boundary forces in the CAZ. The pore-sizes occupied by the brine phase are very similar in the entire length of the core after the viscous-dominated drainage.

Two main conclusions can be drawn based on the observation of capillary end effect:

- The capillary end effect is associated with anomalous accumulations of the brine phase near the production face which implies that the rock is preferentially wetting towards the aqueous phase. This is in agreement with the wettability analysis based on the fluid saturation distributions after drainage, section 1. The results are in agreement with experiments of Vinegar and Wellington (1987) who referred to the observation of capillary end effect as an indicator of the rock wettability.
- In tomographic studies of multiple-phase fluid transport in porous media in order to avoid the influences of the boundary effects it is essential to use (a) a longer test piece and select the imaging region of interest away from its boundary, e.g. Kumar et al. (2009) (b) porous end pieces to shift the capillary end effect out of the porous media under inspection, as suggested by O'Meara Jr and Vinegar (1990) . In the present case the observed length of CAZ is 15 mm, which is greater than the total length of some experimental plugs used in other studies. Any reliable quantitative analysis of fluid saturation distributions based on μCT images should exclude the CAZ, if present.

- Experimental designs should seek to mitigate the impact of these boundary effects.
- The capillary end effect becomes more pronounced where the rock is strongly wetting towards one of the fluids, and during the drainage process in the capillary dominated regime.

The CAZ was excluded from all the quantitative analysis presented in this study.

4. Fluid Redistribution

Figure 4.11 shows a slice of the core plug from four μCT images captured after the two drainage steps, with 11.25 μm and 24μm resolutions. There are time delays of 23, 74, and 22 hours between the subsequent scans, respectively. The oil and brine saturation distributions are stable after the capillary-dominated drainage, Figure 4.11A and 4.11B. The stability of the fluid saturation distributions is because the injections performed within the capillary dominated flow regime.

Comparing the two 11.25 μm and 24 μm resolution images captured after the viscous-dominated drainage step reveals that the fluid saturations exhibited a significant redistribution after fluid injections was stopped and the cell locked off. Figure 4.11C shows the saturation state just after the viscous-dominated oil injection. Figure 4.11D shows the same slice of the core scanned after a time delay of 22 hours. The oil saturations calculated based on the 24 μm and 11.25 μm resolution images for the central section of the plug (8 to 26 mm) are 93 % and 69 % respectively. In total 24 % of the oil has moved out of the 18 mm central section of the core plug as a result of this redistribution. It should be mentioned that the entire field of view of the 11.25 μm resolution images was 20.5 mm, from which 2.5 mm from the top appeared to be affected by the boundary effects and hence was excluded from the saturation calculations.

The driving force for such a significant redistribution could be: (a) gravity driven forces, (b) capillary force acting at pore level. Since the density of the two fluid phases were precisely matched for the fluid pair used in this experiment (1.005 gr/cm^3) the gravity forces are not considered here.

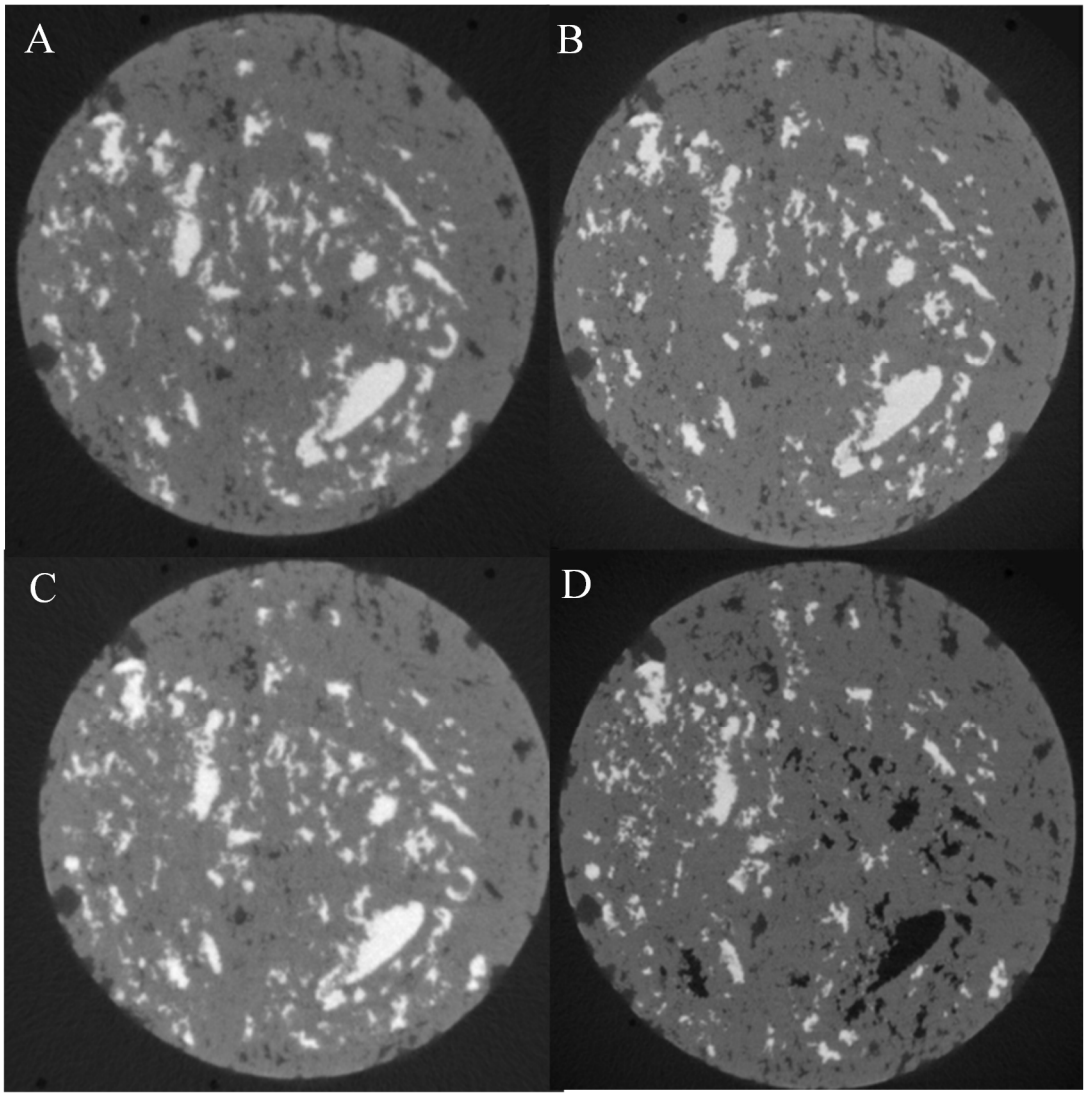

Figure 4.11: Same µCT slice of the core plug captured after capillary-dominated drainage with 24µm resolution (A), capillary-dominated drainage with 11.25 µm resolution (B), viscous-dominated drainage with 24µm resolution (C), viscous-dominated drainage with 11.25 µm resolution (D). A fluid saturation redistribution is observed between C and D. There are time delays of 23, 74, and 22 hours between the subsequent scans, respectively.

It is demonstrated in sections 2 and 3 that the rock is preferentially water-wet. By increasing the oil injection rate from 10 µl/min to 700 µl/min, oil pressure increases dramatically. If brine is present in form of corner films established all over the pore space (this is illustrated in chapter 5, section 1), then during the drainage process the pressure of the brine phase should remain equal to the back pressure applied at the production end of the plug, in this case ~517 kPa (75 psi). On this basis the capillary

pressure (the pressure across the oil-brine interface, $P_c = P_o - P_w$) becomes significantly higher when the injection is done under the viscous-dominated regime compared to the capillary-dominated injections. Upon stopping the flow at the end of the 700 µl/min oil injection, no external force maintains the oil pressure, therefore in a zero flow condition the pressure of the oil phase drops which results in a decrease in the capillary pressure. The change in capillary forces over the fluid interfaces results in a fluid redistribution. One interesting observation is the relaxation time required for the redistribution to take place. The process seems to be a slow process since the 24 µm resolution scan (collected two hours after the flow was stopped) has not captured any significant fluid redistribution. It should be mentioned that the scanning time was 150 minutes during which no fluid movements is recorded. Fluid movements during a scan would make the reconstructed images blurry. The saturation redistribution therefore needed more time.

It should be noted that the observed fluid redistribution is an experimental artifact resulted from having to stop the fluid injections to perform the imaging. Due to the extended data acquisition times of the available laboratory-based µCT scanner it was not possible to scan the specimen during the injection period. Tomographic monitoring of such dynamic processes can be performed at synchrotron imaging facilities with data acquisition times approaching less than a second.

Figure 4.12 shows example µCT slices parallel to the flow direction from the 11.25 µm resolution images captured after the capillary and viscous dominated drainage steps. The flow injections were done from bottom to top of these images.

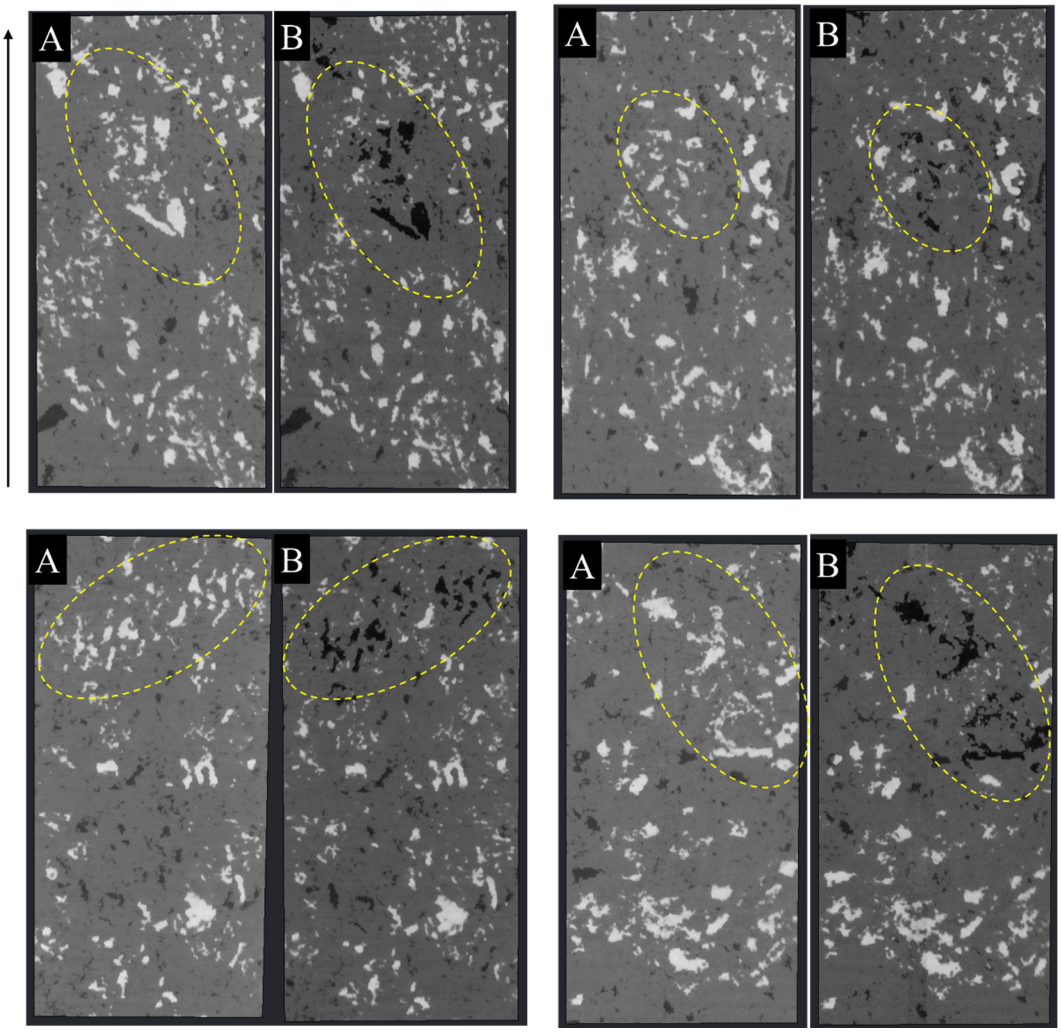

Figure 4.12: Exemplary 2D µCT slices (11.25 µm resolution) in the main flow direction (see the arrow) after capillary-dominated (A) and viscous-dominated (B) drainage. Areas highlighted by the dotted yellow envelopes are the pores from which the oil has been displaced as a result of fluid redistribution.

4.1. Where Has the Oil Migrated?

The only available image after the fluid redistribution occurred is an 11.25 µm resolution scan captured from the central section of the plug. No image of the entire core length is available after the saturation redistribution, therefore it is uncertain to where the oil has migrated. Figure 4.13A shows the image captured after the viscous-dominated drainage subtracted from that of the capillary-dominated, rendered in 3D (11.25 µm resolution images). The negative values are clipped to zero. This image highlights the pores from which the oil has been displaced as a result of the

redistribution. Figure 4.13B shows the capillary-dominated image subtracted from the viscous-dominated image. The image shows the pores invaded by oil as a result of the viscous-dominated drainage (followed by the redistribution).

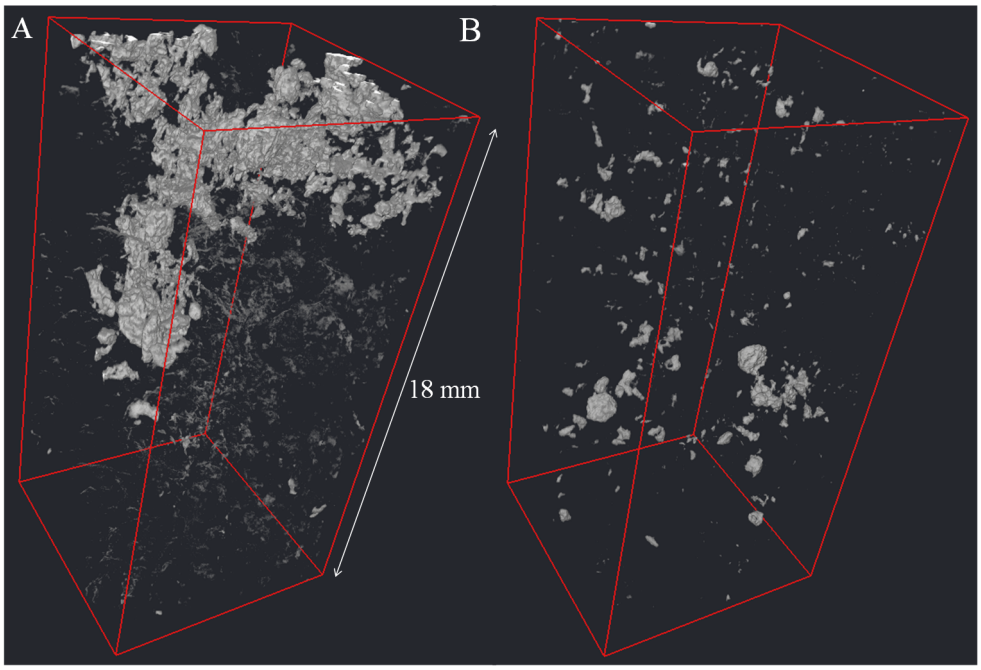

Figure 4.13: 3D rendering of the pores occupied by the brine phase as a result of the redistribution (A), the pores invaded by oil phase as a result of viscous-dominated drainage followed by the redistribution (B). The redistributions has occurred in a top section of the field of view of the 11.25 µm resolution images.

Oil saturation profile along the core can be extracted from the images. After the viscous-dominated drainage two images were acquired at 24 and 11.25 µm resolutions (Figure 4.11C and 4.11D). The redistribution has happened between these two scans. It is possible to extract the oil saturation profile from these images. However, different resolutions result in different uncertainties associated with the image processing steps. Therefore, in order to keep the comparison consistent oil saturation profiles were extracted from the data acquired at 11.25 µm resolution are compared in Figure 4.14. The two profiles indicate the oil saturation after the capillary and viscous-dominated drainage steps for the 18 mm central portion of core. The difference between the two profiles indicate the effect of viscous-dominated drainage followed by the redistribution. The oil saturation is expected to be higher after the viscous-dominated

drainage compared to the capillary-dominated drainage, if no redistribution occurred. However, the significant gap between the two profiles at the top section of the plug implies that the oil phase has moved out of this section (18 to 26 mm from the injection face) of the plug as a result of the redistribution.

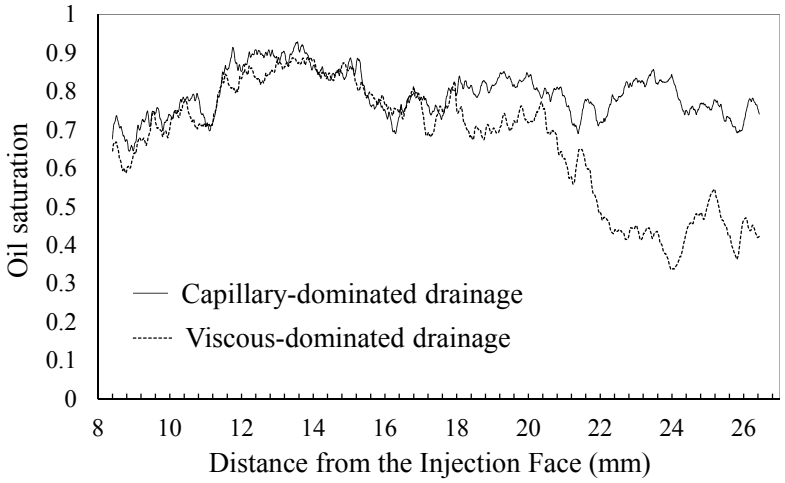

Figure 4.14: Oil saturation profile after the capillary and viscous-dominated drainage cycles along the 18 mm central portion of core. The redistribution has occurred in a section between 18 to 26 mm from the injection face.

4.2. Effect of Fluid Redistributions on the Cluster Sizes

As a result of the fluid saturation redistribution there is 24 % less oil in the pore space of the 18 mm central section of the core plug. Figure 4.15A shows 3D rendering of the labelled oil phase after the capillary-dominated drainage. Clusters with volumes ≤10 voxels (here each voxel is 1.42×10^{-6} mm^3) were excluded to remove the effect of digital noise in reconstructed data from the analysis. At this stage in total there were 4142 oil clusters with volumes >10 voxels. Figure 4.15B shows the oil labels with volumes > 10^6 voxels (1.42 mm^3). The very large label rendered in yellow colour (volume: 9.4×10^7 voxels, 133.86 mm^3) is a single well-connected oil cluster with 76% of the total oil volume.

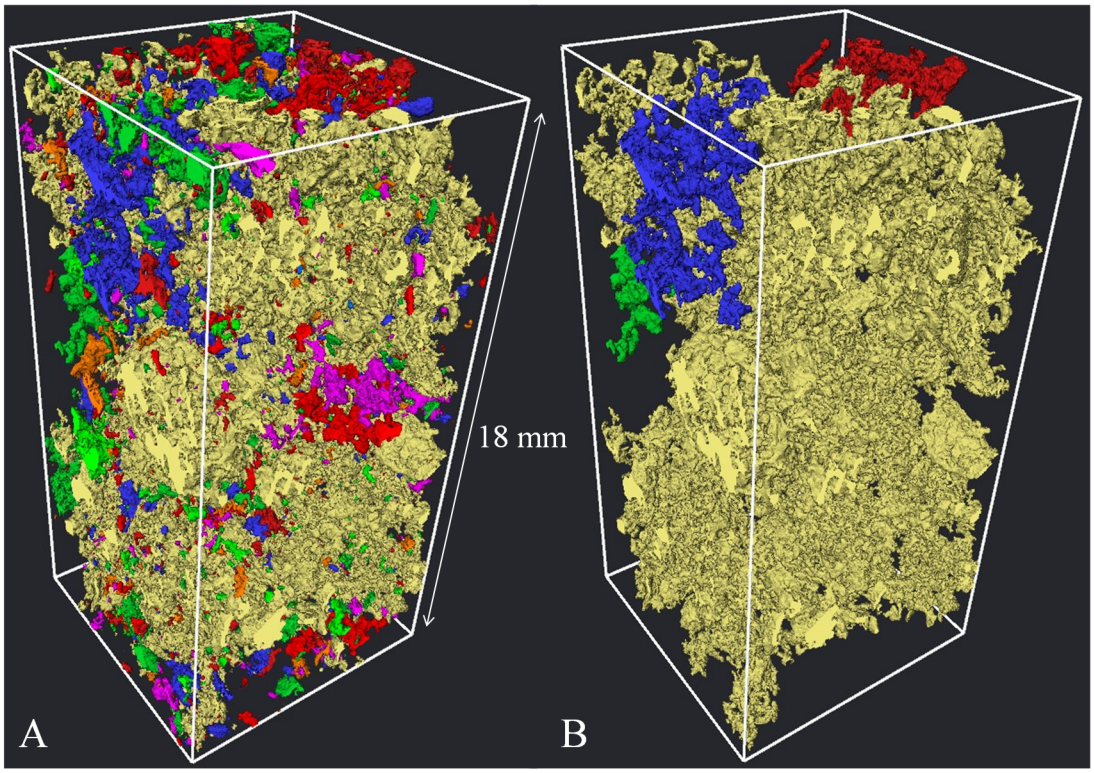

Figure 4.15: 3D rendering of the labelled oil clusters after the capillary-dominated drainage, displaying clusters with volumes > 10 voxels (1.42×10^{-5} mm^3) (A), and clusters with volumes > 10^6 voxels (1.42 mm^3) (B). The yellow cluster occupies 76% of the total oil volume, and spans over the analysed section.

This oil cluster spans over the entire length of the section analysed here and is therefore a percolating cluster over this section of the core. There are two possibilities for the remaining 25 % of the imaged oil saturation:

(1) The oil is connected in reality but the connections are below the image resolution, therefore the oil phase is represented by disconnected clusters. For comparison between the image resolutions and pore-throat size distributions see Figure 4.5.

(2) The oil is disconnected in reality. At each scanning step the fluid injection was stopped and the flow lines were disconnected from the core holder to allow 360 degrees rotation of the core plug during image acquisition. As a result some oil clusters may have experienced break-down at the very narrow pore throats as sketched in Figure 4.16. This type of cluster break-down is a limitation of

the method used here. In experiments conducted at synchrotron facilities images can be acquired by rotating the sample only 180 degrees, this along with the high speed of data acquisition achievable at synchrotron facilities allow imaging the fluid saturations during fluid injections, without having to stop the flow and disconnecting the lines.

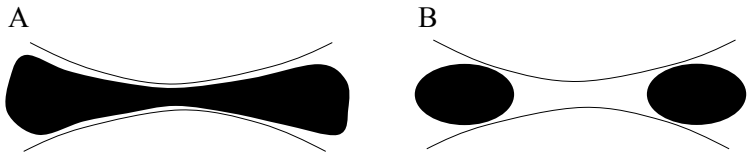

Figure 4.16: Oil clusters break-down at the narrow pore-throats that may occur after the flow cessation, (A and B) show the oil clusters under the flowing condition and snapped clusters after stopping the flow, respectively (Roof, 1970)

Table 4.1 lists the volume fraction of the "pores connected to the throats that are smaller than the image resolution" (of the acquired data in these experiments) for three SD core plugs, based on MICP pore-throat size distribution curves (chapter 3, section 1). The volume fraction of pores connected to throats smaller than 24 μm varies between ~75 to ~87 with an average value of 83% for these three SD core plugs. These percentages suggest that the imaged fluid phases captured on the 24 μm resolution images are significantly and unrealistically disconnected. Therefore it is not possible to study the connectivity of the oil phase based on the 24 μm resolution images.

Table 4.1: Volume fraction of the pores connected to the throats smaller than the image resolution of the present data sets, for three SD core plugs, based on MICP pore-throat size distribution curves (chapter 3, section 1) Images with 11.25 μm resolution can capture ~69% of the connections in SD.

Image Voxel Resolution (μm)	11.25	24
SD1	41.39	86.98
SD2	27.42	74.99
SD3	26.16	87.03
Average	31.66	83.00

The percentage of pores connected to throats smaller than the 11.25 μm varies between ~26 and ~41 with an average of ~31% for these three SD core plugs. Moreover, the

largest oil cluster captured in the 11.25 μm resolution images (after the capillary-dominated drainage) displayed connectivity of 64.5 % of the pore space at this resolution (76% of the oil saturation, the cluster rendered in yellow on Figure 4.15). On this basis the high resolution images can be used to study the connectivity of the oil phase during the fluid displacement processes. Therefore, cluster analysis can be achieved by quantitative analysis of the labelled oil phase.

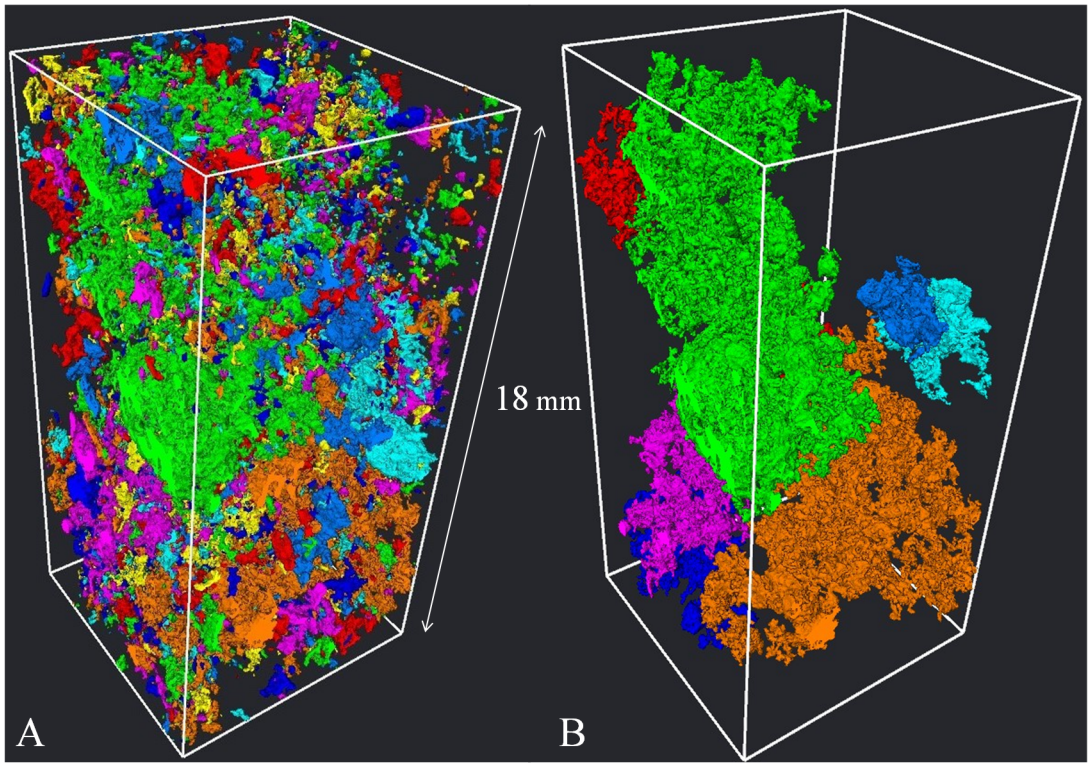

Figure 4.17: 3D rendering of the labelled oil clusters after the viscous-dominated oil injection stage, volumes > 10 voxels (1.42×10^{-5} mm^3) (A), volumes > 10^6 voxels (1.42 mm^3) (B). Fluid redistribution has caused a significant oil cluster break-down.

Figure 4.17A shows the oil clusters with volumes > 10 voxels after the viscous-dominated drainage. The largest oil clusters with volumes > 10^6 voxels (1.42 mm^3) are rendered in Figure 4.17B. It is clear that the fluid redistribution has caused the largest cluster of oil in Figure 4.15 to break down to smaller ones. This is consistent with observations reported in Berg et al. (2014). The volume of the largest oil cluster (shown in green on Figure 4.17B) is 22.35 % of the total remaining oil volume. The total number of oil clusters has almost doubled as a result of the fluid redistributions

(increased from 4562 to 8922), and the remaining oil is significantly less connected, although large connected clusters spanning many individual pores do remain. Figures 4.18 and 4.19 plot normalised cumulative oil saturation as well as the frequency of oil clusters against the oil cluster volumes (voxels) for the two drainage steps. These plots demonstrate the oil phase is broken down into smaller clusters as a result of the viscous-dominated drainage followed by the redistribution.

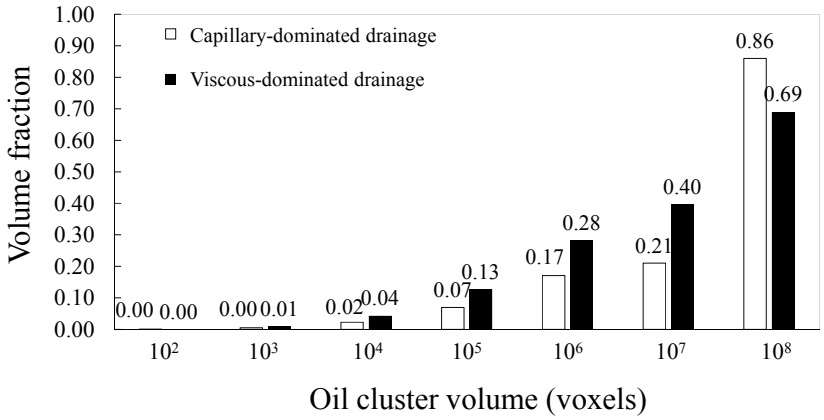

Figure 4.18: Oil clusters volume fraction vs oil cluster volumes (voxels) for the two drainage steps. The sharp increase in the distributions for the capillary-dominated drainage corresponds to the large connected oil cluster, rendered in yellow in Figure 4.15.

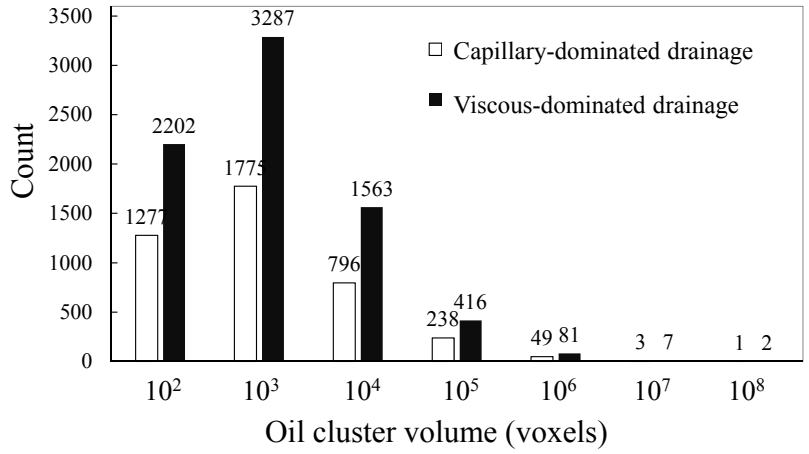

Figure 4.19: Frequency of oil clusters vs oil cluster volumes (voxels) for the two oil injection steps. There are significantly more number of oil clusters in the core plug as a result of the redistribution.

5. Summary

This chapter describes μCT observations of drainage processes in a water-wet carbonate rock, at core-scale. The analysis of core-scale processes occurred during imbibition steps are discussed in chapter 5. Literature suggests that the cluster-size distributions of the organic and aqueous phases in porous media, directly extracted from the pore-scale imaging, can provide insight into the wetting preference of the system. In consistent with the literature this chapter demonstrates that the analysis of the pore-size distribution occupied by oil and brine clusters can act as an indicative of the wettability of the rock. For the presented experiments, as a result of the drainage processes the smaller pores have remained brine saturated while the larger and medium-size pores are occupied by the invading oil phase. This along with the observation of capillary end effect for the brine phase implies that the rock is preferentially water-wet.

In the presented study, under capillary dominated flow regime, which is the typical flow regime in hydrocarbon reservoirs, the brine phase accumulated close to the production face of the core plug. The accumulated brine phase was produced immediately after the oil was injected under viscous regime. This is consistent with the capillary end effect which is a common experimental artifact in core-flooding experiments. More specifically the boundary effects cause errors on fluid saturation calculations. Mitigating the boundary effects by using longer cores is a common practice in most core-analysis laboratories. Alternatively, porous end pieces are placed at the core boundaries to shift the end effect out of the media under investigation. The presented data indicates that the small core plugs commonly used in μCT studies are prone to be completely under the influence of capillary boundary effect. This may result in an overestimation of the wetting phase saturation. The presented data demonstrates that it is essential to use longer core plugs and exclude the boundary affected part of the porous media from the calculations.

Another observation was the fluid re-arrangements probably caused by capillary forces acting at pore-scale that changed the fluid distributions at core-scale. The oil saturation displayed a decrease of 24 % over 18 mm central section of the core plug. The fluid

redistributions also resulted in break-down of the oil clusters into smaller ones. This can be caused by brine imbibition into smaller pores and oil snap-off over the narrower pore throats. The effect is an artifact of the test procedure used and is caused by the extensive scanning time of the utilised laboratory-based μCT scanner.

References

AL-RAOUSH, R. I. 2009. Impact of Wettability on Pore-Scale Characteristics of Residual Nonaqueous Phase Liquids. *Environmental Science & Technology,* 43**,** 4796-4801.

ANDREW, M., BIJELJIC, B. & BLUNT, M. J. 2014. Pore-scale imaging of trapped supercritical carbon dioxide in sandstones and carbonates. *International Journal of Greenhouse Gas Control,* 22**,** 1-14.

BEAR, J. 1972. *Dynamics of Fluids in Porous Media,* New York, Elsevier.

BERG, S., ARMSTRONG, R., GEORGIADIS, A., OTT, H., SCHWING, A., NEITELER, R., BRUSSEE, N., MAKURAT, A., RÜCKER, M. & LEU, L. 2014. ONSET OF OIL MOBILIZATION AND NON-WETTIGNG PHASE CLUSTER SIZE DISTRIBUTION. *SCA2014-022*.

BLUNT, M. J. & SCHER, H. 1995. Pore-level modeling of wetting. *Physical Review E,* 52**,** 6387-6403.

CHANG, Y., MOHANTY, K., HUANG, D. & HONARPOUR, M. 1997. The impact of wettability and core-scale heterogeneities on relative permeability. *Journal of Petroleum Science and Engineering,* 18**,** 1-19.

CLAUSET, A., SHALIZI, C. R. & NEWMAN, M. E. 2009. Power-law distributions in empirical data. *SIAM review,* 51**,** 661-703.

IGLAUER, S., FAVRETTO, S., SPINELLI, G., SCHENA, G. & BLUNT, M. J. 2010. X-ray tomography measurements of power-law cluster size distributions for the nonwetting phase in sandstones. *Physical Review E,* 82**,** 056315.

IGLAUER, S., FERNØ, M., SHEARING, P. & BLUNT, M. 2012. Comparison of residual oil cluster size distribution, morphology and saturation in oil-wet and water-wet sandstone. *Journal of Colloid and Interface Science,* 375**,** 187-192.

IGLAUER, S., PALUSZNY, A., PENTLAND, C. H. & BLUNT, M. J. 2011. Residual CO_2 imaged with X-ray micro-tomography. *Geophysical Research Letters,* 38**,** L21403.

JIANG, Z., VAN DIJKE, M., WU, K., COUPLES, G., SORBIE, K. & MA, J. 2012. Stochastic pore network generation from 3D rock images. *Transport in Porous Media,* 94**,** 571-593.

KARPYN, Z. T., PIRI, M. & SINGH, G. 2010. Experimental investigation of trapped oil clusters in a water-wet bead pack using X-ray microtomography. *Water Resources Research,* 46.

KUMAR, M., SOK, R., KNACKSTEDT, M. A., LATHAM, S., SENDEN, T. J., SHEPPARD, A. P., VARSLOT, T. & ARNS, C. Mapping fluid distributions in 3D at the pore scale: Quantifying the influence of wettability and saturation history on rock resistivity. SPWLA 50th Annual Logging Symposium, 2009. Society of Petrophysicists and Well-Log Analysts.

LANDRY, C., KARPYN, Z. & PIRI, M. 2011. Pore-scale analysis of trapped immiscible fluid structures and fluid interfacial areas in oil-wet and water-wet bead packs. *Geofluids,* 11**,** 209-227.

LORENZ, C. D. & ZIFF, R. M. 1998. Precise determination of the bond percolation thresholds and finite-size scaling corrections for the sc, fcc, and bcc lattices. *Physical Review E,* 57**,** 230-236.

O'MEARA JR, D. J. & VINEGAR, H. J. 1990. Method for determining capillary pressure and relative permeability by imaging. Google Patents.

ROOF, J. G. 1970. Snap-Off of Oil Droplets in Water-Wet Pores.

SAHIMI, M. 1994. *Applications of percolation theory*, CRC Press.

STAUFFER, D. 1979. Scaling theory of percolation clusters. *Physics reports,* 54**,** 1-74.
STRENSKI, P. N., BRADLEY, R. M. & DEBIERRE, J.-M. 1991. Scaling behavior of percolation surfaces in three dimensions. *Physical Review Letters,* 66**,** 1330-1333.
VINEGAR, H. J. & WELLINGTON, S. L. 1987. Method of analyzing fluid saturation using computerized axial tomography. Google Patents.
WILKINSON, D. 1986. Percolation effects in immiscible displacement. *Physical Review A,* 34**,** 1380-1391.
WILKINSON, D. & WILLEMSEN, J. F. 1983. Invasion percolation: a new form of percolation theory. *Journal of Physics A: Mathematical and General,* 16**,** 3365.
YOUNG, T. 1805. An essay on the cohesion of fluids. *Philosophical Transactions of the Royal Society of London***,** 65-87.

Chapter 5

Pore-Scale Fluid Displacement Mechanisms

As outlined in Table 2.1, most studies that monitored fluid displacement in porous media using μCT techniques have used homogeneous samples such as sintered glass samples, bead packs, sand packs, and sandstones. Homogeneous porous media are easier to sample, characterise, and study. A limited number of μCT imaging studies performed on carbonate rocks, mainly due to the technical challenges involved in (a) selecting a representative sample, and (b) reliably imaging their broad range of porosity with the limited achievable resolutions of the existing tomography instruments (Andrew et al., 2013, Andrew et al., 2014).

This chapter presents a pore-level investigation of fluid displacement mechanisms in a complex carbonate system. 3D visualisation of pore-scale fluid mechanisms during capillary and viscous dominated drainage and imbibition processes are presented. The observed displacement processes include piston-like displacement, snap-off, and a new pore-scale event termed as "droplet fragmentation". This new pore-scale mechanism may offer an explanation to the capillary desaturation phenomena (more details are provided in section 2).

1. Pore-scale Observation of Immiscible Fluid Displacement Mechanisms in a Carbonate Rock

1.1. Primary Drainage - Piston-Like Displacement

Figure 5.1 shows exemplary μCT slices captured after the drainage and imbibition. The initial saturation state with the brine phase is shown in Figure 5.2A. Figure 5.2B and 2C are from the data acquired after capillary and viscous-dominated drainage steps, respectively. Although these images do not show brine films in the corners of the pores after primary drainage, it is likely that brine films were masked by a partial volume or contrast effect which is a common artifact in μCT images (chapter 2, section 5.2). The thickness of the wetting films is typically few micro-meters (Blunt, 2001) which could not be resolved in the images acquired in this study. However, upon re-injection of the brine phase into the plug with q=10 μl/min the thickness of the brine films increased such that they became resolvable on the images captured after this injection step (Figure 5.3D). Although injections had to be stopped for image acquisitions (i.e. the images were not visualised in real time), the observed sequence of fluid occupancy in the pore space are consistent with piston-like

displacement mechanism. The development of the wetting film as well as the brine-oil contact angles θ_{ow} depicted in Figures 5.1D and 2D suggest that the rock is water-wet (see chapter 6, section 3 for further discussion).

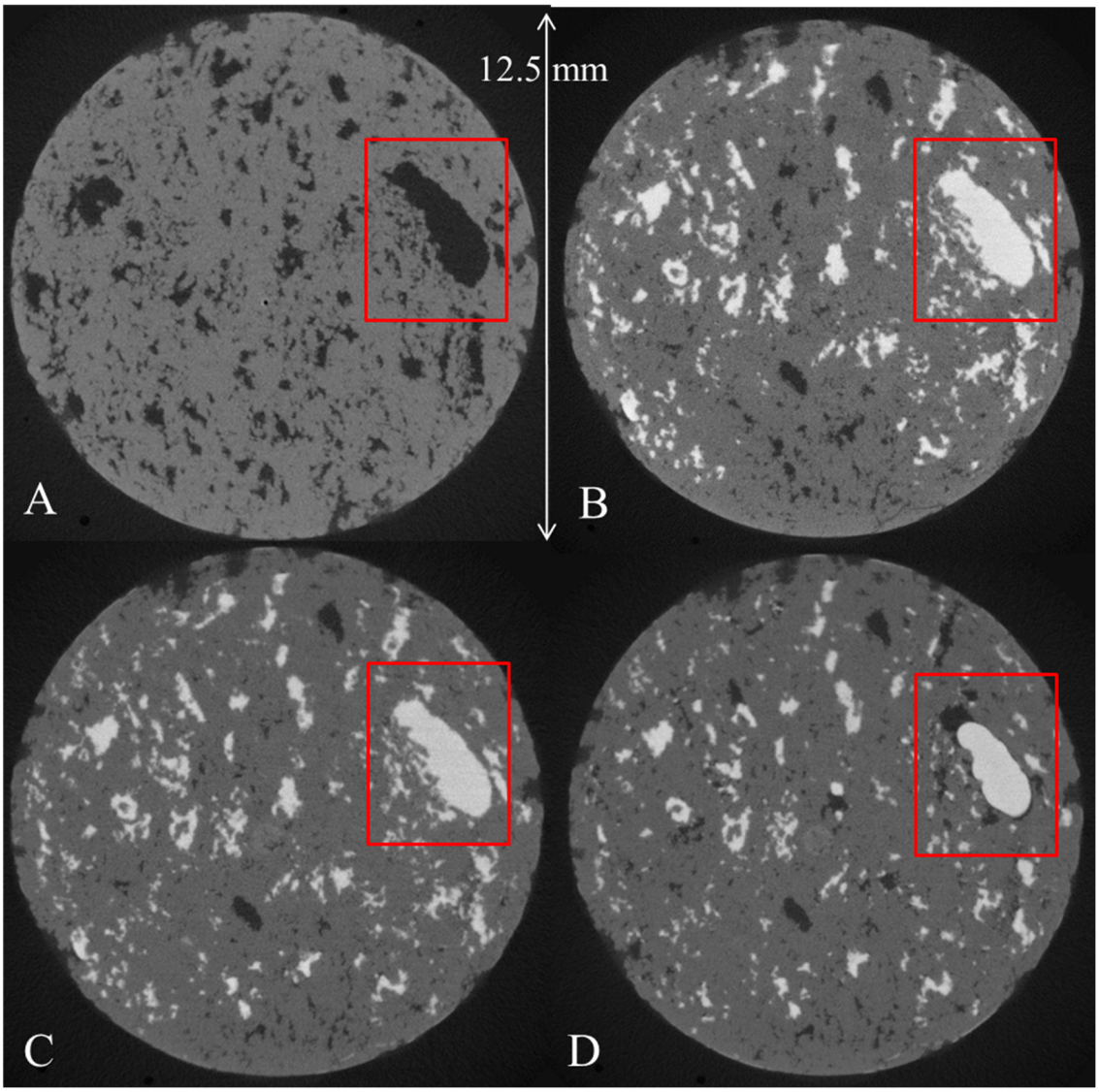

Figure 5.1: Pore-scale displacement events observed in one exemplary slice of the 3D images captured after initial brine saturation (A), capillary-dominated drainage (B), viscous-dominated drainage (C), and capillary-dominated imbibition (D). Black, white, and grey phases are brine and oil, and rock, respectively. The observed sequence of fluid saturations is consistent with piston-like displacement. A magnification of the area denoted by the red box is shown in Figure 5.2.

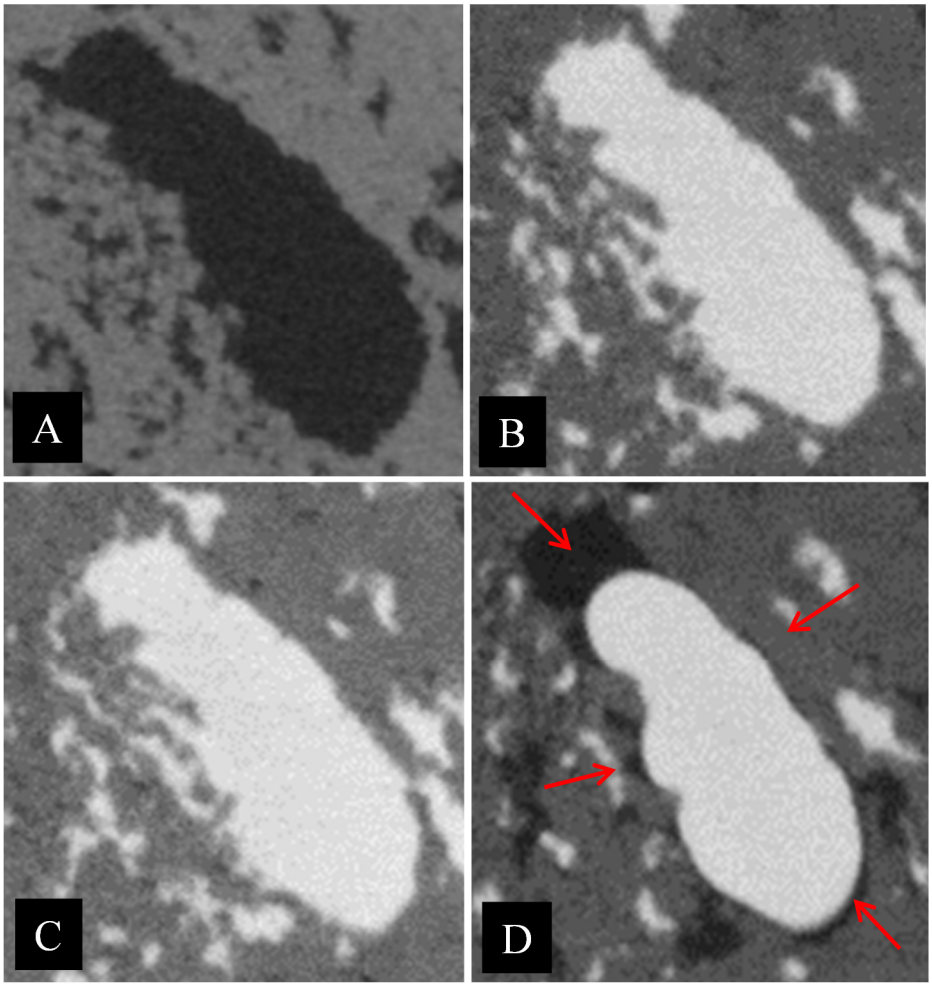

Figure 5.2: Magnified area marked by the red box in Figure 5.1. The development of the wetting film as well as the brine-oil contact angles θ_{ow} in (D) suggest that the rock is water-wet. Black, white, and grey phases are brine and oil, and rock, respectively. The red arrows indicate a visible brine films surrounding an oil droplet.

1.2. Capillary-Dominated Imbibition - Snap-off

Figures 5.1B, 5.1C, 5.2B, and 5.2C show an example of a well-connected oil cluster that occupies a large pore but is also connected to many adjacent pores after the primary drainage. Capillary-dominated imbibition resulted in swelling of the brine corner films and eventually caused snap-off of an oil droplet from the connected oil cluster (Figure 5.2D). Figure 5.3 shows 3D renderings of the oil phase before and after the snap-off event has occurred. The pore in Figure 5.3 is the same as the pore in Figure 5.2. The 3D view clearly demonstrates that the oil cluster is connected to its neighbouring pores at the end of primary drainage. The snap-off event resulted in an

isolated oil droplet that is no longer connected to its neighbouring pores. The established brine films in this pore and the adjacent ones provides a pathway to the flowing brine phase during imbibition. The trapped oil droplet causes resistance to the flow by narrowing down the available flow-path. The oil-brine configuration shown in Figure 5.3B, i.e. an isolated oil droplet surrounded by brine films, was captured after the injection of more than 10 pore volumes of brine under capillary-controlled regime. The configuration displayed stability during the data acquisition time and for a further 24 hours during which two separate scans were acquired. This stability along with the length of the brine imbibition indicate that the recovery of such trapped oil droplet is difficult under capillary-dominated imbibition.

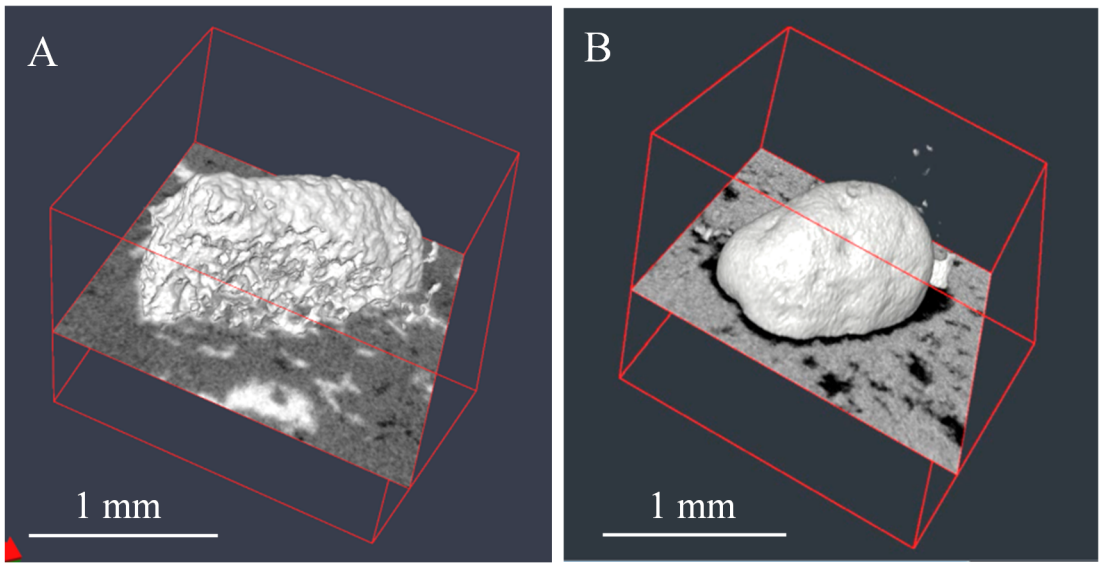

Figure 5.3: 3D renderings of the oil phase after viscous-dominated drainage (A), and capillary-dominated imbibition (B). The isolated droplet of oil trapped under capillary forces was caused by a snap-off event. Black, white, and grey phases are brine and oil, and rock, respectively.

Figure 5.4 shows another example of a snap-off event. A connected cluster of oil is shown to occupy a network of connected neighbouring pores after the drainage steps (Figure 5.4A). Figure 5.4C shows 3D rendering of the labelled oil cluster. The cluster is rendered in one colour since it is a connected structure, and hence a single label was assigned to the entire oil phase occupying these neighbouring pores. In this image the complex structure of the oil phase indicates the complexity of the pore structure of this set of neighbouring pores in 3D.

After the capillary-dominated imbibition, the pore space contains disconnected droplets of oil while the corners of the pore and the pore-throats are occupied by the brine phase (Figure 5.4B). The disconnected oil droplets are assigned individual labels, and hence rendered in different colours in 3D, Figure 5.4D.

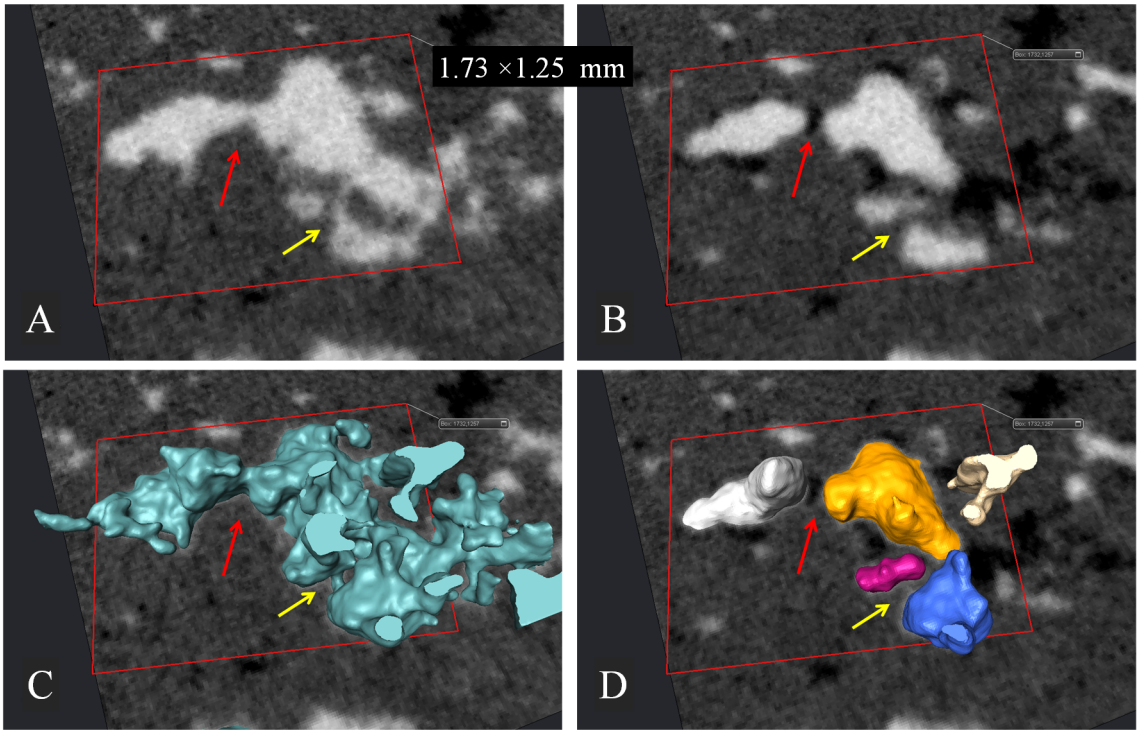

Figure 5.4: An example of snap-off event. A connected cluster of oil occupies a network of connected neighbouring pores after drainage steps (A). A set of disconnected oil droplets occupying the same pores after the capillary-dominated imbibition (B). The pore-throats and pore corners are occupied by the brine phase. Black, white, and grey phases are brine and oil, and rock, respectively. (C and D) show 3D rendering of labelled oil phase at (A and B). Each individual label is rendered in a different colour. The arrows indicate the oil connections at pore-throats that are broken as a result of snap-off events.

1.3. Discussion

Image analysis of our data shows that 69% and 54% of the pore space of the studied section of the core contained oil phase, after the viscous-dominated drainage and capillary-dominated imbibition, respectively. Therefore, 15% oil was produced during slow imbibition. Literature suggests that the competition between the different pore-scale events, in particular piston-like displacement and snap-off, controls the microscopic sweep efficiency and hence the residual oil saturation during the water

flooding process. Experimental and modelling studies suggest that this interplay is mainly governed by the following processes (Mogensen and Stenby, 1998, Yu and Wardlaw, 1986, Jerauld and Salter, 1990, Al-Gharbi and Blunt, 2005, Nguyen et al., 2006):

- The flow regime: Using dynamic pore network modelling approach Nguyen et al. (2006) studied the impact of flow regimes (with N_C spanning over several orders of magnitude) on the frequency of the pore-scale events. They demonstrated that an increase in capillary number causes the number of snap-off events to decrease. This is because there is insufficient time for swelling of wetting films to develop.
- Wettability of the rock: More snap-off events take place in strongly water-wet rocks compared to weakly-water wet rocks because snap-off events are in competition with piston-like displacement in weakly water-wet rock. Hence trapping caused by snap-off events is reduced (Zhou et al., 2010). In their experimental study Yu and Wardlaw (1986) reported that snap-off was completely absent for micro-models with contact angles above 70°.
- The distribution of pore aspect ratios and coordination numbers: The aspect ratio is defined as the ratio between pore-size and pore-throat size. It has been observed that the probability of snap-off event and hence the amount of trapped non-wetting phase correlates directly to the aspect ratio and is inversely proportional to the coordination number (Yu and Wardlaw, 1986, Jerauld and Salter, 1990, Tanino and Blunt, 2012). Figure 5.5 shows the effect of aspect ratio on snap-off event: The smaller the aspect ratio ($\frac{r_2}{r_1} < \frac{r_3}{r_4}$), the larger the chance that the oil phase is displaced by water through piston-like displacement. On the other hand, snap-off can trap the oil phase more readily in the pores with higher aspect ratios.

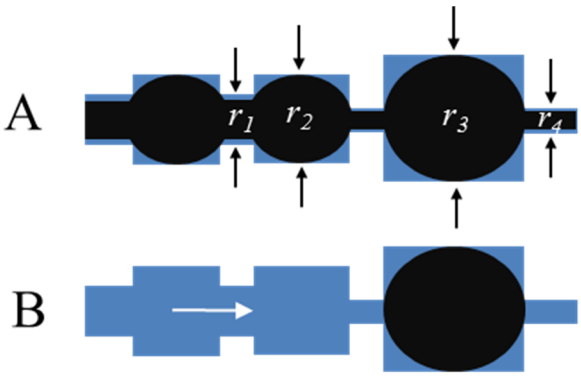

Figure 5.5: The cartoon shows the effect of pore aspect ratio on snap-off. The capillaries are water-wet. Black and blue colours indicate oil and water, respectively. (A) Shows the oil-water configurations when the capillaries are saturated by the two phases, with established water phase in the capillary corners, and (B) shows water imbibition in the capillaries, the oil phase is displaced piston-likely from the lower aspect ratio pores, while snap-off has trapped the oil in the pore with the higher aspect ratio.

Figures 5.6 to 5.9 show exemplary µCT slices in the main direction of fluid flow after the viscous-dominated drainage and capillary-dominated imbibition. Red and yellow arrows indicate the pores in which snap-off events and piston-like displacements have occurred, respectively. Due to resolution limitations, the pore-throat size distribution could not be quantified. However, form visual inspections, snap-off is observed in pores between 0.4 and 2.75 mm side length in the 2D slices. In particular snap-off occurs in medium-sized and large pores which have the highest aspect ratios. The blue arrows highlight the pores which remained oil saturated after brine injection. These may be parts of by-passed oil clusters that are locally connected but only over a limited number of neighbouring pores, i.e. they do not form clusters that span the entire length of the sample.

A trapped oil droplet can have much smaller volume compared to the pore confining it, an example is the pore with side length of 1.4 mm in Figure 5.6, the oil droplet appears to be much smaller than the pore it partially occupies, but it has remained trapped inside the pore. The likely reason why such small droplets are trapped is because they are much larger than the neighbouring pore-throats. In addition, the surface roughness can assist trapping the oil droplets. However, in most cases, the

trapped droplets are of similar size to the pore confining them and are surrounded by a thin brine film.

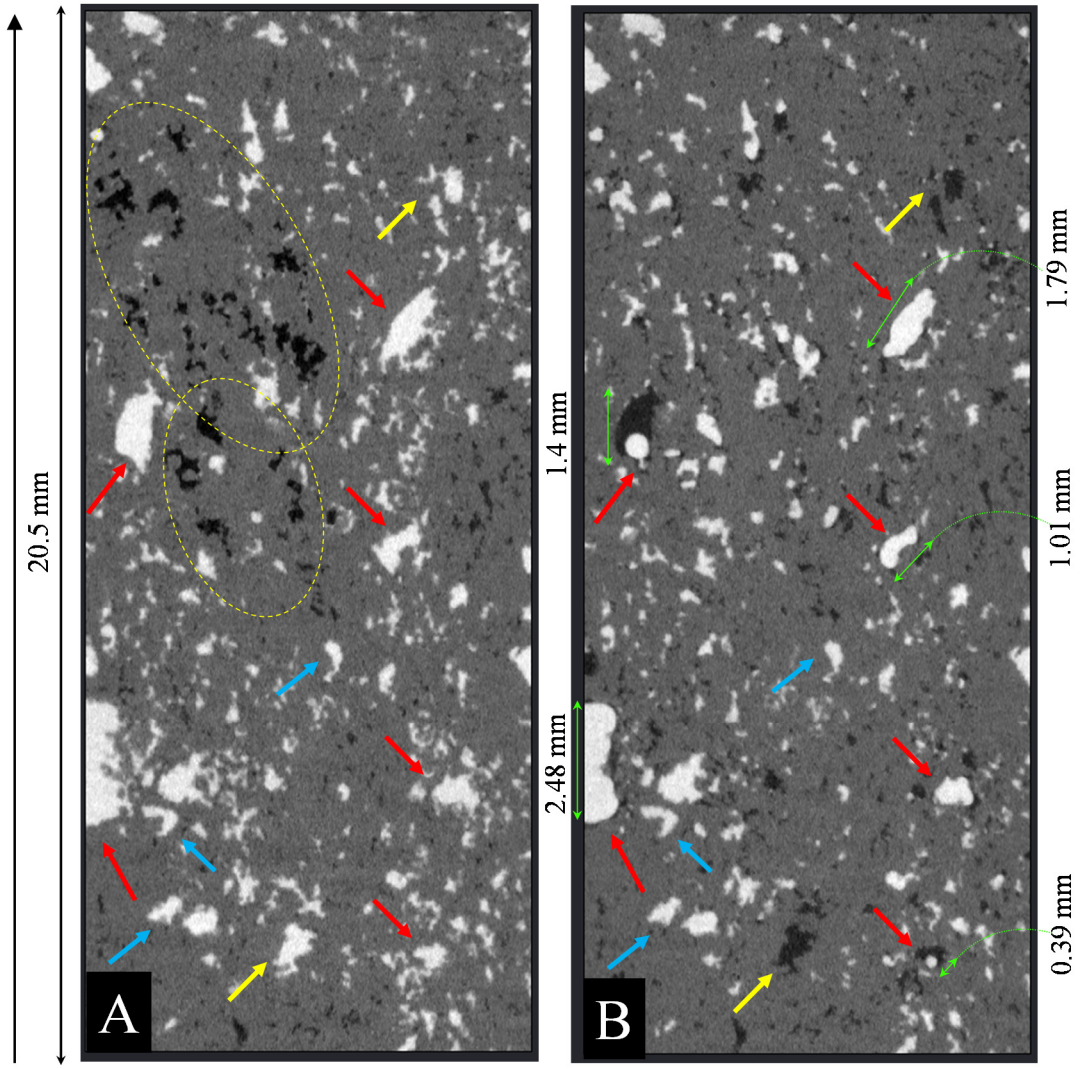

Figure 5.6: Exemplary 2D µCT slices in the main flow direction (see black arrow) after viscous-dominated drainage (A) and capillary-dominated imbibition (B). Red and yellow arrows indicate the pores in which snap-off events and piston-like displacements have occurred, respectively. Blue arrows highlight the pores which remained oil saturated after brine injection. The dashed yellow ellipses indicate pores from which the oil has been displaced as a result of fluid redistribution viscous-dominated drainage.

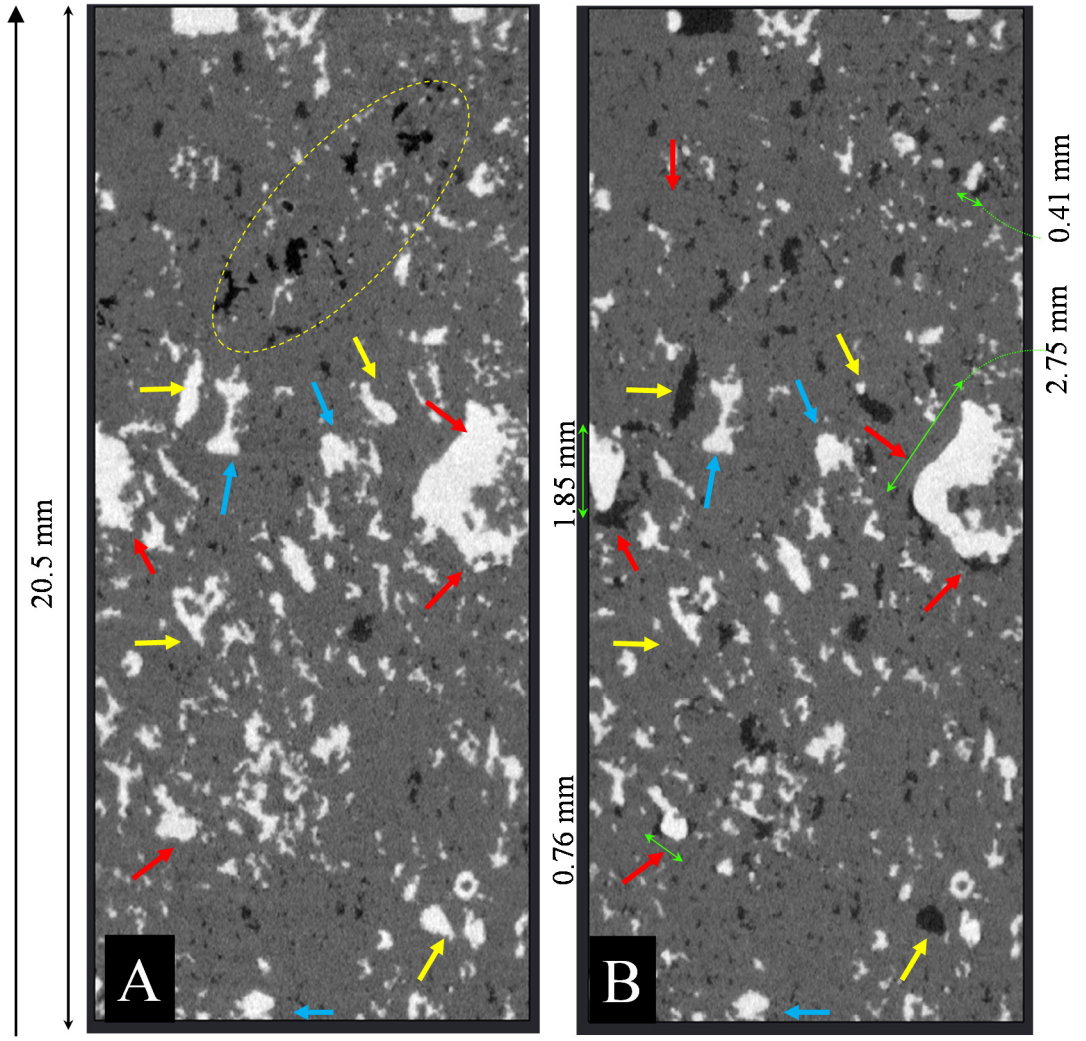

Figure 5.7: Exemplary 2D µCT slices in the main flow direction (see black arrow) after viscous-dominated drainage (A) and capillary-dominated imbibition (B). Red and yellow arrows indicate the pores in which snap-off events and piston-like displacements have occurred, respectively. Blue arrows highlight the pores which remained oil saturated after brine injection. The dashed yellow ellipses indicate pores from which the oil has been displaced as a result of fluid redistribution viscous-dominated drainage.

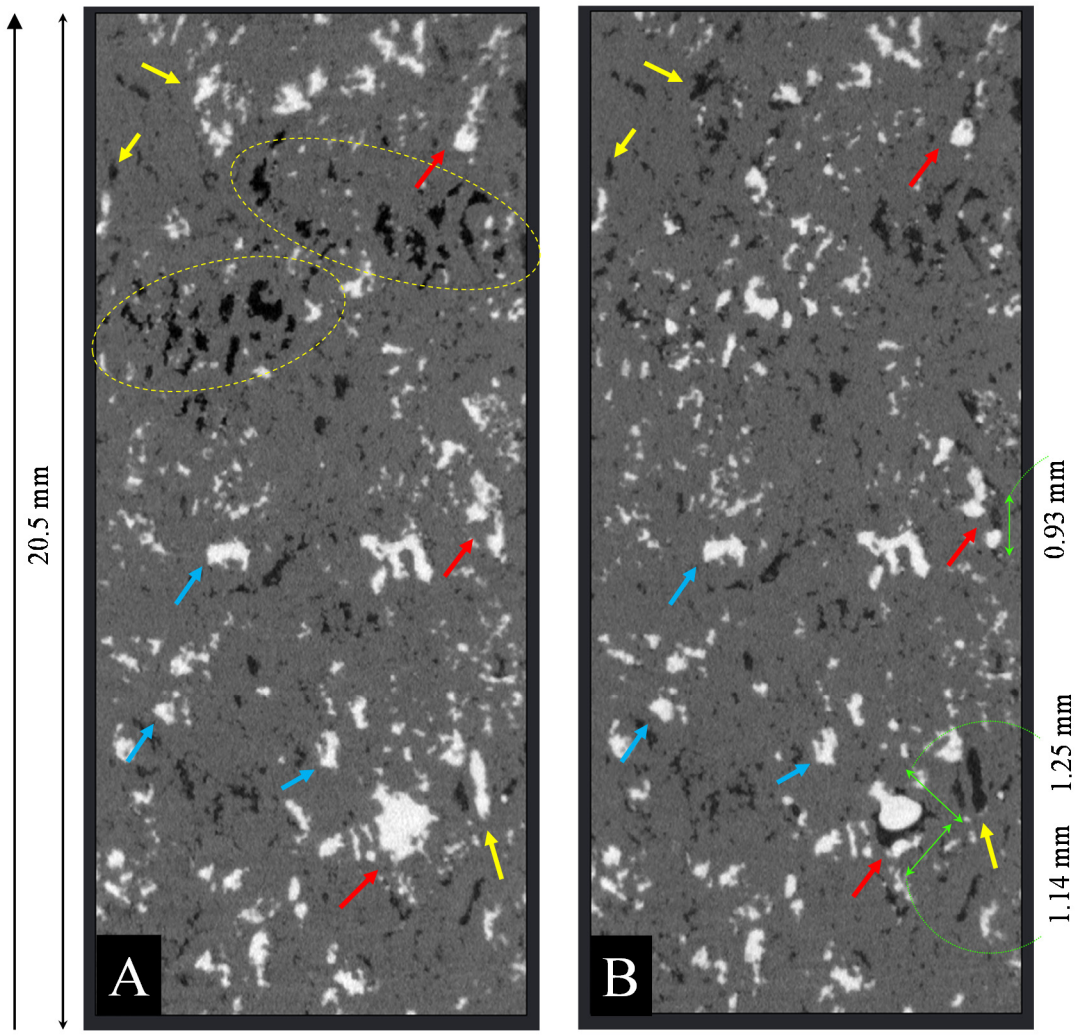

Figure 5.8: Exemplary 2D µCT slices in the main flow direction (see black arrow) after viscous-dominated drainage (A) and capillary-dominated imbibition (B). Red and yellow arrows indicate the pores in which snap-off events and piston-like displacements have occurred, respectively. Blue arrows highlight the pores which remained oil saturated after brine injection. The dashed yellow ellipses indicate pores from which the oil has been displaced as a result of fluid redistribution viscous-dominated drainage.

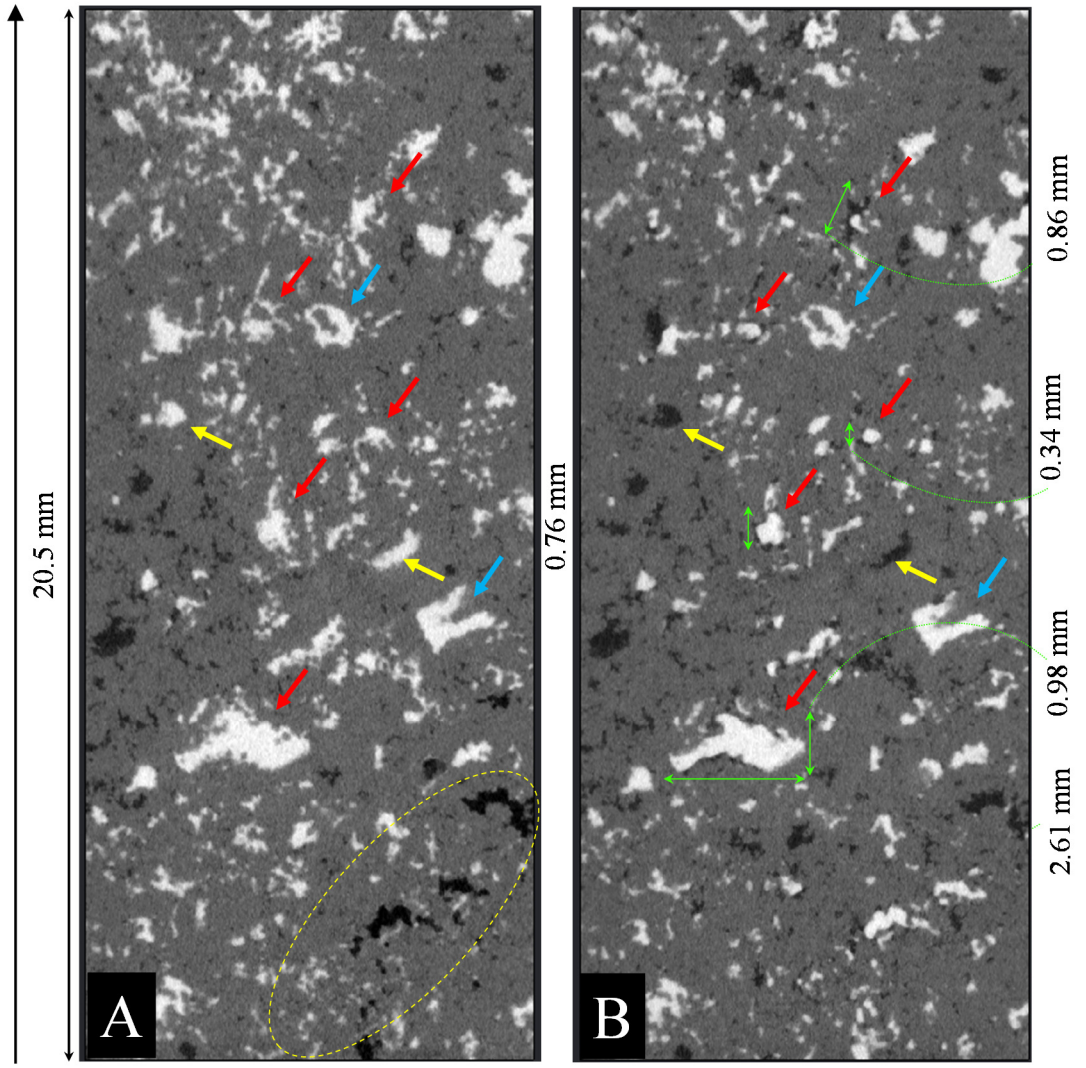

Figure 5.9: Exemplary 2D µCT slices in the main flow direction (see black arrow) after viscous-dominated drainage (A) and capillary-dominated imbibition (B). Red and yellow arrows indicate the pores in which snap-off events and piston-like displacements have occurred, respectively. Blue arrows highlight the pores which remained oil saturated after brine injection. The dashed yellow ellipses indicate pores from which the oil has been displaced as a result of fluid redistribution viscous-dominated drainage.

It should be noted that brine was injected only for 10 pore volumes. It hence may be possible that some connected oil clusters remained in the core that could have been produced if the brine injection would have been continued. Also in some places the brine films were not fully captured due to their limited thickness compared to the image resolution (Figures 5.6 to 5.9).

In pore network modelling simulations the population of the pores at which the two piston-like and snap-off displacements have happened is easily obtainable. In a pore network each element is individually identified, and all its characteristics are known (including its location, shape factor, volume, connecting pores, coordination number, aspect ratio and saturation state at each step of the displacement processes). Therefore, it is possible to track the changes in saturation state of each element throughout a fluid displacement process. Statistical analysis of the competition between the different pore-scale events can hence be derived easily (Blunt and Scher, 1995). However, individual identification of pores and throats on a μCT image of a rock saturated with multiple fluid phases is not readily achievable using the available image processing tools. For a pore that contains two or more fluid phases, the volume of each fluid phase may indicate the type of displacement process that occurred.

During piston-like displacement, almost entire volume of the pore is displaced by the invading phase. Only a small volume of the defending phase may remain in the pore. This volume can be in two different forms: (1) for drainage it is the wetting phase in form of films established in the corners of the pore, (2) for imbibition it is the non-wetting phase droplets that may be trapped by the surface roughness of the pore.

In contrast, when a snap-off event occurs, a significant volume of the pore remains occupied with the defending phase. Recall that in this imbibition process oil is the defending phase. Figures 5.10A and 5.10B show exemplary μCT slices before and after capillary-dominated imbibition, respectively. The yellow and red arrows indicate pores where piston-like displacement and snap-off events occurred, respectively. Figure, 5.10C was obtained by subtracting Figure 5.10A from Figure 5.10B. Figure 5.10C depicts the invaded brine phase, which corresponds to the displaced oil during imbibition. The comparison between the invading brine volume and the pore volume confining it may provide an insight in the type of pore-scale displacement events that has occurred,

$$S_{invading} = \frac{invading\ phase\ volume}{volume\ of\ the\ pore\ confing\ it}. \quad (5.1)$$

To classify the pore-scale event one can consider a cut-off "*a*" for the saturation of the invading phase, $S_{invading}$. Using the cut-off *a* the displacement events can be classified as follows:

- Snap-off event if $0 < S_{invading} < a$,
- Piston-like displacement if $S_{invading} > a$.

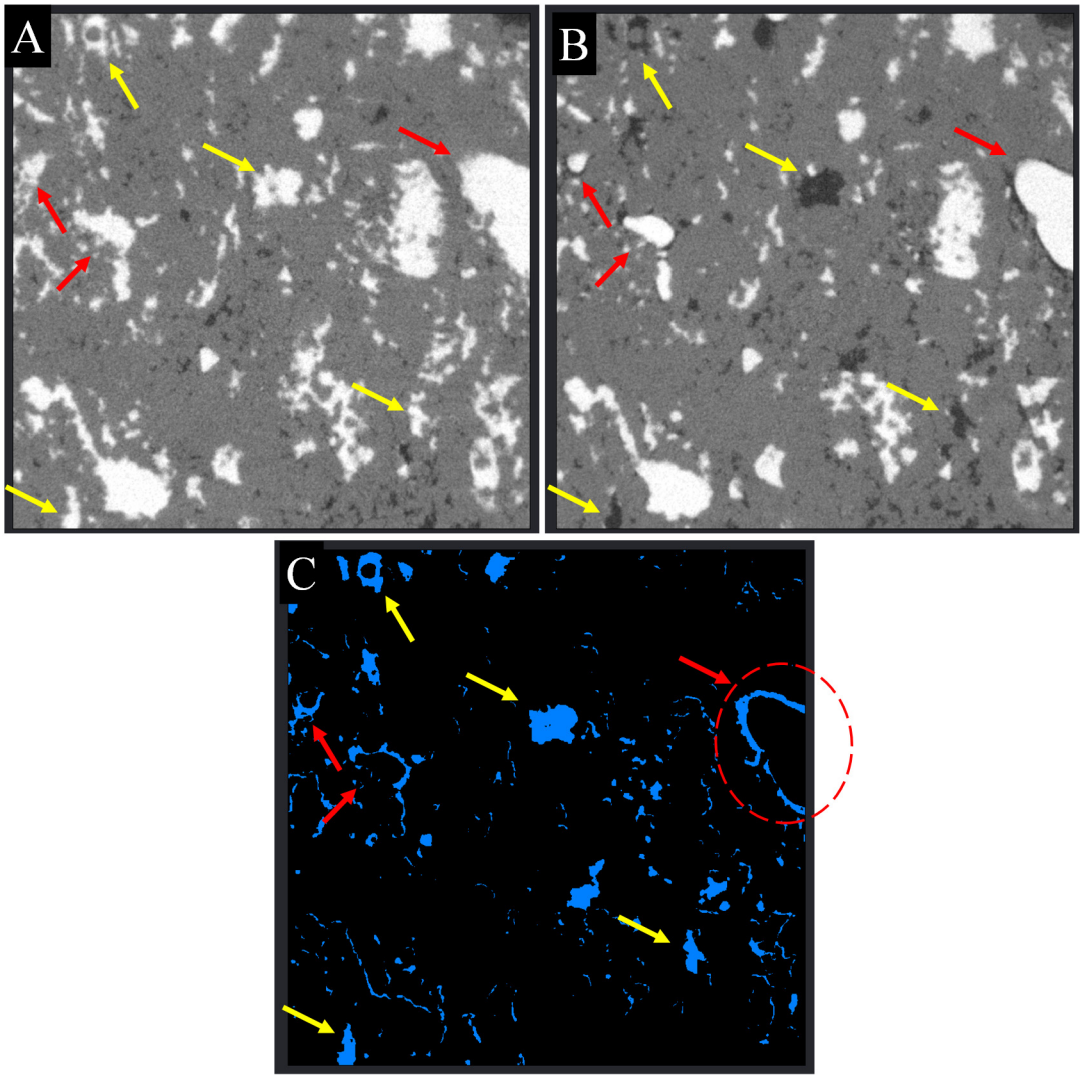

Figure 5.10: Attempts to classify the pore-scale displacement events using image analysis. Exemplary µCT slices before (A) and after (B) imbibition. (C) Shows the difference between B and A. Note that this difference was obtained by subtracting the image in (B) from the image in (A). Red and yellow arrows indicate the pores in which snap-off events and piston-like displacements have occurred, respectively. The dashed red ellipse shows an example hollow structure of the invaded brine phase (recovered oil).

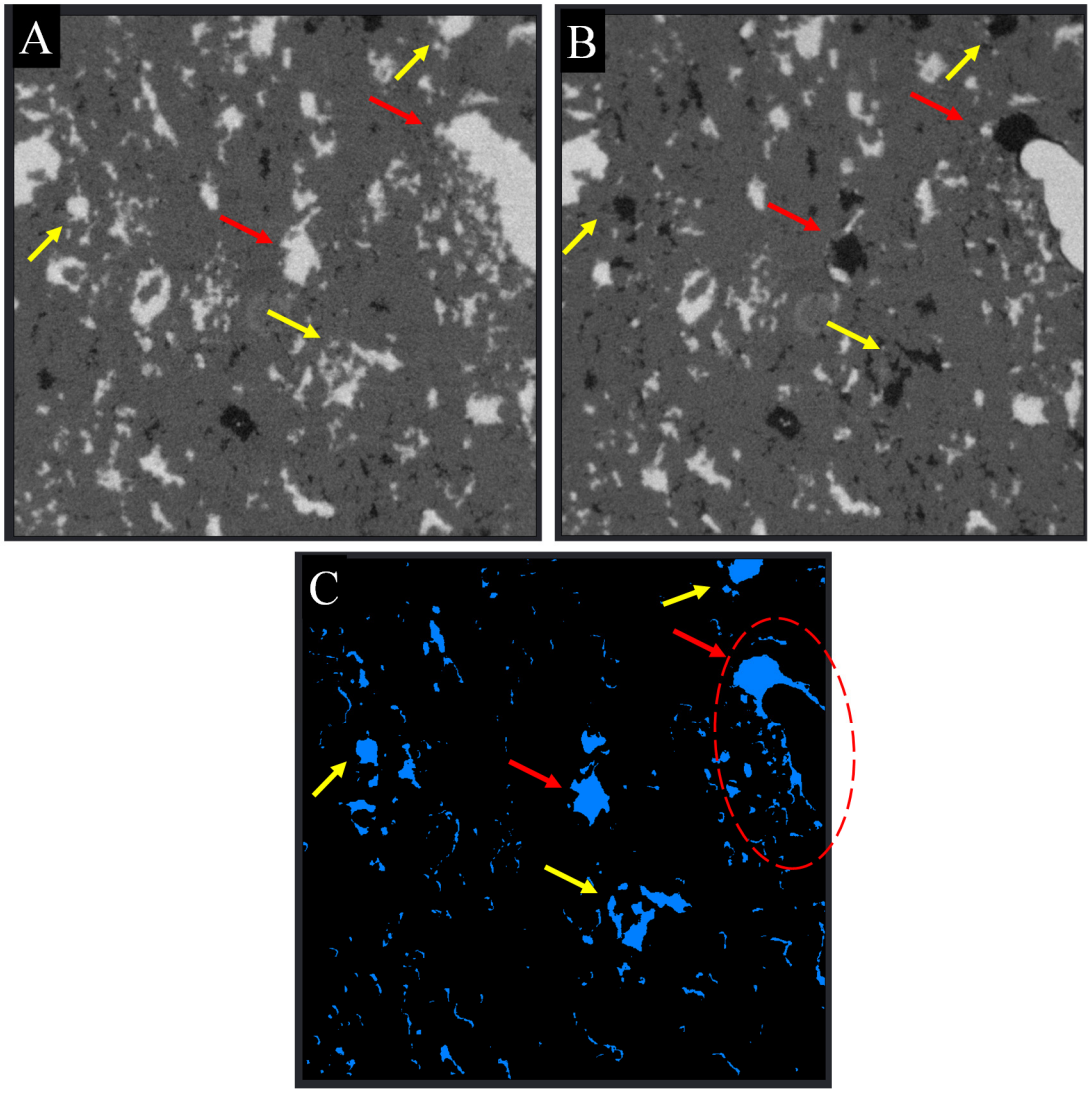

Figure 5.11: Classification of pore-scale displacement events. Exemplary µCT slices before (A) and after (B) imbibition. (C) Shows the difference between B and A. Note that this difference was obtained by subtraction the image in (B) from the image in (A). Red and yellow arrows indicate the pores in which snap-off events and piston-like displacements have occurred, respectively. The dashed red ellipse shows a hollow structure of the invaded brine phase (recovered oil).

The value of *a* can range from 0 to 1 but should normally be closer to 0 since only small fractions of oil volume are produced during snap-off event, i.e. the volume of the invaded brine films are small. In addition to the fluid volumes, the structure and shape of the invaded volume (recovered volume) provides valuable information about the displacement process that is likely to have occurred. For instance, if the

brine phase appears as a hollow structure (see the pore marked by the dashed red ellipse on Figures 5.10C and 11C), a snap-off event has probably occurred. Hollow structures can be identified by their shape factor, defined as the ratio of surface area to their volume. Hollow structures display larger shape factors compared to solid structures of the similar surface area, due to their smaller volumes. If the invaded brine phase has a shape that is similar to that of the pore, piston-like displacement has probably occurred (pores marked with red arrows on Figures 5.10 and 5.11). Such a shape analysis can be performed if the fluid phases can be identified individually as the volume and shape of each fluid phase needs to be compared to volume and shape of the pores that contain the phases.

In defining the threshold value, *a,* factors such as pore geometries, aspect ratio and coordination number should be considered. These factors determine the volume of the wetting films a pore can accommodate before a snap-off event occurs. An example analysis of the fluid occupancies in capillary ducts of rectangular cross-sections for snap-off and piston-like can be found in Lenormand et al. (1983). However, analytical calculation of *a* may prove difficult for heterogeneous pore system due to their broad range of properties (pore geometries, aspect ratio and coordination number). It may be possible to estimate the value of *a* from μCT images of multiple-phase saturated rocks using digital image-correlation techniques (Hild and Roux, 2012). Digital image-correlation provides the means to track and identify individual objects between different μCT images. This enables identification of pores and monitoring their fluid occupancy throughout the data set.

2. Capillary-desaturation- Remobilization of Trapped Oil Phase

2.1. Background

Numerous core flooding experiments reported a relationship between the flow regime and the remaining non-wetting phase (Morrow et al., 1982, Anton and Hilfer, 1999, Lake, 1989). It was observed that a trapped non-wetting phase is re-mobilised and recovered when the capillary number of injections exceeds a critical level ($N_C \sim 10^{-5}$). The effect is known as “capillary desaturation”. Direct pore-scale imaging

of this effect in natural pore space of carbonate rocks is not addressed in the literature.

In order to remobilise a trapped cluster of a non-wetting phase, the viscous shear force applied on the surface of the cluster needs to overcome the capillary forces (Ng et al., 1978). The remobilisation of the trapped non-wetting phase starts when the capillary number of the flow exceeds a critical level (Nc_{crit}). Capillary desaturation curves plot the capillary number against the residual saturations of the wetting ($S_{w,r}$) and non-wetting phases ($S_{nw,r}$). Figure 5.12 shows such a set of exemplary capillary desaturation curves. The curves are plotted based on results of numerous laboratory experiments performed where one fluid phase displaced another one in core plugs (Stegemeier, 1977, Lake, 1989, Morrow et al., 1982, Chatzis et al., 1988).

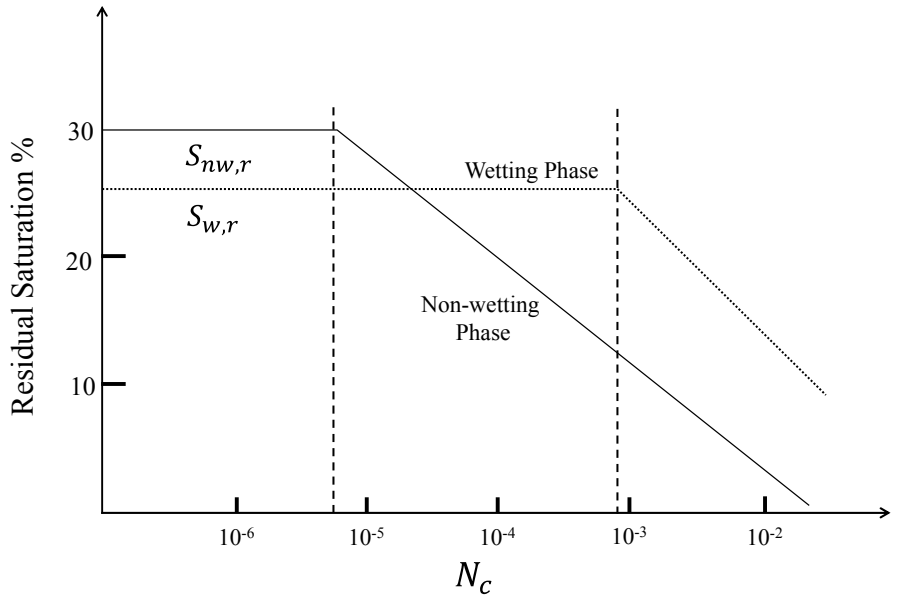

Figure 5.12: Exemplary capillary desaturation curves for the residual saturations for the wetting ($S_{w,r}$) and non-wetting phase ($S_{nw,r}$). The residual saturations decrease when the capillary number exceeds a critical level. After Lake (1989).

Many core floods measured an increase in non-wetting phase recovery by passing the effluent fluid volumes through a separation unit and measuring the total oil volume that was produced. Among the earliest attempts to study the structure of the trapped oil phase in pore space of real rocks was the study by Chatzis et al. (1988). Oil phase

trapping was established by saturating sandstone plugs with a styrene monomer and allowing brine to imbibe under different capillary numbers, ranging from 8.1×10^{-7} to 6.9×10^{-4}. The oil phase was solidified in the pore space using a polymerisation method before the rock was dissolved with hydrofluoric acid. Hence, the trapped oil could be recovered in a solid state. The resulting experimental data showed that capillary desaturation started at $Nc_{crit}\sim1.9\times10^{-5}$. A detailed statistical analysis of the shape and size of the trapped oil clusters revealed that some oil phase clusters had volumes that were smaller than the average pore volume of the sandstone. Overall, the experimental data of Chatzis et al. (1988) showed a weak correlation between the trapped oil cluster sizes and the capillary number. However, this lack of clear correlation may be due to the fact that, because the rock was dissolved, information about the geometry and structure of the pores that contained the trapped non-wetting phase was absent.

At reservoir-scale natural flow occurs at capillary numbers of approximately $\sim10^{-7}$ (Ng et al., 1978). In order to mobilise the trapped oil, the capillary number needs to increase until it becomes larger than the critical capillary number. Increasing the N_c can be achieved by either increasing the viscous forces (e.g. by increasing the injection rate), or by reducing the capillary forces by decreasing the interfacial tension (e.g. by injecting surfactants).

Experimental studies have demonstrated that the critical capillary number depends on the structure of the pore space, in particular the distributions of pore and pore-throat radius. Morrow et al. (1988) reported different critical capillary numbers for different pore structures including bead-packs and sandstones. They reported that, for bead packs and sandstones the onset of capillary desaturation occurs at $Nc_{crit}\sim10^{-3}$ and 10^{-5}, respectively.

In the classical formulation of the capillary number, $N_C=\mu v/\sigma$, the capillary number is implicitly linked to the pore structure through the velocity. The value of velocity used here is the average velocity at core-scale. The velocity, however, varies at pore-scale, especially for the heterogeneous pore-structures. Therefore, the N_c can be variable at pore-scale. Several attempts have been made to derive a dimensionless

number which directly relates the pore structure characteristic (that can be measured at macro-scale) to the critical capillary number (Morrow et al., 1982, Taber, 1981, Dullien and MacDonald, 1976, Dullien, 1991, Armstrong et al., 2014). Typical parameters that have been suggested to formulate such a dimensionless number are the size of the pores and pore-throats as well as their aspect ratio but also the permeability and porosity of the rock, and the mean length of the oil clusters. The observation of oil remobilisation at capillary numbers of approximately 10^{-5} is controversial since it suggests that the oil clusters are mobilised while the capillary forces are ~10^5 times larger than the viscous forces. This controversy is discussed in the literature (Dullien, 1991, Anton and Hilfer, 1999, Cense and Berg, 2009, Armstrong et al., 2014). Dullien (1991) suggested that the capillary number at which the mobilisation occurs (Nc_{mob}) should be defined such that it accounts for the pore (R) and throat (R_e) radius sizes as well as the oil cluster length and oil clusters are mobilised if

$$Nc_{mob} = \frac{\mu v}{\sigma} \frac{4l}{\left(\frac{R_e^2}{r_{dr}} - \frac{R^2}{r_{im}}\right)} = N_C \times \xi > 1, \tag{5.2}$$

where l is the oil cluster length, r_{dr} and r_{im} are the equilibrium drainage and imbibition radius of curvature of the oil-brine interface at the mobilisation threshold and ξ is the correlation factor between N_C and Nc_{mob} The value of ξ is cluster specific. Therefore, each trapped cluster has its own specific onset of mobilisation but any given cluster can only mobilise if, Nc_{mob}>1 which explains the trend of the capillary desaturation curves in Figure 5.12.

A trapped oil cluster should experience similar capillary and viscous forces, i.e. $F_c \sim F_v$, under equilibrium conditions. In other words, the oil cluster would be mobilised if $F_c < F_v$ and, likewise, the fluid phases will redistribute if $F_c > F_v$ until a new equilibrium is achieved. This condition is in agreement with our observations of fluid auto-redistribution presented in chapter 3, section 5. Consider an oil cluster trapped in a strongly water-wet rock. The rock surface can be expected to be coated by water-films, which may be very thin in places but are still present. The trapped oil cluster would hence be only in contact with the brine phase at its outer surface.

Under such circumstances, the area over which the viscous and capillary forces are acting is equal to the entire external surface area of the trapped oil cluster. Therefore, the ratio of viscous to capillary forces is equal to the ratio of viscous to capillary pressures applied on the surface of the trapped oil clusters, i.e.

$$N_C = \frac{F_V}{F_C} = \frac{P_v\, A}{P_C\, A} = \frac{P_v}{P_C} = \frac{l_{cl}\, \mu_w v}{k_{rw} P_C}, \tag{5.3}$$

where, l_{cl} is the cluster length and k_{rw} is the relative permeability of water. Note that here the Darcy's law is used to correlate the pressure drop across the oil cluster with the macroscopic parameters such as k_{rw} and v. Thus, the suggested Nc in eq. 4.3 is a combination of micro-scale (l_{cl}) and macro-scale (k_{rw} and v) parameters. Armstrong et al. (2014) measured oil (decane) cluster lengths trapped in a sandstone media directly using μCT. From their experimental data, a macroscopic capillary number was defined such that capillary desaturation occurs if

$$Nc_{\,macro} = \frac{l^{cl} \mu^w v^{Darcy}}{k^{rw}\, P^C} \sim 1 \tag{5.4}$$

where the superscripts denotes macroscopic parameters. l^{cl} (m) is an average cluster length, defined as $l^{cl} = \frac{\sum S_c\, l_{cl}}{\sum S_c}$, S_c is the saturation of each cluster, μ^w (Pa.S) is the wetting-phase viscosity, v^{Darcy} (m/s) is the Darcy velocity, k^{rw} (m^2) is the relative permeability of the wetting phase , and P^c (Pa) is the average capillary pressure.

In this study, despite being able to extract the trapped cluster length distributions from collected images, we could not obtain values for Nc_{macro} since relative permeability data could not be measured over the time frame of this thesis. Therefore, the conventional definition of capillary number ($N_C = \mu v/\sigma$) is used here to discuss the flow regimes and desaturation process.

2.2. Droplet Fragmentation – Introducing a New Immiscible Fluid Displacement Process

2.2.1. Observation

In a series of micro-model studies, Avraam and Payatakes (1995) observed that oil clusters can break down into smaller droplets during high capillary number

displacements, i.e. if $N_c > 5 \times 10^{-6}$. They defined droplets as oil blobs with sizes comparable to the diameter of throats of the micro-model. This displacement mechanism was referred to as drop-traffic flow (Figure 5.13). Due to the high flow rates used in these experiments, the droplets were transported by the flow of water phase and hence had insufficient time to coalesce.

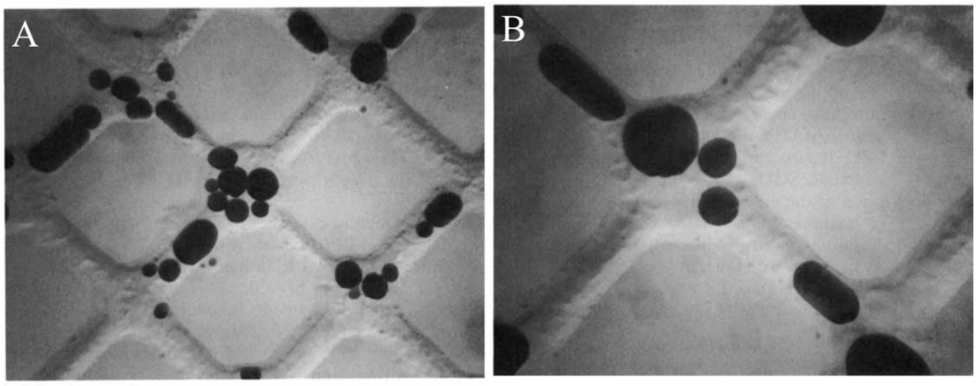

Figure 5.13: Drop-traffic flow observed in the micro-model experiments of Avraam and Payatakes (1995) at *Nc* = 5×10^{-6}. (A) Drop-traffic flow observed in a small number of connected pores and (B) drop-traffic flow inside a single pore.

One of the specifications of their micro-model, which has probably assisted the observation of this pore-scale event, is the relatively high average aspect ratio of their network model, which was approximately 5. Larger differences between the pore and pore-throat size assist the break-down of the oil connections at the pore-throats. However, the average aspect ratio for sandstones is commonly smaller. Also, the viscous forces applied in 3D pore structures are not enough to mobilise the small droplets. Hence, the drop-traffic flow is not observed in pore-scale imaging studies of fluid displacement in sandstone samples.

In this thesis, however, we were able to observe a similar mechanism where oil clusters break down during brine imbibition into a SD core plug where imbibition is dominated by viscous forces. All observations are in 3D in complex pore geometries of variable size.

Subsequent to capillary-dominated imbibition (*Nc* = 3.95 × 10^{-7}) and imaging (which is discussed in section 2.2) brine was injected under viscous forces (*Nc* = 2.77 ×10^{-5}),

for details of the injection parameters refer to chapter 2, section 5.3. Injections performed until 10 pore volumes of brine had been injected into the plug, and no more oil was observed to be produced. The remaining oil saturation in the 18 mm central section of the plug (from the 11.25 μm resolution data, excluding the capillary end effect) was measured to be 54% and 44 % after the capillary-dominated and viscous-dominated imbibition steps, respectively. Therefore, an extra 10 % of oil was recovered during this viscous-dominated imbibition.

Figure 5.14A shows an oil droplet trapped in a large vug after capillary-dominated imbibition. As shown in 3D in Figure 5.3B, this trapped oil droplet was surrounded by a visible brine film and hence could not be recovered in a capillary dominated flow regime and while $N_C < Nc_{crit}$. The existence of such isolated droplets in the pore space of the rock increases the resistance to the flow of the brine phase and hence decreases the relative permeability to the brine phase during imbibition.

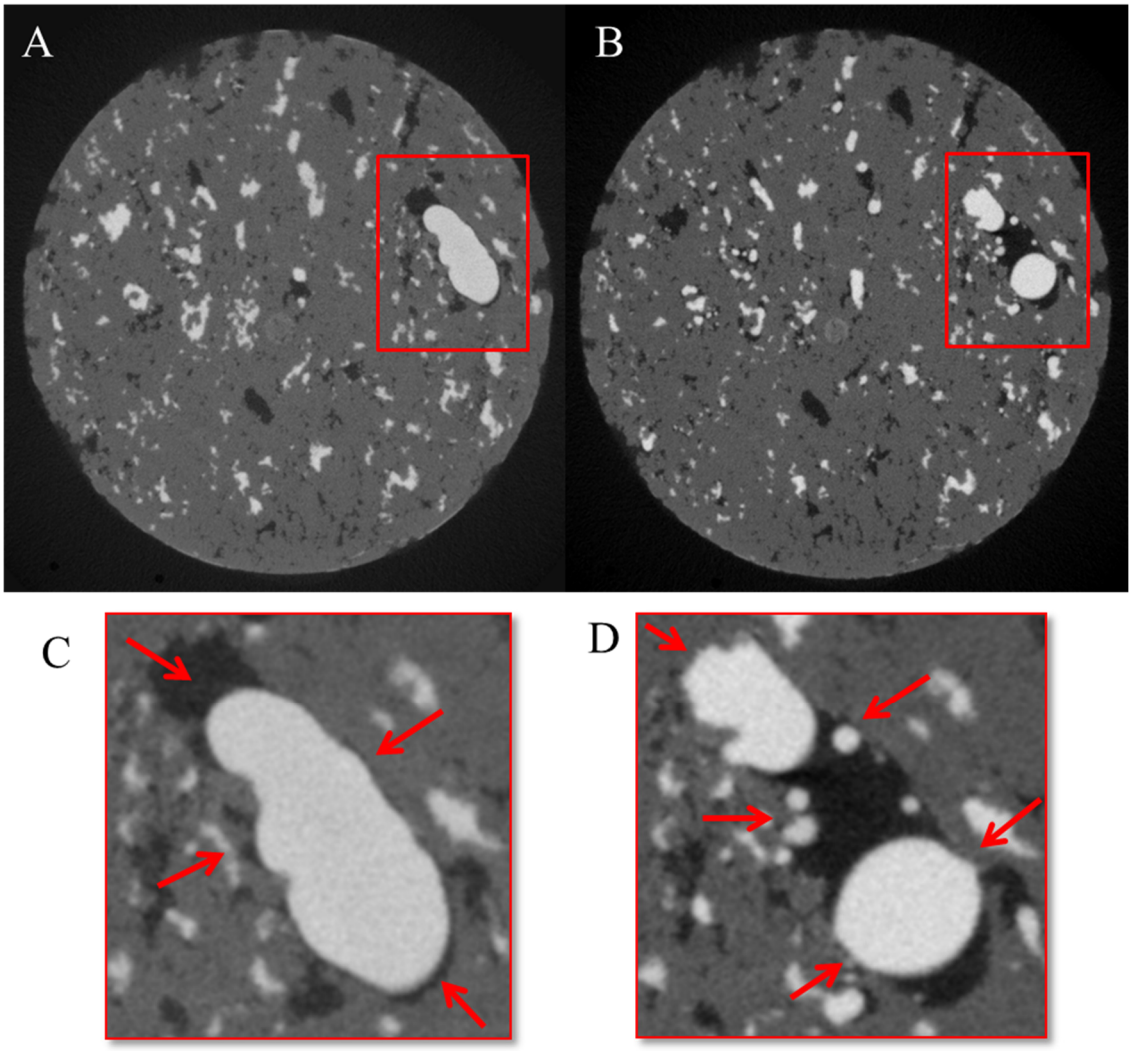

Figure 5.14: Trapped oil structure in the pore space of a large vug (same as the vug shown in Figures 5.1D, 5.2D and 5.3B), after capillary-dominated (A) and viscous-dominated (B) imbibition. (C and D) show magnified views of the large pore. Red arrows show the trapped oil droplets.

Figure 5.14B shows the same slice after viscous-dominated imbibition. The large oil droplet that was previously trapped under capillary forces has replaced by hundreds of smaller oil droplets. In fact 83 oil droplets were trapped in the large pore and its neighbours, after the capillary-dominated imbibition, while after the viscous-dominated imbibition the presence of 276 oil droplets was recorded in the same large pore (and in its neighbours). The volumes of trapped oil in this pore reduced from 9.99×10^{9} to 2.95×10^{9} (corresponding to 0.85 and 0.27 fractions of the pore volume) after the injection rate increased and displacement became dominated by viscous

forces. Hence, almost 68% of the oil that was originally trapped under capillary forces at low injection rates has been recovered during high injection rates. It is likely that the produced oil has been in form of smaller oil droplets with sizes similar to the pore-throats that are connected to this pore.

Figure 5.15A shows the same pores depicted in Figure 5.3B but from another angle. Figure 5.15B shows the 276 small oil droplets in 3D that remained in the pore after the viscous dominated brine injection. All these oil droplets are observed to be in contact with the rock surface.

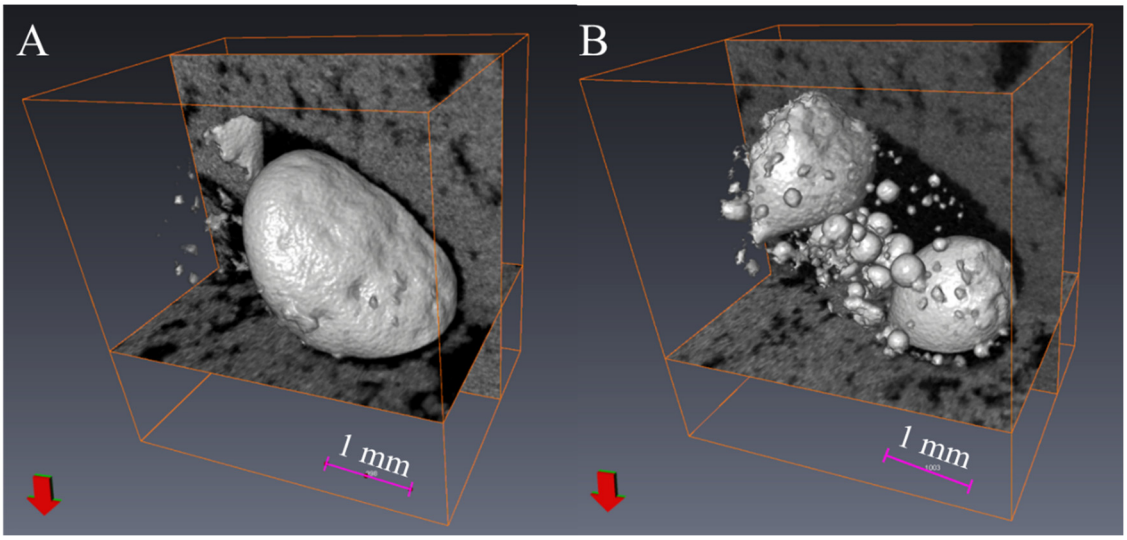

Figure 5.15: 3D rendering of the oil phase after capillary-dominated (A) and viscous-dominated (B) imbibition. The large droplet of oil trapped under capillary forces is fragmented into 276 droplets as a result of viscous dominated imbibition.

Figures 5.14 and 5.15 show an example of capillary desaturation in a very heterogeneous pore structure. The displacement process that has been observed may offer an alternative explanation for the pore-scale mechanisms that cause capillary desaturation and additional oil production if fluid flow becomes viscous dominated and N_C exceed the Nc_{crit}. It is probable that, beyond a critical level, the viscous force exerted on trapped oil droplet has exceeded the maximum interfacial energy the trapped oil droplet can accommodate. Therefore, the larger oil droplet fragmented into numerous smaller droplets in order to accommodate more of the invading brine phase. During this process, the oil-brine interface is increased as result of the work

done. Calculations of changes in energy are discussed in section 3.2.5. This new pore-scale event is referred to as "droplet fragmentation".

The fragmentation of a large oil droplet into many smaller droplets at high capillary numbers is not restricted to this particular pore but has been observed throughout the experimental plug. The fragmentation of oil into multiple discrete droplets is most strikingly observed in the larger pores but occurs in pores with volumes spanning over three orders of magnitudes, from 10^8 to $10^{10}\mu m^3$. Figures 5.16 and 5.17 illustrate two other examples of droplet fragmentation in pores with 10^{10} and 10^8 μm^3 volume, respectively.

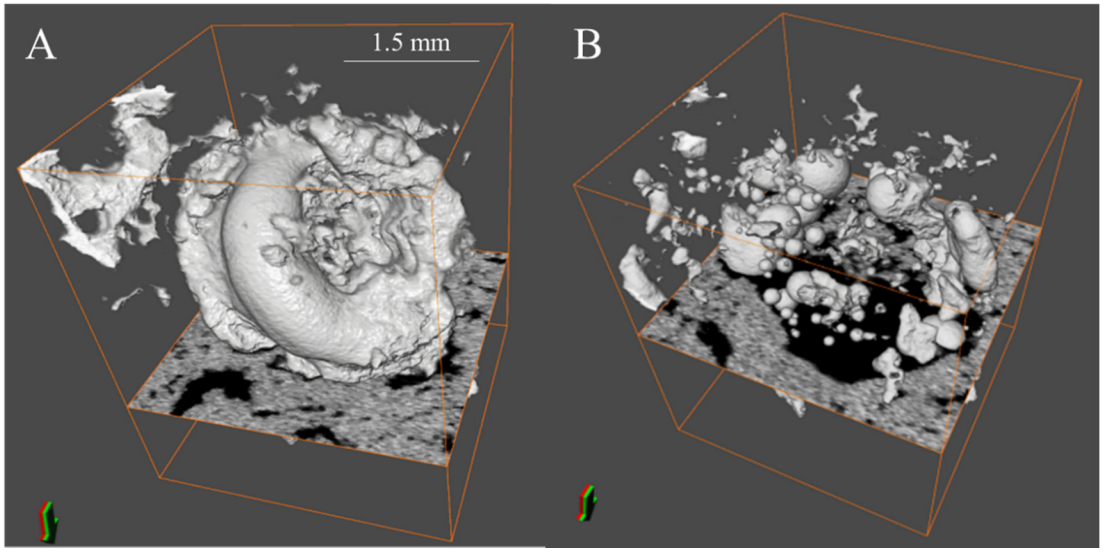

Figure 5.16: Example droplet fragmentation event in a pore with volume of the order of 10^{10} μm^3. 3D rendering of oil phase after capillary-dominated (A) and viscous-dominated (B) imbibition.

The observation and quantitative analysis of this effect within pores with volumes smaller than 10^8 μm^3 is limited by image resolution but qualitative inspection of our images shows that fragmentation is more prevalent in larger pores. It is probable that this phenomenon is observed so clearly because the range of pore-sizes in this carbonate rock is very wide (i.e. from less than 1µm to few mm).

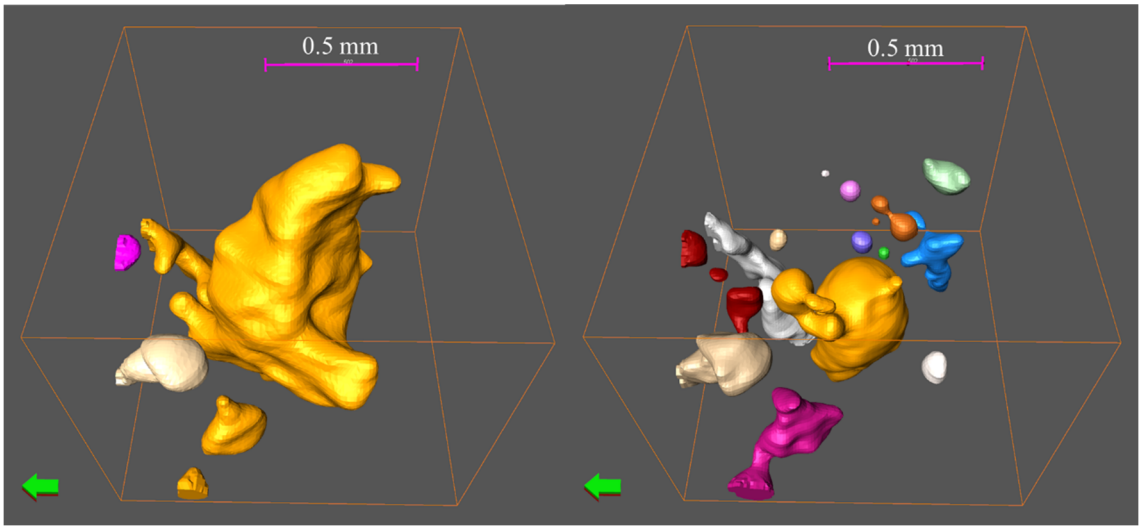

Figure 5.17: Example droplet fragmentation event in a pore with volume of the order of 10^8 µm^3. 3D visualisation of surfaces fitted to labelled oil phase after capillary-dominated (A) and viscous-dominated (B) imbibition.

Figure 5.18 shows more examples of fragmented oil droplets trapped in pores of the scale of a few millimetres. All fragmented droplets are in contact with the pore walls when they are visualised in 3D.

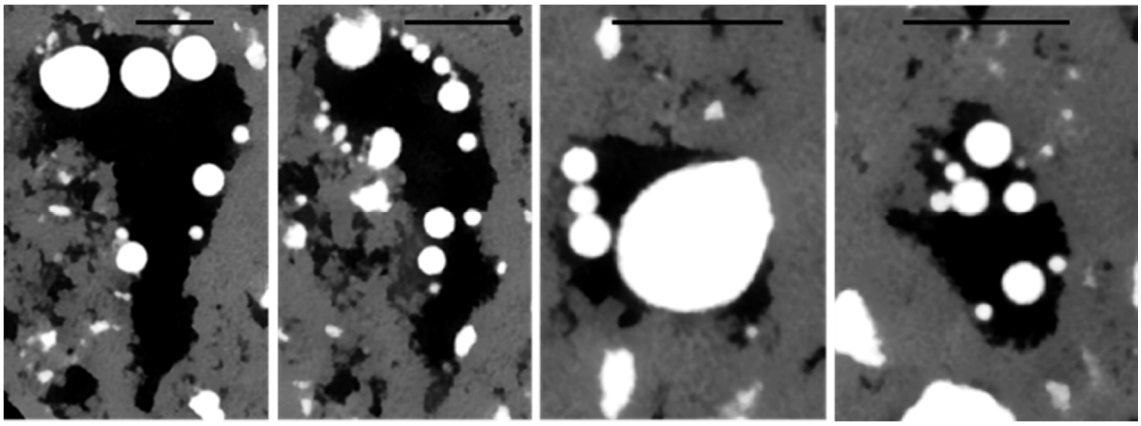

Figure 5.18: 2D examples of fragmented oil droplets in pores that are a few millimetres in size. Droplets that appear to be in free suspension are in contact with the pore surface when viewed in 3D. The scale bar is 1 mm.

2.2.2. Cluster Size Analysis

The oil saturation in the analysed section of the core plug is 86%, 69%, 54%, and 44%, respectively after the capillary-dominated and viscous-dominated drainage and

imbibition processes. The saturations are calculated relative to the pore volume. The cluster size analysis after the two drainage processes are presented in chapter 3 section 3. Figure 5.19 shows the normalised distribution of "oil cluster volumes" for logarithmic bins, (e.g. for the first bin 10 < cluster volume in voxels < 100). For normalisation the volume of each cluster is divided by the total oil volume in the analysed section for each injection stage. Figure 5.20 shows the cluster frequency of the oil phase as a function of the same cluster volumes. Figure 5.21 shows 3D renderings of labelled oil clusters in each bin for the four injection steps. Comparing the cluster size distributions of the oil phase throughout the test cycle leads to the following points:

(a) After the capillary-dominated drainage step one single very large spanning cluster of oil saturated 65.36 % of the pore space of the rock. It formed 76 % of the oil saturation at this stage (S_o=86%). This cluster, rendered in yellow in Figure 5.21A2, is clearly a percolating cluster connected to the inlet and outlet of the analysed volume. At this stage the total number of clusters was 4142.

(b) After the viscous-dominated drainage, the capillary-dominated fluid redistributions were shown (refer to chapter 3, section 5) to cause some degree of cluster breakdown such that the largest re-arranged cluster occupied only 14.49% of the pore space (22.35% of the 69% oil saturation). 17% of oil saturation migrated out of the region of interest. The total number of oil clusters increased to 7561.

(c) As a result of capillary-dominated imbibition 15% oil was recovered from the analysed section. Clusters exceeding 10^7 voxels volume and spanning the analysed volume are absent. Further cluster break-down is observed and the total number of oil clusters increased to 9054.

(d) After viscous-dominated imbibition a further 10% of the trapped oil was recovered. Further break-down of the oil clusters has occurred, doubling the total number of oil clusters present to 18130.

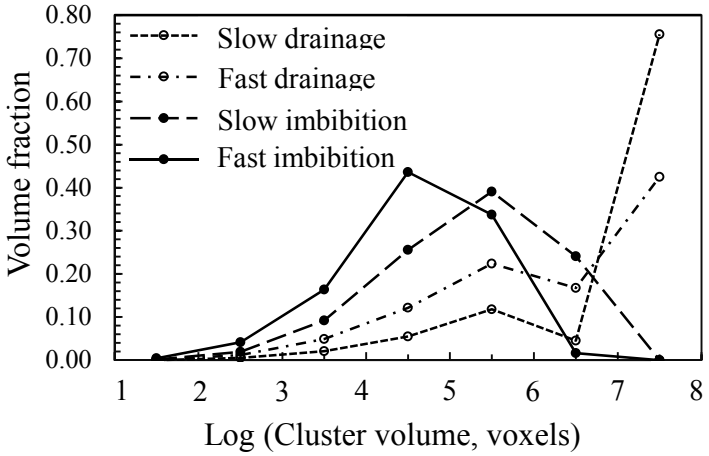

Figure 5.19: Volumetric cluster size distribution for logarithmic bins (e.g. for the first bin 10 < cluster volume (voxels) < 100). The normalisation has been done with respect to the total oil volume in the analysed section for each injection stage.

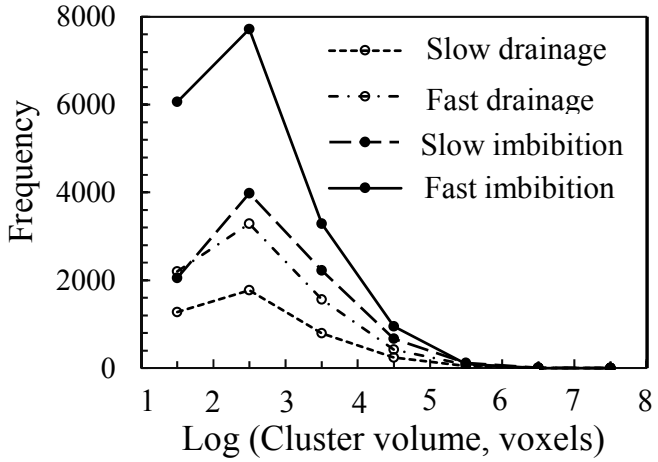

Figure 5.20: Cluster frequency of the oil phase as a function of the same cluster volumes (voxels) for each injection stage. A continuous increase in number of clusters along with decrease in the cluster volumes indicates the change in oil structure during the drainage and imbibition processes.

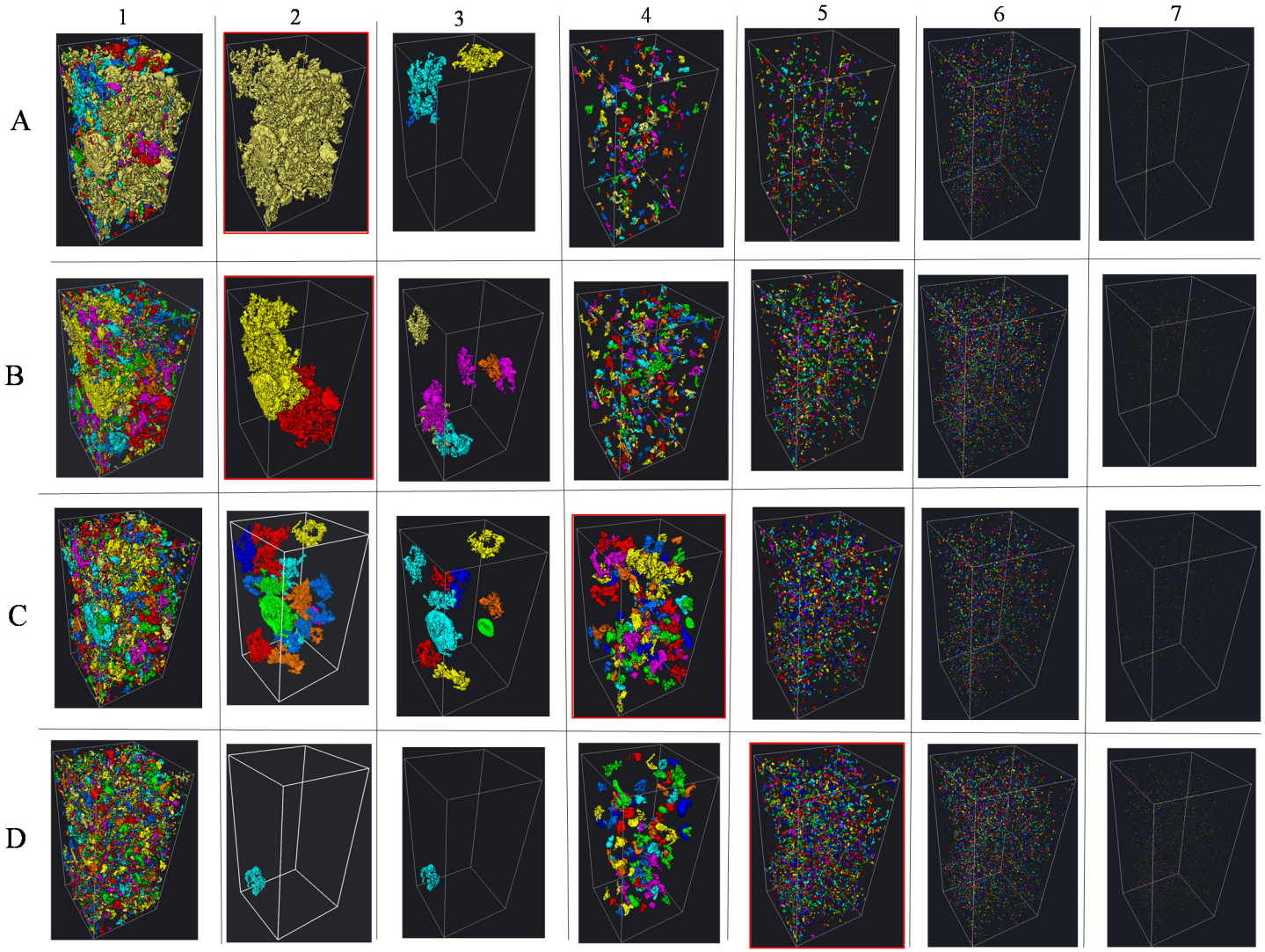

Figure 5.21: 3D rendering of the labelled oil clusters in each bin for the four injection steps. (A and B) refer to capillary-dominated and viscous-dominated drainage, respectively. (C and D) refer to capillary-dominated and viscous-dominated imbibition, respectively. Red borders correspond to peaks in Figure 5.19.

The volumetric cluster size distributions for the two imbibition steps show two peaks at 10^4 <cluster volume (voxels) <10^5 and 10^5 <cluster volume (voxels) <10^6, respectively. These are two orders of magnitude smaller than the peaks observed during both primary drainage scenarios (10^7 <cluster volume (voxels) <10^8). The continuous increase in cluster number and decrease in cluster size during both imbibition cycles indicate that oil structure has changed during the drainage and imbibition processes.

2.2.3. Euler Number Calculation

Euler number is used to measure the global connectivity of a structure, (refer to chapter 2, section 7.2.2). Herring et al. (2013) have used Euler number to analyse the connectivity of a non-wetting phase occupying the pore space of four different porous materials. They reported Euler numbers of the connected pore space of the samples to be large and negative. Connectivity and hence Euler number calculated for the pore space and/or the fluid clusters are sensitive to the resolution of μCT images. Insufficient resolution may result in the structures to appear as unrealistically disconnected on the segmented images, shifting the Euler number towards positive values. The calculated Euler numbers for the oil phase are shown in Figure 5.22 for all four injection steps. The calculated Euler number is negative only for slow drainage. This negative value corresponds to the large connected cluster of oil rendered in yellow in Figure 5.21A. For the other injection steps, the Euler number is always positive and increases with injection rate. This trend is in agreement with the observed pore-scale mechanisms because capillary redistribution, snap-off and droplet fragmentation have caused the oil phase to become progressively more disconnected, resulting in positive and increasingly larger Euler numbers.

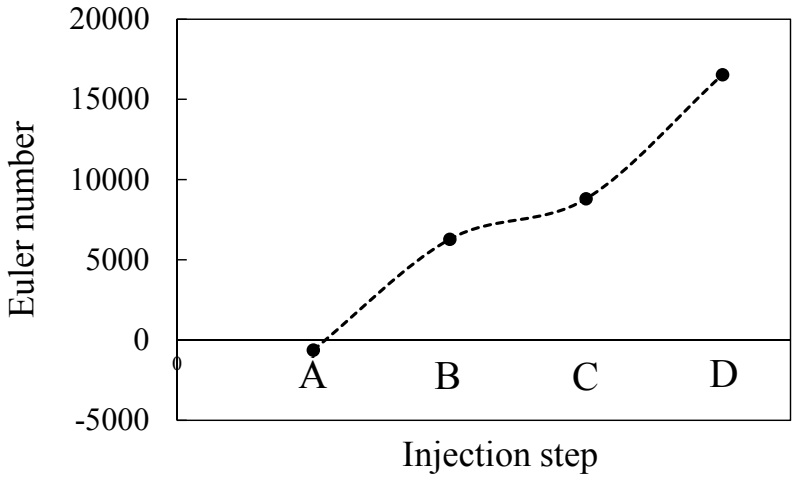

Figure 5.22: Euler numbers calculated based on binary images of oil phase in different injection steps. (A and B) refer to capillary-dominated and viscous-dominated drainage, respectively. (C and D) refer to capillary-dominated and viscous-dominated imbibition, respectively. The calculated Euler number is a negative value only for the slow drainage as the oil phase still forms a percolating cluster (Figure 5.21A).

2.2.4. Analysis of Fragmented Oil Droplets

The images captured before and after the fragmentation event were segmented into three phases of oil, brine and rock using watershed segmentation method. The oil and brine binary volumes were subsequently labelled. Labeling allows individual analysis of the trapped droplets, such as shape and size distribution analysis (refer to chapter 2, section 4.5). 3D renderings of the segmented and labelled phases of the three pores presented in Figures 5.15 to 5.17 are shown in Figures 5.23 to 5.25.

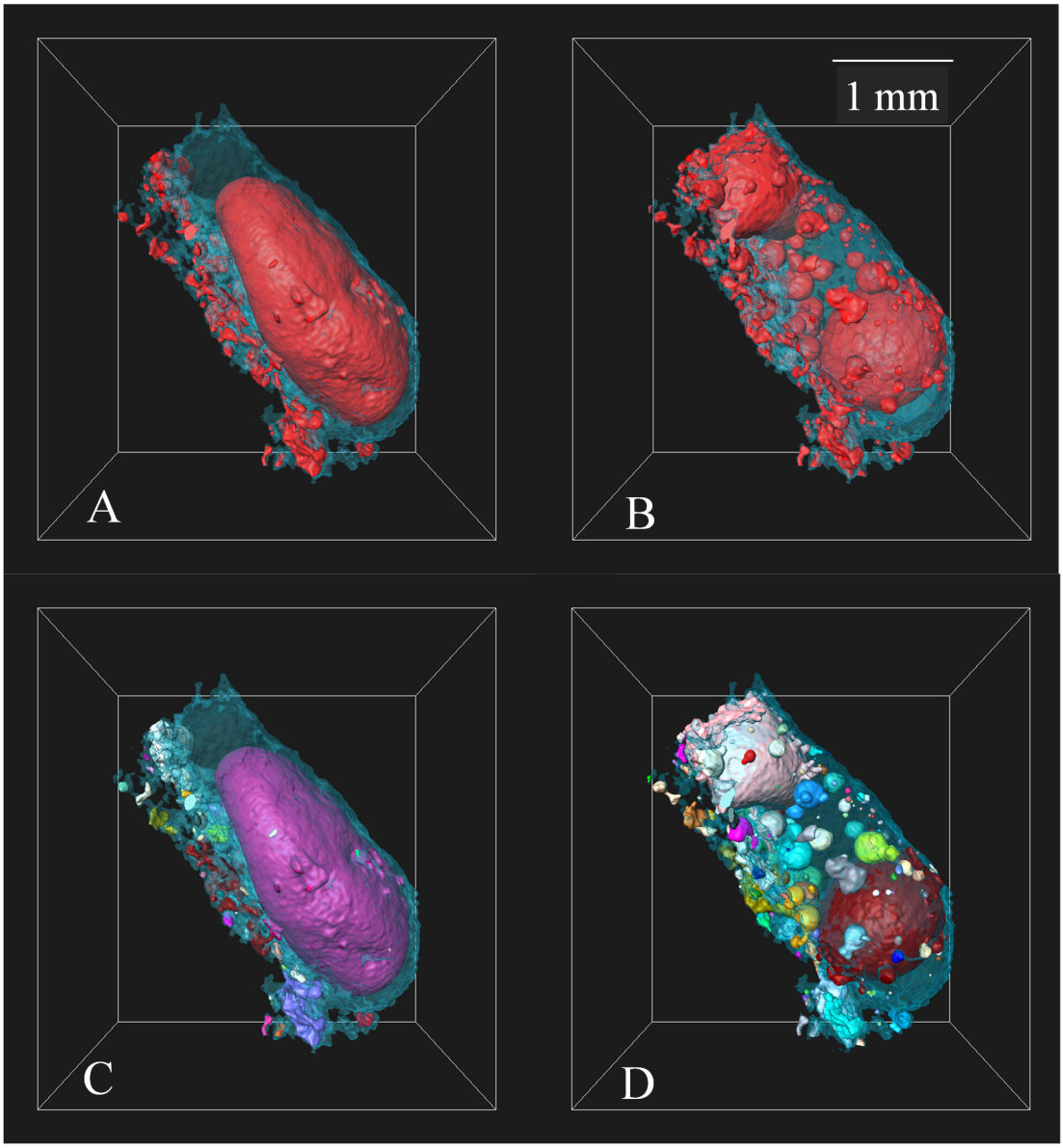

Figure 5.23: 3D rendering of oil and brine phases in the pore shown in Figure 5.15 before (A and C) and after (B and D) fragmentation. (A and B) Blue and red colours denote the brine and oil, respectively. (C and D) Blue denote the brine phase. Different colour droplets depict the labelled oil phase.

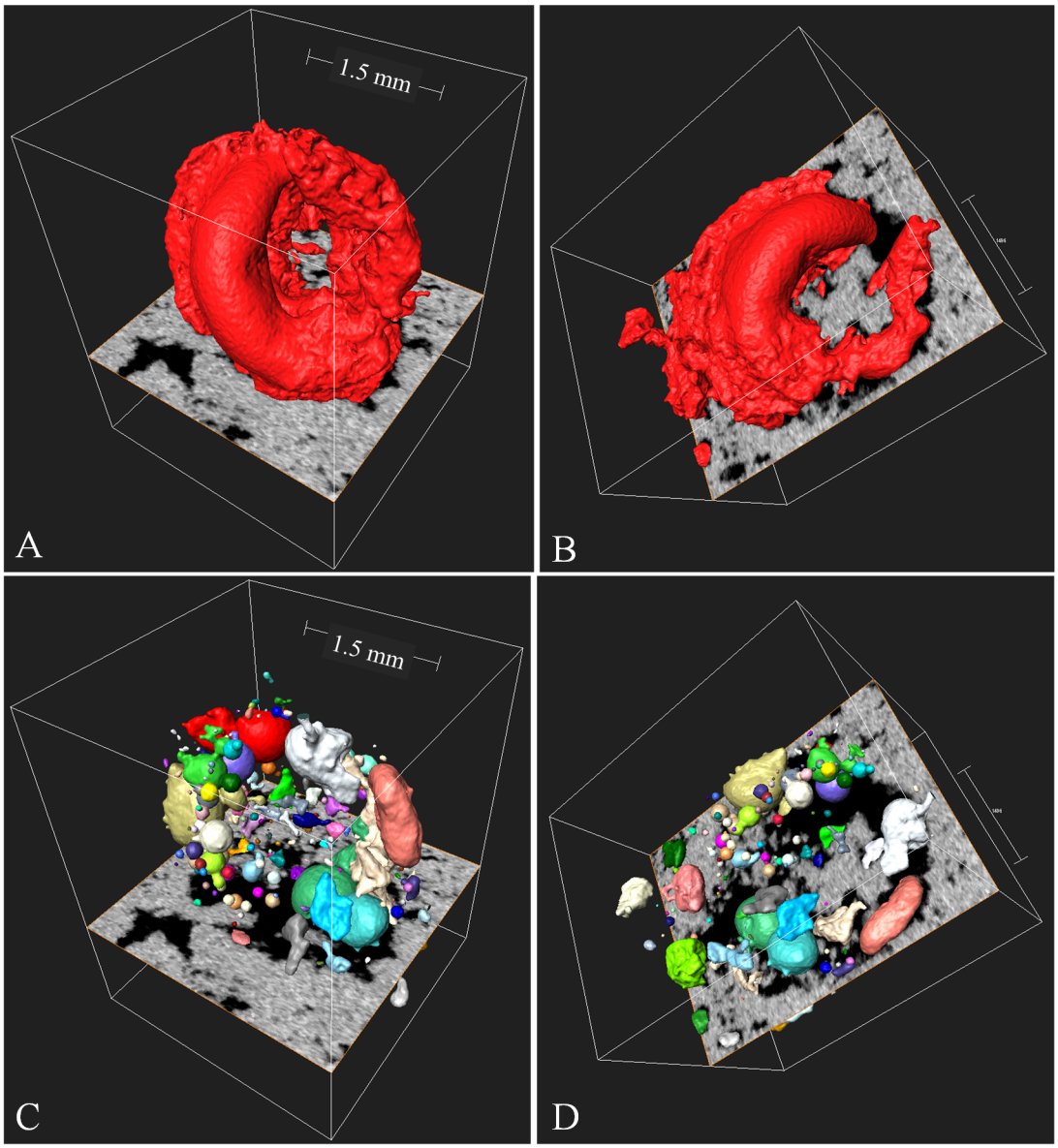

Figure 5.24: 3D rendering of labelled oil phase in the pore shown in Figure 5.16 before (A and B) and after (C and D) fragmentation.

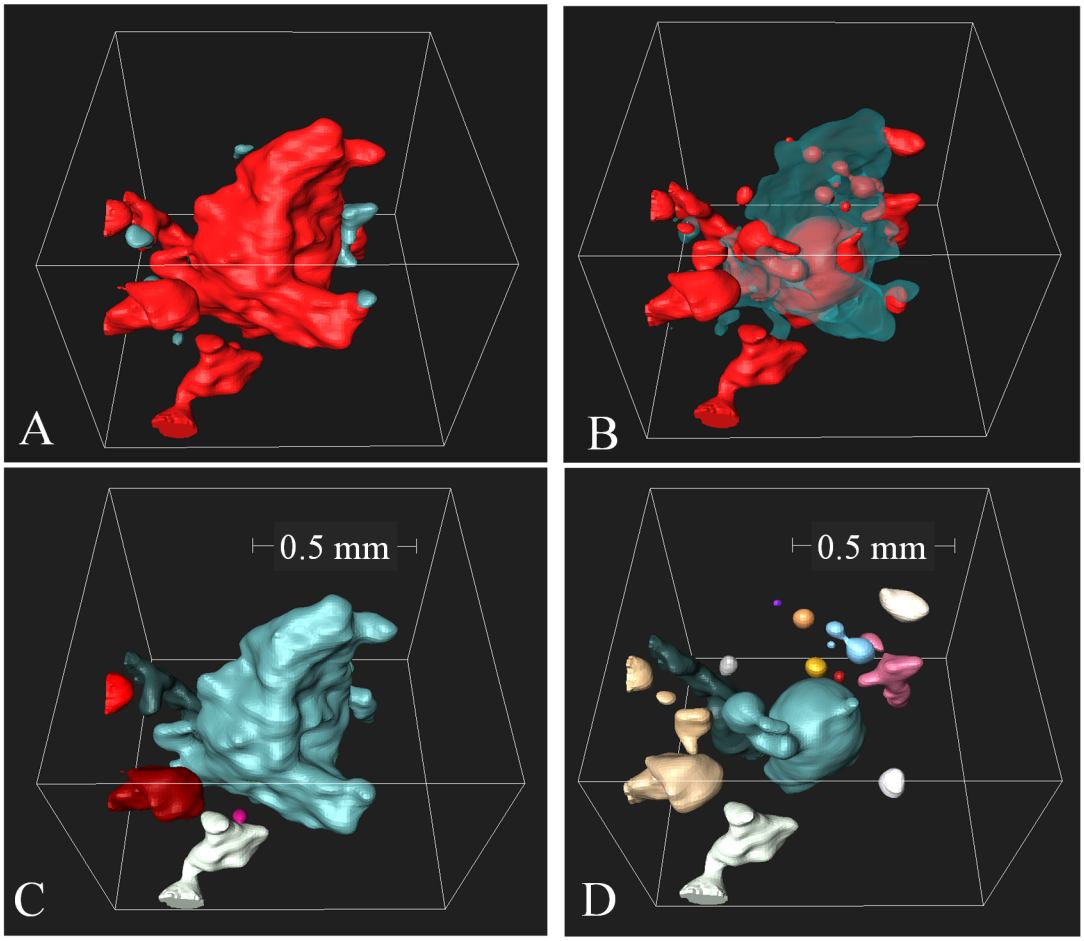

Figure 5.25: 3D rendering of oil and brine phases in the pore shown in Figure 5.17 before (A and C) and after (B and D) fragmentation. (A and B) Blue and red colours denote the brine and oil, respectively. (C and D) Different colour droplets depict the labelled oil phase.

A suspended oil droplet with a given volume of V forms a spherical shape to minimize its surface area and hence its surface free energy ($\sigma_{ob} A$), where σ_{ob} is the oil-brine interfacial tension, and A is the interfacial area of the two phase. The minimisation of surface energy maximises the stability of the oil droplet. Analysing the images shows that most of the fragmented oil droplets have close to spherical shapes to minimise their surface energy. Figure 5.26 provides a measure of the sphericity of the fragmented oil droplets in the three pores depicted in Figures 5.23 to 5.25. This measure is achieved by comparing the shape factor, defined as the ratio of surface area to volume, of each oil droplet with the shape factor of an equivalent sphere (3/r) in these depicted three pores. The larger droplets have shapes that

deviate from perfect spheres due to the geometry of the pores confining them. For the smallest pore with a volume of 10^8 μm^3, the deviations stem from resolution limitations.

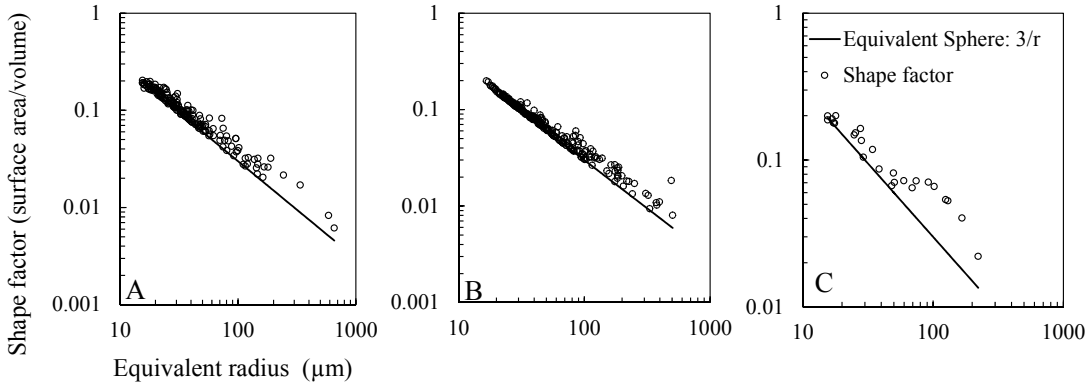

Figure 5.26: Measure of sphericity of the fragmented oil droplets for the fragmented droplets trapped in the three pores presented in Figures 5.23 to 5.25 by comparing their shape factor (surface area/volume) with that of an equivalent sphere (3/r). Most fragmented droplets form close to spherical shapes.

Figure 5.27 shows the volume distribution of the fragmented oil droplets for the three pores shown in Figures 5.23 to 5.25. The volumes are normalised with respect to the volume of the original oil droplets before fragmentation. In these three pores, 90%, 89 %, and 44 %, respectively, of the fragmented oil droplets have volumes after fragmentation that are by at least two orders of magnitude smaller than the volume of the oil droplets before fragmentation. This effect is more pronounced in the two larger pores.

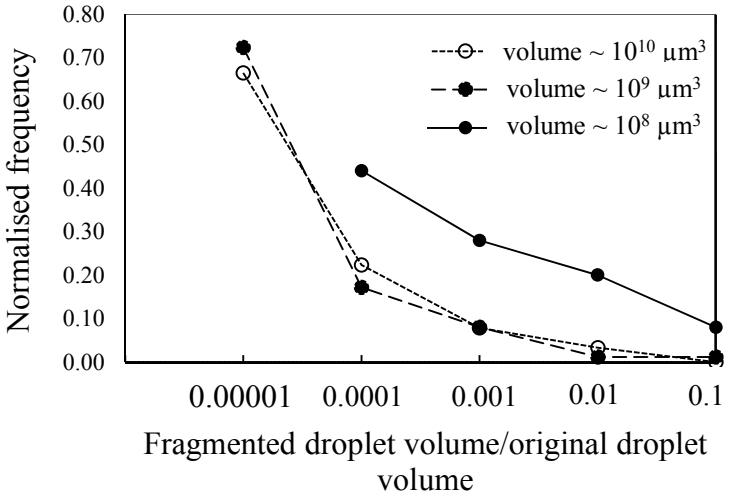

Figure 5.27: Distribution of the volume of the oil droplets relative to the volume of the original oil droplets before fragmentation for the three pores with volumes 10^{10}, 10^{9}, and 10^{8} µm^3, respectively shown in Figures 5.23 to 5.25. The majority of the trapped oil droplets are smaller than the original oil droplets before fragmentation by at least two orders of magnitude.

2.2.5. Stability of the Fragmented Oil Droplets

The immediate result of the fragmentation event is a significant increase in the oil-brine interfacial area per unit volume of oil (Table 5.1). Based on the principle of minimum free energy, the internal energy of any closed system should decrease and ultimately reach a minimum value if an equilibrium state is achieved. After the viscous-dominated imbibition, the flow cell was locked and therefore the system (the core holder plus the connected lines) comprised a closed system. The most stable configuration for the residual fragmented droplets in each pore occurs when all of them join up to form a larger oil droplet as such a large oil droplet would have the smaller surface area. It should be noted that the fragmented droplets were static in the same configuration in two different scans that were separated by over 24 hours. For both scans, the droplets also did not move during the three hours period of data acquisition for each scan. All oil droplets appear to be in contact with the rock surface in 3D. Therefore, it is likely that the system is experiencing a meta-stable state in which each individual droplet is stabilised through its contact with the rock surface. The surface roughness of the rock is a key parameter which can keep the droplets in place by trapping them between the dolomite crystals. Moreover, any

adhesive forces between the oil droplets and the rock surface can also act as a stabilising factor.

Since the two fluid phases had precisely matched densities, the system was able to remain at this meta-stable state because gravitational forces were absent. This provided the chance to image the oil-brine-rock configurations with a laboratory-based μCT scanner. Any transition from this energy level to the most stable level requires an extra amount of work to overcome the stabilisation forces (acting through surface roughness or possible local oil-rock adhesive forces) and to re-mobilise the trapped oil droplets.

In natural reservoirs where oil and brine densities are different, gravity forces may cause the trapped oil droplets to coalesce after fragmentation to form larger droplets with minimum surface energy. The droplet coalescence depends on the competition between the stabilising forces, and the gravitational forces.

2.2.6. Fragmentation Energy Calculation

Figure 5.28 shows a conceptual model of the droplet fragmentation mechanism. A spherical oil droplet of radius r_o fragments into N smaller spherical droplets of equal volumes with radius $\frac{r_o}{\sqrt[3]{N}}$.

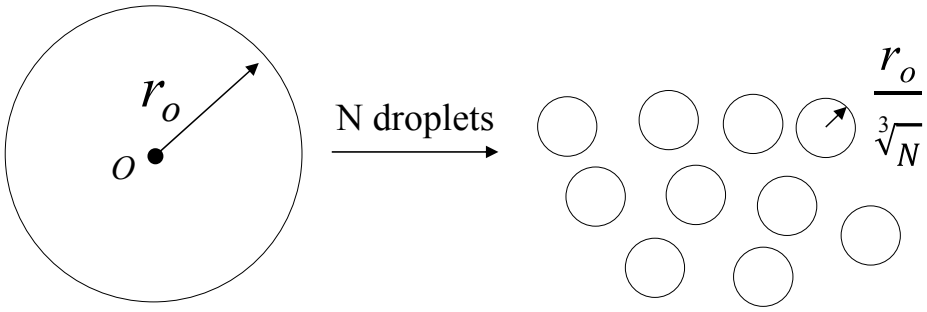

Figure 5.28: Schematic model of droplet fragmentation mechanism in which a spherical oil droplet fragments into *N* smaller droplets of spherical shape.

Assuming that a fraction f of the fragmented oil droplets' surface area is in contact with the rock surface, the fraction of the oil droplets' surface area that is in contact with the brine phase is 1-*f*. The oil-solid interfacial tension acting on *f* stabilises the

droplets. Therefore, for an oil droplet of arbitrary radius being fragmented into *N* fragments, the change in surface energy ΔE relative to the surface energy of the original droplet can be calculated using as

$$\Delta E = \frac{A_o\,\sigma_{ob} - N A_i\,[(1-f)\,\sigma_{ob} + f\sigma_{os}\,]}{A_o\,\sigma_{ob}}. \tag{5.5}$$

Assuming oil-brine (σ_{ob}) and oil-solid (σ_{os}) interfacial tension of 35 mN/m and 5 mN/m, respectively (Gassin et al., 2012) for any given value of *f* a minor change in incremental energy is required to fragment the original oil droplet extensively. A droplet with radius of 50 μm requires a change in surface energy of $\Delta E \sim 5.3\times10^{-9}$. This value is less than five times the original surface energy of approximately 1.1×10^{-9} J (to fragment into *N* (< 200) droplets). This is the maximum energy required considering $f = 0$. The required ΔE decreases as *f* increases. Figure 5.29 shows the additional energy required to fragment an oil droplet of arbitrary size into *N* smaller oil droplets. The figure indicates that droplet fragmentation can occur for relatively small changes in interfacial energy that are consistent with the fluid properties used in these experiments.

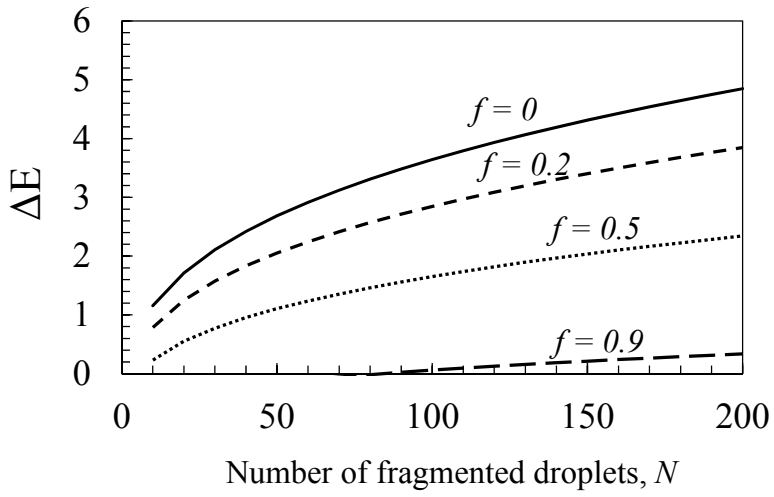

Figure 5.29: Additional energy of fragmentation for an oil drop of arbitrary size relative to the surface energy of the original oil droplet as a function of the number of fragments *N* and the fraction of the drop surface that is in contact with the rock *f*. The additional energy required for fragmentation is less than five times the original surface energy, which indicates that droplet fragmentation can occur for relatively small changes in interfacial energy that are consistent with the fluid properties used in the experiments.

2.2.7. Image-based Fragmentation Energy Calculation

In this section the fragmentation energy is calculated for the three examples of fragmentation event presented in Figures 5.23 to 5.25. Interfacial areas are required for calculation of the fragmentation energy. For interfacial area calculations the Porter and Wildenschild (2010) method is used in which:

$$a_{nw/w}=\frac{1}{2}\left(a_w + a_{nw} - a_s\right), \tag{5.6}$$

and

$$a_{nw/s}= a_{nw} - a_{nw/w}, \tag{5.7}$$

where a_w, a_{nw}, a_s are surface area of the wetting, non-wetting phases and the pore respectively, and $a_{nw/w}$, $a_{nw/s}$ are the non-wetting/wetting interfacial area as well as non-wetting/solid interfacial area. Table 5.1 lists the total trapped oil volume as well as the normalised oil-brine and oil-rock contact surfaces for the three pores presented in Figures 5.23 to 5.25. The surface areas are normalised against the oil volumes present in the pores at each stage.

Table 5.1: Energy analysis the three pores presented in Figures 5.23 - 5.25.

	Pore 1		Pore 2		Pore 3	
Pore Volume (μm^3)	1.1×10^{10}		6.84×10^{9}		2.01×10^{8}	
Imbibition flow rate (µl/min)	10	700	10	700	10	700
Number of droplets	1	242	83	276	5	23
Oil Volume (μm^3)	9.99×10^{9}	2.95×10^{9}	4.58×10^{9}	2.49×10^{9}	1.88×10^{8}	9.03×10^{7}
Oil Saturation (%)	85%	27 %	67%	36%	93%	45%
O-B Interface/ Oil Volume (1/µm)	2.17×10^{-4}	5.03×10^{-3}	3.78×10^{-3}	6.14×10^{-3}	7.09×10^{-4}	8.45×10^{-3}
O-R Interface / Oil Volume (1/µm)	7.28×10^{-3}	1.09×10^{-2}	1.16×10^{-3}	4.71×10^{-3}	1.87×10^{-2}	2.15×10^{-2}
E/ Oil Volume ($J/\mu m^3$)	0.04×10^{-15}	0.23×10^{-15}	0.14×10^{-15}	0.24×10^{-15}	0.12×10^{-15}	0.4×10^{-15}
ΔE (based on eq. 4.5)	4.75		0.73		2.32	
f	0.97	0.68	0.24	0.43	0.96	0.72

According to Table 5.1 58%, 31% and 48% of the trapped oil has been recovered from these three pores, respectively, as a result of the fragmentation event. The percentages are with respect to the pore volume. The pre-requisite of a correct calculation of the interfacial areas (and hence the surface energies) is that the fluid phases appear on the segmented images correctly. Of particular importance in the present analysis is representation of the brine phase on the segmented images. The thickness of the brine films is observed to be different in different pores. Due to resolution limitations the brine films which are very thin in places may not be fully represented on the segmented images. This causes the oil phase to appear in contact with the rock rather than the brine phase. Since the IFT of the oil-rock (assumed here 5 mN/m) is much less than the IFT of oil-brine (assumed here 35 mN/m) the interfacial energy is underestimated if the brine films is not successfully represented.

Figures 5.30 to 5.32 show the segmented brine phase on the images of the three pores presented in Figures 5.23 to 5.25, after the slow imbibition step. It is apparent that the brine film is fully resolved only on pore shown in Figure 5.30. While due to the water-wetness of the rock it is probable that an existing brine film is coating the rock surface all over the plug the resolution limitations do not permit a reliable segmentation of this thin brine film.

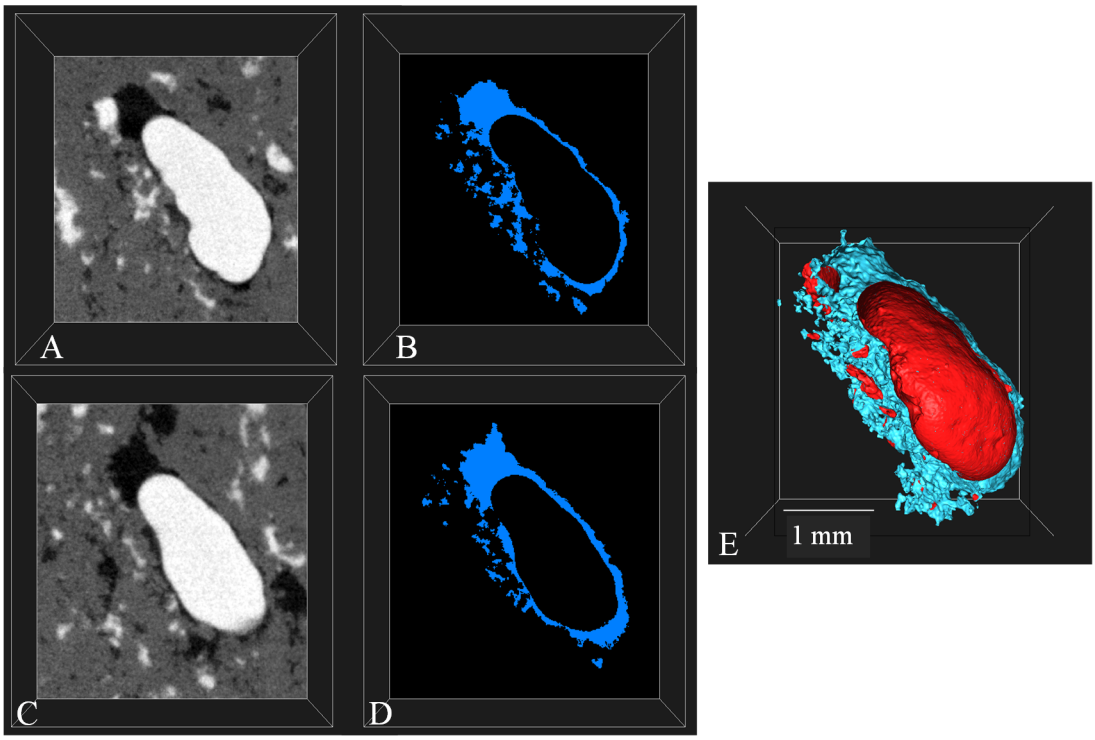

Figure 5.30: Successful segmentation of the brine phase after the slow imbibition step for the pore presented in Figure 5.23. (A, C) Example grey scale slices, (B, D) corresponding binary images of the brine phase. (E) A slice through a 3D rendering of the oil (red) and brine (blue) phases saturating this pore.

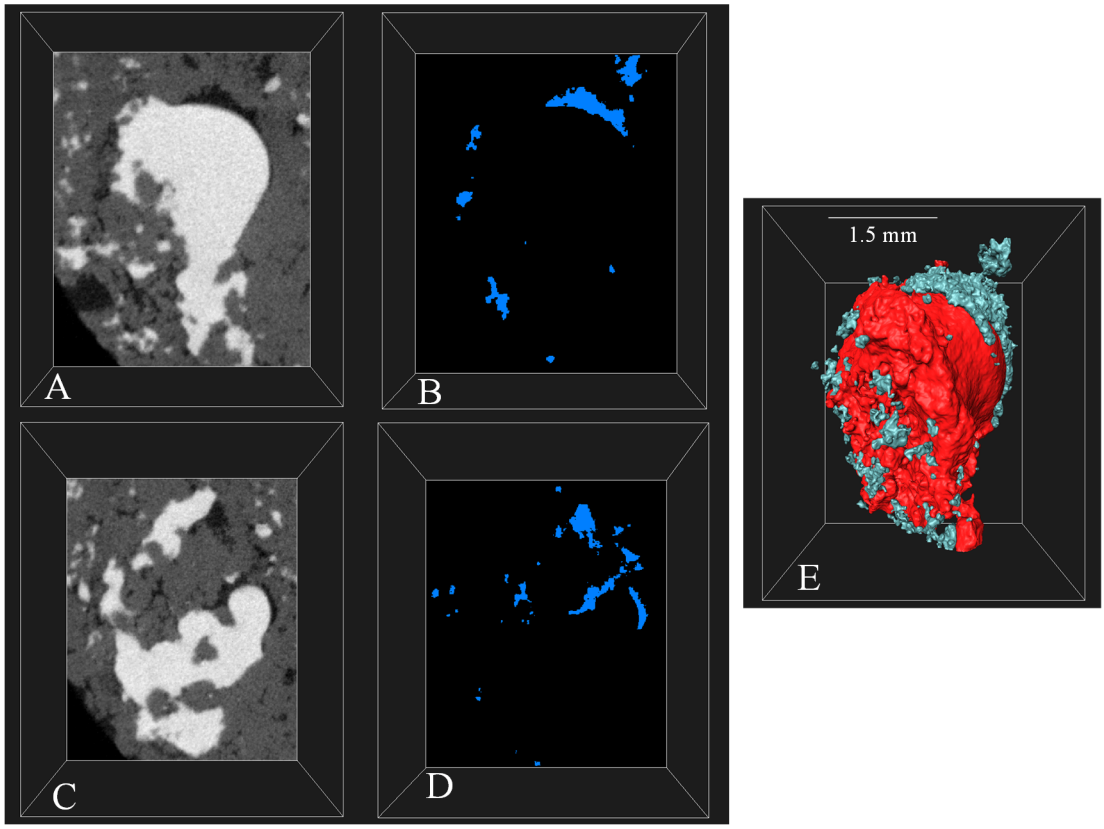

Figure 5.31: Unreliable segmentation of the brine phase after the slow imbibition step for the pore presented in Figure 5.24. (A, C) Example grey scale slices, (B, D) corresponding binary images of the brine phase. (E) 3D rendering of the oil (red) and brine (blue) phases saturating this pore.

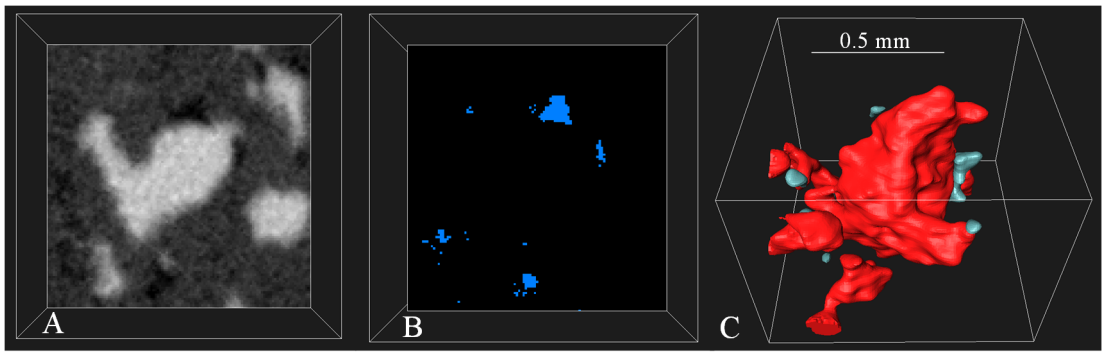

Figure 5.32: Unreliable segmentation of the brine phase after the slow imbibition step for the pore presented in Figure 5.28. (A) Example grey scale slice, (B) corresponding binary image of the brine phase. (C) 3D rendering of the oil (red) and brine (blue) phases saturating this pore.

According to Table 5.1 the additional fragmentation energy (ΔE) for these three pores (per volume of trapped oil) are 4.8, 0.73, and 2.32, respectively. The slow

imbibition values of f for the 10^{10} and 10^{8} pores is 0.97, 0.96, respectively. This indicates that the brine films were not successfully captured on the segmented images of these two pores. Therefore, the calculated change in energy as a result of fragmentation may not be reliable for these examples. In contrast, the calculated energy change (ΔE) for the 10^{9} pore (0.73) appears to be reliable due to full representation of the brine film on the segmented image. It suggests that the energy required to fragment the oil droplet was higher than the initial surface energy of the trapped oil droplet before fragmentation by a factor of 1.73.

The two 10^{10} and 10^{9} examples clearly demonstrate that the fragmentation event happens in the cases where: (a) a droplet of oil is trapped in a single pore as a result of snap-off event (10^{9} pore), or (b) a locally connected cluster of oil is trapped in a number of neighbouring pores (10^{10} pore). For the latter it may be the case that as a result of the fast brine injection, the brine films swell ahead of the displacement front, resulting in snap-off of the local connections of the trapped oil clusters over the narrowest throats. In other words, the locally connected oil clusters may first snap-off at the pore junctions producing a set of disconnected oil droplets each trapped in a single pore body. As the displacement front approaches the high influx of the brine phase causes the fragmentation. Time resolved experiments using synchrotron facilities may be used to investigate the details of the changes in the non-wetting fluid structure during the fragmentation event.

2.2.8. Implication of Droplet Fragmentation Mechanism

The fragmentation mechanism enlarges the surface area between the wetting and the remaining non-wetting phase. The increase in surface area enhances mass transfer between both phases, which can be a critical mechanism for all a number of applications. For example, in groundwater remediation, fragmentation displacement could not only lower the residual saturation of the trapped non-aqueous phase and mobilise this phase, it also increases the fluid-fluid contact surface which improves the effectiveness of surfactant addition and can accelerate the rate at which inorganic reagents and/or microbial treatments degrade non-aqueous phase liquids (e.g., Imhoff and Miller (1996), McCray et al. (2001)). Similarly, during enhanced oil recovery, droplet fragmentation could reduce the residual oil saturation and enhance the rate at

which chemicals and gases dissolve in the oil (e.g., Lake (1989)). Both effects increase oil recovery. The dissolution of trapped CO_2 in brine during solubility trapping is one important mechanism for secure subsurface CO_2 sequestration e.g. Riaz et al. (2006) and Neufeld et al. (2010). An increased CO_2-brine surface area due to droplet fragmentation will accelerate this process. Although droplet fragmentation may be limited to carbonate formations as they normally contain a wide range of pore-sizes, it is to be expected that this mechanism is still of global importance considering that carbonates contain about 50% of the world's hydrocarbon reserves and are a major host to the world's groundwater resources. Droplet Fragmentation is an additional mechanism that may need to be included in pore scale models of displacement processes.

3. Summary

In this chapter pore-scale fluid displacement mechanisms observed in a heterogeneous, water-wet carbonate rock are reported. Flooding cycles included *low* and *high* flow rates during drainage and imbibition processes for a pair of immiscible fluid phases. The previously known pore-scale displacement mechanisms of piston-like and snap-off (or at least the clear result of these processes) are identified. Moreover, a new non-wetting phase displacement mechanism was observed in larger pores, referred to as "droplet fragmentation". The displacement of the trapped non-wetting phase oil droplets by water-flooding in the viscous flow regime can occur via a fragmentation mechanism, which has not previously been reported in 3D studies of fluid displacement in natural porous media. Approximate estimates of the additional energy requirements for fragmentation under various plausible assumptions are presented. Calculations of the required energy to fragment a spherical droplet into *N* smaller ones as well as detailed analysis of the fragmentation energies for 3 example pores (with volumes of $10^{10}, 10^{9}, and\ 10^{8}\ \mu m^{3}$) indicate that the additional quantities of energy required for fragmentation are modest, especially if some surface stabilisation of the fragmented droplets is considered (this is actually observed).

The observed fragmentation mechanism has a wide range of implications for understanding fluid displacement in a number of applications including: (a) NAPL contamination studies, (b) enhanced oil recovery, and (c) carbon capture and storage. This new fragmentation pore-scale event may help to explain capillary de-saturation curves for the non-wetting phase. Droplet fragmentation should be included in pore-scale network models of the viscous dominated imbibition processes.

References

AL-GHARBI, M. S. & BLUNT, M. J. 2005. Dynamic network modeling of two-phase drainage in porous media. *Physical Review E,* 71**,** 016308.

ANDREW, M., BIJELJIC, B. & BLUNT, M. J. 2013. Pore-scale imaging of geological carbon dioxide storage under in situ conditions. *Geophysical Research Letters,* 40**,** 3915-3918.

ANDREW, M., BIJELJIC, B. & BLUNT, M. J. 2014. Pore-scale imaging of trapped supercritical carbon dioxide in sandstones and carbonates. *International Journal of Greenhouse Gas Control,* 22**,** 1-14.

ANTON, L. & HILFER, R. 1999. Trapping and mobilization of residual fluid during capillary desaturation in porous media. *Physical Review E,* 59**,** 6819-6823.

ARMSTRONG, R. T., GEORGIADIS, A., OTT, H., KLEMIN, D. & BERG, S. 2014. Critical capillary number: Desaturation studied with fast X-ray computed microtomography. *Geophysical Research Letters,* 41**,** 55-60.

AVRAAM, D. G. & PAYATAKES, A. C. 1995. Flow regimes and relative permeabilities during steady-state two-phase flow in porous media. *Journal of Fluid Mechanics,* 293**,** 207-236.

BLUNT, M. J. 2001. Flow in porous media — pore-network models and multiphase flow. *Current Opinion in Colloid & Interface Science,* 6**,** 197-207.

BLUNT, M. J., JACKSON, M. D., PIRI, M. & VALVATNE, P. H. 2002. Detailed physics, predictive capabilities and macroscopic consequences for pore-network models of multiphase flow. *Advances in Water Resources,* 25**,** 1069-1089.

BLUNT, M. J. & SCHER, H. 1995. Pore-level modeling of wetting. *Physical Review E,* 52**,** 6387-6403.

CENSE, A. & BERG, S. The viscous-capillary paradox in 2-phase flow in porous media. International Symposium of the Society of Core Analysts held in Noordwijk, The Netherlands, 2009. 27-30.

CHATZIS, I., KUNTAMUKKULA, M. & MORROW, N. 1988. Effect of capillary number on the microstructure of residual oil in strongly water-wet sandstones. *SPE Reservoir Engineering,* 3**,** 902-912.

DULLIEN, F. & MACDONALD, I. 1976. Correlating tertiary oil recovery in water-wet systems. *Society of Petroleum Engineers Journal,* 16**,** 7-9.

DULLIEN, F. A. 1991. *Porous media: fluid transport and pore structure*, Academic press.

GASSIN, P.-M., MARTIN-GASSIN, G., MEYER, D., DUFRÊCHE, J.-F. & DIAT, O. 2012. Kinetics of Triton-X100 Transfer Across the Water/Dodecane Interface: Analysis of the Interfacial Tension Variation. *The Journal of Physical Chemistry C,* 116**,** 13152-13160.

HERRING, A. L., HARPER, E. J., ANDERSSON, L., SHEPPARD, A., BAY, B. K. & WILDENSCHILD, D. 2013. Effect of fluid topology on residual nonwetting phase trapping: Implications for geologic CO_2 sequestration. *Advances in Water Resources,* 62, Part A**,** 47-58.

HILD, F. & ROUX, S. 2012. *Digital image correlation*, Wiley-VCH, Weinheim.

IMHOFF, P. T. & MILLER, C. T. 1996. Dissolution Fingering During the Solubilization of Nonaqueous Phase Liquids in Saturated Porous Media: 1. Model Predictions. *Water Resources Research,* 32**,** 1919-1928.

JERAULD, G. & SALTER, S. 1990. The effect of pore-structure on hysteresis in relative permeability and capillary pressure: pore-level modeling. *Transport in Porous Media,* 5**,** 103-151.

LAKE, L. W. 1989. *Enhanced Oil Recovery*, Prentice Hall, Englewood Cliffs, NJ.

LENORMAND, R., ZARCONE, C. & SARR, A. 1983. Mechanisms of the displacement of one fluid by another in a network of capillary ducts. *Journal of Fluid Mechanics,* 135**,** 337-353.

MCCRAY, J. E., BAI, G., MAIER, R. M. & BRUSSEAU, M. L. 2001. Biosurfactant-enhanced solubilization of NAPL mixtures. *Journal of Contaminant Hydrology,* 48**,** 45-68.

MOGENSEN, K. & STENBY, E. H. 1998. A dynamic two-phase pore-scale model of imbibition. *Transport in Porous Media,* 32**,** 299-327.

MORROW, N., CHATZIS, I. & TABER, J. 1988. Entrapment and mobilization of residual oil in bead packs. *SPE Reservoir Engineering,* 3**,** 927-934.

MORROW, N. R., CHATZIS, I., THURAISINGHAM, S. T., KUNTAMUKKULA, M. & LIM, H. T. 1982. Measurement and correlation of conditions for entrapment and mobilization of residual oil. First annual report.

NEUFELD, J. A., HESSE, M. A., RIAZ, A., HALLWORTH, M. A., TCHELEPI, H. A. & HUPPERT, H. E. 2010. Convective dissolution of carbon dioxide in saline aquifers. *Geophysical Research Letters,* 37**,** L22404.

NG, K., DAVIS, H. & SCRIVEN, L. 1978. Visualization of blob mechanics in flow through porous media. *Chemical Engineering Science,* 33**,** 1009-1017.

NGUYEN, V. H., SHEPPARD, A. P., KNACKSTEDT, M. A. & VAL PINCZEWSKI, W. 2006. The effect of displacement rate on imbibition relative permeability and residual saturation. *Journal of Petroleum Science and Engineering,* 52**,** 54-70.

PORTER, M. & WILDENSCHILD, D. 2010. Image analysis algorithms for estimating porous media multiphase flow variables from computed microtomography data: a validation study. *Computational Geosciences,* 14**,** 15-30.

RIAZ, A., HESSE, M., TCHELEPI, H. A. & ORR, F. M. 2006. Onset of convection in a gravitationally unstable diffusive boundary layer in porous media. *Journal of Fluid Mechanics,* 548**,** 87-111.

STEGEMEIER, G. 1977. Mechanisms of entrapment and mobilization of oil in porous media. *Improved Oil Recovery by Surfactant and Polymer Flooding***,** 55-91.

TABER, J. J. 1981. Research on enhanced oil recovery: past, present and future. *Surface phenomena in enhanced oil recovery.* Springer.

TANINO, Y. & BLUNT, M. J. 2012. Capillary trapping in sandstones and carbonates: Dependence on pore structure. *Water Resources Research,* 48.

YU, L. & WARDLAW, N. C. 1986. The influence of wettability and critical pore-throat size ratio on snap—off. *Journal of Colloid and Interface Science,* 109**,** 461-472.

ZHOU, N., MATSUMOTO, T., HOSOKAWA, T. & SUEKANE, T. 2010. Pore-scale visualization of gas trapping in porous media by X-ray CT scanning. *Flow Measurement and Instrumentation,* 21**,** 262-267.

Chapter 6

Pore-scale Wettability Assessment

The core plug used for experiments that are reported in chapters 4 and 5 was shown to be water-wet based on a number of evidences including: (a) the size distribution of the pores occupied by the brine and oil phases after the drainage process (refer to chapter 4, section 1), (b) the observed contact angle between the oil-brine interface and the rock surface (refer to section 2), (c) the development of the brine films, and (d) the snap-off and capillary trapping of the oil phase. In order to investigate the effect of wettability on the pore-scale fluid distributions this water-wet core plug was aged in a crude oil sample to alter its wettability. The mechanism of wettability alteration by aging in crude oil is described in chapter 2, section 6. The aging procedure can be found in chapter 3 section 4.

Results of a similar drainage-imbibition core flooding experiment performed on the oil-aged core plug are presented in this chapter, as are results of a similar cycle performed on a separate core which proved to have heterogeneous wettability at the pore-scale. The details of the test procedures are described in chapter 3 section 4.

1. Pore-scale Wettability Indicators

1.1. Slow Brine Injection

As a result of wettability alteration the surface of the rock is no longer water-wet, therefore, brine film development and corner film flow was not observed. In addition, the brine injection is no longer an imbibition process (i.e. it is not spontaneous), rather the brine injection can be classified as a drainage process if the core was uniformly oil-wet.

The experiment started by slow brine injection into the altered wettability core plug initially saturated with oil. The injection flow rate was 5 µl/min, corresponding to N_c=9.77×10^{-8}. Hence, this slow brine injection occurred in capillary-dominated flow regime. During the brine injection (here drainage process) the main displacement mechanism expected is piston-like displacement which should result in high oil recoveries and development of oil-films on the walls and in the corners of the oil-wet pores. Figure 6.1 shows three example µCT slices of the core captured before and after the 5 µl/min brine injection step. Brine has displaced the oil phase from the

majority of the larger pores. No visible oil film was explicitly observed at this stage. In addition, no features associated with intra-pore physics were observed at this stage, meaning that the pores were mainly occupied by a single fluid phase. It is probable that very thin films of oil (of sub-micron thickness) existed on the rock surface but were not captured on these images due to the resolution and sharpness limitations.

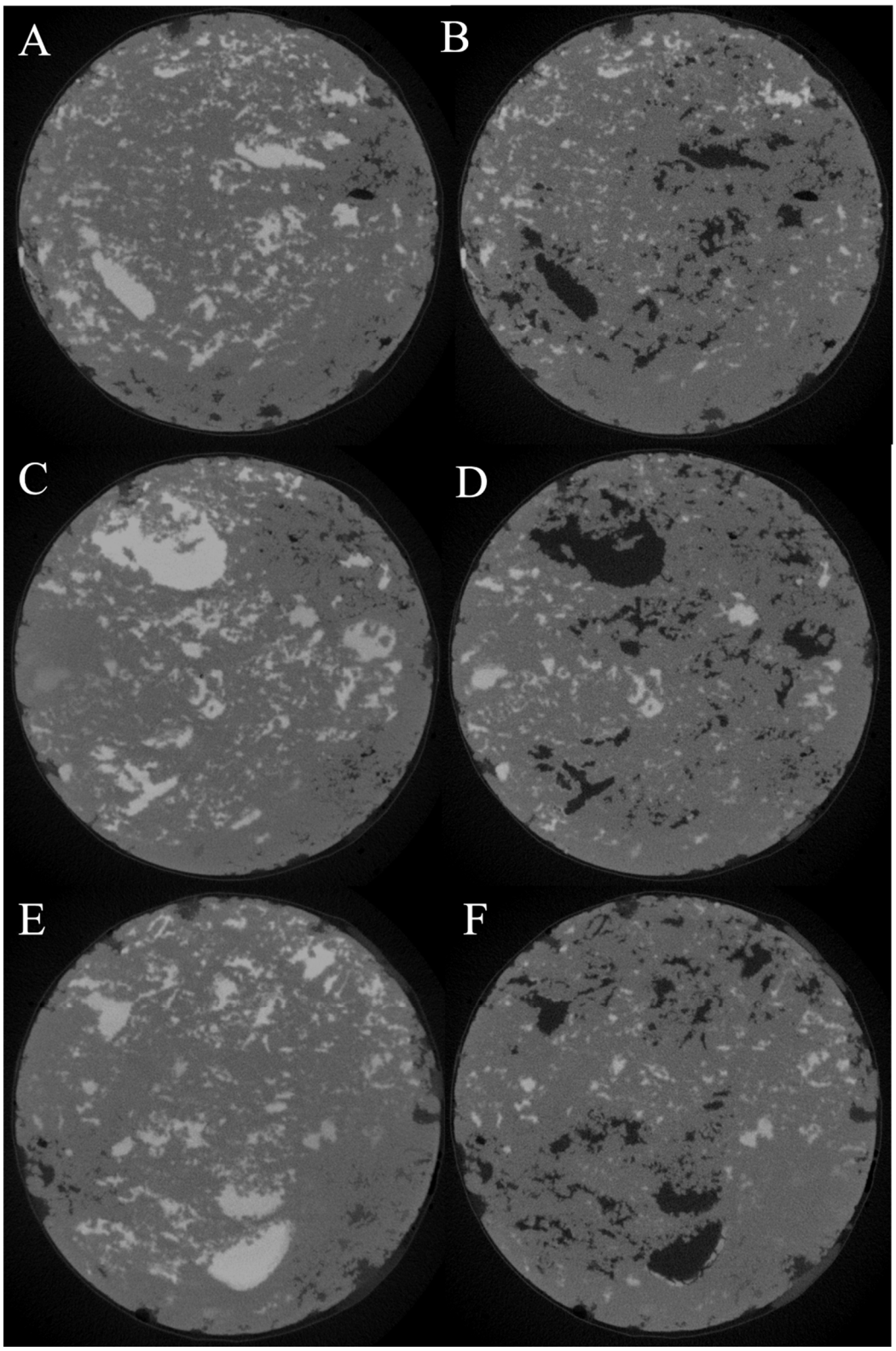

Figure 6.1: Example µCT slices of the core captured before (A, C, and E) and after (B, D, and F) the 5 µl/min brine injection step. Brine has displaced the oil phase out of the majority of the larger pores. No visible oil film is explicitly observed in the images collected at this stage.

In the capillary-dominated drainage process of the water-wet experiment (oil displacing brine with 10 µl/min) 86% of the saturating brine was recovered, leaving behind only 14% of brine in smaller pores (see chapter 4, section 1, these saturations are based on high magnification images). However, for the altered wettability experiment, it was observed that some of the pores (few larger ones but mostly medium to small sized ones) have remained oil-saturated after the capillary-dominated drainage. Overall 62 % of the oil saturation was recovered leaving behind 38 % of remaining oil in the pore space of the core plug. These un-invaded pores may be connected only through narrower throats that could not be accessed at the injection pressures used.

1.1.1. Cluster Size Distribution

The reconstructed images were cropped to 820×890×1580 voxels before being filtered using a non-local means filter to suppress the noise but preserve sharpness (refer to chapter 3, section 3). Oil and brine phases were segmented using watershed segmentation (refer to chapter 3, section 3). The binary images were subsequently labelled with the labeling criteria set to 26 such that any two voxels with at least one common vertex are considered as connected (refer to chapter 3, section 3). Based on MICP test results (refer to chapter 3, section 3) an average of ~26% of the pore space is connected to pore-throats narrower than the image resolution (10µm). The resolution limitation made it impossible to distinguish between the clusters that are linked by narrow pore-throats and the disconnected clusters. Based on the discussion in (refer to chapter 3, section 3) here the fluid labels are assumed to represent the fluid clusters.

Figure 6.2A and 2B shows 3D renderings of brine and oil clusters occupying the core plug after the capillary-dominated brine injection, respectively. Figure 6.2C and 6.2D shows only the brine and oil clusters with volumes larger than 10^6 voxels, respectively. It is clear that most of the larger pores have become occupied by the brine phase during the capillary-dominated brine injection step.

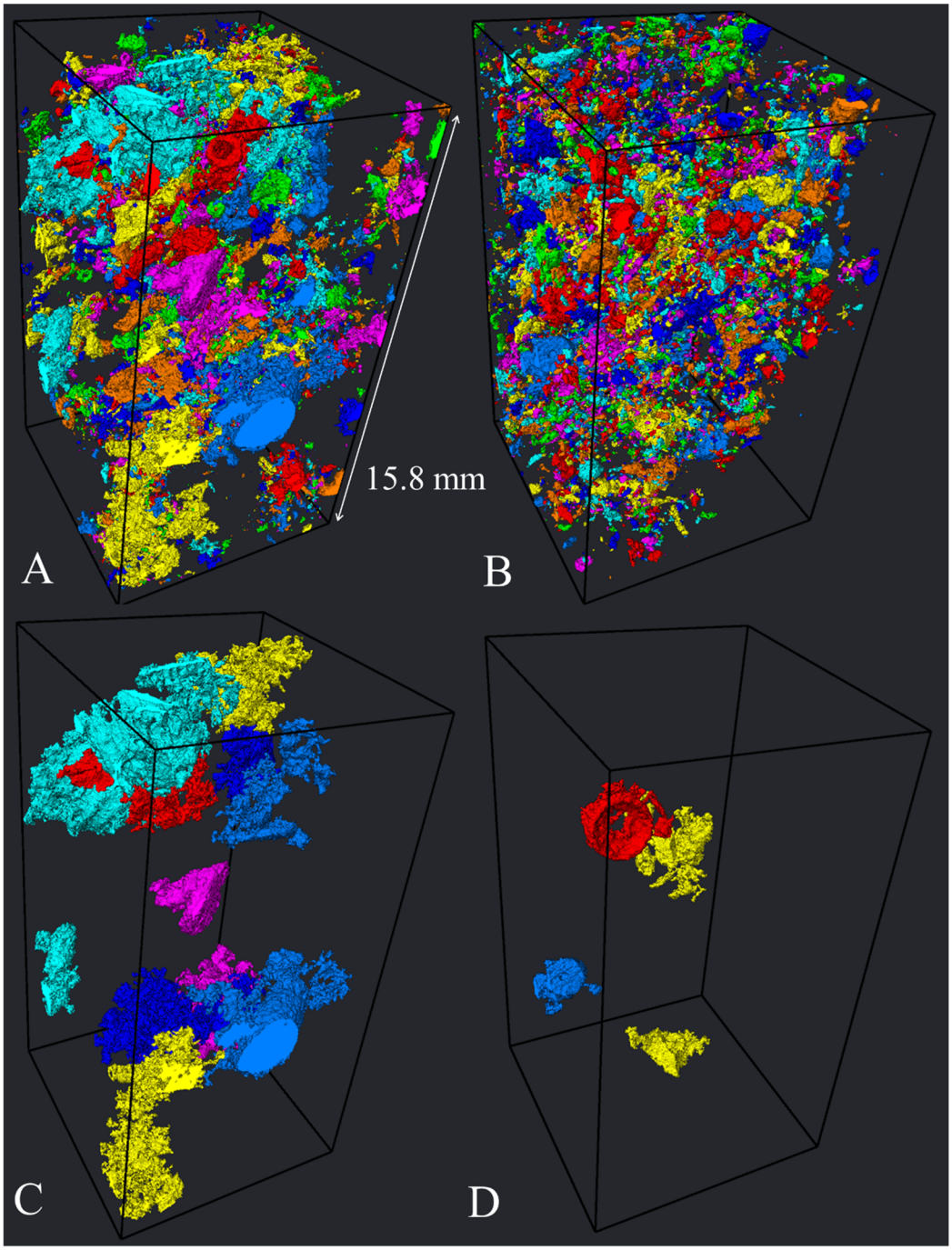

Figure 6.2: 3D rendering of brine (A) and oil (B) clusters after the the capillary-dominated brine injection step. (C, D) show respective brine and oil clusters with volumes larger than 10^6 voxels.

Figures 6.3 and 6.4 show the cluster size distributions (volume fraction and frequency) for the brine and oil phases shown in Figure 6.2A and 6.2B. The volumetric fraction is the saturation of each phase (i.e. fluid volume relative to the pore volume). The two plots confirm what is visually observable from Figure 6.2 that

is 0.36 (i.e. 0.62-0.26) of the pore space was occupied by brine clusters larger than 10^9 voxels in volume. This forms ~58% (i.e. (0.62-0.26)/0.62) of the brine saturation (S_b = 0.62) which appears to form 12 clusters of 10^9< volume <10^{10} and one cluster of volume > 10^{10} (Figure 6.4). However, only 0.05 (i.e. 0.38-0.33) of the pore space was occupied by oil clusters larger than 10^9 voxels in volume, that is ~87% (i.e. (0.38-0.33)/0.38) of the remaining oil saturation (S_{or} = 0.38) in form of oil clusters with volumes < 10^9 voxels.

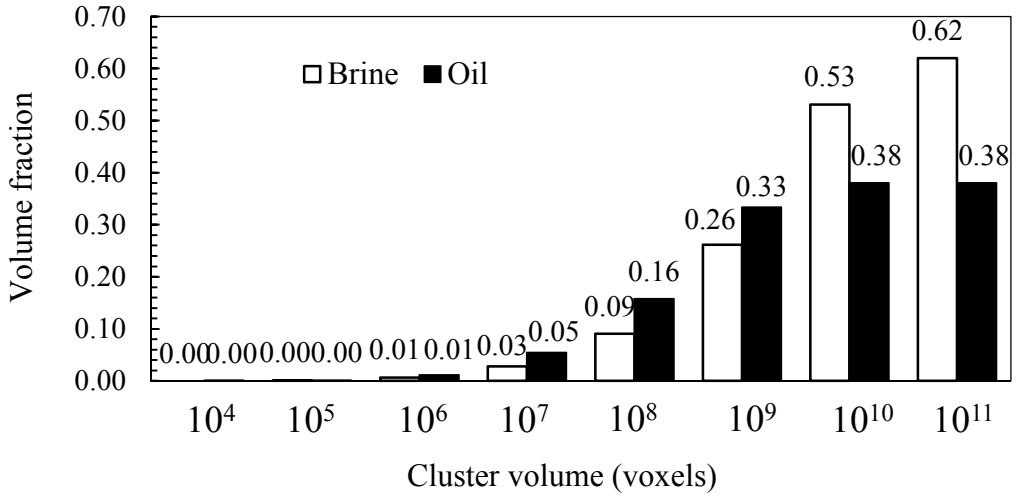

Figure 6.3: Volumetric distribution of oil and brine clusters after the capillary-dominated brine injection step. The larger clusters saturating the pore space are mostly brine and few oil clusters.

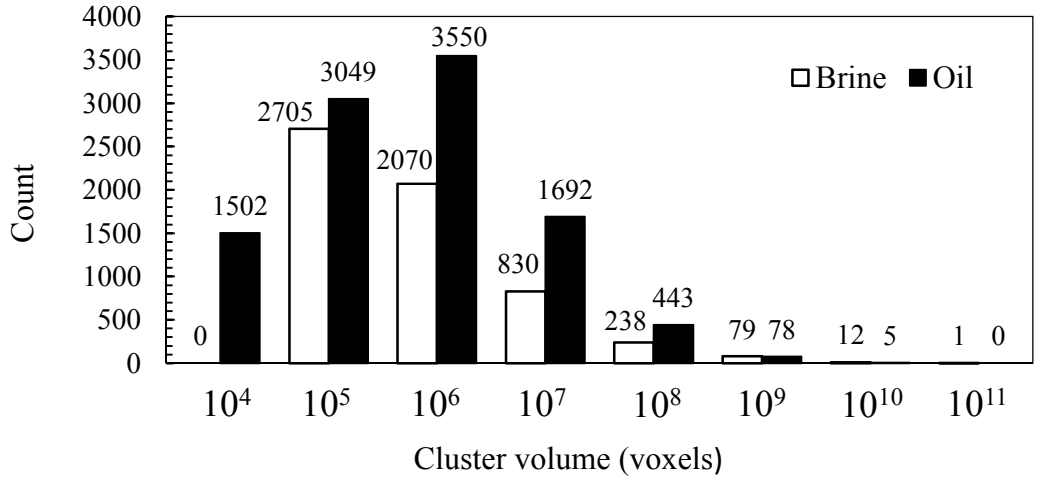

Figure 6.4: Number-based distribution of oil and brine clusters occupying the pore space of the core after the capillary-dominated brine injection step. Larger clusters are found to be brine clusters mostly.

1.1.2. Comparison between Fluid Cluster Size Distributions Occupying the Water-wet and Oil-wet Core Plugs

In this section the volumetric distributions of oil and brine clusters for the water-wet (WW) and oil-wet (OW) core plugs after the *slow brine injection* steps are discussed. The cluster size distributions are compared for a 16 mm section of the core plug that was imaged in both experiments, see Figure 6.5.

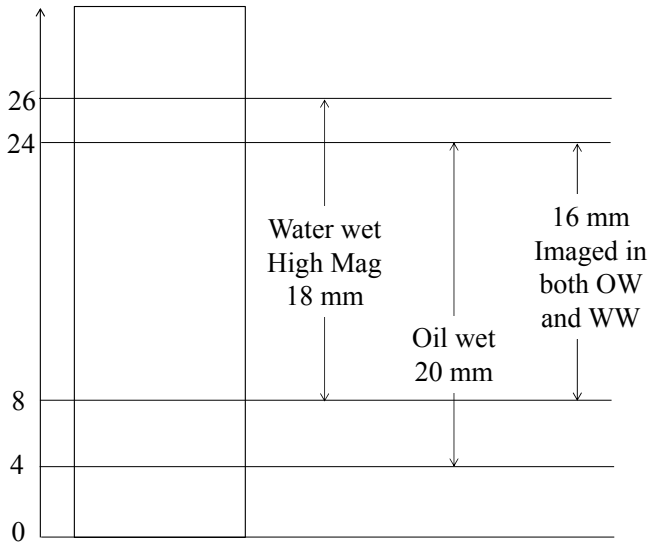

Figure 6.5: Common section of the core plug imaged in both WW and OW experiments, L ~ 16 mm

The remaining oil saturation in this section of the plug was 38% and 55% for the OW and WW cases, respectively, this means 17% more oil recovery for the OW conditions. In addition to the amount of remaining oil the structure of it was different under the two wetting conditions. Under WW conditions the oil production ceased in the very early stages of brine injection. The remaining oil was in form of isolated oil droplets trapped in a single or multiple connected pores. In the OW case production of oil continued for more than 20 pore volumes of brine injection. This extended production indicates that the oil films (although not visible on the images) were established across the pore surfaces maintaining the connectivity of the oil phase, assisting the oil flow and recovery. Further oil might have been recovered if the brine injection was continued. Due to time limitations the injections had to be stopped after 20 pore volumes. The remaining oil at this stage (38%) may not represent the

achievable residual oil saturation at this pressure levels.The remaining oil clusters after the slow brine injection steps are shown in Figure 6.6A and 6.6C for the OW, WW states. Figure 6.6B and 6.6D shows oil clusters larger than 10^9 µm^3. The resolution of the images acquired in the WW and OW experiments were different (11.25 and 10 µm respectively), therefore to make the volumes comparable the cluster sizes were converted to real volumes (µm^3).

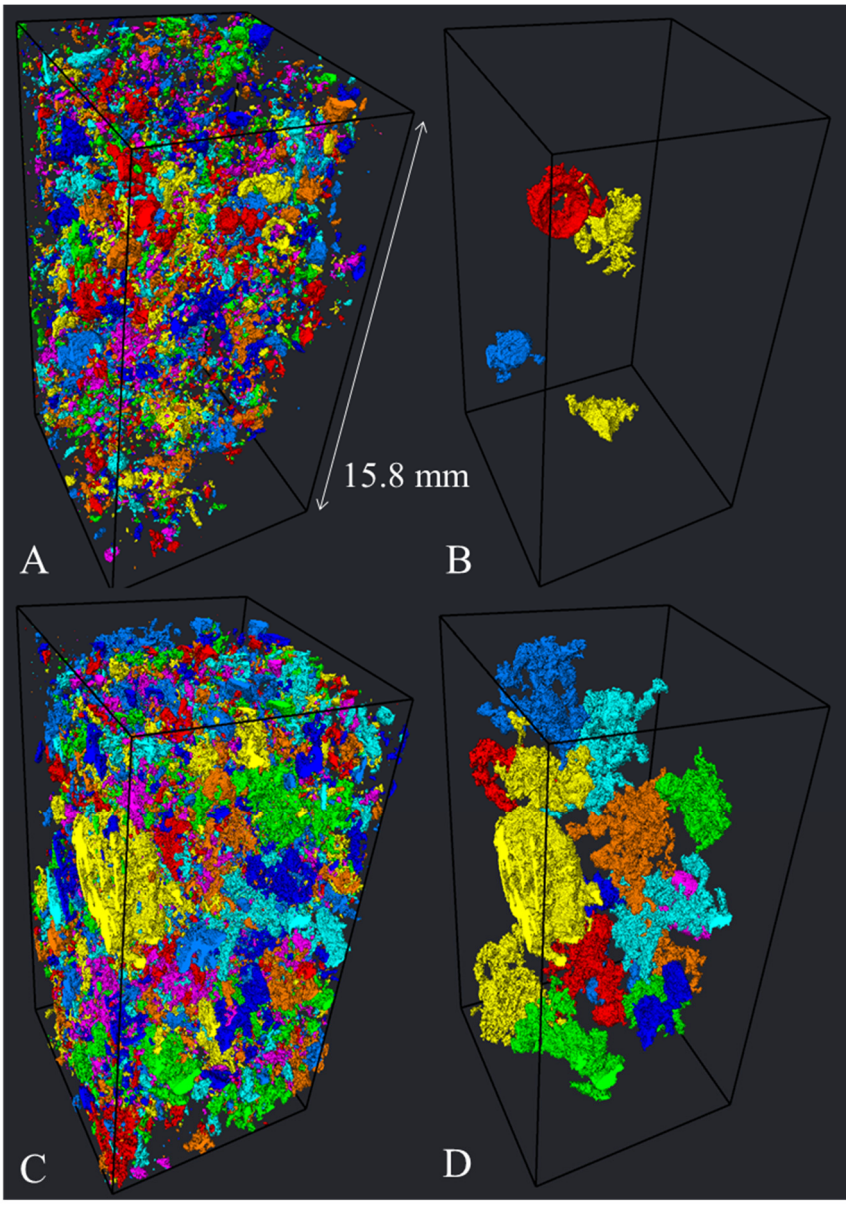

Figure 6.6: 3D rendering of the remaining oil clusters after the *slow brine injection* steps from OW (A and B) and WW (C and D) experiments. For the WW case the remaining oil was trapped in the larger pores as a result of snap-off. B and D show oil clusters larger than 10^9 µm^3.

Figures 6.7 and 6.8 show cluster size distributions (volume fraction and frequency) of the oil phase after the slow brine injection for the WW and OW cases. The volume fraction distribution is the saturation of each fluid phase. The distributions show what is visually clear in Figure 6.6. The WW core had 40% (i.e. (0.55-0.33)/0.55) of the trapped oil in form of 19 large oil clusters with volume > 10^9 μm^3, whereas in the OW case only ~13% (i.e. (0.38-0.34)/0.38) of the remaining oil clusters had volumes exceeding 10^9 μm^3. The 5 clusters shown in Figure 6.6B are these large residual oil clusters.

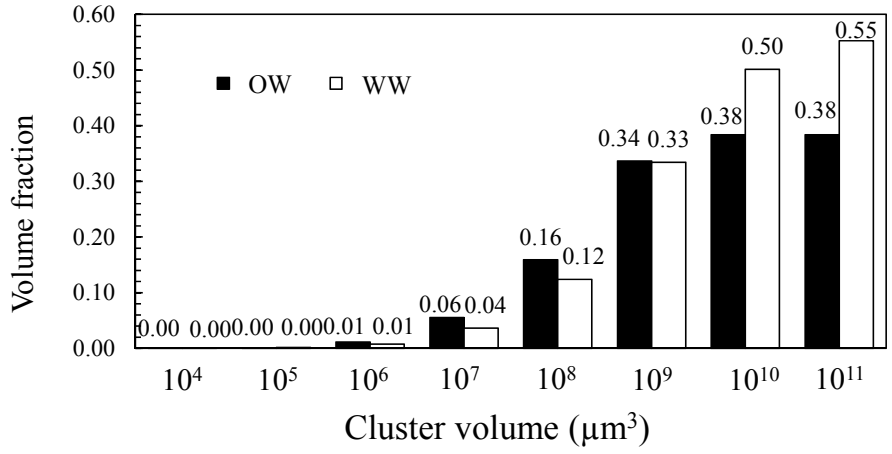

Figure 6.7: Volume fraction of oil clusters based on oil cluster volumes after the slow brine injection steps for the WW and OW cases. The oil clusters saturating the pore space of the WW case are larger as a result of snap-off events.

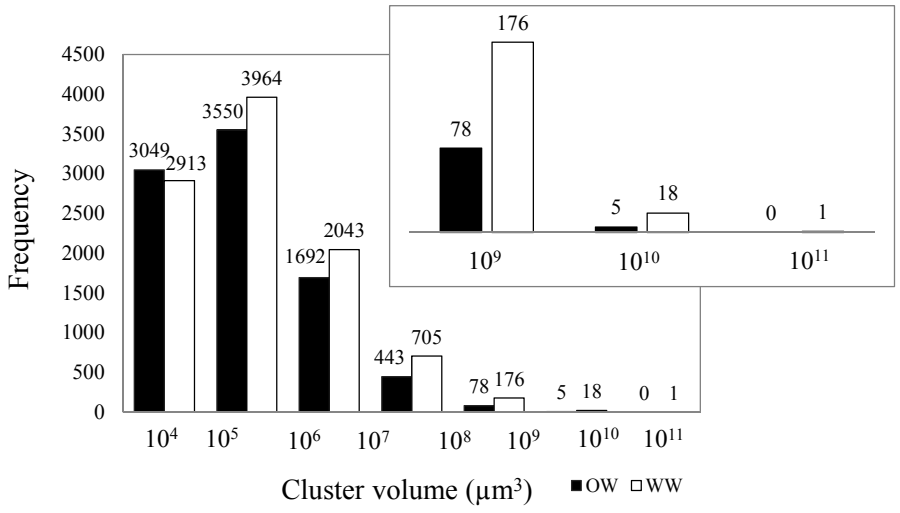

Figure 6.8: Frequency of oil clusters saturating the pore space after the slow brine injection steps. More of the larger oil clusters were trapped in the core under WW state.

1.2. Fast Brine Injection

As a result of brine injection at a higher flow rate of 250 µl/min (corresponding to N_c=4.88×10^{-6}) a further 5 % of original oil saturation was displaced out of the pore space. In particular the 6 oil clusters of volume > 10^6 voxels (Figure 6.2D) were no longer present in the pore space of the rock after this faster brine injection. In addition, oil films surrounding brine droplets were observed, see Figure 6.9C and 9E. The observation of oil films is an indication of the success of the aging process in rending parts of the rock oil-wet. However, the development of oil films were not observed throughout the core plug at this stage, i.e. there were limited number of oil film examples resolved, one of which is presented in Figure 6.9.

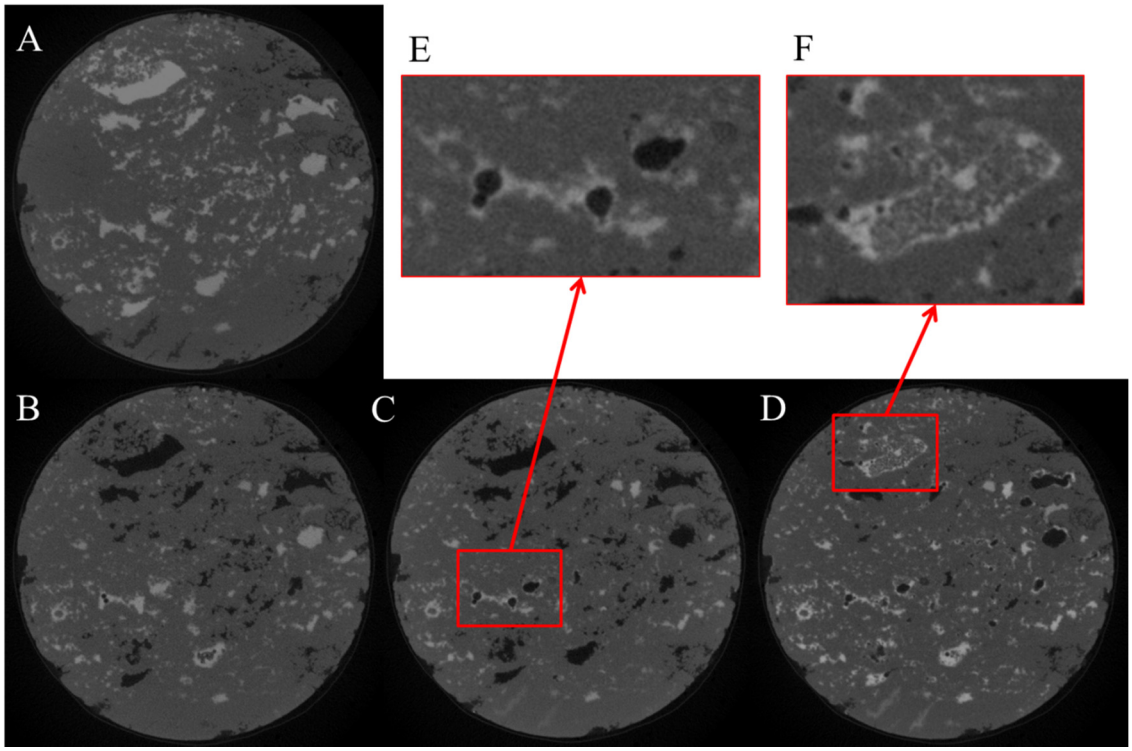

Figure 6.9: Example µCT slice after primary oil saturation (A), 5 µl/min brine injection (B), 250 µl/min brine injection (C), and 5 µl/min oil injection (D). (E) Visible oil films surrounding the brine phase shows the rock is preferentially oil-wet. A fine structured brine in oil emulsion is formed as a result of subsequent oil injection step at 5 µl/min (F).

1.3. Oil Injection Steps

Subsequent to the brine injection steps oil was injected into the core plug with 5 and 150 µl/min (corresponding to N_c=1.98×10^{-7} and 5.93×10^{-6}, respectively). Swelling of

the (probably previously established) oil films provided the chance to capture them on the µCT images. Figures 6.9 and 6.10 show examples of the oil films (white) surrounding the brine phase (black) after the slow oil injection step.

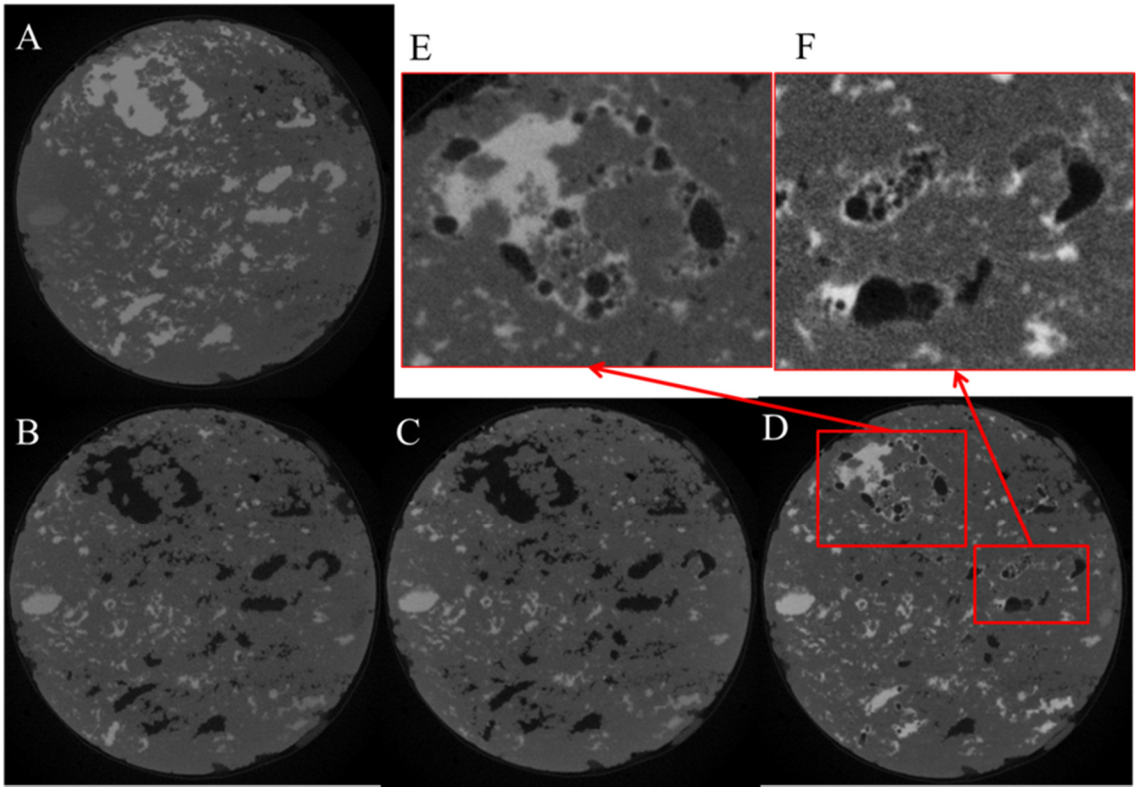

Figure 6.10: Example µCT slice after primary oil saturation (A), 5 µl/min brine injection (B), 250 µl/min brine injection (C), and 5 µl/min oil injection (D). A fine structured brine in oil emulsion is formed after the oil injection step (E, F).

A *brine in oil emulsion* phase has been formed during the slow oil injection step and was present in the larger pores (Figures 6.9F, 6.10E and 6.10F). The continuous phase of the emulsion was the oil phase. Visible oil films were captured in contact with the rock surface. The formation of emulsions is a well-known process in the oil industry and occurs at different stages from oil production to downstream refining processes (Taylor, 1992, Schramm, 1992). Formation of emulsions can change the properties of the oil phase dramatically. Of particular importance is the viscosity of the emulsion which depending on the type of emulsion (oil in water or water in oil) can be significantly different from that of the oil phase. This viscosity alteration can have adverse or beneficial impact on the oil recovery facilitated by water flooding.

For heavy oil reservoirs the oil in water emulsions (o/w), induced by alkali surfactants, display lower viscosity compared to the crude oil, which improves the oil recovery by water flooding (Sheng, 2010, McAuliffe, 1973, Liu et al., 2006, Bryan and Kantzas, 2007). In contrast water in oil emulsions (w/o) can have exponentially increased viscosities compared to that of the crude oil phase. This increase in viscosity results in a significant drop in relative permeability, and hence increase in the pressure drop across the porous media, causing severe problems for water-flooding processes. *In-situ* formation of water in oil emulsions has been observed in 2D micro-models (Rezaei and Firoozabadi, 2014), see Figure 6.11. However, to the best of the author's knowledge there has been no report on direct visualization of emulsion formation and flow in 3D space of rocks.

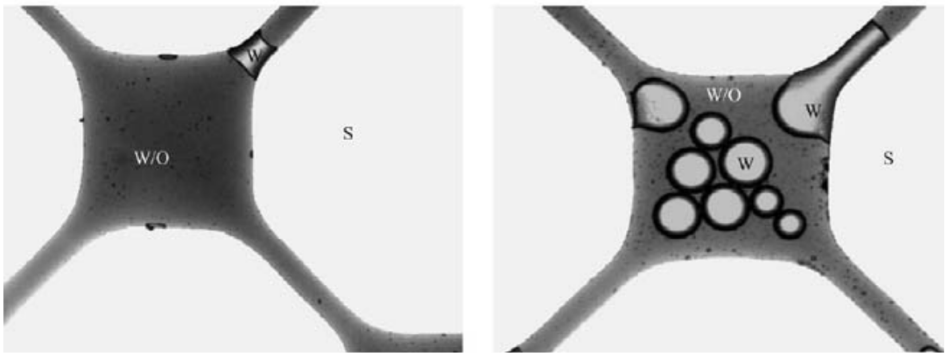

Figure 6.11: Formation of micro-emulsion (A) and micro and macro emulsions (B) observed in a micro-model. Oil and water phases were crude oil and 0.013 M KCL, respectively. Image from Rezaei and Firoozabadi (2014)

The aspect ratio of the micro-model shown in Figure 6.11 is very large (~8), and that is probably why the macro-scale emulsion is formed (i.e. the formation of a macro-scale emulsion is caused by snap-off of the water phase).

The process of emulsification by forcing a liquid through capillaries (grooves) into another liquid to which it is immiscible is a well-established emulsion production method. The method is referred to as micro-channel (MC) technique (Kawakatsu et al., 1997). Figure 6.12 shows the structure of MC channels and the emulsion formation process, schematically. The droplet size of the produced emulsion is related to the aspect ratio of the micro-structure used (Kobayashi et al., 2004).

Literature suggests that high-aspect-ratio microstructures (more than 3), in particular, can produce stable and uniform emulsions (Kobayashi et al., 2004). Here uniform refers to small variations in the droplet size.

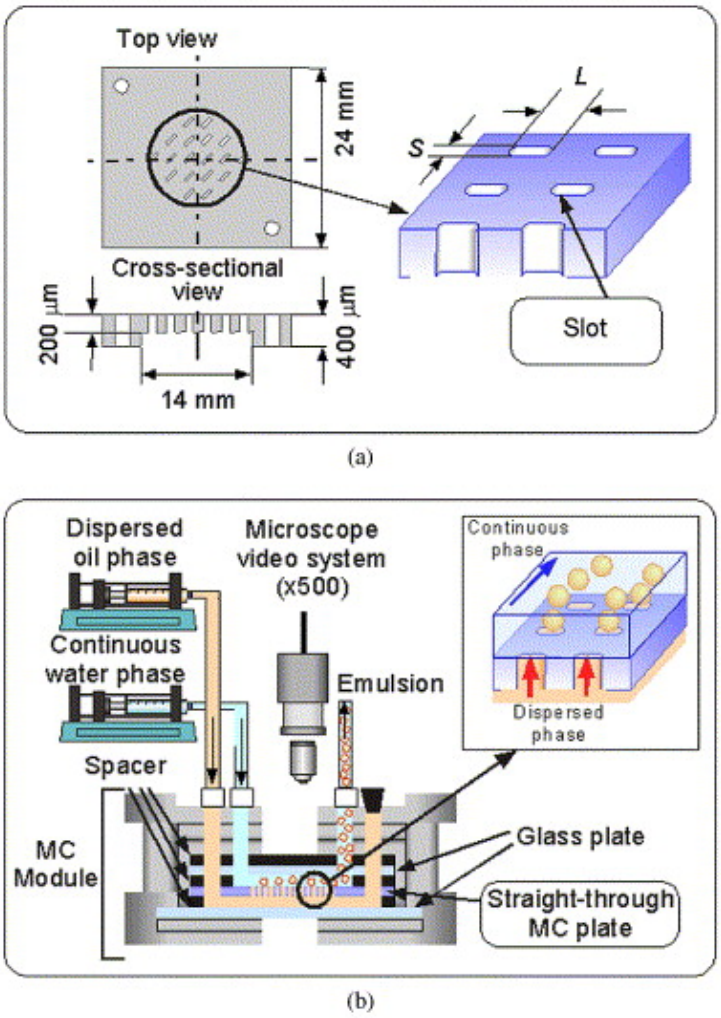

Figure 6.12: MC emulsification plates' structure (a). MC emulsification system (b). Image from Kobayashi et al. (2004).

Immiscible displacement of brine and oil in porous carbonate media studied here involves processes similar to MC technique. The two phases are immiscible and the carbonate has many narrow throats that can act similar to the grooves used in MC technique. While the conditions are suitable for emulsion formation, not all oil-brine displacement processes performed in this study displayed emulsification. The existence of organic particles (asphaltene aggregates) in the OW core plug may be a

key factor in stabilisation of produced emulsions. In absence of such stabilising factors any produced dispersed droplets may readily coalesce. Real time imaging may provide insight in the mechanism of emulsion formation and the effects of crude oil residues on the occurrence of such emulsions. Another factor seems to be the displacement process (i.e. drainage or imbibition). The emulsion, mostly, has formed in the pores which were occupied by the brine phase upon injection of the oil phase. The continuous phase is the wetting phase (i.e. oil) and the dispersed phase is the non-wetting brine phase. Due to the formation of the emulsion in the pore space of the rock (and hence a substantial increase in pressure drop across the core), for the final fast oil injection the back pressure regulator had to be removed and the injection flow rate had to be reduced to 150 μl/min to stay within the pressure limitations of the set-up ($P_{injection}$<690 kPa).

Due to small structure of the emulsion and the limited sharpness of the acquired images quantitative analysis of the emulsion phase is not possible. Particularly important factors to study (where image quality permits) are the emulsion droplet size distribution as well as the changes in the droplet sizes with time. Such information can be used to model the viscosity and hence the flow behaviour of the emulsion in porous media. Qualitative analysis of the images that captured the emulsion phase leads to the following points:

- In agreement with the MC emulsion preparation technique in the present experiments the emulsions were mostly observed in the larger pores with higher aspect ratios. The emulsion is composed of brine droplets with a range of sizes, from hundreds of microns diameter (clearly visible on the images) down to few microns diameter (sub-resolution, visible through a partial volume effect).
- The emulsion was a persistent, stable feature in the pore space of the rock. Three independent scans of the core plug acquired on the same day as the injection, and subsequently at 33, and 73 days post injection all have recorded the presence of the emulsion and little apparent reduction in the amount of emulsion present. The structure of the fluid phases and brine in oil emulsion

is shown to be very similar after 33 days (Figure 6.13A and 13B), whereas although still present the structure of the emulsion displays some differences after 73 days. This was mainly caused by a saturation redistribution in the core plug. The oil phase had moved towards the bottom of the plug. It is speculated that this long term segregation may be driven by very slight density difference between the brine and the crude mixed oil phase.

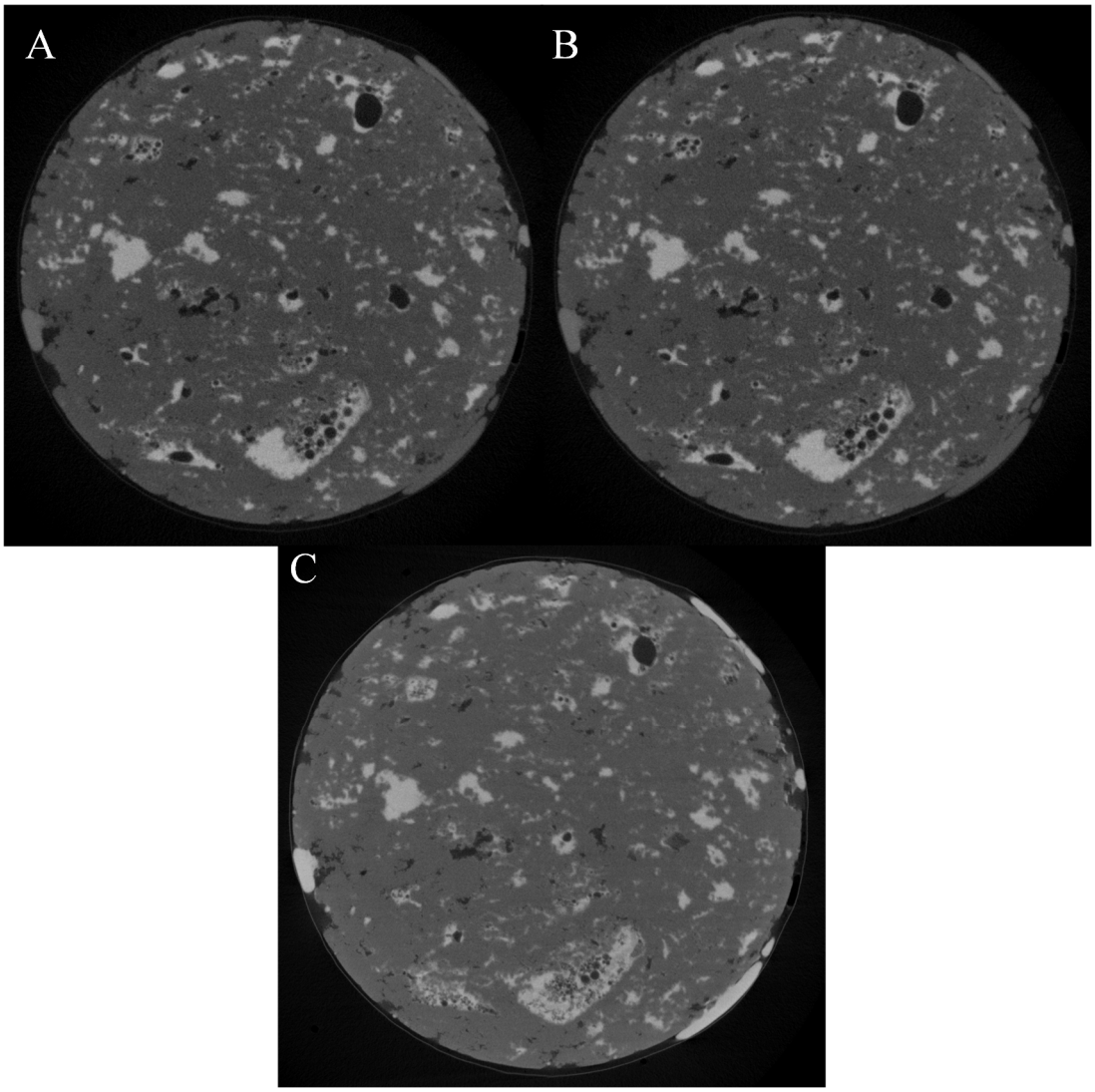

Figure 6.13: Example µCT slice from the data captured after the 150 µl/min oil injection step collected at same day (A), and with time delay of 33, 73 days, respectively (B and C). The emulsion appears to be mostly stable in the first two scans; the third scan shows the presence of the emulsion with slight changes in its structure due to the slow fluid redistributions probably caused by slight density differences.

Two mechanisms that can stabilize an emulsion are:

- *Stabilization by organic polar compounds:* Asphaltene and resins are organic polar components of crude oil (refer to chapter 2, section 6) which can act as emulsion stabilizers (Mansurov et al., 1987, Eley et al., 1987, McLean and Kilpatrick, 1997, Sjöblom et al., 1990). The mechanism of stabilization of oil-water emulsions is shown in Figure 6.14. Accumulation of asphaltene-resin colloidal aggregates (Figure 6.14C) on the oil-water interface makes the interface thicker and hence harder to collapse (Sullivan and Kilpatrick, 2002).

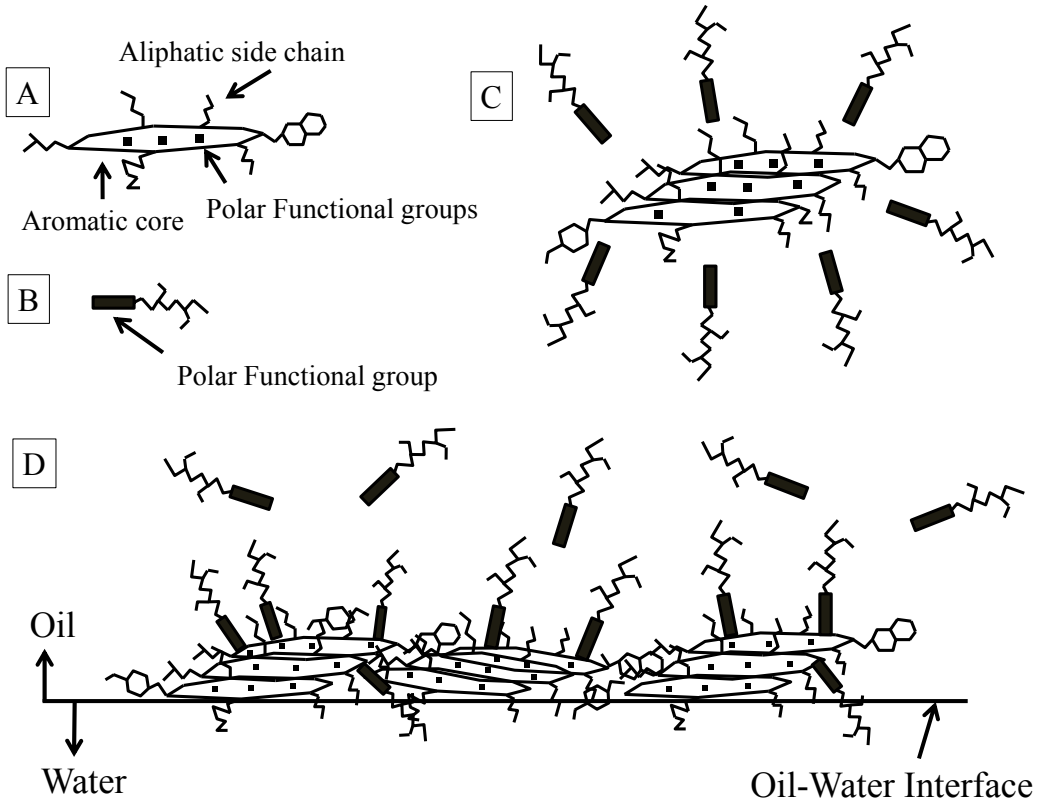

Figure 6.14: Molecular structure of asphaltene and resin (A, B). Resin stabilised asphaltene aggregates (C). Resins interacts with asphaltene aggregates through polar functional groups (D) Resin-asphaltene aggregate deposition on the oil-water interface makes the interface rigid and harder to break. Figure adopted from Sullivan and Kilpatrick (2002)

- *Particle stabilized (Pickering) emulsions*: Stabilization caused by µm-scale inorganic solid particles such as clay, shale and silica which (if present) adsorb to the oil-water interface (Figure 6.15), making the interface thicker,

which prevents the coalescence of the emulsion droplets (Pickering, 1907). The particle size (Schramm, 1992, Schulman and Leja, 1954, Kitchener and Mussellwhite, 1968) and concentration (Menon and Wasan, 1986, Tambe and Sharma, 1993) and wettability (Arditty et al., 2004) are among the most influential factors in assisting the emulsion stabilization.

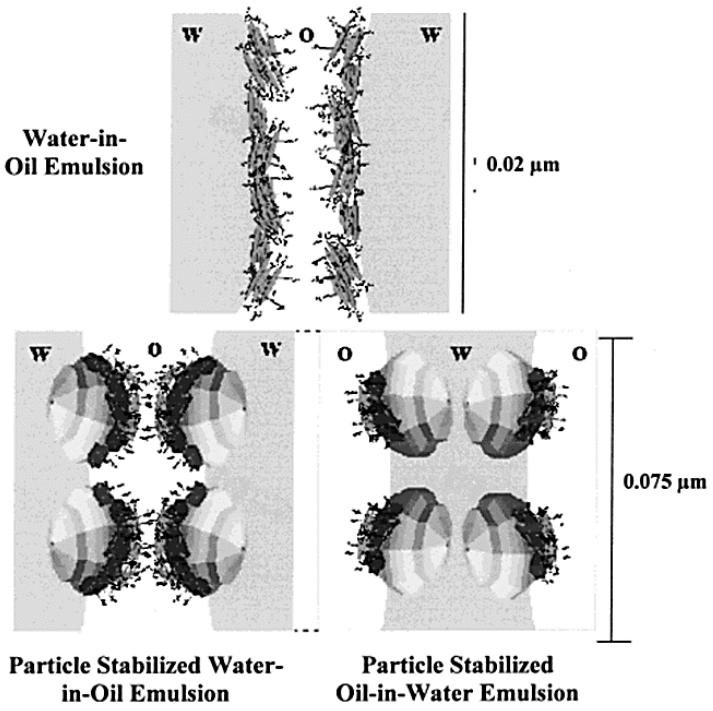

Figure 6.15: Schematic model of stabilization mechanism of oil-water emulsions using organic particles alone (A) or a combination of organic and inorganic particles (B). The presence of solid particles makes the oil-brine interface thicker and hence more stable, after Sullivan and Kilpatrick (2002).

It is possible that the crude oil used for the aging process contained some inorganic solid particles which combined with the present asphaltene and resin compounds have stabilised the observed emulsion.

The presented data demonstrate that µCT technique can provide excellent means to monitor in situ emulsion formation and evolution. Investigating the oil in water emulsions has implications in heavy oil production. For example, direct 3D visualization (and subsequent quantitative analysis of the images) can provide a

means to study the effectiveness of the different surfactants in heavy oil mobilization and production.

2. Pore-scale Wettability Analysis – Comparison between WW and OW Contact Angle Distributions

2.1. Background

Andrew et al. (2014) reported μCT imaging of non-wetting fluid phase droplets (CO_2) trapped in the pore space of an oolitic limestone. They manually measured the contact angle on 300 locations on the planes perpendicular to the contact lines. The surface they studied was preferentially WW for which they reported a distribution of contact angles with average of 45 ± 6. They argued the different contact angles may occur due to surface roughness and hysteresis in contact angle, which is the difference between the drainage and imbibition contact angles. Using a similar approach, in this study oil-brine-dolomite contact angles were measured and compared for the OW and WW states. Two comparisons are presented, (a) the contact angles measured for two discrete oil and brine droplets (through different 2D slices) trapped in the same pore under the WW and OW states, respectively, and (b) the contact angles measured on a random selection of pores distributed in the entire length of the OW and WW cores.

2.2. Contact Angle Measurements for a Single Pore

Here contact angle measurements over various slices through one specific pore is presented. Figure 6.16 shows the corresponding μCT slices from the SD core plug under the WW (A) and OW (B) states after the fast brine (700 μl/min, refer to chapter 3, section 4) and fast oil (150 μl/min, refer to chapter 3, section 4) injection steps, respectively. Figure 6.16C and 6.16D shows the same slice of the core plug saturated by the respective wetting phases, (i.e. brine and oil), these were the initial saturation states of the WW and OW experiments, respectively. The yellow arrows indicate that the WW images are rotated with respect to the OW images by almost 90 degrees, counter clockwise. The pore highlighted by the red arrow hosts an oil droplet surrounded by brine and a brine droplet surrounded by oil in the WW and OW cases, respectively. The clear contrast between the oil-brine-rock configurations is ruled by the difference in the wettability of the rock surface at the pore-scale.

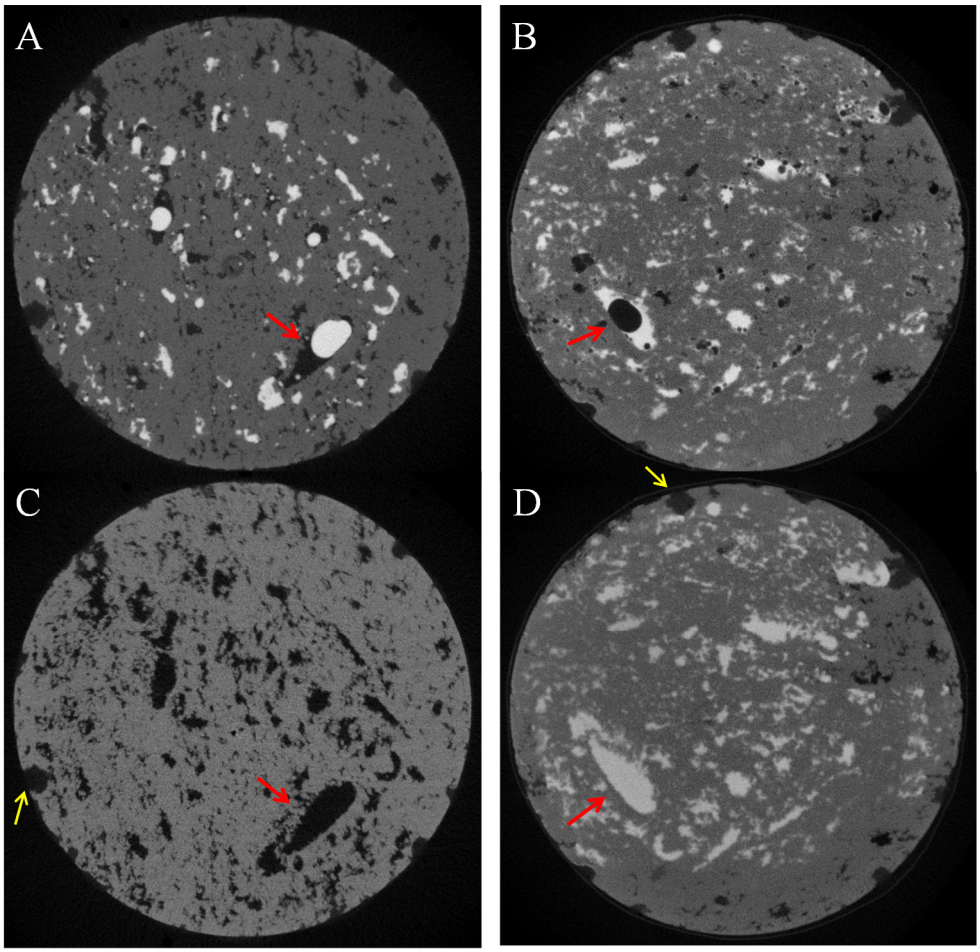

Figure 6.16: Corresponding µCT slice from WW core after the fast brine injection (A) and OW core after the fast oil injection (B). The oil and brine phases are shown in white and black colours, respectively. (C, D) Corresponding µCT slice of the core plug at their initial saturation stages. Fluid-fluid-rock configurations display two different wetting systems.

Figure 6.17A and 6.17B shows 3D rendering of two surfaces fitted to the oil and brine droplets that are shown in Figure 6.16A and 6.16B.

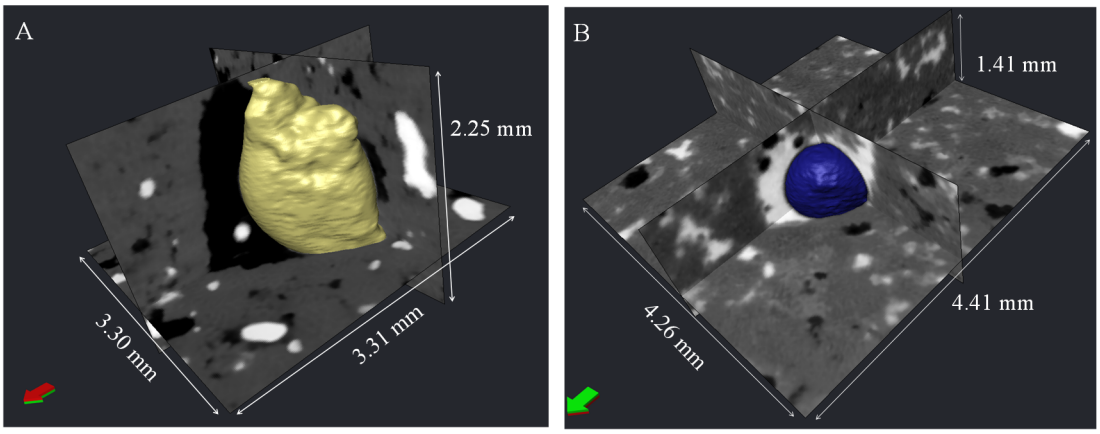

Figure 6.17: 3D rendering of two surfaces fitted to the oil and brine droplets highlighted by the red arrows in Figure 6.16A and 6.16B.

2.2.1. Water-wet State

Example contact angle measurements from different slices on the XY plane are shown in Figure 6.18. Figure 6.19A shows an example contact angle measurement based on a XZ slice. In an ideal case the solid surface should exhibit no roughness to permit identification of the surface line on 2D images. In natural pore systems, however, the surfaces are inevitably rough. Therefore, where possible, the measurements should be constricted to the examples with less distinctive surface roughness. The YZ slices shown in Figure 6.19B could not be used for reliable contact angle measurements due to the curved shape of the pore wall and the visible surface roughness created by the crystals of the dolomite.

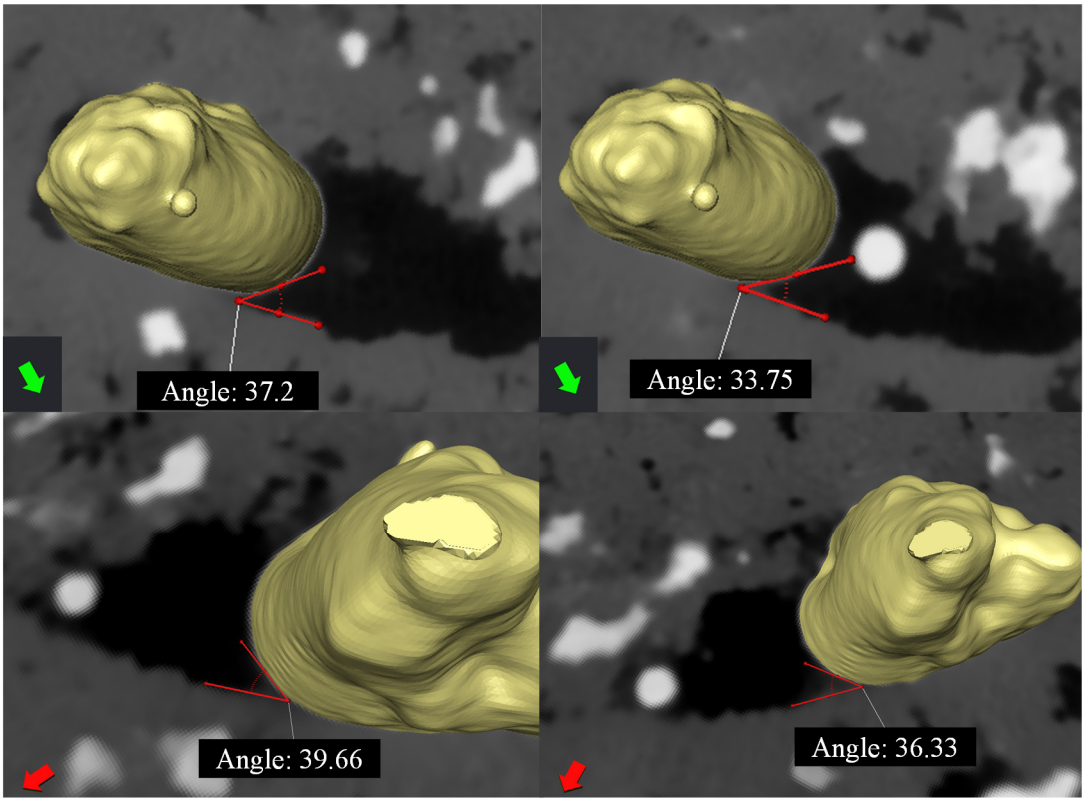

Figure 6.18: Example contact angle measurements on different XY slices. Contact angles measured through the wetting phase (here brine).

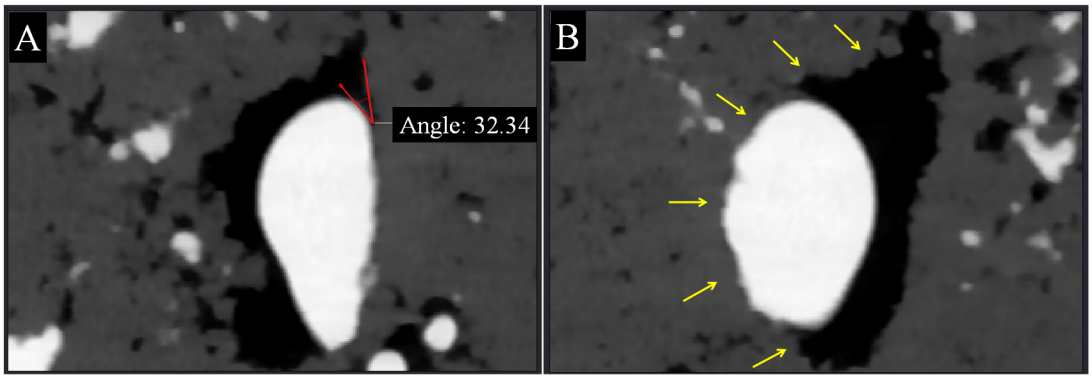

Figure 6.19: Example contact angle measurements on a XZ slice (A). The curved pore wall on YZ slices (indicated by yellow arrows) may not provide reliable contact angle measurements (B).

2.2.2. Oil-wet State

Figure 6.20 shows contact angle measurements for the brine droplet trapped in the same pore, under the OW condition. The 2D slices are on XY plane, 10 slices apart (0.1 mm).

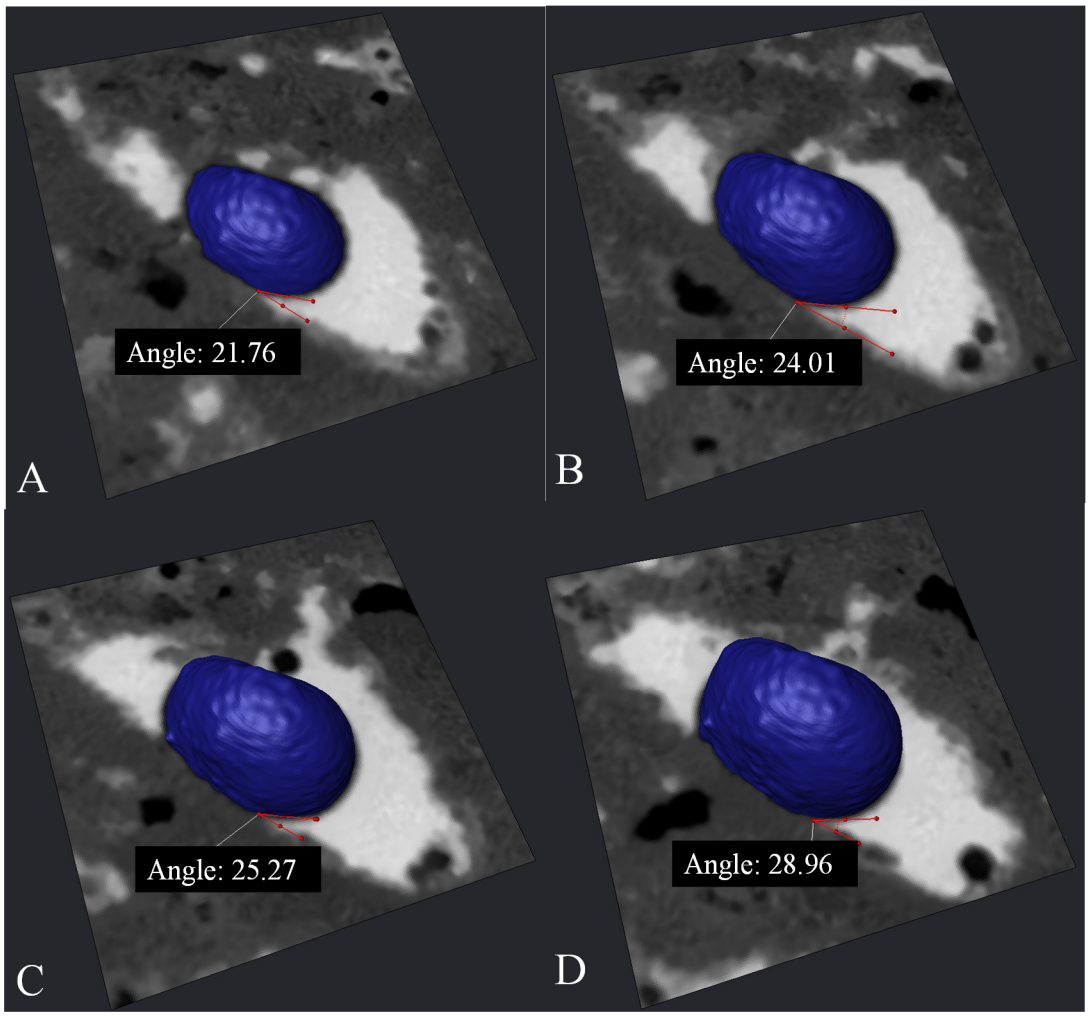

Figure 6.20: Example contact angle measurements on different XY slices. Contact angles measured through the wetting phase (here oil)

More contact angle measurements for this specific pore are shown in Figure 6.21 where the brine droplet shows 4 triple points on each slice. Figure 6.22 shows the droplet in the XZ and YZ planes. The contact angles measured on these planes are larger than the XY plane angles.

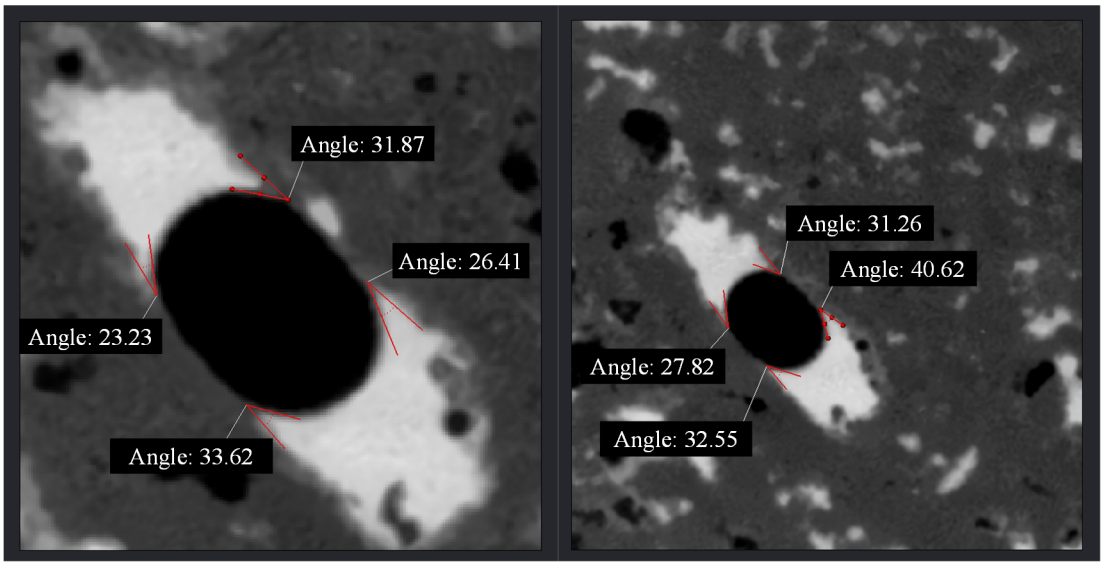

Figure 6.21: Example contact angle measurements on different XY slices. Contact angles measured through the wetting phase (here oil).

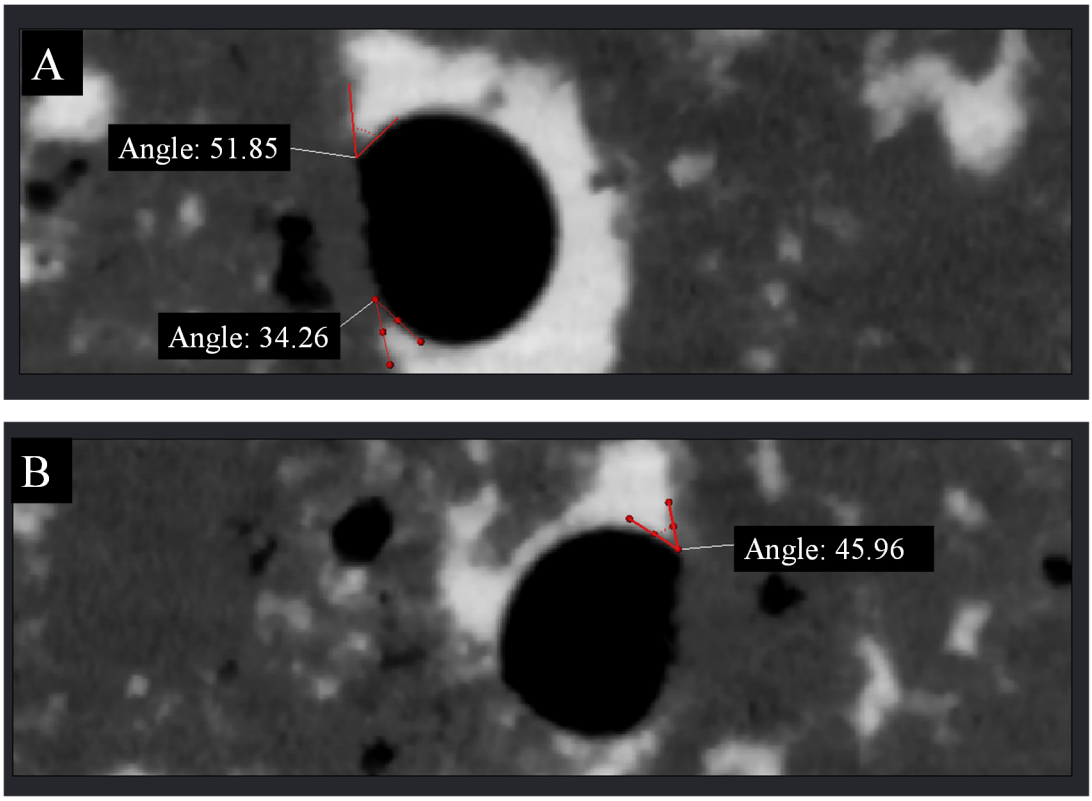

Figure 6.22: Contact angles measured on example XZ and YZ slices. Contact angles were measured through the wetting phase (here oil).

2.2.3. Comparison between the OW and WW Contact Angle Distributions

The presented contact angles in the sections 2.2.1 and 2.2.2 are measured through the wetting phase, and hence for both OW and WW cases the reported angles are less than 90°. In order to make the angles comparable here the complementary OW angles are considered. Figure 6.23 compares the distribution of the contact angles measured through the brine phase for this pore under the two OW and WW. The distributions are based on 14 measurements for each wetting state, some of them presented in Figures 6.18 to 6.22.

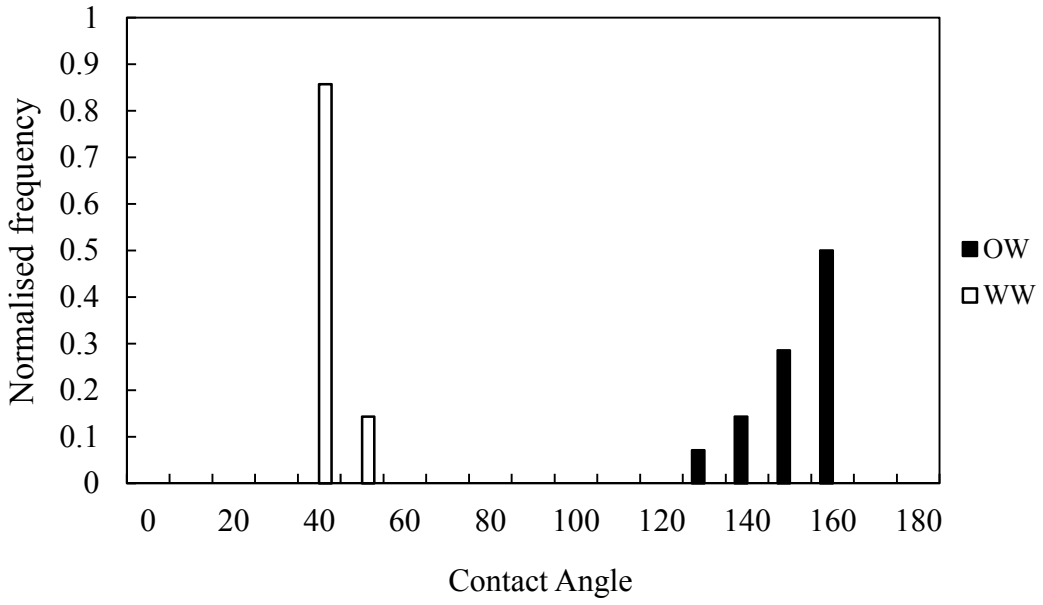

Figure 6.23: Contact angle distribution for the OW and WW systems. The angles are measured through the brine phase.

The distribution of the measured contact angles for the WW and OW cases display a significant contrast for these two wetting systems. This contrast indicates the direct contact angle analysis has successfully captured the two different wetting systems. The measurements are distributed over a range of (30.56-44.95) and (128.15-158.24) with 36.44±3.46 and 148.16±8.53, for the two WW and OW cases, respectively. The distribution of the measured angles may be influenced by a number of factors, including:

(a) The exact solid surface lines and the triple point positions are not clear on these images due to resolution limitations and partial volume effects (refer to chapter 2, section 3). In the example shown in Figure 6.24 selection of two different triple points has resulted in 22 degrees difference in the measured contact angle. These two angles display two possible extreme cases, and therefore indicates the degree of subjectivity associated with the manual contact angle measurement for this image. The image filtering process introduces some degree of blurring over the image. Hence, the feature boundaries have become less sharp making the selection of the triple point less certain.

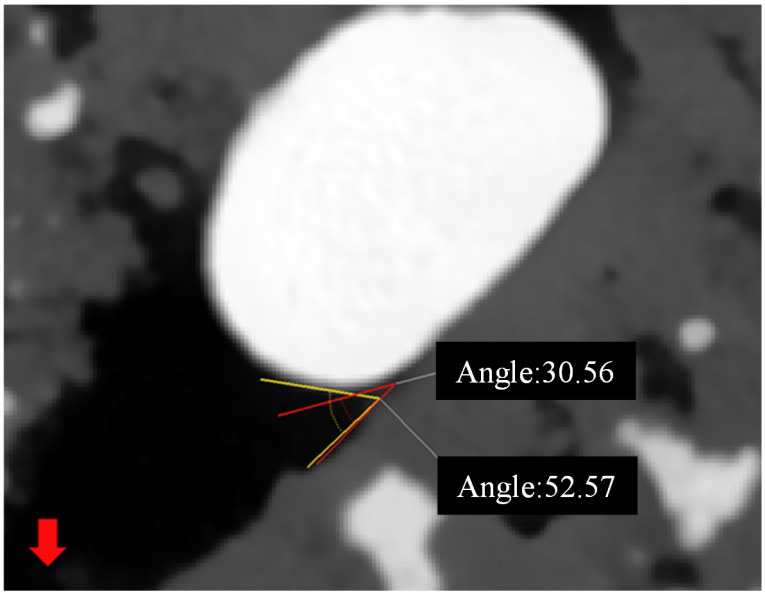

Figure 6.24: Effect of the triple point location on the measured contact angle. Lack of sharpness makes the selection of the triple point subjective. Here the two contact angles display ~22° difference

(b) Surface roughness can affect the shape of a trapped non-wetting droplet. In well sorted sandstones made of pure quartz the surface roughness may be relatively uniform. However, arkosic sandstones, or sandstones rich in a variety of lithic fragments exhibit a more variable surface. In carbonates surface roughness can be complex, ranging from smooth surfaces on sparry calcite cements, to rough surfaces on clastic fragments, or fragmented shells, etc. Lime muds display high roughness at the small scale (sub-micron), however they would appear as smooth at µCT scales. Limestones with more complex components comprising fragments, fossils, spars and

fine cements can have more complex surface roughness. For SD recrystallization to dolomite has produced a structure in which the pores are lined by the apices and edges of dolomite rhombs. This dolomite displays a very consistent type of surface roughness.

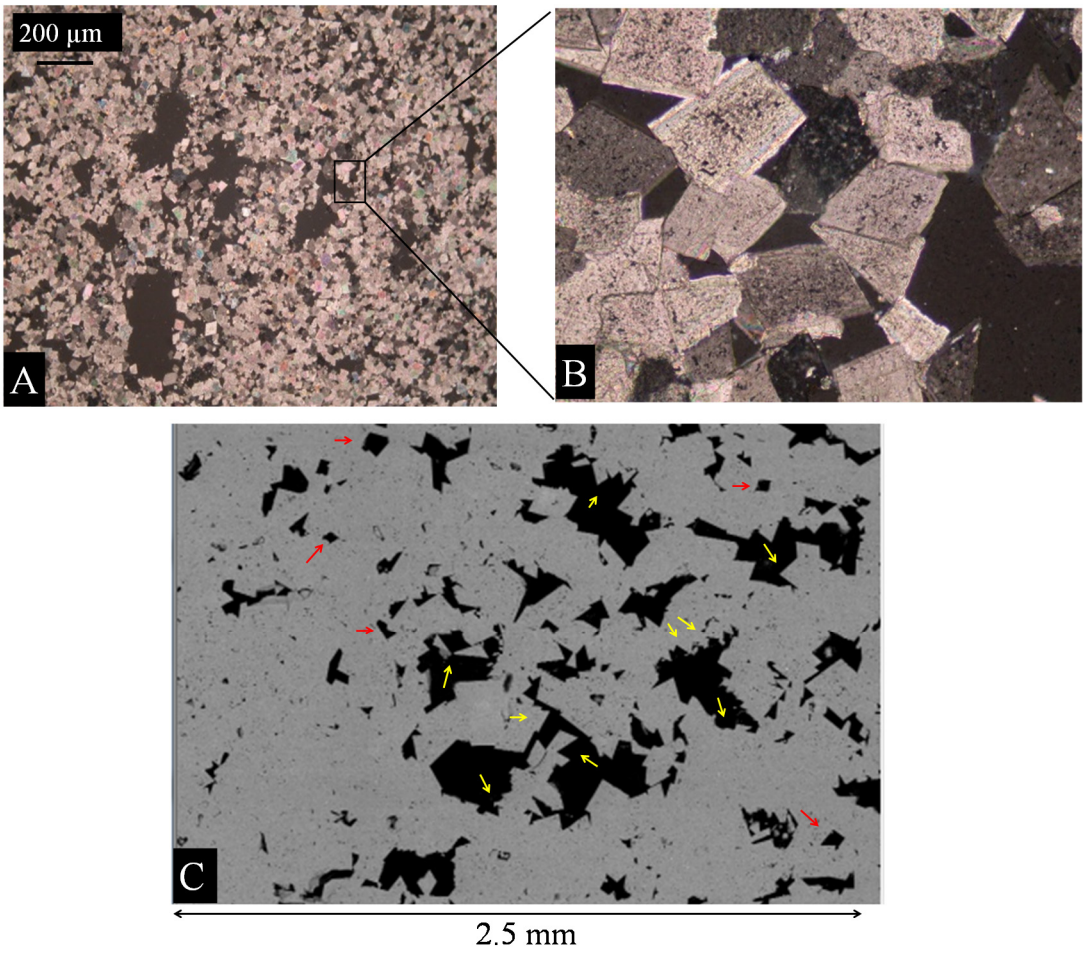

Figure 25: (A and B) Images of a SD thin section acquired using a light microscope under cross-polar mode, (C) BSEM image of the SD dolomite. Yellow arrows indicate the surface roughness in the pores larger than the mean crystallite size. Red arrows indicate the smaller pores that span only one or two crystals. These small pores are substantially smoother at the µm scale.

Figure 25A and 25B shows images of a SD thin section acquired using a light microscope under cross-polar mode. The dolomite crystals have a narrow size distribution. This implies that the pores that are significantly larger than the mean crystal size display significant roughness (Figure 25C, yellow arrows). However, smaller pores that may span only one or two crystals are substantially smoother at the

μm scale (Figure 25C, red arrows). These crystals may be rough on the nm scale that is beyond the resolution limitations of μCT technique. Such small scales (a few 10s of nm) require an atomic force microscopy technique to observe the surface roughness. Surface roughness of nm scale is less likely to have substantial impact on the contact angles measured at tens-to hundreds of microns scale.

Droplets trapped in smaller pores may be less disturbed by the surface roughness, however due to their small sizes (approaching the image resolution) detecting the oil-brine-rock interfaces and hence the triple point becomes less certain for smaller droplets. It is recommended to perform the angle measurement on a variety of different pore-sizes to account for the possible sources of contact angle variations (such as surface roughness at a specific scale). The overall distribution should be indicative of the predominate wetting preference of the rock.

2.3. Contact Angles Measured for the Whole Core

In order to investigate the distribution of contact angles over the entire length of the core plugs 70 contact angle measurements were done on a random selection of pores for the WW and OW cases. The selected pores were distributed throughout the core plug (i.e. one measurement per pore). The measurements are based on 2D μCT slices. Figure 6.26 shows the distribution of the measured contact angles for the WW and OW cases. The contact angles were measured through the brine phase. The average contact angles are 48.6±9.93 and 126.79 ±14.9 for the WW and OW cases, respectively. The two distributions display a significant contrast which is an indication of the significant change in the wetting preference of the rock caused by aging in crude oil. The contrast in wetting state is also confirmed by the development of brine and oil films under the WW and OW conditions, respectively. The WW data exhibits a narrower distribution compared to the OW data, this may be associated with the lower sharpness of the OW images which has resulted in higher uncertainty in the measured values. The possible factors that contribute to the variability of the measured contact angles are discussed in further details in section 2.4.

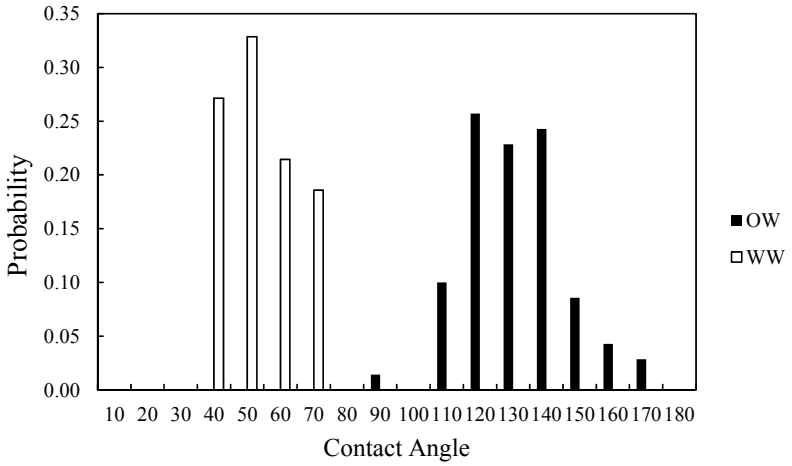

Figure 6.26: Contact angles distributions for the WW and OW cases, measured on a random selection of pores distributed in the entire core plugs. The average contact angles are 48.6±9.93 and 126.79 ±14.9 for the WW and OW cases, respectively. The significant contrast between the two distributions indicate the difference in the rock wettability.

The distributions of contact angles for the specific pore presented in section 2.2 (36.44±3.46 and 148.16±8.53, for the WW and OW cases, respectively) differ from the distributions measured on whole core (48.6±9.93 and 126.79 ±14.9, for the WW and OW cases, respectively). There are 12.16 and 21.37 degrees difference between the average contact angles for the entire core and that specific pore, respectively for the WW and OW cases. The primary reason may be due to the fact that the measurements of the entire core are performed on droplets with a range of sizes confined in pores with different sizes, shapes and roughnesses. The 14 measurements of this specific pore, also, display lower ranges of variability (i.e. smaller standard deviation). This smaller variations are however expected since for the single pore the measurements were performed on close slices through a single droplet. Despite the differences the distributions fall in the same class of OW and WW for the entire core and single pore analysis.

2.4. Discussion

According to Anderson (1986), a surface is classified as preferentially WW if the contact angle between the water-oil interface and the surface is between 0-75°. In this classification natural-wet and OW systems display contact angles of 75°-120°

and 120°-180°, respectively. The contact angle is measured through the water phase, as shown in Figure 6.27.

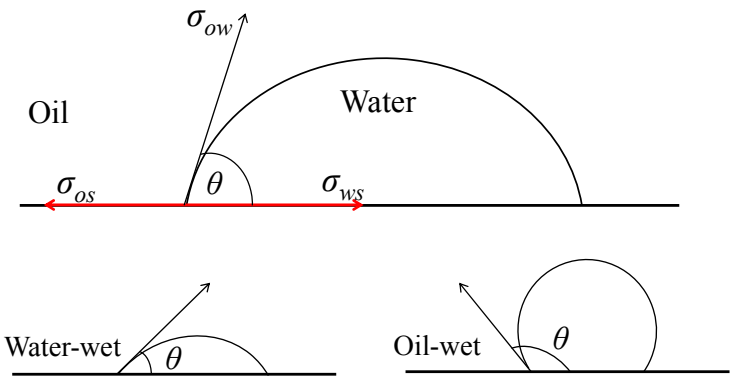

Figure 6.27: Schematic configuration of oil-water-rock system for a water droplet placed over a solid surface in presence of oil phase. The figure shows the different wetting classes, after Anderson (1986). Note that here the angles are measured through the water phase.

In the Sessile drop method a free droplet of water is placed on a surface in presence of air and there is only a *single* contact surface between the droplet and the solid surface. The contact angle between the water-air interface and the solid surface is governed by the interplay between the interfacial tensions acting over the droplet (Young, 1805). The direct µCT analysis of contact angle is not equivalent to the Sessile drop method. In µCT method in addition to surface forces fluid configurations inside a porous media are under the influence of viscosity and capillary forces. Moreover, non-wetting phase droplets confined within the pores often display *multiple* contacts with the pore walls. Therefore, interfacial forces can act over the droplets in various directions over the contact surfaces. The equilibrium contact angles are hence governed by the resultant of all these forces acting on the droplet. In most time-resolved experiments conducted at synchrotron facilities the images are captured under dynamic conditions (i.e. while the fluid injections are happening) and hence at least one fluid is flowing in the pore space (say the wetting phase is flowing in an imbibition process). Under such circumstances a drag force acts on the trapped non-wetting droplets, which may not be enough to mobilise them but still can have an effect of the fluid-fluid-rock configuration. In cases where the

images are captured under zero flow conditions, the impact of viscous forces does not occur.

Figure 6.28 compares the contact angle measurement practice performed in a sessile drop test and a µCT analysis. Here, the contact angles are measured for a droplet that is (a) placed on a solid surface (Sessile drop conditions, θ_s), (b) confined in a triangular shape pore (µCT measurement conditions, $\theta_{\mu CT}$), and (C) confined in a triangular shape pore but is much smaller than the pore, hence displaying contact with a single pre wall.

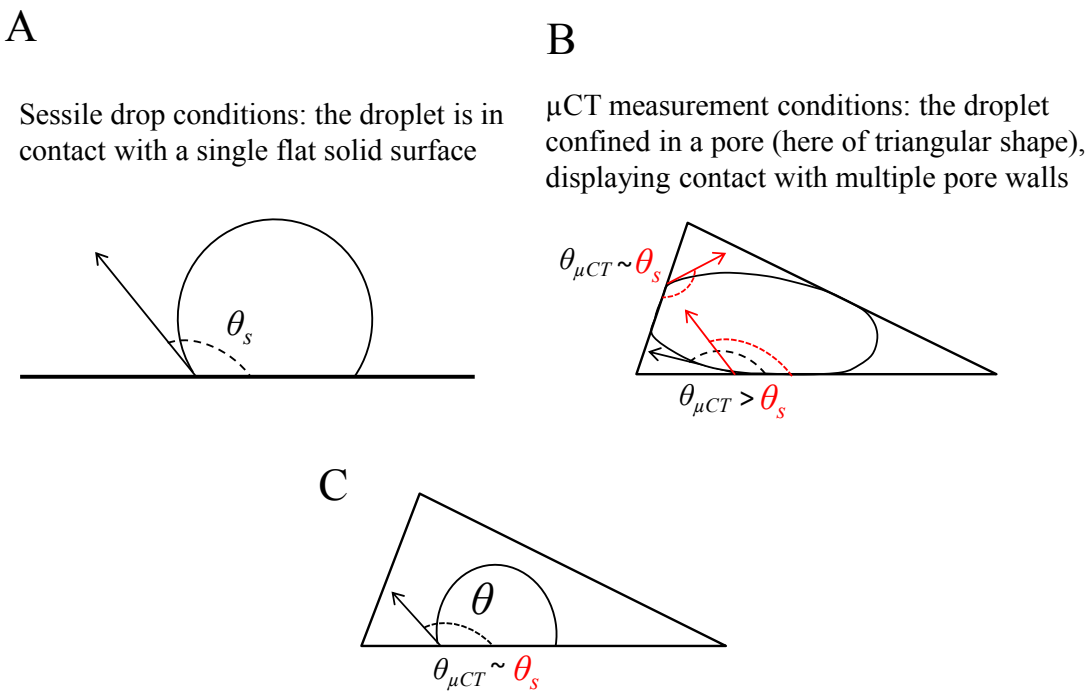

Figure 6.28: Comparison between the contact angle measuremnet using Sessile drop (A) and µCT based analysis (B and C). The $\theta_{\mu CT}$ may differ from the θ_s.

As shown for cases where the droplet is of comparable size to the pore confining it (Figure 6.28B) the $\theta_{\mu CT}$ may differ from the θ_s. In this example the $\theta_{\mu CT}$ (measured through the droplet) overestimates the θ_s in one place whereas the two measurements can approach at other contact points. The factors influencing the comparison between

$\theta_{\mu CT}$ and θ_s can be: the forces acting in the system including gravity, viscous, capillary and the orientation of the pore walls that are in contact with the droplet.

For cases where the droplet size is much smaller than the pore confining it (Figure 6.28C) the two $\theta_{\mu CT}$ and θ_s may be comparable since the droplet displays contact with only one pore wall.

Therefore, for a fluid pair and a pore structure the contact angles measured based on μCT images are expected to display some degree of variability due to the realistic difference in fluid-fluid-rock configurations in difference places in the pore system. The outcome is a distribution of contact angles instead of a single measurement, which still contains valuable information about the wettability of the system.

Despite the limitations of the presented pore-scale wettability assessment, the clear contrast between the contact angle distributions for the two OW and WW cores implies that the method is capable of distinguishing between different wetting systems. This contrast is more pronounced for surfaces with strong wetting preferences. Pore-scale wettability assessment is not limited to contact angle measurements. The observed fluid displacement mechanisms happening in different drainage and imbibition processes along with the development of wetting films and corner film flow are other indications of wetting preference of the system.

3. Intra-pore Wettability Heterogeneity

A SD plug (L=28 mm, D=12.5 mm, porosity ~17.6 %) was used to perform a two-phase (drainage and imbibition) experiment as outlined in Table 6.1. The core plug was first saturated with 0.03 M KI brine. The oil injection steps were performed using 318 μl/min (0.5 pore volume/min). This flow rate was selected to avoid fluid redistributions induced by high flow rate oil injections (refer to chapter 4, section 4). In this experiment, subsequent to the first oil injection, brine was injected into the plug using three different flow rates: 5, 50, and 500 μl/min, injecting 10 pore volumes at each stage. μCT scans comprising of 1200 projections were collected after each brine injection step. Each projection was a summation of 3 acquisitions

(1.1 second exposure times) to reduce digital noise and artifacts due to sensor non-linearity.

Table 6.1: Experimental test cycle consisted of drainage and imbibition steps.

	Injection process	q (µl/min)	q (m^3/ Sec)	N_C	Pore-Volumes Injected
1	First oil saturation				
2	Brine-flooding	5	8.3×10^{-11}	9.43×10^{-8}	10
3	Brine-flooding	50	8.3×10^{-10}	9.43×10^{-7}	10
4	Brine-flooding	500	8.3×10^{-09}	9.43×10^{-6}	10
1	Second oil saturation				
2	Brine-flooding	10	1.7×10^{-10}	1.89×10^{-7}	10
3	Brine-flooding	750	1.2×10^{-08}	1.42×10^{-5}	10

For a 2nd time the core was saturated with oil. Subsequently, brine was injected with 10 and 750 µl/min. The fluid injections were done from the bottom to the top of the core. The images collected from the bottom 21 mm of the core plug to avoid boundary effects subjacent to the production face.

Figure 6.29 shows example µCT sections of the core plug along the injection direction for the steps listed in Table 6.1. Snap-off was not observed in most pores of the rock at the slow brine injection steps, i.e. q=5, 10, 50 µl/min (Figure 6.29B, 6.29C, and 6.29F). Most pores were saturated with only one phase. However, during the faster brine injections (Figure 6.29D and 6.29G) there were more partial occupies in the pores, red arrows in Figure 6.29D and 6.29G indicate example isolated oil droplets trapped in pores (surrounded by brine films). The pre-requisite of droplet fragmentation (refer to chapter 5, section 2) is to have oil droplets trapped in the pores, causing resistance to the flow of the brine at higher rates. The lack of trapped oil droplets in the pore space of the plug at the end of the slow imbibition steps is probably why the droplet fragmentation is not observed in this experiment.

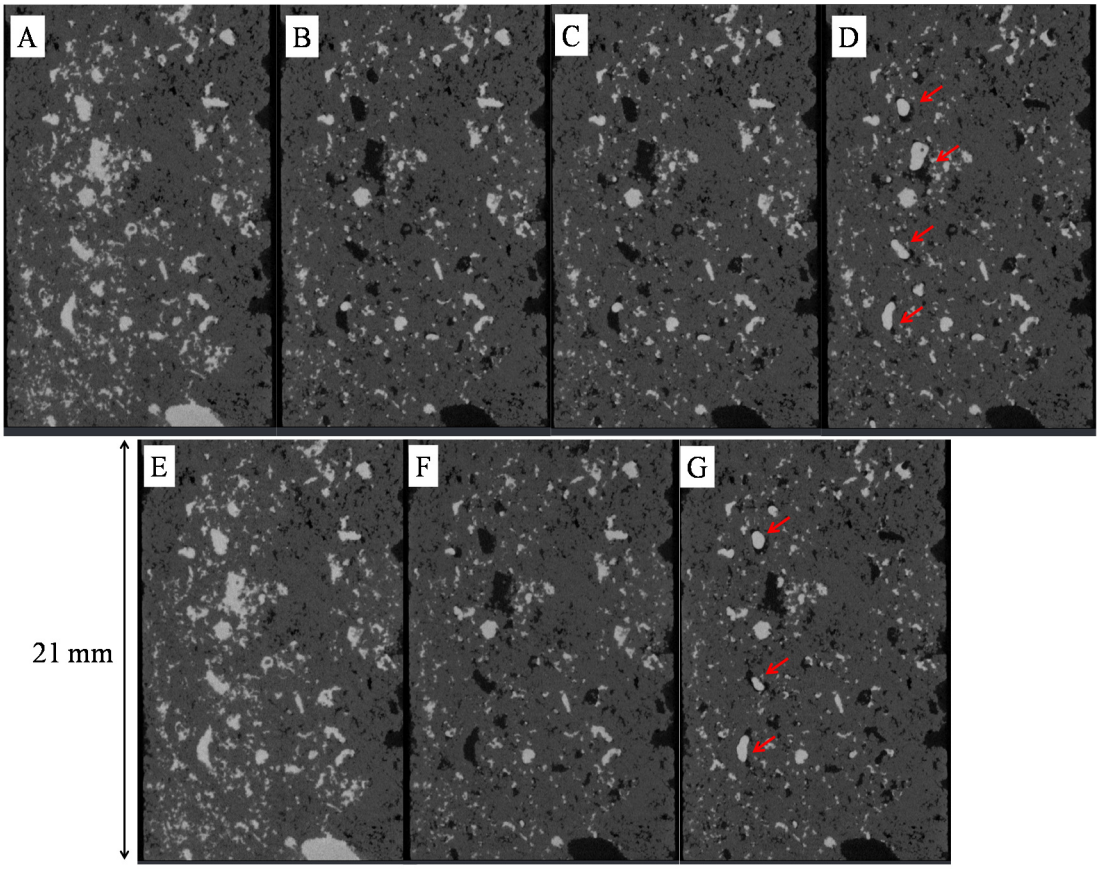

Figure 6.29: Example µCT sections of the core plug along the injection direction for the steps listed in Table 6.1. Droplet fragmentation is not observed since the snap-off event (which is the pre-requisite of the droplet fragmentation) has not happened at the slow brine injection steps (B, C, and F). Red arrows show oil droplets trapped in the pores after the fast brine injection steps (D, G).

Reviewing the two-phase fluid saturations as well as the intra-pore oil-brine-rock configurations reveals that this core plug contains pores which do not display uniform wettability. Intra-pore wettability heterogeneity was observed, meaning that in some pores parts of the pore walls were preferentially OW while some other rock surfaces in the same pore displayed to be WW. One example is shown in Figure 6.30, the red arrows indicate a pore which is initially saturated with 1M and 0.03 KI M brines (Figure 6.30A and 6.30B). The pore was subsequently displaced by oil (Figure 6.30C). A visible brine film was retained in the upper corner of the pore indicating the water-wetness of that part of the pore. Brine was injected into the core at 5µl/min (Figure 6.30D), the oil-brine configuration remains the same. Upon

increasing the brine injection flow rate to 50 µl/min the oil-brine interface curvature goes from concave shape to convex (Figure 6.30E). The brine saturation as well as the oil-brine contact surface increases in the pore. The upper corner of the pore remains in contact with the brine phase while other pore walls appear to stay in contact with the defending oil phase. The thick oil film developed at this stage became thinner as the brine flow rate increased to 500µl/min (Figure 6.30E). It should be noted that at some stages the thickness of fluid films may become smaller than the image resolution and hence the films may become *partially* captured on the images. In this example after the 500 µl/min brine injection step (Figure 6.30F) the thickness of the oil film appeared to be close to image resolution in some areas. Yellow arrows indicate the surface roughness which may have an effect on the shape of the oil-brine interface.

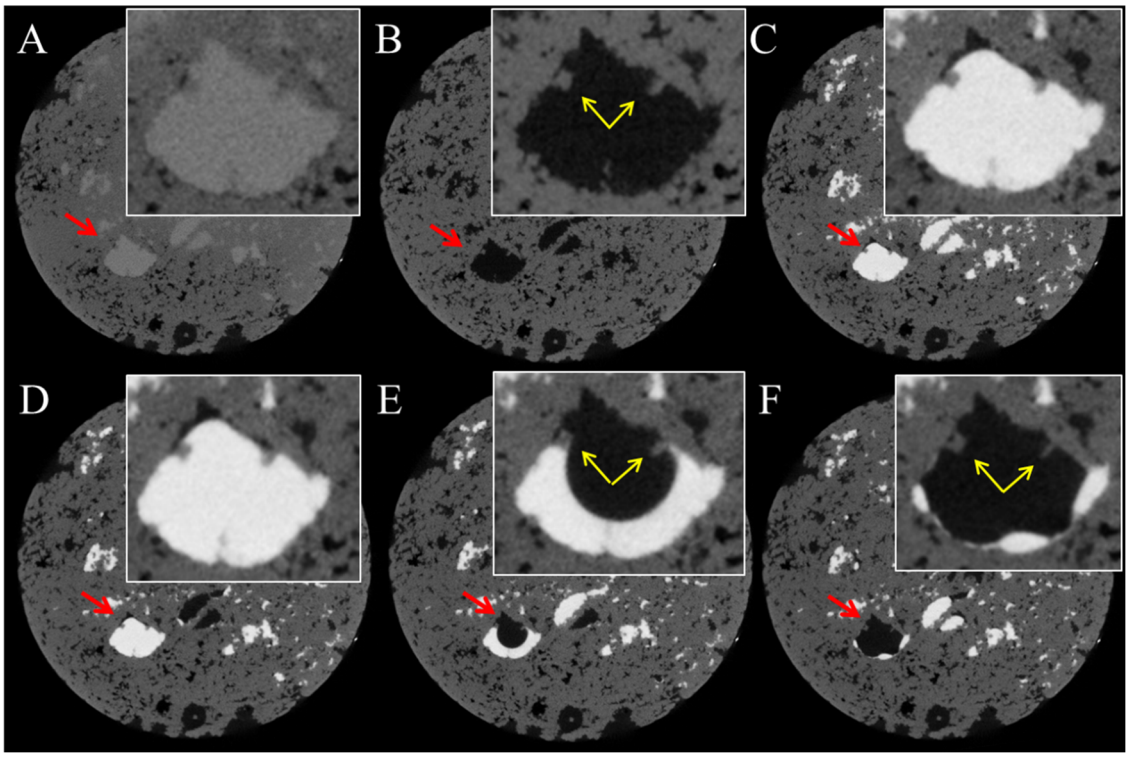

Figure 6.30: Example of intra-pore wettability heterogeneity. Core saturated with 1M KI (A), 0.03 KI (B), oil (C), and 0.03 KI brine injection with 5, 50, 500 µl/min (D, E, F).

Figure 6.31 shows 3D surfaces fitted to the oil and brine phases after the three brine injection stages, shown in Figure 6.30D to 6.30F. The brine and oil phases are shown

in blue and red, respectively. The oil surface appears to be disconnected in some areas on Figure 6.31C. Based on the apparent wetting of some parts of the rock surface by oil Figure 6.30E an 6.30F, the oil film may be of thicknesses smaller than the µCT resolution.

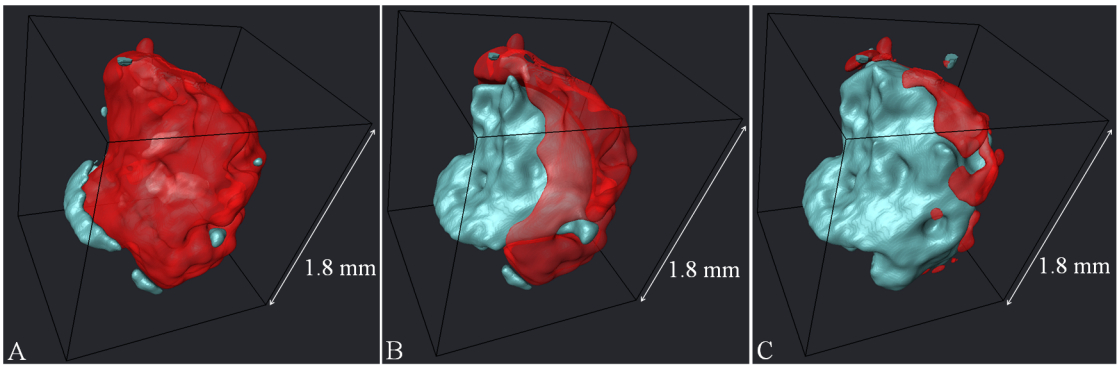

Figure 6.31: 3D rendering of surfaces fitted to the oil and brine phases after brine injection with: 5, 50, and 500 µl/min (A, B, and C). Brine and oil are shown in blue and red respectively. Heterogeneous wetting preference is shown by coexistence of oil and brine films in the same pore.

The fraction of OW and WW surfaces in the core plug can be measured based on these µCT images and can serve as an input to pore network models for mixed-wet systems. Table 6.2 lists the contact areas for the three brine injection steps, as well as the surface area of the rock in this pore. The fluid-rock contact areas were calculated based on the method of Porter and Wildenschild (2010), which was also used in chapter 5, section 2.

Table 6.2: Quantitative analysis of the OW and WW surfaces for the pore shown in Figure 6.31, measured based on these µCT images

q (µl/min)	5	50	500
S_b	0.05	0.54	0.89
S_o	0.95	0.46	0.11
A_{bo}	5.37×10^3	2.76×10^4	1.49×10^4
A_{br}	2.44×10^4	4.83×10^4	8.46×10^4
A_{or}	9.40×10^4	7.01×10^4	3.38×10^4
A_{br}/A_{pore}	0.21	0.41	0.71
A_{or}/A_{pore}	0.79	0.59	0.29

According to these data the fraction of the pore surface in contact with the fluid phases has varied (0.21-0.79) for the different brine injection steps, where fluids have different saturations in this pore. This should not be the case if the surfaces stay in contact with the preferentially wetting fluid throughout the injection cycle, and if the images can capture all the fluid films. However, due to the resolution limitation the technique misses out the fluid films with thicknesses approaching the image resolution. On this basis, higher resolution images are essential for realistic estimation of the ratio of OW and WW surfaces in this pore.

4. Summary

In this chapter direct visualisation of oil-brine-rock configurations at the pore-scale is presented based on μCT images of drainage and imbibition experiments performed on a SD core plug under WW and OW states. The dolomite core plug presented in chapters 4 and 5 was rendered OW by crude oil aging. The saturating oil and brine phases display different structures under the two different wetting systems. Of particular importance is the structure of the *remaining* oil phase. For the WW system the remaining oil was shown to be trapped in the larger pores in form of isolated droplets or clusters trapped in a few connected pores surrounded by brine films. For the OW system, however, the remaining oil mainly saturated the smaller to medium size pores, also displaying connected oil films in contact with the rock surface.

In situ formation of a brine in oil emulsion phase was captured in the flooding experiments performed on the OW plug. The formation and displacement of emulsions in pore space of rocks is a well-known process in the oil production process. The emulsion phase displays higher and lower viscosity compared to the oil phase in the water in oil and oil in water emulsions, respectively. On this basis water in oil emulsions are undesired whereas the formation of oil in water emulsions are considered as a main mechanism that assist the heavy oil production (surfactant flooding). Micromodel studies have directly observed formation and flow of emulsions in 2D. 3D visualization of emulsion formation and evolution in real pore space of natural rocks using X-ray μCT technique, however, has not been reported in the literature. Such studies can assist the design of surfactant flooding processes in

heavy oil reservoirs. The observed emulsion was shown to be stable over a period of at least 77 days. Although images were not quantitatively analysable (due to sharpness and resolution limitations) they displayed a range of droplets sizes for the captured emulsion phase, from sub-resolution scales (few microns) to hundreds of microns. Such quantitative analysis of the emulsion droplet size distribution can be useful for the modelling of emulsion flow in porous media.

Contact angle measurements performed on images of WW and OW experiments are presented and compared. Although subject to uncertainties, it is demonstrated that the pore-scale contact angle measurement method is capable of distinguishing between the studied WW and OW systems. Analysing contact angles over the entire length of the core plugs considering droplets trapped in pores of different sizes has demonstrated that the contact angles are statistically consistent throughout the sample. Pore-scale wettability assessment is not limited to contact angle measurements. In addition to that, observation of fluid displacement mechanisms along with direct observation of wetting film development and corner film flow are other factors that indicate the predominate wetting preference of the rock.

Oil-brine-rock configurations consistent with intra-pore wettability heterogeneity was observed in a similar experiment performed on another core plug of SD rock. Heterogeneous wettability may occur in rocks that are composed of different minerals or as a result of organic matter deposition on parts of the pore space. Here, the observed difference in wettability of pore walls in a single vug may be associated with possible deposition of organic matters on those parts of the pore since SD is a mono-mineralic rock. This is possible since the SD rock is an outcrop.

Direct micro-scale wettability data can be extracted from the images to generate a pore-scale wettability distribution map for the more complex systems such as multiple-mineral surfaces. Derived local wettability data can serve as an input to pore-scale network modelling simulations. Future work can include developing computer codes to automate the contact angle measurement and optimise the selection of the triple point by finding the best tangent line to the fluid-fluid-rock interfaces.

References

ANDERSON, W. 1986. Wettability literature survey-part 2: Wettability measurement. *Journal of Petroleum Technology,* 38**,** 1,246-1,262.

ANDREW, M., BIJELJIC, B. & BLUNT, M. J. 2014. Pore-scale contact angle measurements at reservoir conditions using X-ray microtomography. *Advances in Water Resources,* 68**,** 24-31.

ARDITTY, S., SCHMITT, V., GIERMANSKA-KAHN, J. & LEAL-CALDERON, F. 2004. Materials based on solid-stabilized emulsions. *Journal of Colloid and Interface Science,* 275**,** 659-664.

BRYAN, J. L. & KANTZAS, A. Enhanced heavy-oil recovery by alkali-surfactant flooding. SPE Annual Technical Conference and Exhibition, 2007. Society of Petroleum Engineers.

ELEY, D., HEY, M. & LEE, M. 1987. Rheological studies of asphaltene films adsorbed at the oil/water interface. *Colloids and Surfaces,* 24**,** 173-182.

KAWAKATSU, T., KIKUCHI, Y. & NAKAJIMA, M. 1997. Regular-sized cell creation in microchannel emulsification by visual microprocessing method. *JAOCS, Journal of the American Oil Chemists' Society,* 74**,** 317-321.

KITCHENER, J. & MUSSELLWHITE, P. 1968. The theory of stability of emulsions. *Emulsion science***,** 122-123.

KOBAYASHI, I., MUKATAKA, S. & NAKAJIMA, M. 2004. Effect of slot aspect ratio on droplet formation from silicon straight-through microchannels. *Journal of Colloid and Interface Science,* 279**,** 277-280.

LIU, Q., DONG, M., YUE, X. & HOU, J. 2006. Synergy of alkali and surfactant in emulsification of heavy oil in brine. *Colloids and Surfaces A: Physicochemical and Engineering Aspects,* 273**,** 219-228.

MANSUROV, I., IL'YASOVA, E. & VYGOVSKOI, V. 1987. Shear strength of interfacial films of asphaltenes. *Chemistry and Technology of Fuels and Oils,* 23**,** 96-98.

MCAULIFFE, C. D. 1973. Oil-in-water emulsions and their flow properties in porous media. *Journal of Petroleum Technology,* 25**,** 727-733.

MCLEAN, J. D. & KILPATRICK, P. K. 1997. Effects of asphaltene aggregation in model heptane–toluene mixtures on stability of water-in-oil emulsions. *Journal of Colloid and Interface Science,* 196**,** 23-34.

MENON, V. & WASAN, D. 1986. Particle—fluid interactions with application to solid-stabilized emulsions part I. The effect of asphaltene adsorption. *Colloids and Surfaces,* 19**,** 89-105.

PICKERING, S. U. M. 1907. Cxcvi. emulsions.

PORTER, M. & WILDENSCHILD, D. 2010. Image analysis algorithms for estimating porous media multiphase flow variables from computed microtomography data: a validation study. *Computational Geosciences,* 14**,** 15-30.

REZAEI, N. & FIROOZABADI, A. 2014. Macro-and Microscale Waterflooding Performances of Crudes which form w/o Emulsions upon Mixing with Brines. *Energy & Fuels,* 28**,** 2092-2103.

SCHRAMM, L. L. 1992. Petroleum Emulsions-Basic Principles. *Advances in Chemistry Series***,** 1-49.

SCHULMAN, J. & LEJA, J. 1954. Control of contact angles at the oil-water-solid interfaces. Emulsions stabilized by solid particles (BaSO 4). *Transactions of the Faraday Society,* 50**,** 598-605.

SHENG, J. 2010. *Modern chemical enhanced oil recovery: theory and practice*, Gulf Professional Publishing.

SJÖBLOM, J., URDAHL, O., HØILAND, H., CHRISTY, A. & JOHANSEN, E. 1990. Water-in-crude oil emulsions. Formation, characterization, and destabilization. *Surfactants and Macromolecules: Self-Assembly at Interfaces and in Bulk.* Springer.

SULLIVAN, A. P. & KILPATRICK, P. K. 2002. The effects of inorganic solid particles on water and crude oil emulsion stability. *Industrial & Engineering Chemistry Research,* 41**,** 3389-3404.

TAMBE, D. E. & SHARMA, M. M. 1993. Factors controlling the stability of colloid-stabilized emulsions: I. An experimental investigation. *Journal of Colloid and Interface Science,* 157**,** 244-253.

TAYLOR, S. E. 1992. Resolving crude oil emulsions[demulsifiers]. *Chemistry and Industry***,** 770-3.

YOUNG, T. 1805. An essay on the cohesion of fluids. *Philosophical Transactions of the Royal Society of London***,** 65-87.

Chapter 7

Pore Network Modelling – Evaluation for Carbonate Media

1. Background

High-resolution X-ray μCT imaging provides the opportunity to study the 3D pore structure of rocks in detail. Laboratory-based μCT instruments as well as synchrotron facilities are now used routinely to analyse rock samples. In such analysis, subsequent to data acquisition and reconstruction the 3D data undergoes a series of post-processing steps including noise filtration and segmentation (refer to chapter 3, section 3). The outcome is a binary image of the pore space of the rock which can be quantitatively analysed to determine porosity, pore and pore-throat size distributions, pore space connectivity, etc. Such a binary image could also act as an input for pore network models which may be used to study fluid displacement processes in porous rocks (refer to chapter 2, section 5).

One target of pore-scale fluid flow simulations is to predict petrophysical properties of reservoir rocks such as capillary pressure (*Pc-Sat*), and relative permeability curves (k_r-*Sat*) and the reader is directed to the review by Blunt et al. (2002) for further details. A typical workflow is shown in Figure 7.1. It starts from a 3D high resolution binary image of the rock's pore space (Figure 7.1A). This input image can be acquired directly using X-ray μCT or generated using statistical information measured from 2D optical microscopy or SEM images (Vogel and Roth, 2001, Wu et al., 2006, Okabe and Blunt, 2007, Al-Kharusi and Blunt, 2007). It is possible to perform fluid flow simulations directly on the 3D binary image of the rock's pore space. However, this can be computationally demanding (Porter et al., 2009) and therefore impractical for complex pore systems. To simplify the fluid simulations, and reduce the computational cost of running the simulations, the structure of the pore space (pore structure) can be represented as a pore network model (Figure 7.1B), the general principles of which are introduced in chapter 2, section 5.

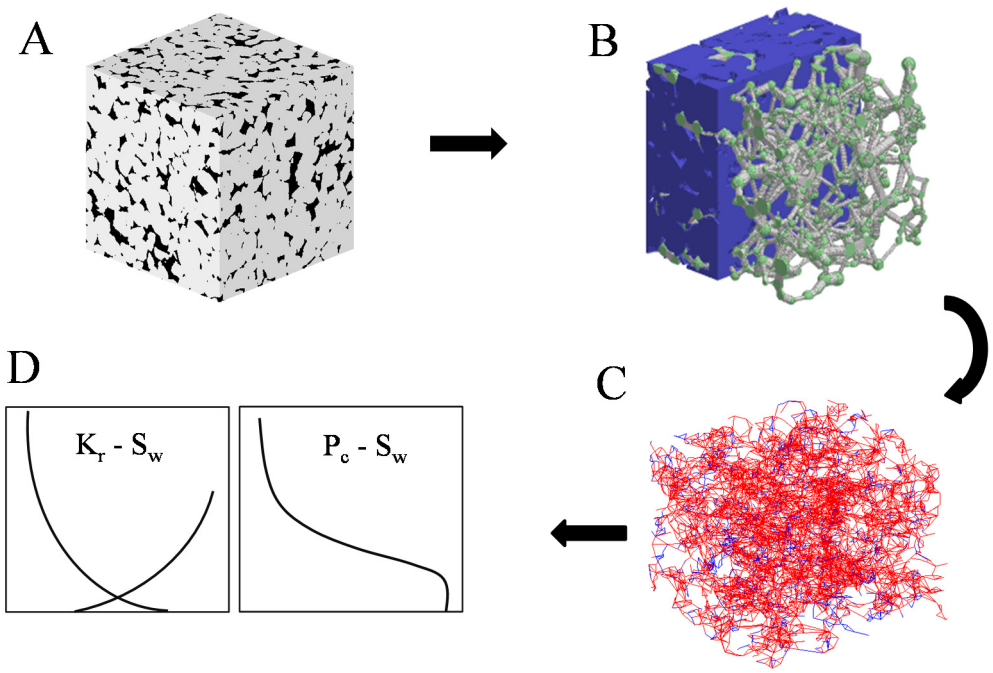

Figure 7.1: Typical work flow for pore network flow simulations. The starting point is a high resolution binary image of a rock in 3D (A). Equivalent pore networks are extracted from the images to simplify the simulations (B). Flow simulations are conducted (C) to calculate the petrophysical properties (D) of the rock.

Digital 3D data and modelling approaches allow calculation of petrophysical properties conventionally measured by means of time-consuming and costly laboratory tests. In particular, generating (k_r-*Sat*) curves in laboratories are practically time-consuming and expensive. Therefore, predictive pore network models capable of simulating (k_r-*Sat*) curves faster and less expensive are very much desired. As discussed in chapter 2, section 5, pore-network models are simple representations of a pore structure. To improve the predictions of pore-network flow simulations it is essential to tie these models to laboratory measurement of more readily obtainable properties of the rock. Properties such as porosity, absolute permeability and (*Pc*-*Sat*) curves are less expensive measurements which can be acquired rapidly in the laboratory. Such readily available data are good candidates for fine tuning the predictions of the pore network models before the models are used for simulation of more complex processes.

Successful pore network simulations rely considerably on the quality of the input images. There are a number of criteria which should be taken into account while applying the routine workflow shown in Figure 7.1.

- Firstly, the rock sample chosen to be imaged should be representative of the rock type. The representative elementary volume (REV) of a rock is defined as the volume of the smallest samples of that rock for which the measured properties can be assigned to the entire system (Bear, 1988). This principle applies equally to laboratory measurement of rock properties. Sampling is not necessarily a straightforward task for samples with heterogeneous pore systems such as carbonates; a problem which is discussed in section 3.1.
- Secondly, the μCT images acquired should, ideally, have sufficient resolution to capture all the existing features of the rock including: micro, meso and macro scale pores, which typically span over decades of length-scales in heterogeneous samples (e.g. from sub-micron to mm).

2. Pore-scale Fluid Flow Simulations for Homogenous Samples

Homogeneous structures exhibit narrow mono-modal pore-size distributions; in most cases a single μCT image with suitable resolution is sufficient to capture the geometry and topology of such pore systems. This homogeneity enables the pore network to successfully represent the pore-structure of the rock which is essential to any successful calculation of the petrophysical properties of the rock. The term "sufficient resolution" is used here since the required resolution for μCT images depends on the feature size distribution of the sample (e.g. pore-size distribution). Over the last decade many researchers have attempted to fine-tune pore networks (mainly for sandstones) as well as the fluid flow simulation algorithms with the aim of improving the predictions of multi-phase flow properties (McDougall and Sorbie, 1997, Øren et al., 1998, Patzek and Silin, 2001, McDougall et al., 2002, Valvatne and Blunt, 2004, Al-Kharusi and Blunt, 2008, Ryazanov et al., 2009). See the review by Joekar-Niasar and Hassanizadeh (2012).

The idea of adjusting pore networks using less expensive and readily obtainable laboratory measurements (such as (*Pc*-*Sat*) data) prior to predicting (k_r-*Sat*) curves

(using the adjusted network) has been suggested in the literature (McDougall et al., 2002, Valvatne and Blunt, 2004). Valvatne and Blunt (2004) used a Berea sandstone pore network as a training model and tuned the network by changing its pore-throat size distribution to match the laboratory measured (*Pc-Sat*) curve. The tuned pore networks were shown to match (k_r-*Sat)* curves successfully through wettability adjustments. The successful matches were obtained only for reasonably homogeneous sandstone rocks (Berea and one reservoir sandstone). The pore network used in the study by Valvatne and Blunt (2004) was extracted from a 3D image of Berea sandstone generated by a process-based reconstruction method (Bakke and Øren, 1997, Øren et al., 1998). The image was a cube of 3 mm side. Using the same image Ryazanov et al. (2009) reported successful calculation of (k_r-*Sat*) curves for Berea sandstone using a quasi-static fluid flow simulator. Figure 7.2 shows results of these two successful simulations of the (k_r-*Sat*) curves using quasi-static fluid flow codes. (Valvatne and Blunt, 2004, Ryazanov et al., 2009). In the present study Ryazanov's code is used for pore-scale flow simulations.

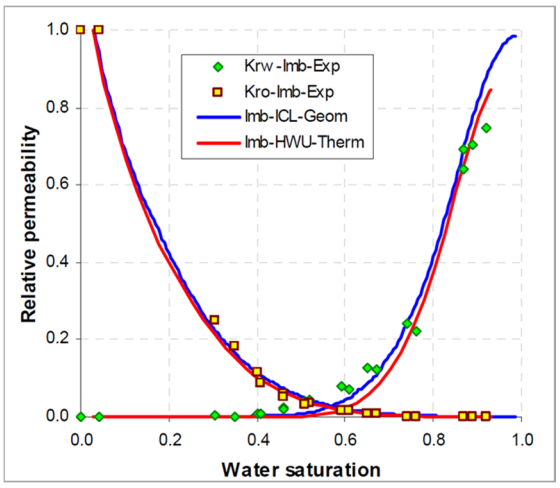

Figure 7.2: Successful simulation of the (k_r-*Sat*) curves using quasi-static fluid flow codes by Valvatne and Blunt (2004), and Ryazanov et al. (2009). The simulated curves are compared to steady-state experimental data for Berea sandstone (Oak et al., 1990). Simulations closely match the experimental data for Berea sandstone. Image from Ryazanov et al. (2014).

Al-Kharusi and Blunt (2008) proposed a workflow starting from high resolution SEM images of a reservoir carbonate rock. The carbonate rock they studied displayed homogeneous micro-scale porosity. Since the pore structure was too small

to be imaged in detail with μCT they obtained 2D SEM images from which multiple-point statistical data were extracted and utilised to construct 3D representations of the rock. The absolute permeability and porosity of the networks were closely matched with the laboratory measurements performed on a larger core plug from which the small sample was taken. The calculated (*Pc-Sat*) closely matched the laboratory measurements performed on samples of the same field with similar permeability value. The (k_r-*Sat*) curves were matched with the laboratory measurements by assigning contact angles. The success of their simulations in matching the experimental data mainly relied on the homogeneity of the rock studied, which enabled them to build a representative pore network based on data extracted from a small 2D image (only 54.1 μm side lengths). A small pore network (only 128^3 voxels) corresponding to a 34.6 μm (side length) image (643 nodes and 2623 bonds) was sufficient to represent the simple pore structure of the rock they studied. One significant advantage of the small network size was the opportunity to run multi-phase flow simulations in less than one minute.

Arns et al. (2003) used several pore-networks extracted from μCT images of Fontainebleau sandstone to investigate the variability of predicted (k_r-*Sat*) curves. They found that despite successful prediction of single phase properties, the small size of the networks (extracted from images of 400^3 voxels, 5.8 μm resolution) resulted in significant variability in the predicted multi-phase flow properties. They demonstrated that this variability was due to some spatial correlation in the pore structure of the rock. They reorganised the network elements (nodes and bonds) randomly to remove any spatial correlation in the pore structure and noticed negligible variability between the flow properties calculated for the randomised networks. They concluded that more heterogeneous rocks require larger samples for a sensible prediction of multi-phase transport properties.

In this study the effect of sample size and integration of networks extracted from μCT data obtained at differing length-scales is addressed. In particular we investigate the applications of these methods for the development of realistic pore network models for heterogeneous carbonate rocks.

3. Pore-scale Fluid Flow Simulations for Heterogeneous Samples

3.1. Sampling Challenge

High resolution μCT imaging of heterogeneous rock samples such as carbonate rocks is a problematic task due to the trade-off between the image resolution and the sample size. It is essential that the selected sample represents all of the existing pore features of the rock. Representative samples from heterogeneous carbonate rocks are often too large to be scanned with enough resolution to capture fine scale pore-throats and micro-porosity while at the same time capturing larger pores and vugs.

Here the complexity of generating a representative pore network model for multiple-scale pore systems is investigated by studying the effect of sample size on the extracted pore network model. μCT images of Silurian Dolomite (SD) rock acquired at several different length-scales are considered. The measured porosity and permeability of a sample (D=38) of SD are ~17% and ~50 mD, respectively. More details about the rock can be found in (refer to chapter 3, section 2). Depending on the sample size the following two cases may apply:

3.1.1. Selecting Larger Samples

Despite additional computational expense involved in working with large pore networks it is essential to have at least one representative elementary volume (REV) of the rock under study (Joekar-Niasar and Hassanizadeh, 2012). However, μCT images of larger rock samples display coarser resolutions, which may fail to represent the smaller (sub-resolution) pores and pore-throats. Consequently, the extracted pore network from a coarse resolution image (referred to as coarse network) tends to underestimate: (a) the porosity of the rock and (b) the connectivity of the pore system. As a result, both the single-phase and multi-phase flow properties are imperfectly predicted. In most cases considered in this chapter, the coarse networks are completely disconnected across the modelled rock volume and consequently simulations result in zero flow. Note that the disconnected network elements may be locally connected to a number of neighbouring network elements forming non-spanning clusters. A network is considered as disconnected as long as there is no connected cluster of pores to both inlet and outlet of the pore network.

Figure 7.3 shows pore networks extracted from three μCT images (21 μm resolution) acquired from three SD core plugs (D=25 mm): SD1, SD2, SD3. For each sample three networks are extracted from the X, Y and Z directions. Networks extracted from the three directions are mainly the same apart from their connections to the inlet and outlet faces. The network elements which are not part of a sample-spanning cluster are shown in pink. The network elements that are connected to a sample-spanning cluster are rendered in blue. Corresponding network parameters can be found in Table 7.1. Only SD1, Y-Net (also shown in Figure 7.4) contains a set of connected elements, resulting in a non-zero permeability. The remaining networks are disconnected at this scale due to the coarse resolution of the μCT images compared to the pore-throat sizes of the rock (further discussed in section 5.2.1*)*.

Table 7.1: Network parameters and measured static properties of the three coarse SD pore networks shown in Figure 7.3.

Sample (voxels)	SD1 (750×750×750)			SD2 (821×860×720)			SD3 (800×800×600)		
Network	X- Net	Y-Net	Z-Net	X- Net	Y-Net	Z-Net	X- Net	Y-Net	Z-Net
Number of Nodes	17377	17377	17377	19897	19897	19897	10617	10617	10617
Number of Bonds	21572	21436	21549	24093	23970	24434	11486	11749	12083
Coordination Number	2.44	2.43	2.44	2.39	2.38	2.40	2.067	2.092	2.12
Connected Porosity	0	3.78	0	0	0	0	0	0	0
Disconnected Porosity	8.06	4.28	8.06	6.03	6.03	6.04	8.12	8.12	8.12
Total Porosity	8.06	8.06	8.06	6.03	6.03	6.03	8.12	8.12	8.12
k_{abs} (mD)	0	85.46	0	0	0	0	0	0	0

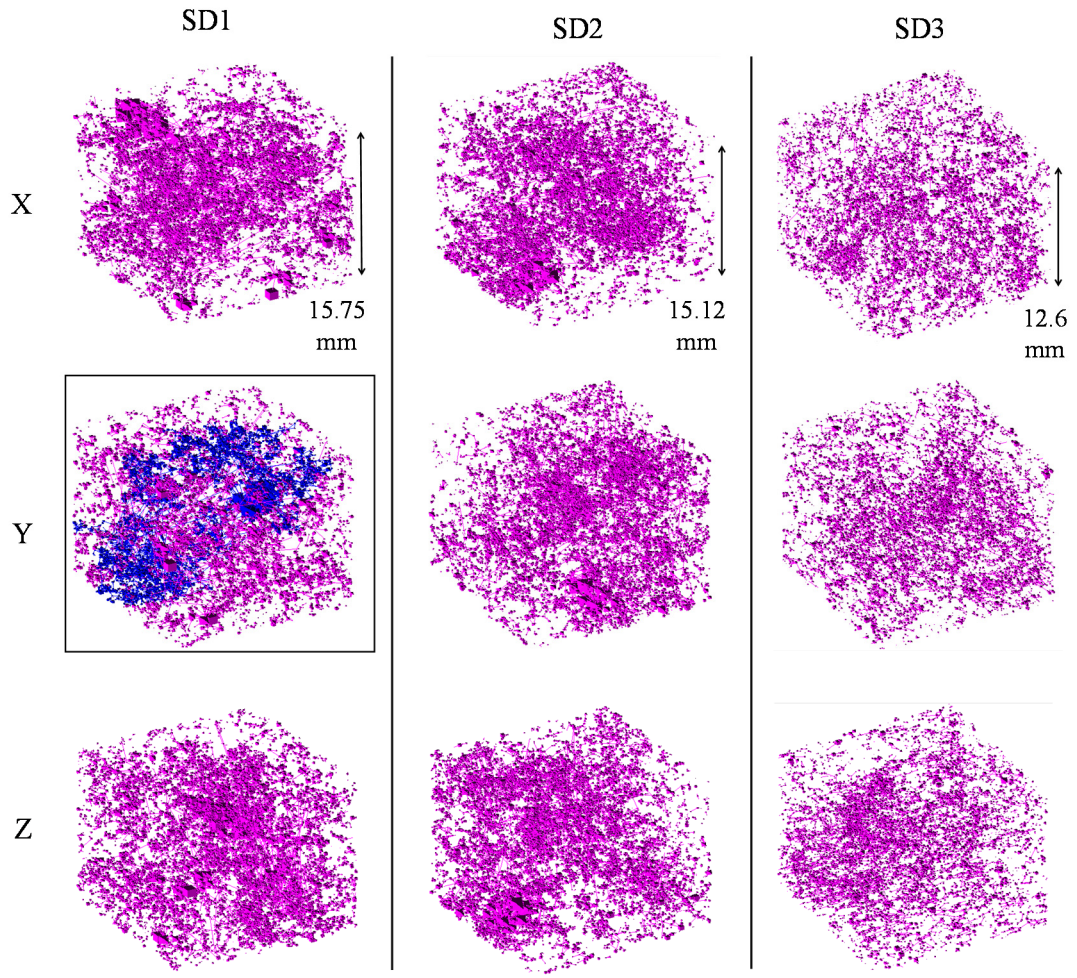

Figure 7.3: Pore networks extracted from µCT images (21 µm resolution) of three SD samples in X, Y, Z directions. Only one pore network is connected at this scale. Pink and blue colours indicate disconnected and connected elements, respectively.

Figure 7.4A shows SD1, Y-Net pore network. Figure 7.4B shows only the connected part of this network. For this network 53 % of the resolved porosity appears to be disconnected (rendered in pink). All other 8 networks are globally disconnected at this resolution. This implies that the larger pores which are captured in these images do not form a spanning cluster, i.e. the connection between the larger pores are provided by the narrower ones that are below the image resolution of these data (21 µm).

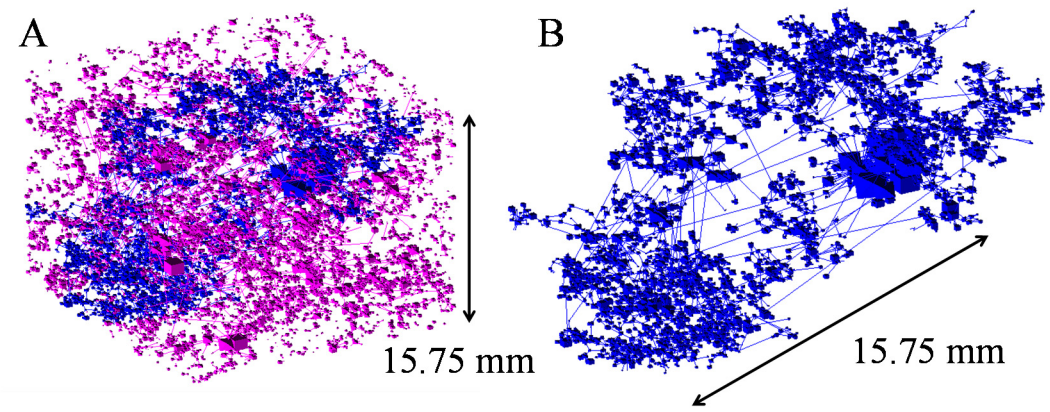

Figure 7.4: SD1, Y-Net pore network extracted from a µCT image of 21 µm resolution. (A and B) display the entire network and the connected elements of it, respectively. Pink and blue colours indicate disconnected and connected elements, respectively. The thin lines do not represent the true size of the bonds.

3.1.2. Selecting Smaller Samples

Smaller samples (of order of few mm) are commonly selected to achieve higher resolution µCT images (resolution of order of few µm). This is a pre-requisite of studying micro-scale porosity as well as dynamic fluid saturation distributions in tighter parts of rocks. Higher resolution images allow capture of more of the existing fine pores and narrower pore throats of the rock. However, considering that SD rock displays vugs of ~3 mm size, clearly a few mm size samples are smaller than 1 REV, and hence cannot be considered as a representative sample. Figure 7.5 shows a pore network extracted from a 5 µm resolution image of a SD core plug (D=5 mm). This core plug was selected from the same sample as the other cores presented in Figure 7.3. Network parameters are listed in Table 7.2. Due to the higher resolution more of the porosity of the rock (including narrower pore-throats) are imaged, as a result the network is connected in all 3 directions.

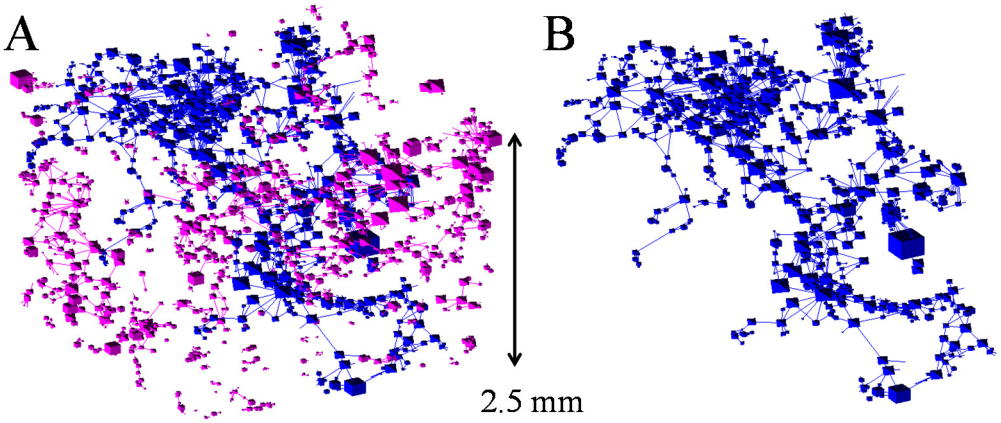

Figure 7.5: Pore network extracted from a 5 µm resolution image of a SD core plug (D=5 mm). Pink and blue colours indicate disconnected and connected elements, respectively.

Table 7.2: Parameters for the network shown in Figure 7.5. The network is connected in all directions.

Image Resolution (µm)	Number of Nodes	Number of Bonds	Connected Porosity %	Disconnected Porosity %	$k_{abs,\,x}$ (mD)	$k_{abs,\,y}$ (mD)	$k_{abs,\,z}$ (mD)	Coordination Number
5	2951	3654	6.1	3.0	75.6	52.7	108.2	2.4

Comparing the larger and smaller networks of SD (shown in Figures 7.3 and 7.5) shows the effect of sampling and hence resolution of the acquired µCT images on the static properties of the extracted networks, e.g. porosity and absolute permeability. For the coarse networks the insufficient resolution has caused the networks to become globally disconnected, with the exception of one network (Figure 7.4). These coarse networks have $6 < \varphi < 8$ % and $k_{abs} = 0$. The φ and k_{abs} of the coarse network is, therefore, not consistent with the laboratory measurements for SD rock (φ~17% and k_{abs}~50 mD). For the fine network φ ~9% and $52.7 < k_{abs} < 108.2$. While the values of k_{abs} of the fine network are consistent with the measured properties of the rock (k_{abs}~50 mD), its φ is an underrepresentation of the laboratory measurements for SD rock (φ~17%). One reason is the pore network extraction code used in this study identifies and removes the pores that are only a few voxels large and are not part of a locally or globally connected cluster of pores (i.e. they are totally disconnected). Such pores are considered to be of similar scale as the possible overlapping measurement noise occurring on µCT images. For example, the porosity of the SD2

sample calculated based on the binary image is 8.56 %. The porosity of the SD2 network is, however, 6.03 %. This implies that ~30 % of the porosity captured on the μCT image was identified as noise and was removed prior to the pore network generation. For a higher resolution image of SD (2 μm), the disconnected pores are fewer since more of the connections are captured. Therefore, the difference between the image-based porosity (14.9 %) and the pore-network porosity (14.3%) is only 0.04 %. In summary, the resolution limitations and the image processing steps involved in pore network extraction can act as two sources of underestimation of porosity.

3.1.3. Pore-scale Simulation of Capillary Pressure Curves for Different Length-scales

3.1.3.1. Randomly-connected Pore System

MICP tests are one of the routine methods used in core analysis laboratories to generate (*Pc-Sat*) curves. Details of this method can be found in (refer to chapter 3, section 1). For the following discussion consider that the pores are randomly connected, i.e. there is no spatial correlation in the pores. In simple pore structures the pore-size distribution (as well as the pore-throat distribution) displays a mono-modal shape (Figure 7.6A), i.e. the majority of the pores (pore-throats) are of similar sizes, with average pore-throat radius $\bar{r}$. For a homogeneous pore system with no spatial correlation, a typical (*Pc-Sat*) curve is shown in in Figure 7.7A. According to the Young-Laplace equation the injection pressure required to invade the pore-throats with average radius $\bar{r}$ is $P_{\bar{r}} = \frac{2\,\sigma\,cos\,\theta}{\bar{r}}$. For pressures $P > P_{\bar{r}}$ the connected pore space instantly becomes almost fully saturated with mercury. The narrower the pore-throat size distribution, the flatter the (*Pc-Sat*) curve becomes.

Heterogeneous pore structures, however, display a multi-modal pore (pore-throat) size distribution spanning over decades of length-scales, Figure 7.6B. The pore space of such systems becomes progressively saturated by mercury as the injection pressure increases. The corresponding (*Pc-Sat*) curve for such pore systems displays a steeper trend of increasing saturation versus pressure (Figure 7.7B). In most natural pore systems the distribution of pore-sizes shows an almost continuous trend, resulting in a smooth gradually increasing *(Pc-Sat)* curve.

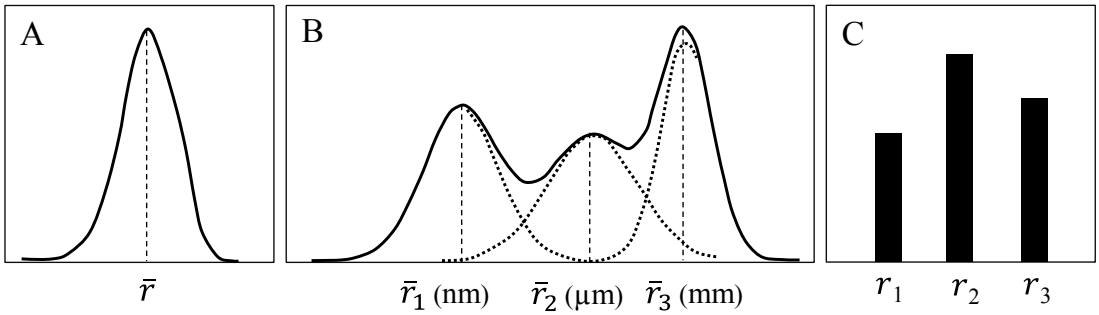

Figure 7.6: Typical pore-size distribution of homogeneous (A), heterogeneous (B), and a synthetic porous media with few discrete pore-sizes (C). The dotted curves show the three possible overlapping normal distributions that make a multi-modal distribution with three peaks. The dotted lines indicate the average radius for each normal distribution.

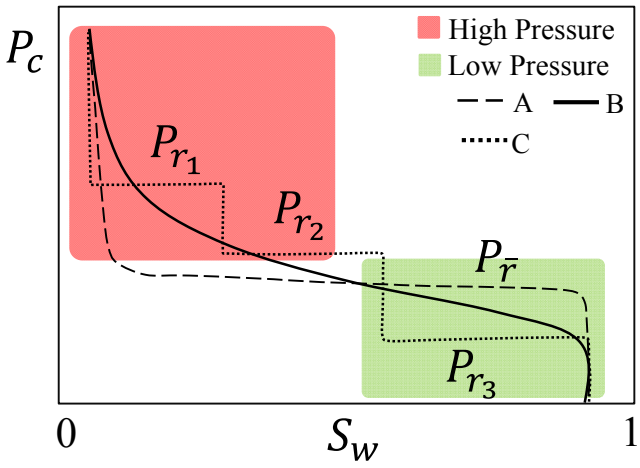

Figure 7.7: Typical (*Pc-Sat*) curves for pore systems shown in Figure 7.6.

For a randomly connected synthetic porous media with a discrete pore-throat size distribution as shown in Figure 7.6C the corresponding (*Pc-Sat*) curve shows a step type trend, (Figure 7.7C). Injection pressure must exceed P_{r_1}, P_{r_2}, P_{r_3} in order to invade pore-throats with radius of r_1, r_2, r_3, respectively.

3.1.3.2. Spatially-correlated Pore System

Now consider a pore system with spatial correlation, i.e. the location of the pores (and pore-throats) is correlated to the pores (and pore-throat) sizes. For such a system, the spatial distribution and connectivity between pore systems influence the shape of the (*Pc-Sat*) curve. For example consider a pore-network with the pore-size

distribution as shown in Figure 7.6C, but with spatial correlation. The following describes two possible cases that may apply:

- If the smallest pores provide overall connectivity for the 2 larger set of pores, the (*Pc-Sat*) curve only displays one step, at $P = P_{r_1}$. In other words, the injection pressure needs to reach P_{r_3} before the fluid can enter the pore space. At $P = P_{r_1}$ the entire pore space becomes invaded with mercury instantly. In this case, MICP data does not detect the presence of larger pore-sizes.
- If the three pore systems provide connections throughout the sample independent of each other, then the (*Pc-Sat*) curve will display 3 steps at $P = P_{r_1}$, P_{r_2} , P_{r_3}.

In cases where the larger pores are well-connected the fluid displacement preferentially occurs through these well-connected clusters of larger pores. Therefore, although contributing to the total porosity of the rock, the smaller pores may not contribute to the rock's flow properties. For such a sample a single-scale model of the larger pores may prove sufficient for calculation of absolute permeability. However, considering all the pore systems may be essential for correct calculation of the saturation values and therefore (*Pc-Sat*) and (k_r-*Sat*) curves.

If elements of a pore-network are positioned in the domain with a spatial correlation to their size, i.e. the larger elements are connected to the network boundaries and the smaller elements are accessible through the larger ones, then the (*Pc-Sat*) curve shows a gradual increasing trend.

3.1.3.3. Discussion

For a spatially disordered pore system the low-pressure end of a (*Pc-Sat*) curve corresponds to (a) the pores that are accessible through the larger pore-throats with smaller capillary entry pressures, and (b) the larger pores which are directly connected to the boundary of the network. The higher pressure part of the (*Pc-Sat*) curve, however, corresponds to the pores accessible through increasingly narrower pore-throats (Figure 7.7). A successful model should replicate closely both the high pressure and low pressure parts of the experimentally obtained (*Pc-Sat*) curve. To

achieve this (a) pores from all existing length-scales that contribute to the porosity as well as provide connection to the pore network should be considered, and (b) the network domain should be large enough to accommodate sufficient number of larger pores such that the displacement of fluid from a few of them does not introduce a sharp change in (*Pc-Sat*) curve.

For the SD rock the larger pores appeared to be connected through the smaller ones, i.e. the larger pores are not directly connected to form highly permeable pathways. This can be concluded from the fact that 8 out of 9 pore networks extracted from samples of this rock (Figure 7.3) are globally disconnected at 21 μm resolution. This implies that the connections between the vugs are provided by the pores (or pore-throats) smaller than 21 μm. The lack of direct connections of the vugs is also evident from the core flooding experiments reported in previous chapters. For the flooding cycles conducted on samples of this rock (D=12.5 mm) the breakthrough was not observed before almost one pore volume of the invading phase was injected. The breakthrough should have occurred at very early stages of injection if the vugs were joined up to form flow pathways with small resistance. Therefore, a single-scale pore network that only captures the vugs cannot predict the flow properties of this rock correctly. This can also be concluded by considering the simulated (*Pc-Sat*) curves for the two coarse and fine network models shown in Figures 7.3 and 7.5 in comparison with MICP laboratory measurements on the core plug SD2. Figure 7.8 shows the comparison. The coarse network is the only connected 21 μm resolution network that is shown in Figure 7.4. The simulations were performed using a quasi-static pore-scale multi-phase flow simulator described in Ryazanov et al. (2009). As shown the low pressure part of the (*Pc-Sat*) curve (P_C < 50 kPa) is closely predicted when the only connected coarse-scale network is used. However, the fluid flow simulations cease at a relatively low pressure (68 kPa). The absence of smaller pores that could have provided connections to the disconnected elements of this network caused 53 % of the coarse network volume to stay uninvaded.

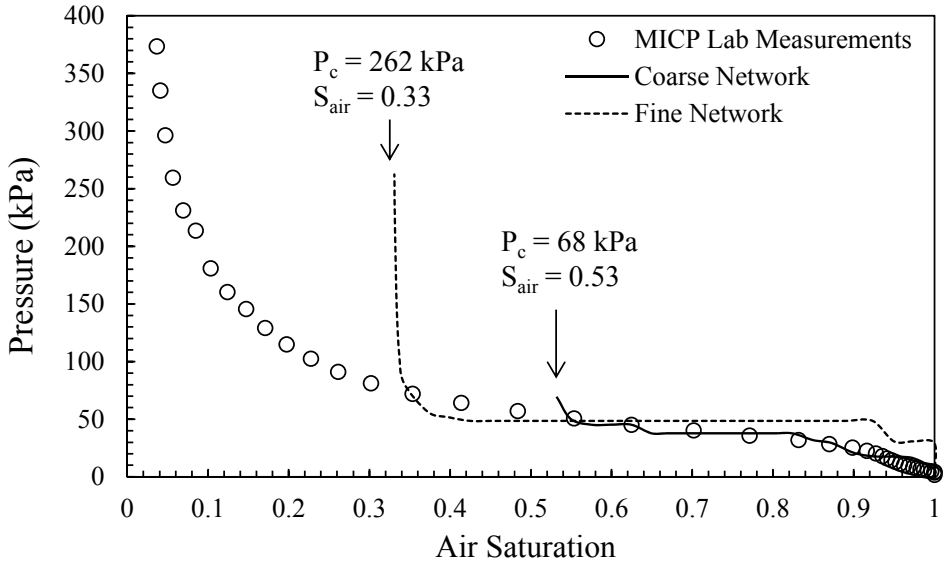

Figure 7.8: Simulated (*Pc-Sat*) curves for the two coarse and fine network models (21 and 5 µm resolution) shown in Figures 7.3 and 7.5, in comparison with MICP measurements for SD2 core plug.

The simulations performed on the fine network, however, provide predictions for pressures up to 262 kPa. It clearly fails to simulate the low pressure end of the curve due to the lack of larger pores that are accessible through the network boundary. For the fine-scale network the (*Pc-Sat*) curve shows a sudden increase in saturation values at pressures ~50 kPa. The invasion of relatively small throats (with *Pc* = 50 kPa) has made a large fraction of the larger pores accessible. Analysing the number and volume fraction of the network elements (including pores and nodes) reveals that this sudden change in saturation is caused by a small number of the network elements that represent a significant 71 % of the total pore volume. This is shown in Figure 7.9 and Table 7.3.

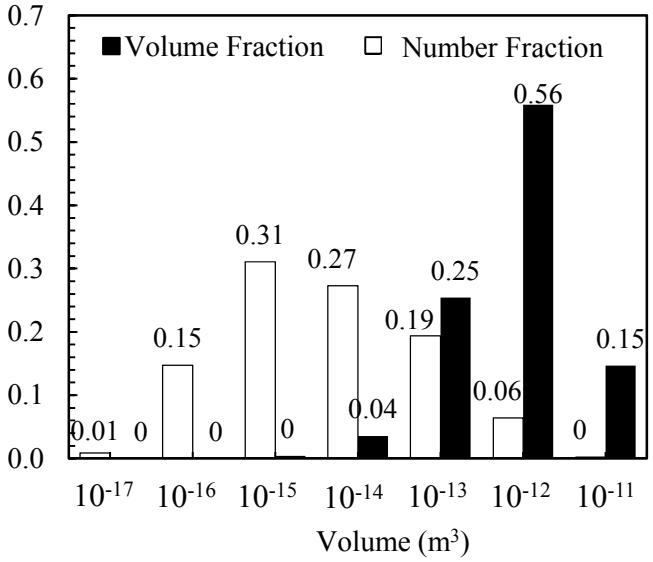

Figure 7.9: Number-based and volume-based distributions of the fine (5µm) network elements. ~ 0.06 of the network elements (frequency) occupy ~0.71 of the network porosity.

Table 7.3: Number-based and volume-based distributions of fine network (5µm) elements.

Bin	Volume	Volume Fraction	Frequency	Frequency Fraction
10^{-17}	2.72×10^{-16}	0.00	34	0.01
10^{-16}	2.80×10^{-14}	0.00	564	0.15
10^{-15}	4.76×10^{-13}	0.00	1186	0.31
10^{-14}	3.87×10^{-12}	0.04	1042	0.27
10^{-13}	2.75×10^{-11}	0.25	740	0.19
10^{-12}	6.05×10^{-11}	0.56	246	0.06
10^{-11}	1.59×10^{-11}	0.15	8	0.00

More precisely there are 254 (246+8) network elements with volumes larger than 10^{-13} m^3. This is only 6 % of the total number of network elements. The saturation can change substantially when these large network elements are invaded. The experimental (*Pc-Sat*) curve shows a more gradual trend compared to these simulated ones. For the fine network the small domain size has probably restricted the number of larger pores accessible through the network boundaries. Therefore, the larger network elements are only accessible through much smaller ones. The injection pressure required to invade those narrower pores are ~50 kPa, following which all their larger connections are invaded instantly.

A multiple-scale network integrated in a domain larger than the fine network's domain is required to include sufficient number of pores from different existing scales.

4. Multiple-scale Pore Network Integration – A Tool to Generate Representative Network Models

Ghous et al. (2008) applied an image registration method to align high resolution (of order of nm) focused ion beam microscope images with coarser resolution (of order of μm) μCT images. Their target was to generate a 3D image of the rock incorporating porosity over several length-scales. Although appealing their method is prone to making substantially heavy 3D images with too many voxels which may be computationally expensive for the subsequent network extraction and flow simulation purposes.

Biswal et al. (2007, 2009) proposed a stochastic method of integrating porosity across several length-scales for carbonate rocks, representing inter-granular, intra-granular and vuggy porosity (based on the classification by Lucia (1995)). They demonstrated successful application of the method to oolitic limestone samples. Biswal's approach includes the deposition of sediments as well as the subsequent diagenesis steps in generation of pore structures. Their algorithms are, however, limited from computational point of view, i.e. for complex carbonate structures networks that are smaller than REV can be generated using this approach.

Jiang et al. (2013) introduced a network integration method to generate pore network models of arbitrarily large volumes incorporating multiple-scale pore systems derived from μCT images captured at a number of different scales (Figure 7.10). The workflow of this method is shown in Figure 7.10 and briefly outlined here. The method takes as its input a number of μCT images (3D binary) of a rock captured from samples at different length-scales. For example for generating a two-scale network model the required inputs are:

- A 3D binary image of a large sample of the rock (representative of larger pores)

- A 3D binary image of a smaller sample of the same rock (representative of smaller pores)

Selecting the length-scales at which the images are acquired requires information detailing the range of pore-sizes present in the rock.

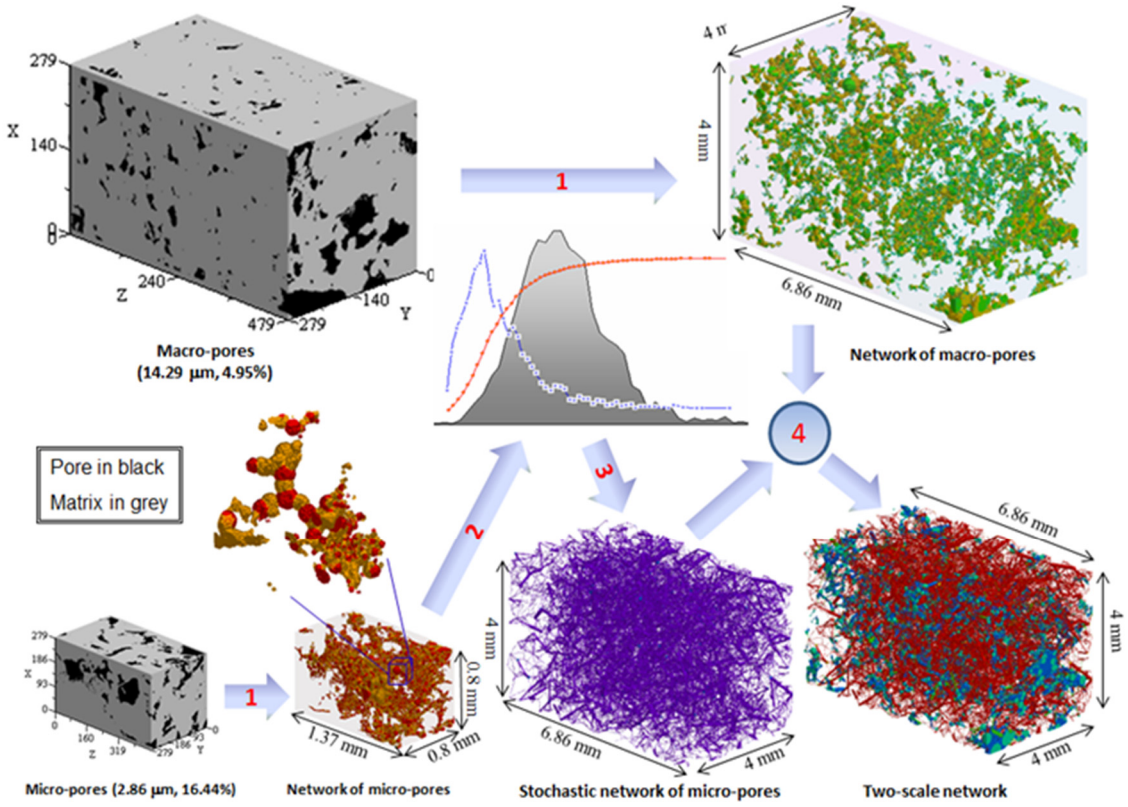

Figure 7.10: Multiple-scale network integration method developed by Jiang et al. (2013). The workflow includes network extraction from binary µCT images of the rock at two different length-scales (1), generating a stochastically equivalent network for the fine network of the size of selected nesting domain (2, 3), and integrating the two networks into one network representative of the two length-scales (4).

4.1. Pore Network Extraction

The first step is to extract pore networks from each 3D binary image. This is labelled in Figure 7.10 as step 1. Here a medial axis-based algorithm is used for the network extraction (Jiang et al., 2007). The extracted networks preserve the geometry and topology of the pore space. More details about this method is presented in (Jiang et

al., 2007). The networks extracted from the images of the larger and smaller samples of the rock are referred to as the coarse and fine networks, respectively.

4.2. Selection of the Size of the Nesting Domain

Due to the difference in the length-scales the domain of the coarse network is usually much larger than that of the fine network, therefore the two networks cannot be integrated directly. In order to be able to integrate the two networks the size of the two-scale network domain (referred to as the nesting domain) should be specified. The size of the nesting domain can be a fraction (δ) of the original coarse image volume ($0 < \delta \leq 1$). The larger the size of the nesting domain the longer the subsequent fluid flow simulations run time becomes.

4.3. Generation of Stochastically Equivalent Networks

The next step is to generate stochastically equivalent networks of the size of the nesting domain. Some statistical information measured from a pore network (see below) can be used to generate stochastically equivalent pore networks of arbitrary sizes. Details of the approach and methodology are presented in (Jiang et al., 2012). Here the method is briefly outlined:

- First, the original network is characterised in terms of the geometric properties (volume, radius, shape factor) as well as topological properties of its elements (connectivity function, coordination number). For definitions of the topological properties refer to chapter 2, section 5.

- Next, based on the size of the requested stochastic network an appropriate number of nodes are generated and randomly positioned in the network domain.

- Finally the nodes are connected using an adequate number of bonds in a way that the topological properties (i.e. connectivity function) of the original network are preserved.

This stochastically equivalent network generation method has previously been validated for sandstone samples using (k_r-*Sat*) and drainage (*Pc*-*Sat*) predictions.

Here stochastically equivalent networks were only generated for the fine network, whereas the entire or sub-domains of the original coarse network was used.

4.4. Integration of the Stochastic Networks

Finally the fine network is integrated with the course network. The stochastically generated fine network elements are positioned in the regions that are not already occupied by the coarse network elements. The network integration can be done *uniformly* or by considering *spatial correlations* i.e. the position of fine network elements can be controlled according to their size. Spatial correlations can be used to introduce small-scale heterogeneities in the integrated model. In the examples presented in this chapter the fine network has been uniformly integrated in the entire nesting domain.

Typically the domain of the original fine network is only a few mms across. Therefore, generating larger stochastic networks (for instance in a nesting domain of a few cms side length) increases the number of network elements radically. For example 1 mm^3 domain with 100 network elements scales to a 1 cm^3 domain with 100,000 network elements. In other words, a 1000 fold increase in network elements for a 10x increase in length-scale of the domain. The resulting two-scale network may no longer be amenable to fluid flow simulations. To tackle this problem Jiang et al. (2013) suggested reducing the number of fine network elements in the domain (i.e. the density of the network) by a fraction they referred to as *fraction of fine-scale network* , $0 < f_F < 1$.

In Jiang's method of generating stochastically equivalent networks the connectivity function is preserved. However if a reduced version of the stochastic network is generated by setting the fraction of fine-scale network $f_F < 1$ then the connectivity decreases. More precisely, the connectivity function of the reduced stochastic network is related to the connectivity function of the original network as: $\chi_{v,r}(r) = f_F\, \chi_{v,o}(r)$.

5. Multiple-scale Network Model Generation - Case Study

In this section generation of multiple-scale pore-network models for a dolomite is evaluated by comparing the (*Pc-Sat*) curves measured using laboratory MICP tests and calculated using pore-scale flow simulations.

5.1. Rock Samples

Four SD samples of D = 2, 5, 25 and 38 mm were imaged with respective resolutions of 2, 5, 21 and 32 μm. Considering that SD is a vuggy carbonate, larger core plugs were selected to capture the network of vugs, while smaller samples were selected to capture the finer porosity of the rock. Figure 7.11 shows example μCT slices of these four SD samples.

The 25 mm diameter core plug shown in Figure 7.11B along with two other same size plugs of SD were used for MICP laboratory measurements, (refer chapter 3, section 2 for the (*Pc-Sat*) curves of these SD samples). These are the three SD1, SD2, SD3 plugs for which the extracted pore networks are shown in Figure 7.3. MICP tests were performed at Petrobras laboratories, Rio de Janeiro, Brazil. Note that since MICP is a destructive test the core plugs used in these tests were lost and therefore there was no opportunity to physically sub-sample the cores for higher resolution μCT imaging. All the SD core plugs used in this study were selected from the same larger sample of this rock.

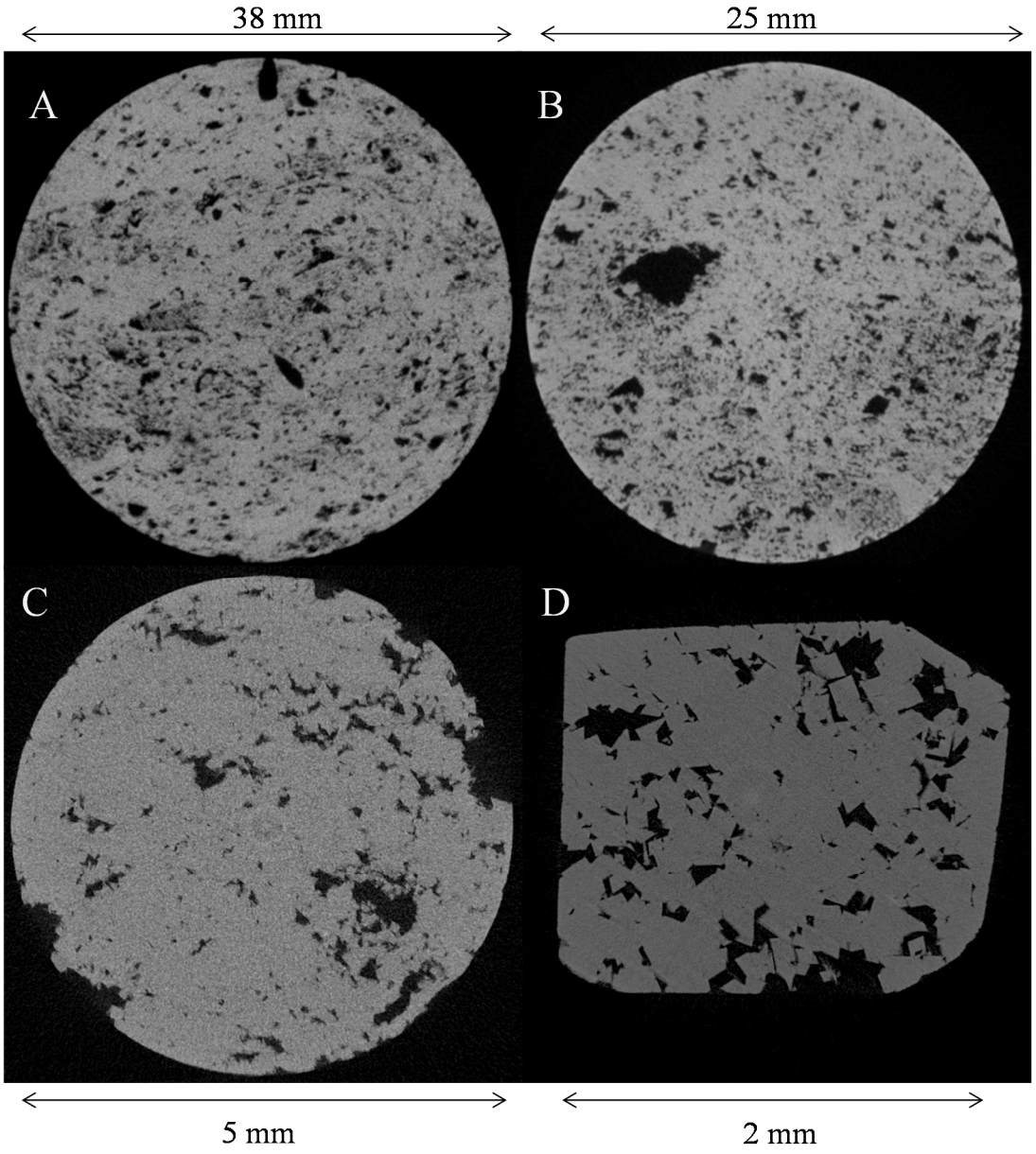

Figure 7.11: Example µCT slices of four SD samples of D=2, 5, 25 and 38 mm imaged with respective resolutions of 2, 5, 21 and 32 µm.

Subsequent to image reconstruction the µCT images were filtered (anisotropic diffusion filter, refer to chapter 3, section 3) and segmented (watershed segmentation method refer to chapter 3, section 3) using Avizo Fire. The resulting binary images were used as the basis for pore network extraction. Figure 7.12 shows 3D rendering of the extracted networks for these four samples. Table 7.4 lists their main parameters.

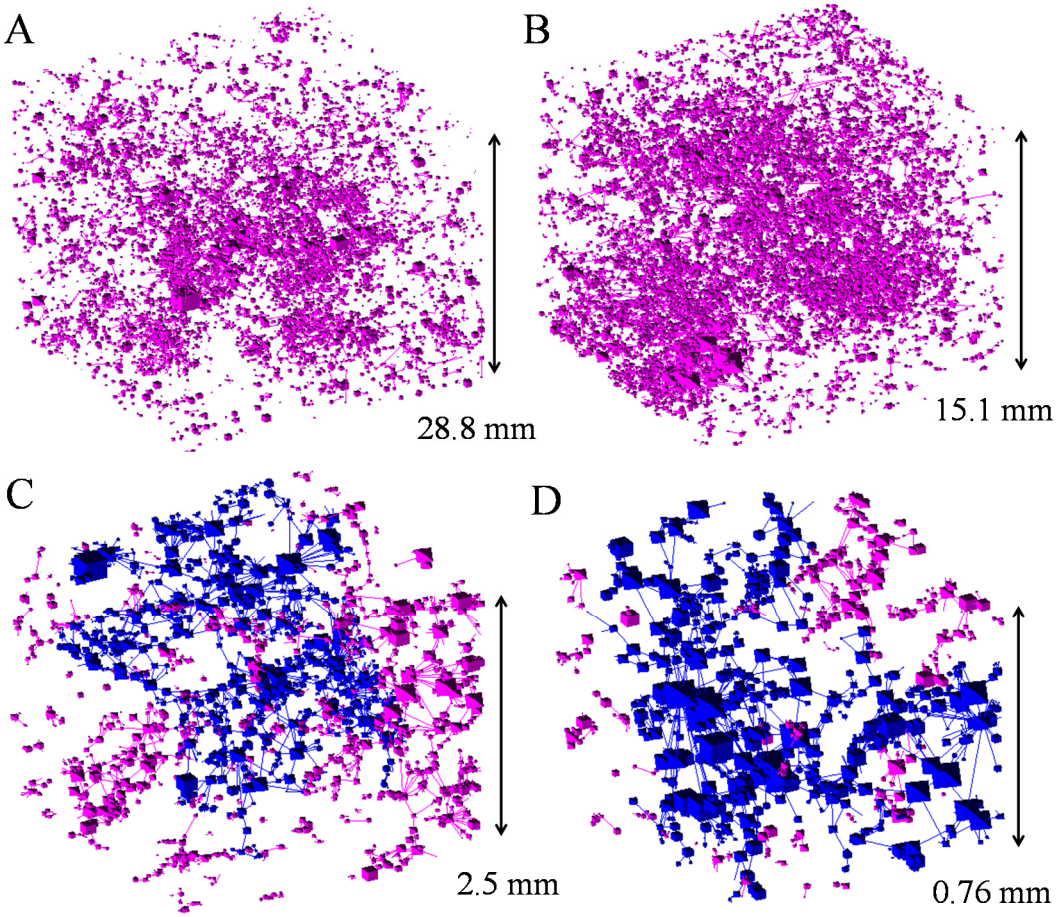

Figure 7.12: Pore networks extracted from the images shown in Figure 7.11. Pink and blue indicate the disconnected and connected elements, respectively. Coarser networks (A, B) are globally disconnected while finer networks display some connectivity (C, D).

Table 7.4: Network parameters for pore networks shown in Figure 7.12.

Image Resolution (μm)	Domain Dimensions (voxels)	Number of Nodes	Number of Bonds	Total Elements	Connected Porosity %	Disconnected Porosity %	Total Porosity %	k_{abs} (mD)
32	881×901×901	10318	12736	23054	0	3.52	3.52	0
21	821×860×720	19897	24093	43990	0	6.03	6.03	0
5	500×500×500	3418	4127	7545	6.15	3.08	9.23	75.63
2	570×450×380	1733	2089	3822	12.72	1.59	14.32	99.75

The two coarser scale pore networks (Figure 7.12A and 7.12B) are globally disconnected while the finer scale networks (Figure 7.12C and 7.12D) are connected displaying $k_{abs} > 0$ mD. The total captured porosity shows an increasing trend with resolution enhancement, as does the total connected porosity, and the calculated

permeability. It should be noted that ~11 % of the pores are disconnected for the highest resolution network. The reason could be: (a) insufficient resolution to image some of the finer pore-throats, (b) truly isolated pores that may exist in the sample resulting from recrystallization during dolomitisation.

Figure 7.13 shows pore-throat size distributions derived from MICP measurements for the three SD core plugs (refer to chapter 3, section 2). The image resolutions for the four µCT images are marked on this plot. The distributions display distinct peaks at ~15 µm, which is smaller than the image resolutions for the two coarser networks.

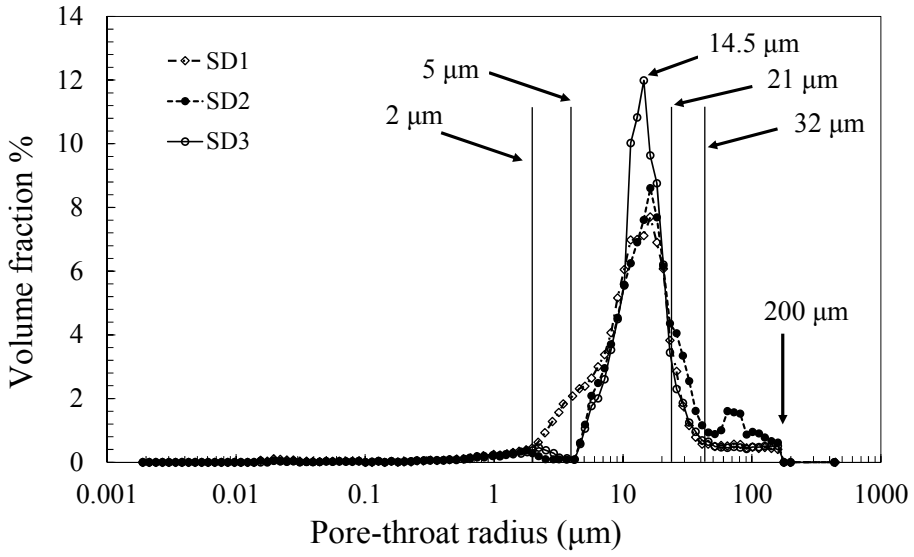

Figure 7.13: Pore-throat size distributions derived from (*Pc-Sat*) curves generated in MICP measurements for three (D=25 mm) SD core plugs. The image resolutions for the four µCT images shown in Figure 7.10 are marked here.

Figure 7.14 shows the volume fraction of the pore space that are accessible only through pore-throats smaller than the image resolution of the 4 µCT images shown in Figure 7.11. The figures are based on injected volumes and pressures recorded during MICP tests. The volume fractions are obtained by summation of the pore volumes accessible through the pore-throats smaller than the image resolution, normalised by the total pore-volume of the sample.

$$volume\ fraction = \frac{\sum_{t_{min}}^{r} v}{\sum_{t_{min}}^{t_{max}} v}, \tag{7.1}$$

where v denotes the accessible volume fraction, while r, t_{min}, t_{max} denote image resolution, smallest and largest throats detected by MICP, respectively. The two coarser resolution images (21 and 32 μm resolution) are missing a significant proportion of the pore-throats (to which more than 60 % of pore-space is connected), while only less than 20 % of pore space appears as disconnected on the two finer resolution images (5 and 2 μm resolution).

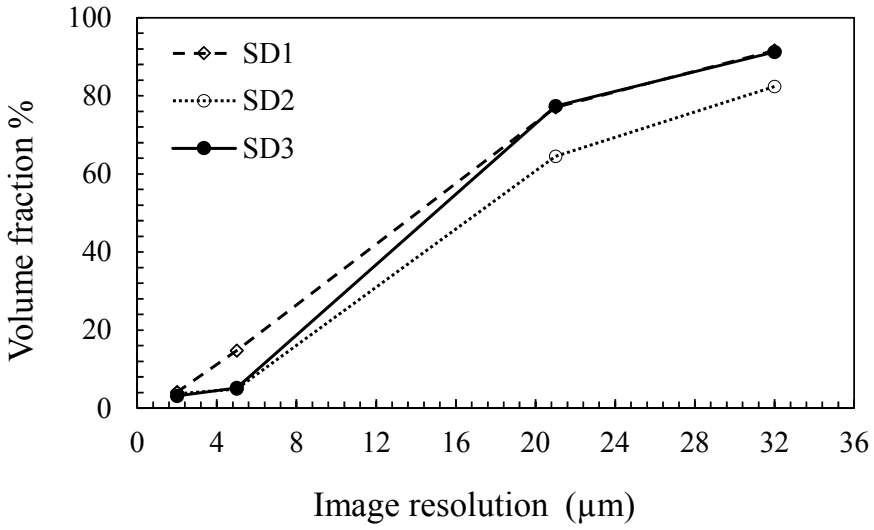

Figure 7.14: Fraction of the pore-space (volume fraction) connected to pore-throats smaller than the image resolution for the 4 μCT images shown in Figure 11. Resolution limitations caused more than 60 % of the pore space to appear as disconnected for the coarser resolution images. This number is less than 20% for the two finer resolution images.

Figure 7.15 shows the pore-size distribution derived from the four μCT images (shown in Figure 7.11) using a sphere fitting method (Jiang et al., 2007). It is clear that depending on the sample size and the image resolution each of these four images has captured *a portion* of the wide range of the pore-size distribution of SD, but that none of these individual pore networks has captured the entirety of the multiple-scale porosity. The aim of this work is to generate a representative pore network by combining these single-scale network models to incorporate all the existing pore-sizes.

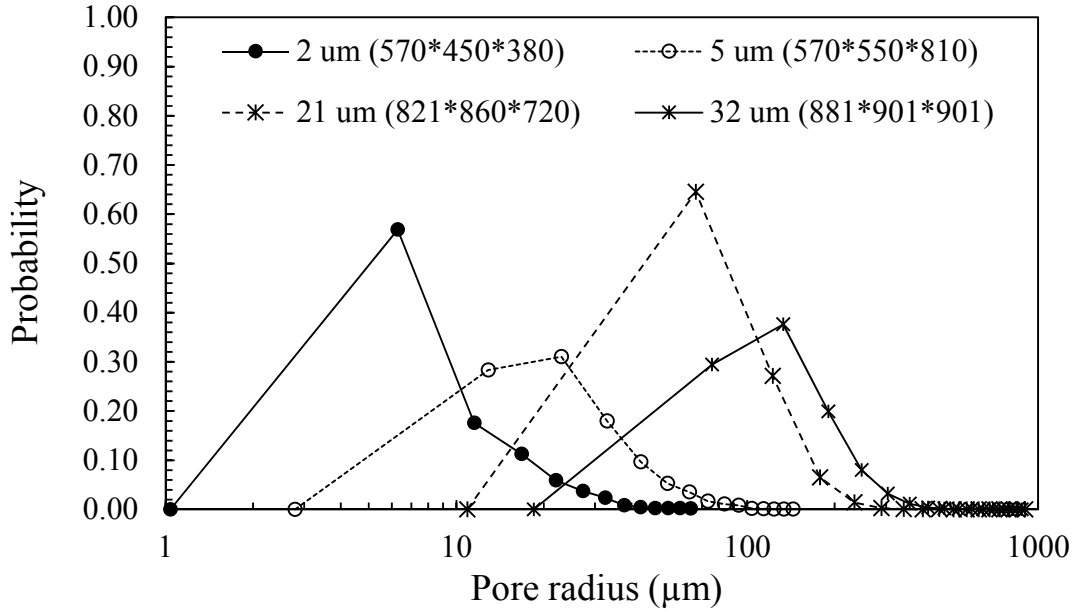

Figure 7.15: Pore-size distribution derived from the four μCT images (shown in Figure 7.11) using a sphere fitting method (Jiang et al., 2007).

5.2. Two-scale Network Integration

5.2.1. Selecting Scales

In this section integration of SD networks from two length-scales is described. In selecting the best pair of networks for the integration, the overlap of their pore-size distributions must be considered. In practice, too much overlap should be avoided to maximise the integrated pore-size range (Figure 7.16A), while at the same time it is always desirable to have some overlap between the two distributions otherwise a range of pore-sizes will be excluded (Figure 7.16B).

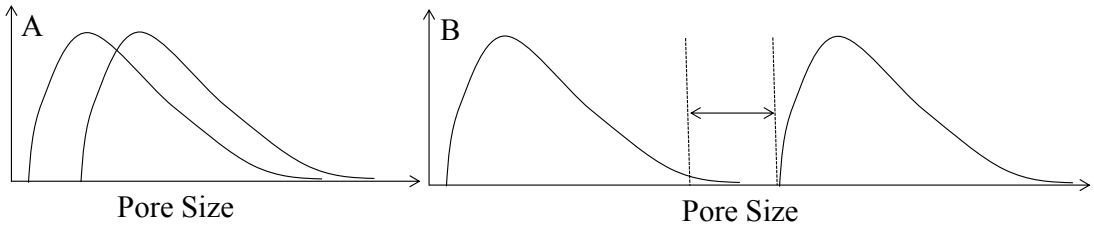

Figure 7.16: Selecting the length-scales for network integration by comparing their pore-size distribution. Too much overlap (A) or (B) insufficient overlap of pore-size distributions should be avoided.

On this basis the 21 μm and 2 μm resolution networks are considered as the coarse and fine networks respectively (Figure 7.12B and 7.12D). The coarse network is completely disconnected (k_{abs} = 0 mD), while only ~11% of the fine network appears to be disconnected.

5.2.2. Input Parameters

5.2.2.1.Size of the Nesting Domain

The domain sizes of the 21 and 2 μm resolution images are (821×860×720) and (570×450×380), respectively (Table 7.3). Due to the difference in the length-scales at which these two images were captured the size of the fine network domain volume is less than 0.02 % of the coarse network domain volume (Table 7.3). To keep the two-scale network computationally manageable it is possible to (a) select a nesting domain smaller than the coarse network domain and (b) reduce the density of the fine network i.e. only use a fraction of the fine network (f_F) < 1. Although selecting smaller nesting domains is desirable from the computational point of view, the nesting domain size should be large enough to be representative, i.e. to accommodate sufficient network elements from all scales. To investigate the effect of the size of nesting domain on the properties of the resulting two-scale domain 10 sub-domains with δ ranging from 0.1 to 1 are considered here. The investigated properties include porosity (connected and disconnected) and absolute permeability of the two-scale network. A similar exercise is presented in Jiang et al. (2012). Here, the sub-domains are sub-sections of the original coarse network and the fraction of fine network is kept as 0.01. Figure 7.17 shows the resulting two-scale pore networks rendered in 3D.

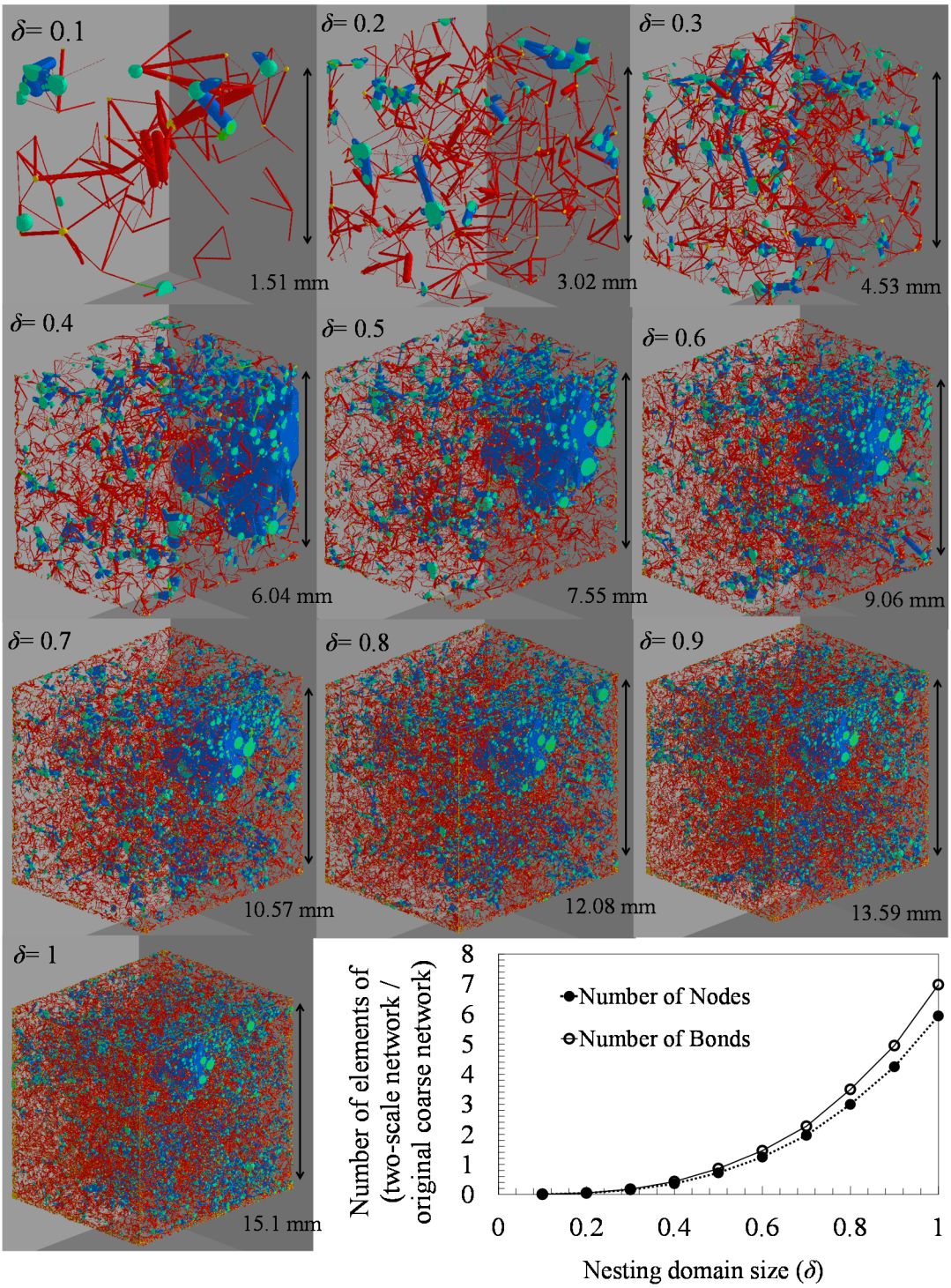

Figure 7.17: Two-scale network models with δ = 0.1 to 1. The plot shows the number of two-scale network elements change with a factor of 0.01 to ~6 relative to the coarse network for 0.1 < δ < 1. Blue/green show the coarse network elements. Red shows the fine network elements.

The number of two-scale network elements (i.e. nodes and bonds) changes with a factor of 0.01 to ~ 6 relative to the number of the coarse network elements as the ratio of nesting sub-domains increase from 0.1 to 1 (Figure 7.17). Therefore, the simulation costs increase but remain within the same order of magnitude as a larger nesting domain is used.

Figure 7.18A to 7.18D shows the effect of the nesting domain size on the static properties of the resulting two-scale network. The single-scale coarse and fine networks are also shown on these plots (red and blue dots). Table 7.5 lists the network parameters. The porosity of the two-scale network displays fluctuations in the smaller nesting domains, i.e. 0.1 to 0.5, which can be associated with the lack of representativity of the two-scale network. In other words, the domain of the two-scale network is too small to contain enough number of elements from all scales.

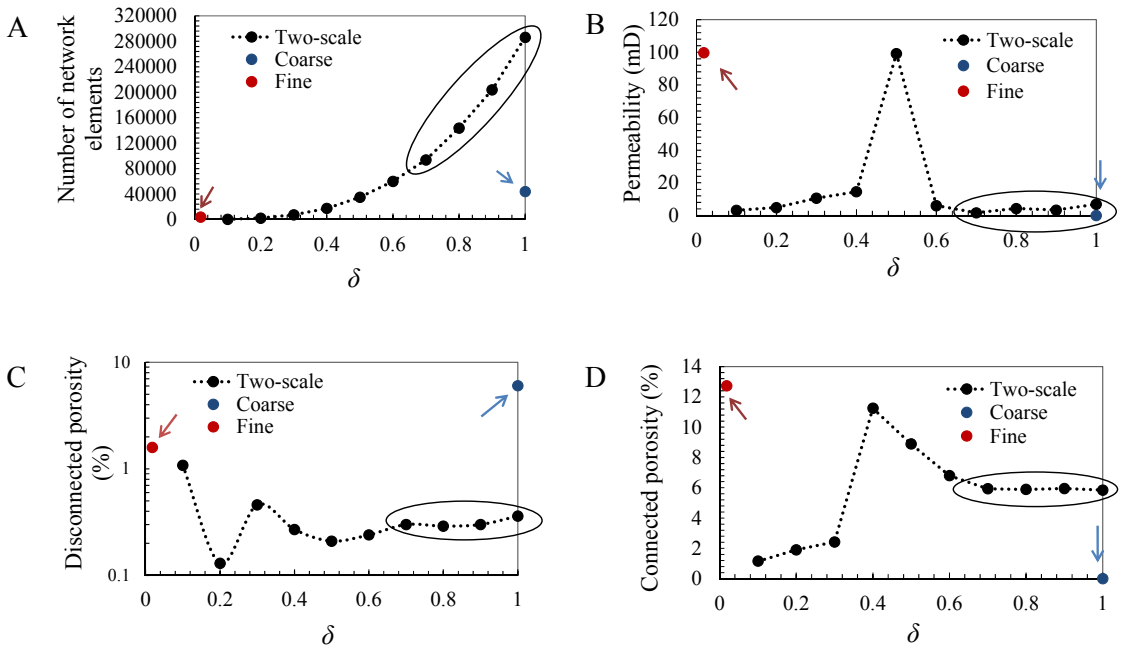

Figure 7.18: Effect of the nesting domain size on the static properties of the resulting two-scale network. The single-scale coarse and fine networks are also shown on these plots (red and blue dots). Nesting domains smaller than 0.6 display fluctuations in their properties. The ellipses indicate data points with converged porosity and permeability values.

The absolute permeability of the two-scale networks shows an abrupt change for the network of $\delta = 0.5$ nesting domain (see Figure 7.18B). The permeability drops as the

nesting domain grows i.e. for $\delta > 0.5$. This may imply that at $\delta = 0.5$ a connected cluster is accommodated which spans across the nesting domain with coarse nodes connected to both inlet and outlet boundary faces, this has therefore increased the permeability unrealistically.

A similar artefact commonly happens during sampling of heterogeneous materials such as a vuggy carbonates. A small sample may contain a number of connected large vugs and therefore display a significantly higher permeability (and porosity) compared to samples of the same size taken from other parts of the rock with fewer vugs. To avoid this sampling artefact the selected sample needs to be large enough to include at least one REV. According to Figure 7.18A to 7.18D nesting domains larger than 0.7 display converged properties. Therefore, the size of nesting domain is set to 0.7 for the two-scale networks presented in the remainder of this chapter.

Table 7.5: Network parameters for two-scale (with δ ranging from 0.1 to 1 and $f_F = 0.01$), stochastic fine ($\delta = 1$, $f_F = 0.01$), and coarse networks ($\delta = 1$).

Nesting Domain Fraction	Number of Nodes	Number of Bonds	Total Elements	Connected Porosity %	Disconnected Porosity %	Total Porosity %	k_{abs} (mD)
0.1	124	171	295	1.15	1.08	2.23	3.14
0.2	904	1192	2096	1.9	0.13	2.03	4.86
0.3	3130	4213	7343	2.42	0.46	2.88	10.6
0.4	7095	10326	17421	11.24	0.27	11.51	14.54
0.5	14319	20743	35062	8.88	0.21	9.09	99.19
0.6	24764	35124	59888	6.8	0.24	7.04	6.05
0.7	39118	54696	93814	5.93	0.30	6.23	1.68
0.8	59594	84218	143812	5.89	0.29	6.18	4.3
0.9	84479	119317	203796	5.95	0.3	6.25	3.29
1	118174	168112	286286	5.84	0.36	6.2	6.9
Coarse	19897	24093	43990	0	6.03	6.03	0
Fine	98277	137611	235888	0.14	0	0.14	0.99

5.2.2.2.Fraction of fine network (f_F)

In this section the effect of the fraction of fine network (f_F) on the static properties of the resulting two-scale network models is presented. The fine network was uniformly integrated in the nesting domain ($\delta = 0.7$) with f_F ranging from 0.01 to 0.08.

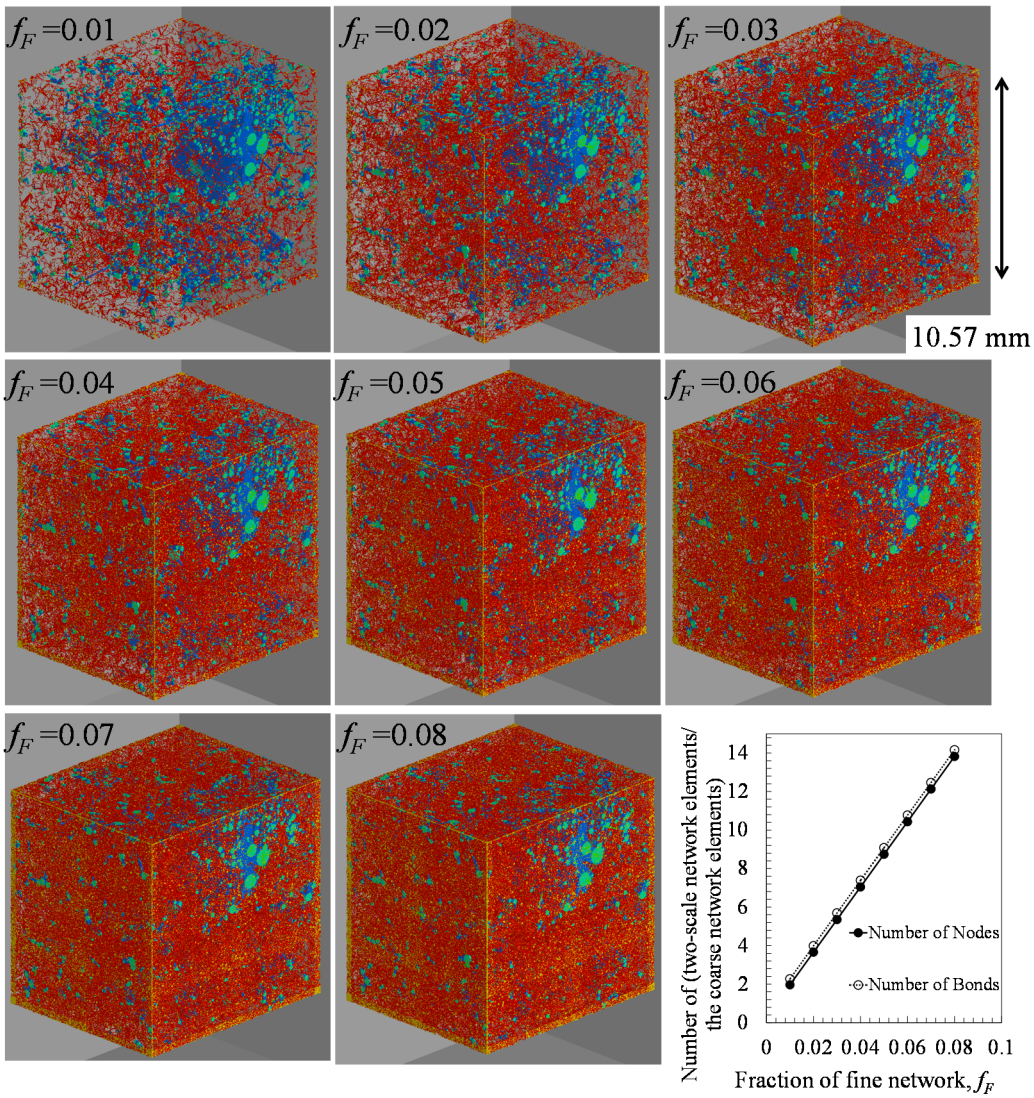

Figure 7.19: 3D renderings of the two-scale networks with $\delta = 0.7$ and $0.01 \leq f_F \leq 0.08$. Blue/green shows the coarse network elements and red shows the fine network elements. The number of two-scale network elements increase with a factor of ~2 to ~14 relative to the coarse network for $0.01 \leq f_F \leq 0.08$.

Larger f_F values resulted in two-scale network models that were not computationally manageable with the existing fluid flow codes and computational power. Figure 7.19 shows 3D renderings of the two-scale networks with $\delta = 0.7$ and $0.01 \leq f_F \leq 0.08$. The number of two-scale network elements increase with a factor of ~2-~14 relative to the coarse network for $0.01 \leq f_F \leq 0.08$.

Figure 7.20 and Table 7.6 show the network parameters for the two-scale networks shown in Figure 7.19. The number of network elements and hence the porosity of the two-scale networks displays a linear increase as f_F increases (Figure 7.20A). However, the permeability increases non-linearly (Figure 7.20B).

The coarse network elements are shown to be disconnected in the absence of any superimposed fine network. Although their sizes are small, the fine network elements provide connections to the isolated vugs of the coarse network, hence the resulting two-scale network becomes globally connected with k_{abs} values larger than zero. By increasing the f_F value the number of connections between the coarse network elements increases. This enhances the global connectivity of the two-scale network, manifested in a large increase in k_{abs} for $0.01 < f_F < 0.06$ (Figure 7.20B). For $f_F \geq 0.06$ the value of k_{abs} appears to converge to ~200 mD. The converged values of k_{abs} are almost four times larger than the laboratory measured value for SD (~50 mD). The two-scale networks with $0.02 < f_F < 0.03$ exhibit closer k_{abs} values to ~50 mD, ($40.24 \text{ mD} < k < 95.82 \text{ mD}$).

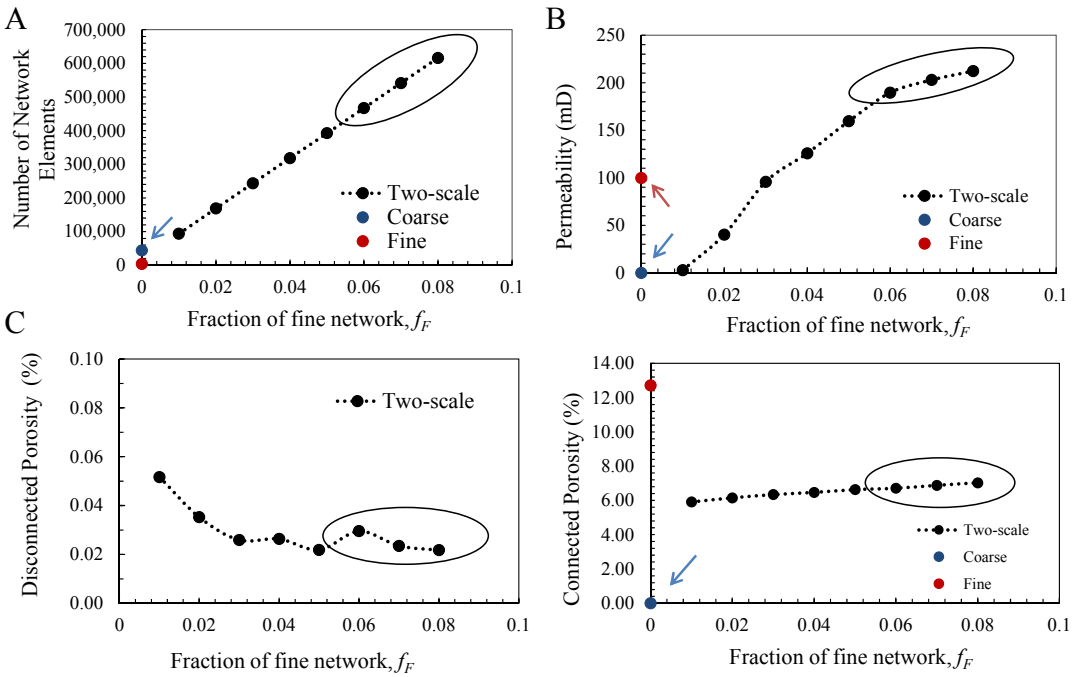

Figure 7.20: Effect of the fraction of fine network on the static properties of the resulting two-scale network. The properties show converging trend for f_F > 0.05. The ellipses show the networks with almost converged porosity and permeability values.

Table 7.6: Network properties for the two-scale network for δ = 0.7, 0.01 ≤ f_F ≤ 0.08, coarse (original), and fine (original).

f_F	Number of Nods	Number of Bonds	Total Elements	Connected Porosity	Disconnected Porosity	Total Porosity	k_{abs} (mD)
0.01	39118	54733	93851	5.91	0.32	6.23	2.80
0.02	72819	96056	168875	6.15	0.22	6.37	40.24
0.03	106521	137103	243624	6.34	0.17	6.51	95.82
0.04	140222	178043	318265	6.47	0.18	6.64	125.85
0.05	173924	218795	392719	6.63	0.15	6.78	159.52
0.06	207625	259555	467180	6.71	0.20	6.91	189.61
0.07	241326	300327	541653	6.88	0.17	7.05	203.01
0.08	275028	341170	616198	7.02	0.16	7.18	212.36
Coarse	19897	24093	43990	0	6.03	6.03	0
Fine	1733	2089	3822	12.72	1.59	14.32	99.75

Note that since the fine network is stochastically generated the connected porosity and permeability of different realisations of generated two-scale network models with δ = 0.7 and f_F = 0.01 (listed in Tables 7.4 and 7.5) are slightly different. For this

case the difference between the connected porosity and permeability are 0.02 % and 1.12 mD, respectively.

5.2.3. Pore-scale Simulation of Capillary Pressure Curves for Two-Scale Pore Networks

It was noted in section 3.1.3 that the single-scale network models extracted from coarse or fine resolution µCT images are not successful in simulation of both the high pressure and low pressure ends of the (*Pc-Sat*) curves. Figure 7.21 shows the results of pore-scale simulations on two-scale network models with increasing f_F, compared to the laboratory measurements.

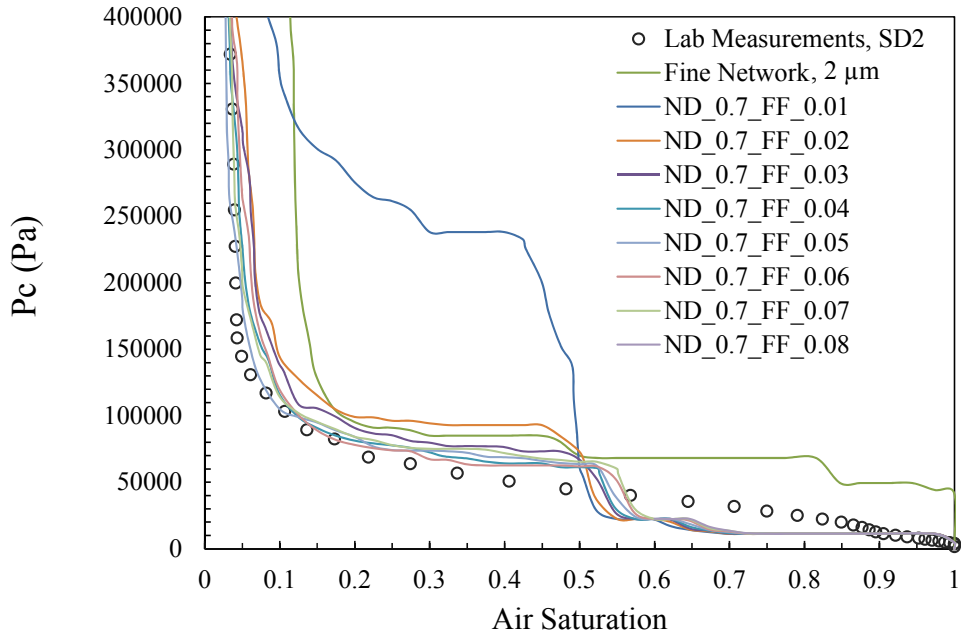

Figure 7.21: Effect of f_F on the calculated (*Pc-Sat*) curves in comparison with MICP laboratory measurement. Fine network is the 2 µm resolution network. The two-scale networks with f_F > 0.02 appear to be close to the laboratory measurements. FF and ND indicate the f_F and δ.

Integrating the two-scale networks has improved the match between the calculated (*Pc-Sat*) curves and the experimental data in two ways: (a) compared to the fine network simulations, using the two-scale networks displays a better estimation of the low pressure part of the curve due to inclusion of the coarse network elements; (b) the high pressure part of the simulated curve is closer to the laboratory measurements. The fine network simulations display a residual air saturation of 11 %

corresponding to the disconnected porosity of the network, (see Table 7.4). This 11 % disconnected porosity may "in reality" be connected through pore-throats smaller than the image resolution (2 μm). Two-scale network integration has enhanced the global connectivity, and hence decreased the disconnected porosity to values between 3 to 5 %. The (*Pc*-*Sat*) curves for the two-scale networks with $f_F > 0.02$ are close to each other. For $f_F \geq 0.03$ the match improves with a diminishing rate. The two-scale network integration provides much closer estimations to the (*Pc*-*Sat*) curves compared to single-scale simulations. However, a jump exists in the two-scale network simulations around the saturations $0.5 < S_{air} < 0.55$. This is probably due to insufficient overlap between the two pore-size distributions of the 2 and 21 μm resolution networks (Figure 7.12). A range of middle-sized pores (~10 μm <radius< ~30 μm) are not well represented in either of these two pore networks. In addition, Figure 7.13 shows the peak values of pore-throat radius distributions for SD rock is in this range which makes the proper inclusion of this pore radius interval substantially important.

The lower *Pc* values ($0.55 < S_{air} < 1$) in the two-scale network correspond to large pores that are from the coarse network since all the pores of the fine network have higher *Pc* values. These large pores must therefore be connected to the boundary of these two-scale networks and immediately accessible to mercury at low injection pressure ranges. Around $S_{air} \sim 0.5$ all the remaining pores are accessible only through finer pores (from the fine network). This is clear from the fact that the values of *Pc* were increased suddenly (jump in the curves) before any further mercury is invaded in the network. Once the fine network elements are invaded the remaining pores from the coarse network and the fine network become simultaneously accessible. Note that the fine network constitutes less than 1% (out of ~7%) of the total porosity of the two-scale networks, i.e. 17% saturation. Moreover, at the jump the simulated *Pc* values overshoot the measured *Pc* values. This is also a clear indication that a range of pore-sizes is underrepresented in these two-scale networks.

A three-scale network that integrates the three 2, 5, and 21 μm resolution networks (Figure 7.15) may provide a better representation of the SD pore structure and hence a smoother (*Pc*-*Sat*) curve.

5.3. Three-scale Network Integration

In order to integrate three pore networks of length-scales (L_1 , L_2 , L_3) where $L_1<L_2<L_3$ the two networks of length-scales L_1 and L_2 are first integrated into a two-scale network, which is subsequently integrated into the network of largest length-scale, L_3. The process involves selecting two sets of appropriate δ, and f_F. For a three-scale network the number of possible choices for these parameters increases with the power of two compared to the two-scale network. Figure 7.22 compares the (*Pc-Sat*) simulation results for a three-scale network model (obtained by integrating the 2, 5 and 21 µm resolution networks), a two-scale network (2, 21 µm resolution networks, $\delta = 0.7, f_F = 0.03$), the fine-scale network (2 µm resolution), and laboratory measurements. The jump is no longer present in the simulation results for the three-scale network, probably due to the inclusion of pores (~10 µm < radius < ~30 µm) that were underrepresented in the two-scale network model. Figure 7.22 shows the closest match obtained for the three-scale network models using the following parameters:

1) Integrating 2, 5 µm resolution networks, $\delta = 1$, $f_F = 1$
2) Integrating the network generated in step 1 into the 21 µm resolution network: $\delta = 1, f_F = 7 \times 10^{-5}$

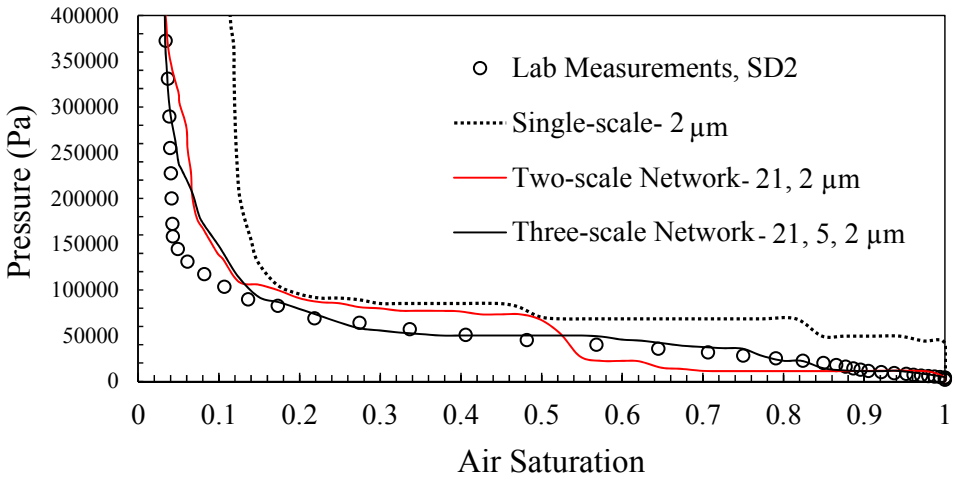

Figure 7.22: Comparison between *(Pc-Sat)* curves calculated on three, two and single scale networks and the laboratory measurement. The jump in the two-scale curve ($\delta = 0.7, f_F = 0.03$) is not observed in the three-scale curve, probably as a result of including the less represented pores.

It should be noted that the three-scale network simulation displays an offset from the measured curve within the last 20% of residual air saturation. This may indicate that there are still a range of finer pores that need better representation in the integrated network. These underrepresented pores are probably the missing connections to the 3% of the pore space, see Figure 7.14.

Table 7.7: Network parameters for single, two-scale and three-scale networks.

Network	Number of Nods	Number of Bonds	Connected Porosity	Disconnected Porosity	Coordination Number	Average Aspect Ratio	Total Porosity	k_{abs} (mD)
Single-scale (2 μm)	1733	2089	12.72	1.59	2.34	1.55	14.32	99.75
Single-scale (5 μm)	3418	4127	6.15	3.09	2.35	1.62	9.24	75.63
Single-scale (21 μm)	19897	24093	0	6.03	2.38	1.30	6.03	0
Two-scale $\delta = 0.7$, $f_F = 0.03$ (2 and 21μm)	106521	137103	6.34	0.17	2.56	10.12	6.51	95.82
Two-scale $\delta = 1$, $f_F = 1$ 2 and 5 μm	34933	45561	20.35	2.52	2.57	1.19	22.87	371.34
Three-scale (2, 5 and 21 μm)	20589	37630	5.93	0.15	3.62	11.75	6.08	165.30

Table 7.7 compares the network properties of the two-scale (δ = 0.7 and f_F = 0.03) and three-scale networks. The total number of elements in the three-scale network is ~24 % of the total number of elements of the two-scale networks (δ = 0.7 and f_F = 0.03). This indicates that a heavier multiple-scale network (with more elements) is not necessarily a more representative one. The selection of the length-scales (resolution of the image) and hence the range of pore-sizes included in the multiple-scale network has the greatest effect on the representativity of the resulting network model.

No laboratory relative permeability measurements were available to this research. Therefore, only *(kr-Sat)* calculated based on single-scale, two-scale, and three-scale networks (Table 7.7) are compared (Figure 7.25). The *(kr-Sat)* curves are calculated for a drainage process; mercury invading a fully air saturated network. The integrated

networks (two-scale and three-scale) display broader range pore-size as well as aspect ratio distributions (Figures 7.23 and 7.24).

The average aspect ratio values are larger for the two-scale (10.12) and three-scale (11.74) networks compared to the single-scale pore networks (0.89, 1.62 and 1.3 for 2, 5, and 21 µm networks, respectively). These higher aspect ratios appear to be more consistent with the multiple-scale pore structure of this dolomite.

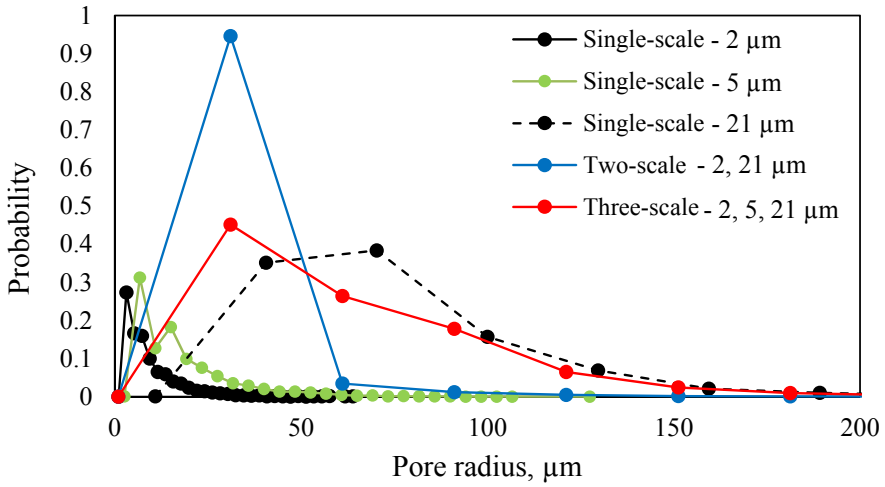

Figure 7.23: Pore-size distribution of single-scale, two-scale and three-scale networks listed in Table 7.7. The integrated networks display wider distributions.

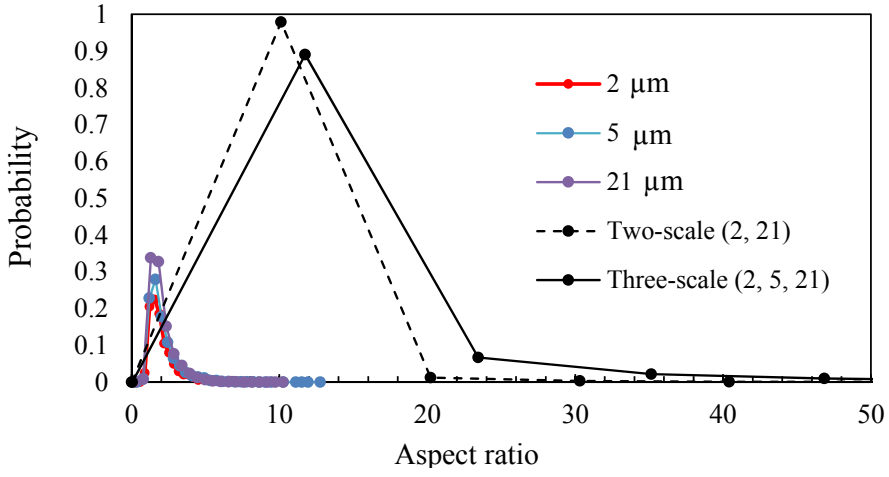

Figure7.24: Aspect ratio distributions for single, two-scale and three-scale networks listed in Table 7.7. The integrated networks display wider distributions with larger average values.

Preliminary investigation of the *(kr-Sat)* curves opens discussions on the following points. The three-scale network shows an earlier mercury breakthrough (at $S_{air} = 0.6$)

compared to the single-scale network (at S_{air} = 0.35), this may be associated to its broader pore-size distribution which can cause fingering of the invading phase. In addition to that, the coordination number of the three scale network is larger than that of the two-scale and single-scale networks (Table 7.7). This also indicates that the three-scale network is locally more connected that can assist the mercury to the early breakthrough. The existence of larger network elements in the three-scale network can provide lower resistivity flow pathways and hence can make the displacement front less uniform which could cause early mercury breakthrough.

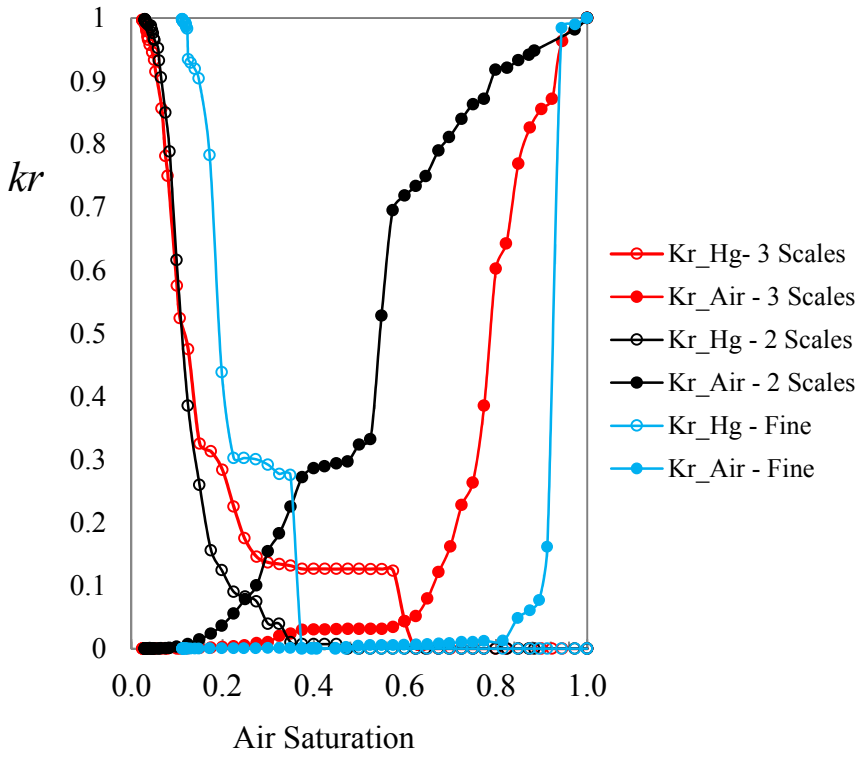

Figure 7.25: Comparison between the calculated *(kr-Sat)* -Sat curves for the single, two-scale and three-scale network models. The curves show irregular shapes probably due to small nesting domain.

Figure 7.26 shows the connectivity function of the three single-scale networks compared to that of the integrated networks. The 2 µm single-scale network displays the highest (negative) values of Euler number, this indicates that, globally, the 2 µm single-scale network is the most connected one. However, due to its small pore sizes the mercury invasion does not occur until the invasion pressure builds up to the entry

pressure required for its small pores, the minimum pressure required for the air displacement is known as displacement pressure. Figure 7.25 shows as the displacement pressure of ~ 4200 Pa is reached the fine network is suddenly invaded with mercury until S_{air} ~ 0.85. Over this period the $k_{r,\,air}$ drops from 1 to 0.06 (Figure 7.25). This may be due to invasion of most of the pores that provide the connections to the network inlet by mercury. Air can still flow through the wetting films (θ = 0, IFT = 397 mN/m). As more mercury is injected the $k_{r,\,air}$ decreases but is still larger than zero. The $k_{r,\,air}$ approaches zero as S_{air} approaches its irreducible saturation of 0.11.

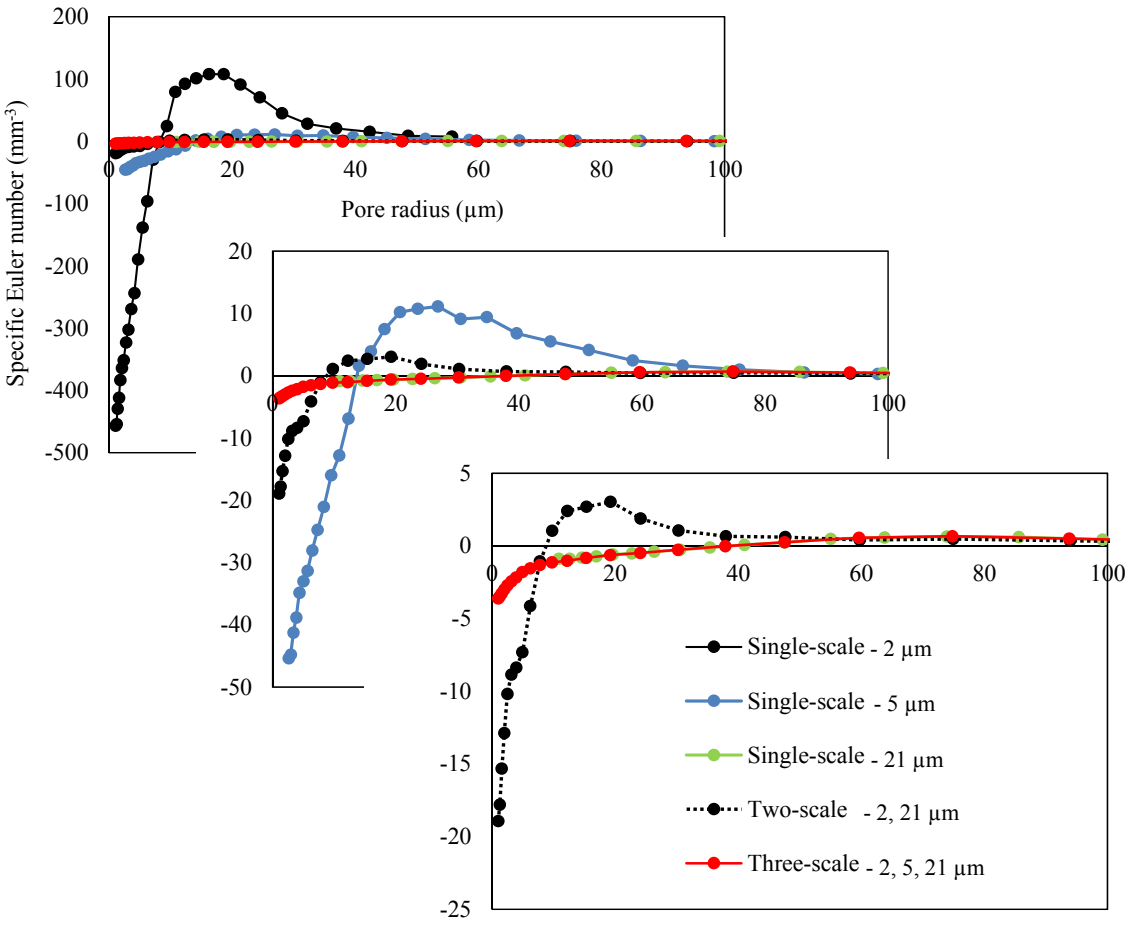

Figure 7.26: Connectivity function of the three single-scale networks compared to that of the integrated networks. The two-scale network is globally more connected than the three scale network, which is probably the reason why the $k_{r,\,air}$ for the two-scale network appears at the top of that of the tree-scale network (Figure 7.25).

The connectivity of the 21 μm single-scale network has increased by network integration. Figure 7.26 shows the two-scale network is globally more connected than the three scale network, despite the fact that the three scale network has higher average coordination number (Table 7.7). This higher global connectivity is probably the reason why the $k_{r,\ air}$ for the two-scale network appears at the top of that of the tree-scale network. It should be mentioned that the three-scale network shows a more gradual fluid displacement (Figure 7.22) compared to the two-scale and single-scale networks. This may be the reason behind a more regular shaped $k_{r,\ air}$ curve.

This work suggests that the parameters involved in the network integration as well as the number and length-scale of the input single-scale networks can have substantial effects on the shape of the *(kr-Sat)* curves calculated based on the multiple-scale network.

6. Sensitivity Analysis- Effect of Image Segmentation on Extracted Pore Network Models

In this section the effect of image segmentation on the properties (porosity and absolute permeability) of the extracted pore network model is considered. The effect depends on how adequately the image captures the details of the pore structure. To illustrate this two images of SD samples (D=25 and 2 mm) with 2 and 21 μm resolutions are segmented using a simple thresholding method but with variable thresholds. The images were first filtered using an anisotropic diffusion filter (refer to chapter 3, section 3) to reduce noise. It is shown that compared to the coarse resolution images, the higher resolution image shows less sensitivity to threshold values used in image segmentation.

6.1. High Resolution Image

Figure 7.27 shows the histogram of the 2 μm resolution image of the SD rock (550 ×550×550, cropped from the data set shown in Figure 7.11D). According to Figure 7.14 only ~3 % of the SD pore space is connected to pore-throats smaller than 2 μm. On the image histogram the two peaks at 0 and 7500 grey levels represent the pore and solid phases in the image. The corresponding distributions overlap across a range of grey scales (1000 to 6000). Image segmentation was performed using a simple

thresholding method (refer to chapter 3, section 3) with thresholds ranging from 1000 to 6000 with a step size of 500 grey levels. Pore networks extracted from the resulting binary images are shown in Figure 7.28. The connected parts of the pore network are rendered in blue while the disconnected patches are shown in pink.

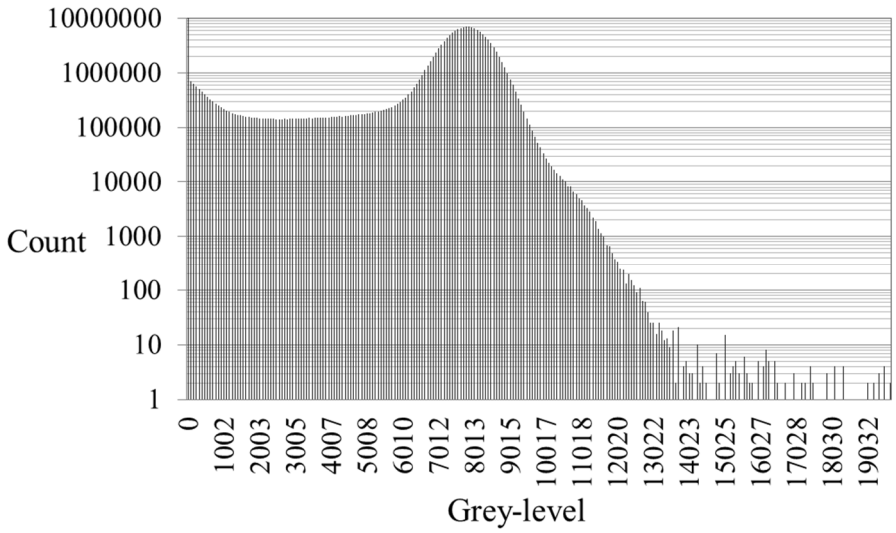

Figure 7.27: Image histogram for a 2 µm resolution image of SD rock.

Table 7.8: Parameters for the networks shown in Figure 7.26 A-K.

Threshold Value	Number of Nodes	Number of Bonds	Coordination Number	Connected Porosity	Disconnected Porosity	Total Porosity	K (mD)
1000	1242	1792	2.68	7.63	4.99	12.62	5.91
1500	968	1332	2.53	8.48	4.99	13.47	11.58
2000	884	1190	2.45	12.69	1.23	13.92	22.25
2500	905	1212	2.44	13.35	1.33	14.68	23.99
3000	945	1278	2.47	14.10	1.26	15.36	60.53
3500	1001	1369	2.51	15.29	1.17	16.46	96.82
4000	1101	1537	2.58	15.05	1.21	16.27	148.90
4500	1120	1594	2.64	16.07	1.00	17.08	171.86
5000	1157	1612	2.58	16.46	1.09	17.55	195.40
5500	1189	1641	2.55	17.34	0.97	18.31	270.93
6000	1301	1772	2.52	19.63	0.92	20.55	321.43

Network parameters are listed in Table 7.8 and plotted in Figure 7.28. For the first three data points (threshold values: 1000, 1500, 2000) the number of network elements decreases, because the selected areas on the image expand, causing them to join up and form larger patches in the binary image. These three points are from thresholding which generates a binary image that underestimates the pore space of the rock. For the remaining data points the number of network elements, connected

(and total) porosity and permeability increase. For thresholds > 2000 the disconnected porosity shows an almost flat, but slowly decreasing trend. This indicates that the main body of the pore space is connected, while increasing the threshold value results in expansion of the existing pores (hence the total porosity) and addition of new smaller pores.

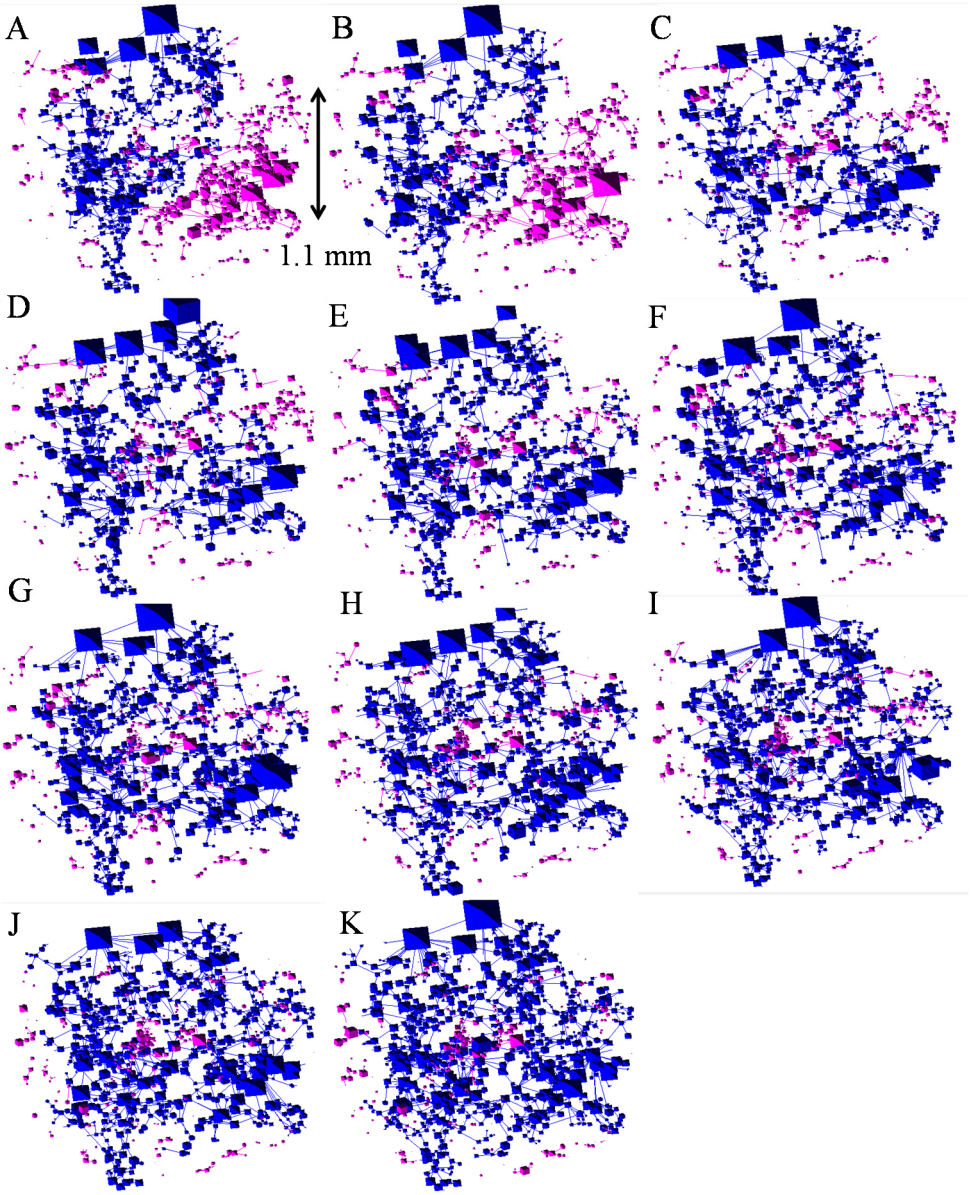

Figure 7.28: Pore networks extracted from binary images (2 µm resolution) segmented using a simple thresholding method. Threshold values ranging from 1000 to 6000 with a step size of 500 grey levels. Pink and blue colours indicate disconnected and connected network elements.

Although the outputs of simple thresholding are subject to variability, users mostly select threshold values around the middle point between the two peaks on the image histogram. For the present image these are the three points with thresholds ranging between 2500 and 3500. For this range of thresholds, k_{abs} increases with a factor of 4 while the porosity changes from 14.68 to16.46 (Figure 7.29).

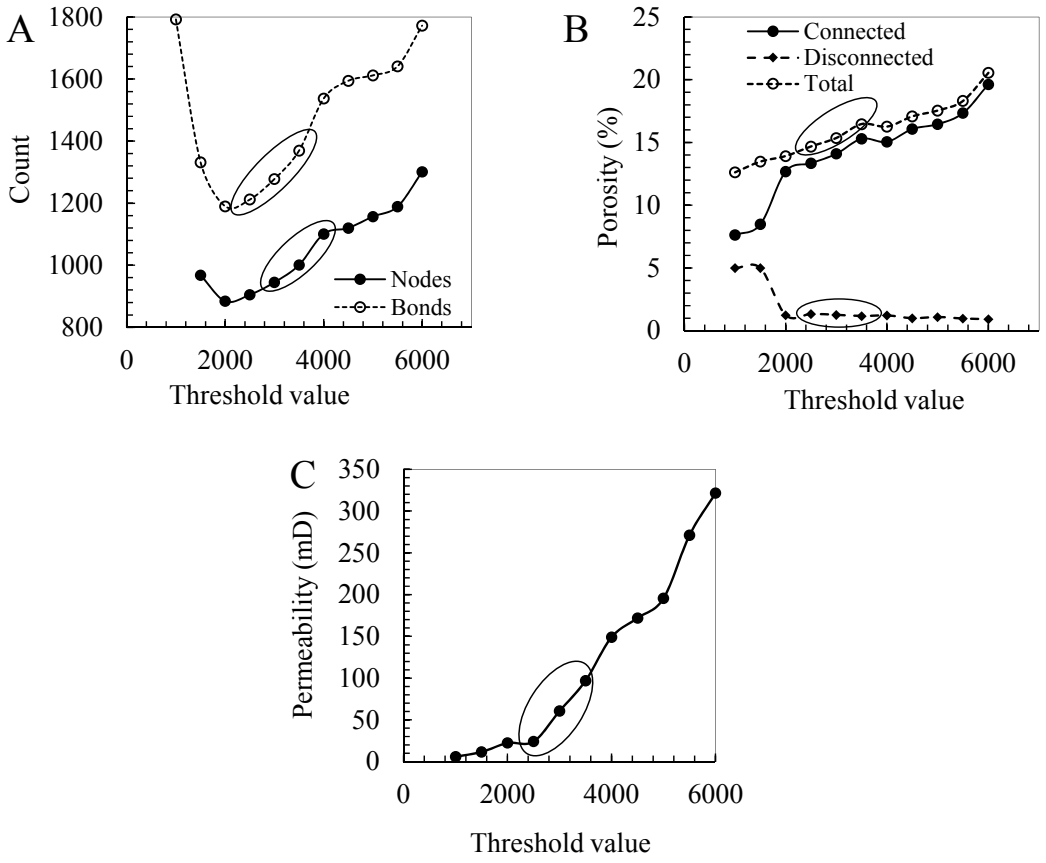

Figure 7.29: Variability of network parameters as a function of the threshold value. For the three points highlighted on the plots, k_{abs} increases with a factor of 4 while the porosity changes from 14.68 to16.46.

This variability of the network properties is one of the limitations of the presented image based modelling. In pore-scale studies more than one network model should be considered to account for the effect of image acquisition and processing uncertainties on the variability of the flow simulation results. It should be mentioned that the effect is image specific and depends heavily on the quality of the input image relative to the feature size distribution of the rock. Independent laboratory

measurements can be considered in order to place limits on the extent of thresholding.

6.2. Coarse Resolution Image

Figure 7.30 shows the histogram of a 21 μm resolution image of SD (870 ×800×610, cropped from a similar image shown in Figure 7.11B). The histogram displays peaks at around 9,000 and 39,000, representing the pore and solid phases, respectively. Due to coarser resolution of the image the two distributions are less distinct, making the selection of threshold value less certain.

Image segmentation was performed with thresholds ranging from 20,000 to 32,000 with a step size of 1000 grey levels. All networks extracted from images (Figure 7.31) with threshold values < 30,000 are completely disconnected. Parameters of the extracted networks are listed in Table 7.9 and plotted in Figure 7.32.

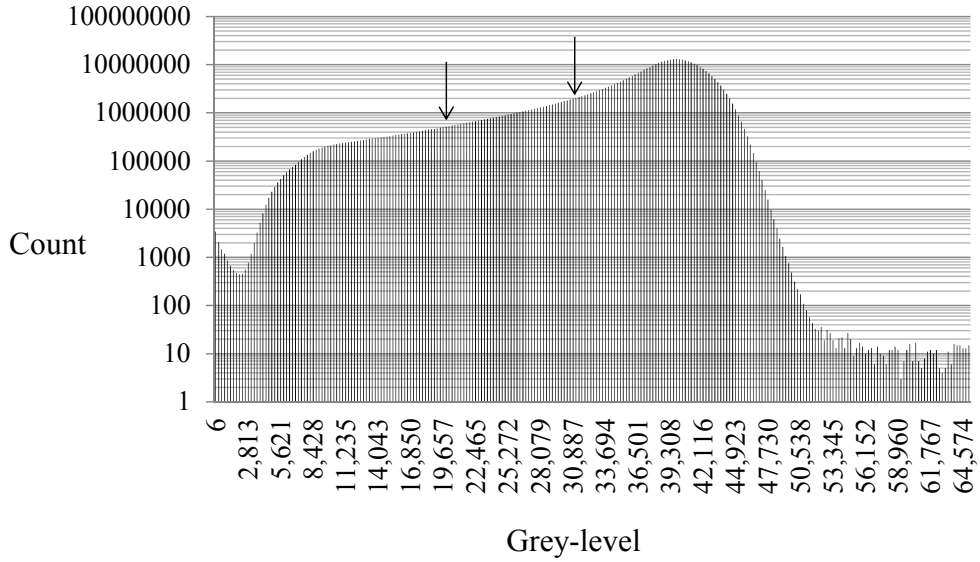

Figure 7.30: Image histogram for a 21 μm resolution image of SD rock. The arrows show the range of thresholds used in this sensitivity analysis.

According to MICP measurements (Figure 7.14) more than 60 % of the SD pore space is connected to the throats smaller than 21 μm. Therefore, a pore network extracted from such a coarse resolution image is expected to be substantially less connected compared to a network extracted from a 2 μm resolution image.

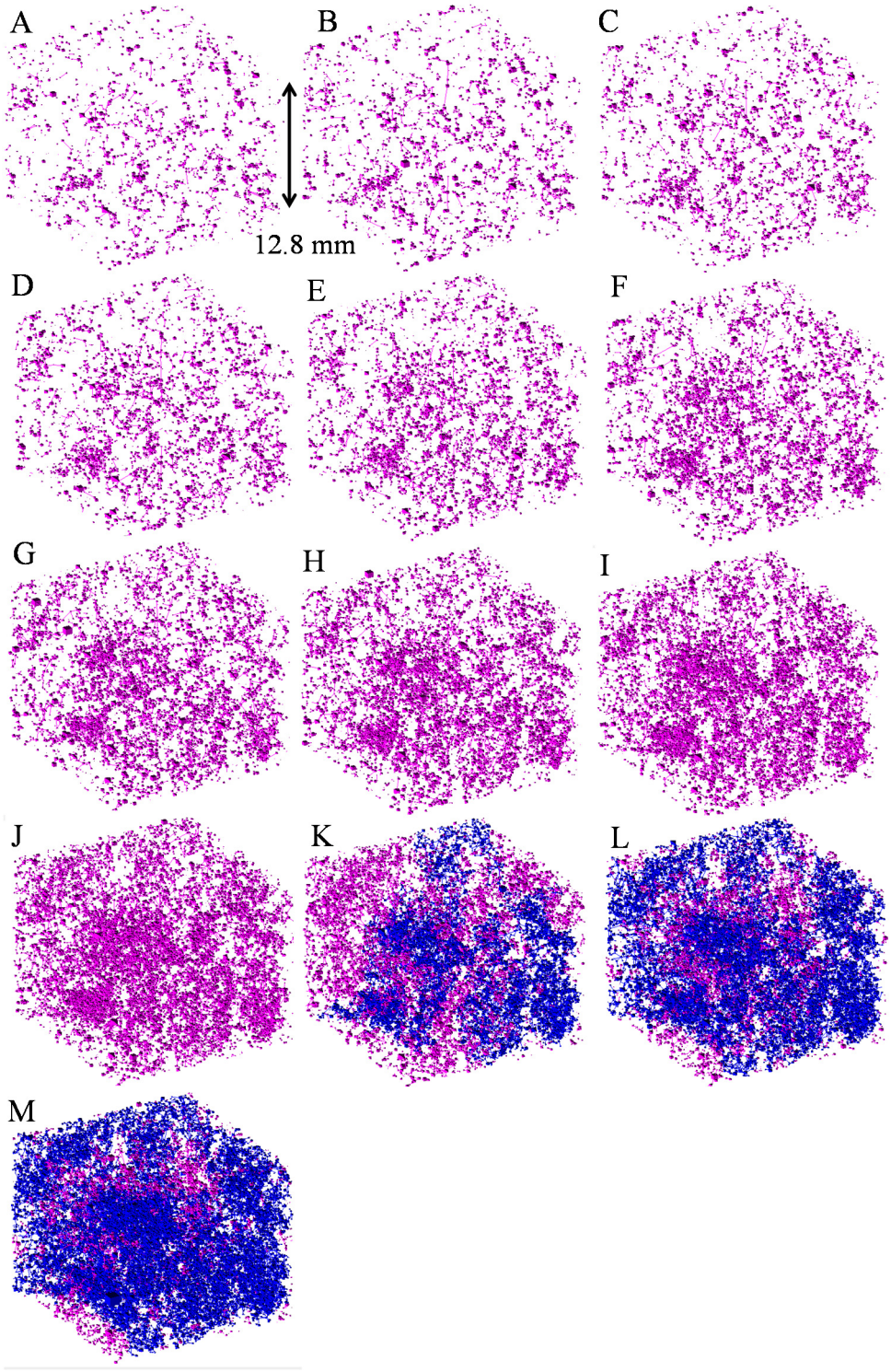

Figure 7.31: Extracted pore networks with threshold values ranging from 1000 to 6000 with a step size of 1000 grey levels. Pink: disconnected, blue: connected network elements.

Table 7.9: Parameters of the extracted networks as a function of threshold value.

Threshold Value	Number of Nods	Number of Bonds	Coordination Number	Connected Porosity	Disconnected Porosity	Total Porosity	k_{abs} (mD)
20000	1982	1721	1.56	0	3.42	3.42	0
21000	2388	2070	1.58	0	3.89	3.89	0
22000	2804	2481	1.62	0	4.45	4.45	0
23000	3515	3298	1.74	0	5.06	5.06	0
24000	4286	4186	1.83	0	5.76	5.76	0
25000	5251	5399	1.94	0	6.55	6.55	0
26000	6344	6786	2.03	0	7.45	7.45	0
27000	7770	8835	2.18	0	8.47	8.47	0
28000	9470	11357	2.31	0	9.58	9.58	0
29000	11968	15147	2.45	0	10.87	10.87	0
30000	14896	19978	2.61	6.61	5.73	12.34	57.70
31000	18311	26008	2.78	10.58	3.46	14.04	262.13
32000	22863	34288	2.94	13.51	2.55	16.05	608.10

The uncertainty of image segmentation appears to be much higher when the input image is of insufficient resolution. For example, for the 2 μm resolution network the k_{abs} varies between 5.91 and 321.43, whereas this variation is observed to occur between 0 and 608.1, for the 21 μm resolution network. In addition to a wider range of variability, change in threshold values may cause the 21 μm resolution networks to change from a completely disconnected network (k_{abs} = 0) to a highly connected one (k_{abs} = 608.1).

Figure 7.32 shows the effects of changing the threshold values on the parameters of the extracted networks. As expected increasing the threshold value increases the number of network elements and hence the total porosity of the extracted networks. However, the networks remain disconnected for threshold values < 30,000. In reality, many disconnected patches of the pore networks shown in Figure 7.31 are connected through pore-throats smaller than the image resolution. By increasing the threshold values the disconnected large pores become connected through pore-throats of at least the size of one voxel on the image (here 21 μm). This results in an unrealistic

over-estimation of the permeability of the network, which is shown in the sharp k_{abs} increase in Figure 7.32C.

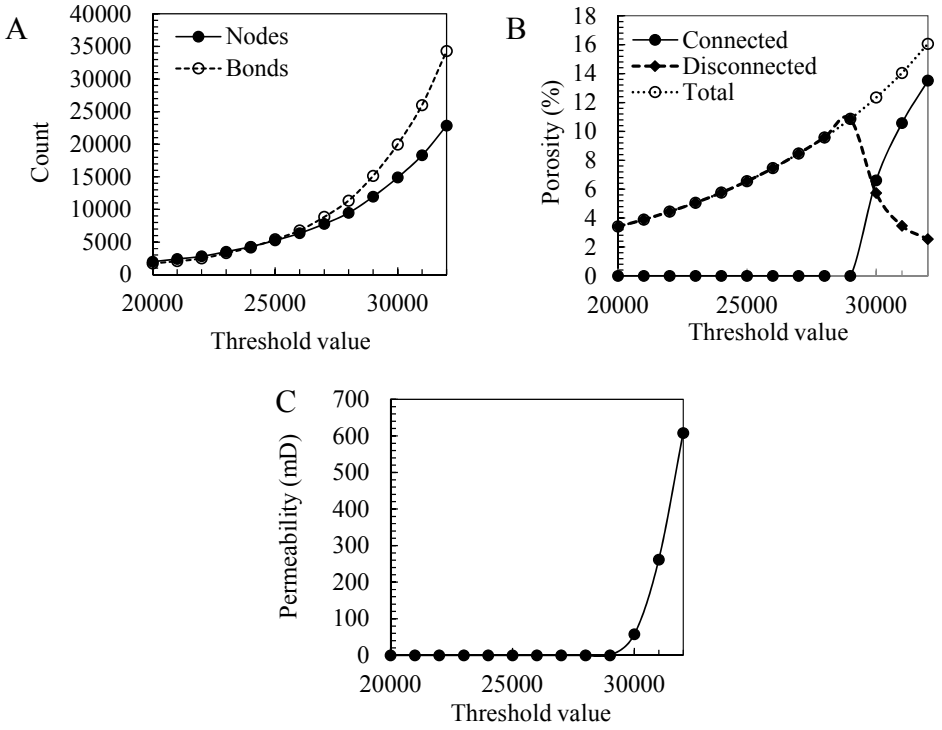

Figure 7.32: Variability of network parameters as a function of threshold value.

6.3. Discussion

The use of independent measurements such as porosity, permeability and MICP data may assist the selection of the threshold value. However, finding a threshold value that matches all the laboratory measurements may not be possible. In this example a significant proportion of the SD rock's porosity is smaller than 21 μm. This is evident from comparing μCT images acquired at different length-scales (Figure 7.12). In confirmation with this is the MICP-based analysis (Figure 7.14) that shows more than 60% of the pore space of the rock is connected to throats smaller than 21 μm. Therefore, for the 21 μm resolution image, attempts to match the laboratory-measured porosity (~17%) by selecting larger threshold values (> 32,000) over-connects the pore space (k_{abs} > 608.1), which is larger than the laboratory measured values for k_{abs} (~50 mD). This is because the smallest possible pore-throat size that can be represented is of one voxel size (21×21×21 μm^3), which is unrealistically

large compared to the pore-throat size distributions derived from MICP data (Figure 7.13).

Considering that the measured k_{abs} values are ~ 50 mD, values ~ 30,000 provide reasonable connection k_{abs} ~57 mD while the fraction of disconnected pore space to the connected ones are ~46 % which is approaching the 60% that is derived from MICP data. It should be noted that the total porosity values remain, inevitably, under-estimated.

For the higher resolution image, however, narrowing down the threshold interval is easier. Threshold values close to 3000 result in networks with k_{abs} ~ 60 mD which is close to the laboratory measurement. Based on MICP analysis the ratio of disconnected to connected porosity for 2 μm resolution networks should be ~ 3 %. This fraction is close to 8 % for threshold values ~ 3000, which may be considered as acceptable. Reducing the threshold values to ~ 2500 reduces the k_{abs} (~ 24 mD) but does not result in considerable changes in the ratio of disconnected to connected porosity (~ 9%).

According to the presented observations a higher resolution image provides better control over the k_{abs} values because (a) all the networks are globally connected for fine network, i.e. $k_{abs} > 0$, whereas in the coarse network the networks becomes connected at threshold between 29,000 and 30,000, (b) tuning the threshold results in smaller changes in k_{abs} due to smaller voxel size ($2\times2\times2$ μm^3), compared to the coarser resolution image ($21\times21\times21$ μm^3).

7. Summary and Conclusions

In this chapter a new approach introduced by Jiang et al. (2013) was used to combine pore networks extracted from μCT images of a carbonate rock, acquired at different length-scales. The integrated networks were used to reproduce (*Pc-Sat)* curves for the rock which were evaluated by comparison with MICP laboratory measurements.

For the studied dolomite sample two-scale and three-scale network models were generated. The (*Pc-Sat)* curves calculated on two-scale and three-scale network

models were shown to be significantly closer to the laboratory measurements compared to the *(Pc-Sat)* curves for single-scale (coarse or fine) network models. The two-scale networks were constructed by integrating networks of 2 and 21 μm resolution. The calculated *(Pc-Sat)* curves for these integrated networks displayed a jump at $S_{air} \sim 0.5$. This was resolved by adding another intermediate scale to generate three-scale networks. Therefore, the three-scale networks were constructed by integrating 2, 5, and 21 μm resolution networks. The likely reason of the observed jump (for the two-scale network) is the insufficient overlap between the pore-size distributions of the 2 and 21 μm networks. This has resulted in a range of pore-sizes (~10 μm < radius < ~ 30 μm) to be less represented in the combined pore network model. This underrepresentation is indicated by having overestimated *Pc* values (compared to the MICP measurements) for $S_{air} < 0.5$, for the two-scale network. The three-scale pore network provides a closer match to the laboratory *(Pc-Sat)* measurements.

The sensitivity of networks were investigated by considering the change in the values of k_{abs} and the fraction of disconnected porosity to the total porosity as a function of the threshold values used for simple thresholding segmentation. It was demonstrated that it may not be possible to simultaneously match laboratory-measured porosity and permeability by controlling the threshold values. However, these independent measurements can assist narrowing down the choice of threshold values.

Moreover, it was shown that a higher resolution image displays a smaller degree of sensitivity to the threshold value compared to a coarser resolution image.

For SD rock a three-scale pore-network model appears to be sufficient, and considering a further finer network to make a four-scale network is not recommended. This is because (a) a three-scale network provided a close match between the calculated *(Pc-Sat)* curves and the MICP measurements, (b) integrating a fourth network involves a significant level of complexity that is caused by the wide range of possible combinations of the δ and f_F values. However, it may be worthwhile to use a higher resolution image (< 2 μm) as the smallest length-scale. This may improve the match obtained in the higher pressure part of the *(Pc-Sat)*

curve, while extending the *(Pc-Sat)* calculations to higher pressures. This may be worthy of future research.

References

AL-KHARUSI, A. S. & BLUNT, M. J. 2007. Network extraction from sandstone and carbonate pore space images. *Journal of Petroleum Science and Engineering,* 56**,** 219-231.

AL-KHARUSI, A. S. & BLUNT, M. J. 2008. Multiphase flow predictions from carbonate pore space images using extracted network models. *Water Resources Research,* 44.

ARNS, J.-Y., ARNS, C. H., SHEPPARD, A. P., SOK, R. M., KNACKSTEDT, M. A. & VAL PINCZEWSKI, W. 2003. Relative permeability from tomographic images; effect of correlated heterogeneity. *Journal of Petroleum Science and Engineering,* 39**,** 247-259.

BAKKE, S. & ØREN, P.-E. 1997. 3-D pore-scale modelling of sandstones and flow simulations in the pore networks. *SPE JOURNAL-RICHARDSON-,* 2**,** 136-149.

BEAR, J. 1988. *Dynamics of Fluids in Porous Media*, Dover Publication.

BISWAL, B., ØREN, P.-E., HELD, R., BAKKE, S. & HILFER, R. 2007. Stochastic multiscale model for carbonate rocks. *Physical Review E,* 75**,** 061303.

BISWAL, B., ØREN, P.-E., HELD, R. J., BAKKE, S. & HILFER, R. 2009. Modeling of multiscale porous media. *Image Analysis and Stereology,* 28**,** 23-34.

BLUNT, M. J., JACKSON, M. D., PIRI, M. & VALVATNE, P. H. 2002. Detailed physics, predictive capabilities and macroscopic consequences for pore-network models of multiphase flow. *Advances in Water Resources,* 25**,** 1069-1089.

GHOUS, A., KNACKSTEDT, M. A., ARNS, C. H., SHEPPARD, A., KUMAR, M., SOK, R., SENDEN, T., LATHAM, S., JONES, A. C., AVERDUNK, H. & PINCZEWSKI, W. V. 2008. 3D Imaging of Reservoir Core at Multiple Scales; Correlations to Petrophysical Properties and Pore Scale Fluid Distributions. International Petroleum Technology Conference.

JIANG, Z., DIJKE, M., SORBIE, K. & COUPLES, G. 2013. Representation of multiscale heterogeneity via multiscale pore networks. *Water Resources Research,* 49**,** 5437-5449.

JIANG, Z., VAN DIJKE, M., WU, K., COUPLES, G., SORBIE, K. & MA, J. 2012. Stochastic pore network generation from 3D rock images. *Transport in Porous Media,* 94**,** 571-593.

JIANG, Z., WU, K., COUPLES, G., VAN DIJKE, M., SORBIE, K. & MA, J. 2007. Efficient extraction of networks from three-dimensional porous media. *Water Resources Research,* 43.

JOEKAR-NIASAR, V. & HASSANIZADEH, S. 2012. Analysis of fundamentals of two-phase flow in porous media using dynamic pore-network models: A review. *Critical Reviews in Environmental Science and Technology,* 42**,** 1895-1976.

LUCIA, F. J. 1995. Rock-fabric/petrophysical classification of carbonate pore space for reservoir characterization. *AAPG bulletin,* 79**,** 1275-1300.

MCDOUGALL, S. & SORBIE, K. 1997. The application of network modelling techniques to multiphase flow in porous media. *Petroleum Geoscience,* 3**,** 161-169.

MCDOUGALL, S. R., CRUICKSHANK, J. & SORBIE, K. S. 2002. Anchoring Methodologies for Pore-Scale Network Models: Application to Relative Permeability and Capillary Pressure Preduction. *PETROPHYSICS-HOUSTON-,* 43**,** 365-375.

OAK, M., BAKER, L. & THOMAS, D. 1990. Three-phase relative permeability of Berea sandstone. *Journal of Petroleum Technology,* 42**,** 1,054-1,061.

OKABE, H. & BLUNT, M. J. 2007. Pore space reconstruction of vuggy carbonates using microtomography and multiple-point statistics. *Water Resources Research,* 43.

ØREN, P.-E., BAKKE, S. & ARNTZEN, O. J. 1998. Extending predictive capabilities to network models. *SPE JOURNAL-RICHARDSON-,* 3**,** 324-336.

PATZEK, T. & SILIN, D. 2001. Shape factor and hydraulic conductance in noncircular capillaries: I. One-phase creeping flow. *Journal of colloid and interface science,* 236**,** 295-304.

PORTER, M. L., SCHAAP, M. G. & WILDENSCHILD, D. 2009. Lattice-Boltzmann simulations of the capillary pressure–saturation–interfacial area relationship for porous media. *Advances in Water Resources,* 32**,** 1632-1640.

RYAZANOV, A. V., SORBIE, K. S. & VAN DIJKE, M. I. J. 2014. Structure of residual oil as a function of wettability using pore-network modelling. *Advances in Water Resources,* 63**,** 11-21.

RYAZANOV, A. V., VAN DIJKE, M. I. J. & SORBIE, K. S. 2009. Two-Phase Pore-Network Modelling: Existence of Oil Layers During Water Invasion. *Transport in Porous Media,* 80**,** 79-99.

VALVATNE, P. H. & BLUNT, M. J. 2004. Predictive pore-scale modeling of two-phase flow in mixed wet media. *Water Resources Research,* 40.

VOGEL, H. J. & ROTH, K. 2001. Quantitative morphology and network representation of soil pore structure. *Advances in Water Resources,* 24**,** 233-242.

WU, K., VAN DIJKE, M. I., COUPLES, G. D., JIANG, Z., MA, J., SORBIE, K. S., CRAWFORD, J., YOUNG, I. & ZHANG, X. 2006. 3D stochastic modelling of heterogeneous porous media–applications to reservoir rocks. *Transport in Porous Media,* 65**,** 443-467.

Chapter 8

Conclusions

The main research questions of this study, outlined in the introduction (chapter 1), were addressed by combining core flooding, X-ray computed micro-tomography, and pore network modelling techniques. The findings presented in this thesis shed light on the physics behind processes that are of major economic and environmental importance and have implications in a number of applications including the remediation of non-aqueous phase liquid contaminants in groundwater aquifers, subsurface CO_2 storage, and enhanced oil recovery.

More specifically, this work addresses the problem of two phase (oil-water) fluid flow in carbonate rocks considering the effects of rock pore structure, wettability, and the flow regime.

1. Study of the Pore-scale Fluid Displacement Processes in Complex Carbonates

2D micro-model experiments were traditionally used to observe and analyse the fluid displacement processes in porous media. Based on observations of such idealised structures, 3D pore-network flow models were developed. The primary assumption of such 3D pore-network simulations was that the displacement processes that have been observed in idealised 2D capillaries also occur in complex 3D pore geometries which are common in real reservoir rocks. Advances in X-ray computed micro-tomography (μCT) technique enabled 4D imaging (time-resolved 3D imaging) and confirmed the occurrence of some of these pore-scale mechanisms (such as snap-off and body filling events) in 3D. However, reviewing the literature indicates that pore-scale imaging studies have mostly focused on more homogeneous porous material such as bead packs, sand packs, and sandstones. There are technical difficulties involved in working with heterogeneous samples, for instance in order to work with a representative elementary volume of a heterogeneous rock larger samples are required, which is a drawback for achieving high resolutions on μCT images. Such difficulties have limited the number of studies performed on more complex pore systems such as carbonate rocks. However, carbonate formations are of particular global importance considering they contain about 50% of the world's hydrocarbon reserves, as well as a major portion of the world's groundwater resources.

The reader is reminded that:

- The experimental set up designed for the present study operated at low pressures not exceeding 690 kPa (100 Psi) and ambient temperature ranges.
- A simple X-ray transparent core holder was designed and manufactured in-house which permitted in situ monitoring of oil and brine saturation distributions.
- To account for the heterogeneity of the rock under study the selected core plug (D = 12.5 mm and L = 44 mm) was larger than the common samples used (D ~ 5mm) in similar studies on more homogeneous systems such as sandstones or bead packs.

The fluid injection test cycle was composed of drainage and imbibition processes at low ($\sim 10^{-7}$) and high ($\sim 10^{-5}$) capillary numbers. The injection flow rates were selected such that the displacement processes occur under capillary and viscous dominated flow regimes. This study reports the observation of piston-like displacement and snap-off mechanisms in 3D (or, rather, the expected outcomes of these processes) for the carbonate sample under study. A new pore-scale mechanism, termed "droplet fragmentation", was observed in the larger pores of the carbonate, spanning at least three orders of magnitude in volume (ranging between 10^8 to 10^{10} μm^3), under water-wet state. The mechanism occurred in the pores where oil was originally trapped after the capillary-dominated imbibition, and as a result of snap-off. Viscous-dominated imbibition caused fragmentation of the trapped oil droplets into hundreds of smaller droplets, some of which remained trapped in the pore, whereas some others were produced to accommodate more of the invading brine phase. The experimental data suggests that droplet fragmentation may provide an explanation to the capillary desaturation at high capillary numbers in porous media with heterogeneous and multi-scale pore-size distributions.

In addition to recovery enhancement, droplet fragmentation changes the structure of the residual non-wetting phase saturation. The mechanism enlarges the surface area between the wetting and non-wetting phase. The increase in surface area can enhance mass transfer between both phases, which can be a critical mechanism

for a number of applications such as groundwater remediation, enhanced oil recovery, and dissolution of trapped CO_2 in brine during solubility trapping. Presently, the pore-scale mechanisms that are implemented in fluid flow models do not take the heterogeneity of the pore system into account, i.e. the same displacement mechanisms occur regardless of how homogeneous or heterogeneous the pore system is. Droplet fragmentation is an additional mechanism that may need to be included in pore-scale models of viscous-dominated displacement in heterogeneous media processes. Including droplet fragmentation may improve the prediction of end point saturations which is, for instance, critical for better prediction of relative permeability curves.

2. Porous Media Wettability Characterisation

Pore-scale imaging provides a means to directly visualise the fluid-fluid-rock configurations which can indicate not only the surface wetting preference, but any spatial variation in wettability across the sample. Traditional wettability characterisation methods such as USBM and Amott can only measure an average wetting index for a core plug. In addition, these conventional measurements methods are lengthy and costly. Findings presented in this study demonstrate that pore-scale imaging is a faster and less expensive approach that can indicate the local wettability of the rock and hence capture a mixed wettability system. With further development of routine X–ray CT compatible core flooding rigs and analytical workflows pore-scale imaging can become an industry standard practice.

To investigate the effect of wettability on the pore-scale configuration of oil and brine phases experiments were performed on the dolomite core plug under water-wet and oil-wet states. The plug was originally water-wet. The oil-wetness was achieved by aging the plug in a crude oil sample with sufficient heavy fractions (asphaltene content). Results show the oil-brine-rock distributions display a significant difference for the two oil-wet and water-wet conditions. Oil-brine-rock contact angles were measured based on the images of the oil-wet and water-wet cores. The measurements were done for a random selection of pores distributed throughout the core plug. The average contact angles display a significant contrast for the oil-wet and water-wet conditions.

In addition to the contact angle measurements a number of other indicative factors were demonstrated to assist pore-scale wettability characterisation. These include:

(a) The observation of specific fluid displacement mechanisms that occur for specific fluid phases, for instance the oil phase snap-off during brine imbibition under the water-wet conditions,

(b) The clear observation of wetting film development, i.e. brine and oil films for the two water-wet and oil-wet conditions, respectively.

(c) The observation of capillary end effect for the water phase during the drainage process for the water-wet experiment.

Taking all these evidences into account the pore-scale imaging is shown to be a promising tool for wettability characterisation at both pore-scale and core-scale. The primary advantage of this method is that it can provide detailed information about the local wetting preference of the rock at pore-scale, as opposed to an average wetting index commonly measured in industry standard routines. Such detailed wettability analysis can inform pore-scale network models for more realistic simulations of systems with heterogeneous wettability.

3. Informing Pore Network Models of the Pore-scale Fluid Displacement Physics for Heterogeneous Media

On the modelling side of this work pore-scale fluid distributions were studied using realistic pore network models extracted from μCT images of the dolomite as well as a quasi-static pore-scale flow simulation code developed by Ryazanov et al. (2009). One target of pore-scale modelling is to predict macro-scale flow properties of rocks which are more difficult to obtain in laboratories (such as relative permeability curves). The prime requirement of successful pore-scale flow simulations is that the input pore-network model of the rock should be representative of the rock's pore structure. Representativity involves including porosity features from all the existing length-scales that contribute to the static and dynamic flow properties of the rock. Pore networks extracted from a single μCT image of sandstone samples have proven sufficient to successfully match laboratory-measured relative permeability curves. However, due to their heterogeneity most carbonates display a wide range of pore-sizes, from nm to cm scales. Different size samples taken from such complex structures capture different range of pore-sizes. At the time of writing this thesis, the

existing μCT scanners are not capable of scanning samples of a few cm size with sub-micron resolution, to capture all the porosity details in a single image. The size of a 1 μm resolution image of a 1 cm^3 sample is larger than that of a 1 mm^3 sample (size of the high resolution images used in this study) by a factor of 1000x. Therefore, even if the imaging facilities were capable of capturing such detailed images, the run time for the image processing (such as image filtering) as well as subsequent flow simulations of such large images are significantly longer. Hence, use of such large images may not be computationally practical. Therefore, a numerical method that can generate a representative network which is at the same time small enough to be handled practically is desired.

A multiple-scale network generation tool (Jiang et al., 2013) that is capable of combining multiple pore network models, each extracted from a single μCT image, into a multiple-scale pore network model was used. Using this tool, two-scale and three-scale pore network representations of the studied dolomite rock was generated. Capillary pressure curves simulated based on these multiple-scale network models were compared with the laboratory measurements (derived from mercury injection tests). It is demonstrated that the two-scale and three-scale network models are both more representative of the studied dolomite compared to the single-scale pore network, as the simulated capillary pressure curves for these integrated pore networks are closer to the laboratory measurements. A range of pore-sizes were, however, under-represented in the two-scale network model and hence the third scale was required to be integrated to fill the gap. The capillary pressure curve of the three-scale network displayed an improved match to the laboratory generated one, and hence the three-scale network is suggested to be a representative model of this dolomite.

A brine in oil emulsion was observed to form during an imbibition process (i.e. oil injection) in the oil-wet experiment. The emulsion's viscosity was significantly higher than that of the oil phase and hence made the injections with higher flow rates impossible for the low-pressure experimental set-up. At reservoir scale such sudden increases in viscosity (and hence pressure drop) causes problems in well injectivity which is undesired. Literature includes studies of emulsion

formation using 2D micro-models, however, to the author's knowledge this is the first report on 3D visualisation of an oil-water emulsion that is formed in situ and has proven stable. Although the observed emulsion was not quantitatively characterised (due to limited resolution and sharpness of the images) it indicates that higher resolution 3D imaging permits characterisation of such emulsions, such as quantitative measurement of its droplet size distribution with the aim of predicting the emulsion's viscosity and flow behaviour in porous media. The implications are for studies of the effectiveness of different surfactants in heavy oil production which involves oil in water emulsion formation and flow. Future studies might focus on techniques to limit emulsion formation or the effectiveness of breaking up emulsions using different surfactants.

In summary, pore-scale imaging of multiphase flow displacement in heterogeneous carbonate media using μCT technique has received less attention in the literature due to technical difficulties associated with such experiments. This study presents both previously known as well as an unobserved displacement processes for a dolomite rock. The pore-scale mechanisms were studied as a function of the rock wettability. The results suggest pore-scale imaging can be a promising tool for wettability characterisation.

This study demonstrates that multiple-scale pore network model generation approach offers a successful means to build a more representative network for complex pore-structures inherent to most carbonate rocks. The achievable image resolutions are limited, and not sufficient to capture all the details of multiple-scale pore-structures (essential to fluid flow modelling) in a single image. In addition, computational power poses another limitation on the feasibility of direct flow simulations on high resolution 3D images. The data presented in this work illustrates that, until direct fluid flow simulations on meshed images of complex pore-systems become practically feasible, the multiple-scale networks construction offers a computationally workable approach.

4. Recommendation for Future Studies

Future studies can involve performing similar experiments using a synchrotron facility to obtain time-resolved analysis of the fragmentation mechanism and the changes in oil structure in more details. Such analysis can assist the implementation of this mechanism in pore-network models. Taking the experiments presented in this work one step forward, the design of the experimental set up can be modified to enable performing similar experiments under high pressure and high temperature conditions, which would reflect the fluid flow processes that occur in oil reservoirs more realistically.

In addition, in order to study the effect of pore-structure on the occurrence of pore-scale mechanisms (specifically droplet fragmentation), similar experiments can be performed on other carbonate structures (such as limestones). This can provide a means to investigate the effects of pore-structure characteristics (such as pore-aspect ratio and size distributions), and rock mineralogy on fluid displacement.

The contact angle analysis presented in chapter 6 can be evaluated against a more conventional contact angle measurement method such as sessile drop that could be performed on powdered samples of the rock. This comparison can aim at introducing a new wettability classification (as opposed to the existing one, introduced by Anderson, 1986) for the contact angles measured in-situ.

On the modelling side it is also worthwhile to obtain a set of relative permeability data for SD rock to further investigate the predictive ability of the approach used in this study in calculating the more difficult to obtain relative permeability curves. Similarly, the multiple-scale network generation approach can be applied to other carbonate rocks to establish a better understanding of the criteria to select the length-scales that are crucial to different rock types.

References

ANDERSON, W. 1986. Wettability literature survey-part 2: Wettability measurement. *Journal of Petroleum Technology,* 38**,** 1,246-1,262.

JIANG, Z., DIJKE, M., SORBIE, K. & COUPLES, G. 2013. Representation of multiscale heterogeneity via multiscale pore networks. *Water Resources Research,* 49**,** 5437-5449.

RYAZANOV, A. V., VAN DIJKE, M. I. J. & SORBIE, K. S. 2009. Two-Phase Pore-Network Modelling: Existence of Oil Layers During Water Invasion. *Transport in Porous Media,* 80**,** 79-99.

Appendices

Appendix A

Image Reconstruction Workflow

Image reconstruction was performed using Octopus software (v.8.5-8.7). Figure A3 shows the image reconstruction workflow followed in this research.

1. Image Conversion

The projections acquired by CT scanner were raw format and were converted into TIFF format prior to reconstruction. A raw image is a 1D string. The image dimensions are required for conversion, i.e. the number of pixels in X and Y direction.

2. Image Rotation and Cropping

In the ECOSSE μCT scanner the X-ray detector is installed on its side for reasons that relate to the shape of the camera housing, therefore the converted projections need to be rotated by 90°.

If the object covers only on a fraction of the projections' field of view it is common to resize the images to make the data set smaller and easier to process and manage. This is done by cropping the image. In octopus cropping is done by selecting a region of interest (ROI) that contains the entire image of the object. To make it easier the crop tool in Octopus provides a summed image of all the projections.

3. Normalisation

Normalisation is performed to remove the source intensity fluctuations and detector offset. This process requires acquisition of Flat Field (FF) and Dark Current (DC) images (Figure A1). FF, also known as open beam, images are captured with the source switched on and in absence of the specimen. DC images are captured with the source switched off. The acquisition time for FF and DC images must be the same as the projections. For the FF images the beam intensity (energy) must also be equal to the intensity selected to capture the projections. This makes the FF and DC images

specific to each scan. In this research 10 FF and DC images were captured and combined automatically by Octopus.

Normalisation process involves three steps of (a) dividing the projections by the FF image and (b) subtracting all the images by the by the DC image and (c) a further correction that is done by selecting a region on the summed projections where the object is not present (Figure A2, the black window). The average intensity of this normalization window is used to correct for the beam intensity fluctuations during the scanning period.

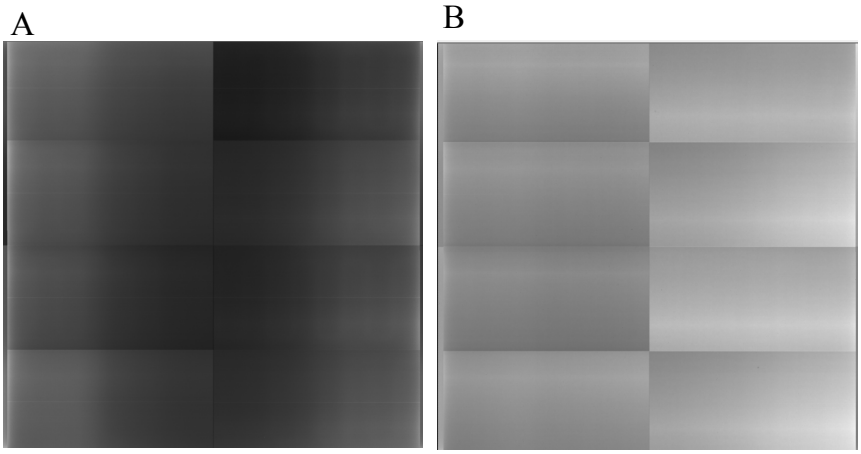

Figure A1: Dark Current (A) and Flat Field (B) images are used in image reconstruction to correct for the source intensity fluctuations and detector offset.

When working on multiple images of a specimen captured at different stages of an experiment all images need to be reconstructed using the same settings. This involves, cropping and normalizing to the same window. This way the reconstructed images will have exactly equal dimensions, providing the chance to perform image processing operations such as summation, averaging, subtraction, etc.

4. Ring Filter

Next step is to remove the ring artefacts. The ring filter implemented in Octopus can be controlled by the user. In Octopus 8.5., which was mainly used in this research, the user can only adjust the weight of the filter that is applied. Adjusting the filter level to higher values makes the processing time longer.

5. Creating Sinograms

Next the projections are converted to sinograms, which are later loaded into the reconstruction wizard for final adjustments and application of the reconstruction algorithm. More information about sinograms are presented in appendix C.

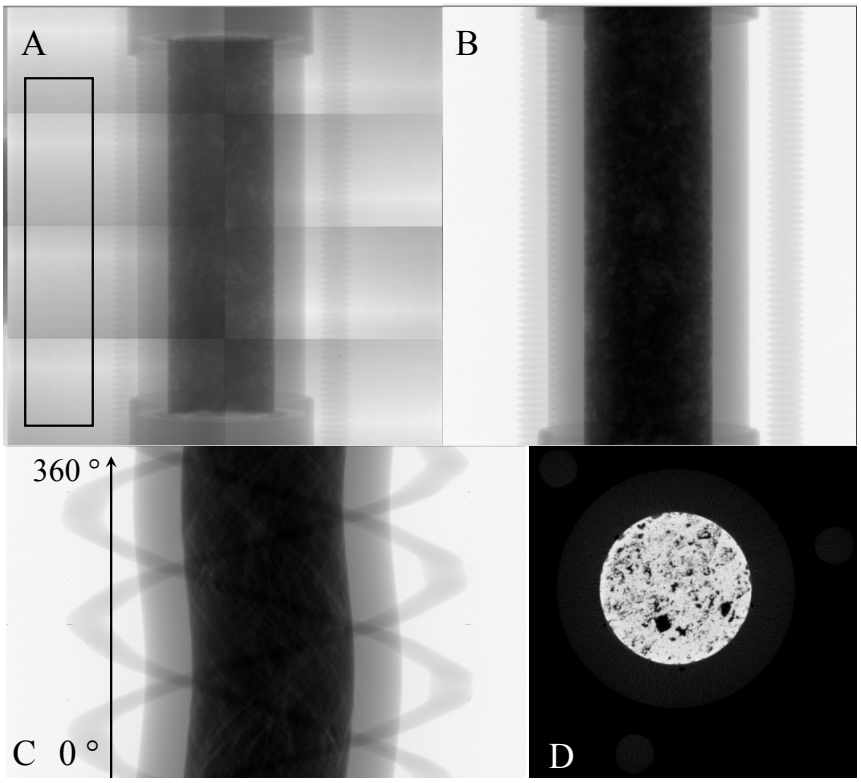

Figure A2: Example converted projection captured from the core flooding cell (A), the window shows an example normalisations window, Normalised projection (B), Example sinogram (C), Example reconstructed slice (D).

The main parameter to adjust in the reconstruction module is the position of the rotational axis that is automatically detected by Octopus. Minor adjustments (by a few pixels or fractions of a pixel) to the rotation of axis can improve the alignment of the image and hence the sharpness of the features appearing on the image such as edges. A good practice to set the rotation of axis is to zoom in onto the specimen edge and check for the best sharpness.

6. Beam Hardening Correction

The beam hardening artifact (see chapter 2, section 3) is corrected during the reconstruction step. Octopus uses a polynomial beam hardening correction method. The user can set the coefficients of a fifth order polynomial. In practice, it is best to keep the polynomial to lower orders by setting the higher order coefficients to zero. The degree of beam hardening correction can be judged by looking at a line profile drawn across the specimen on the reconstructed slice. The target is to remove the cupping effect (a lower density in the centre of the sample compared to its edges) and push the line profile to a flat line for a homogenous sample.

It should be mentioned that there is a noise filtering option in the reconstructions step, however, since Avizo offers a good selection of more advanced image filters it is best to perform the noise filtering after the reconstructed images are loaded in Avizo. Image reconstruction is done using filtered back projection method, for more details see chapter 2, section 3.

7. Rescaling

Subsequent to image reconstruction the images can be re-scaled to achieve a desired contrast. Octopus facilitates the re-scaling by plotting the histogram of the reconstructed image. Rescaling the images to a narrow range is not a good practice since it can amplify image noise, produce clipped images and impair the image quality.

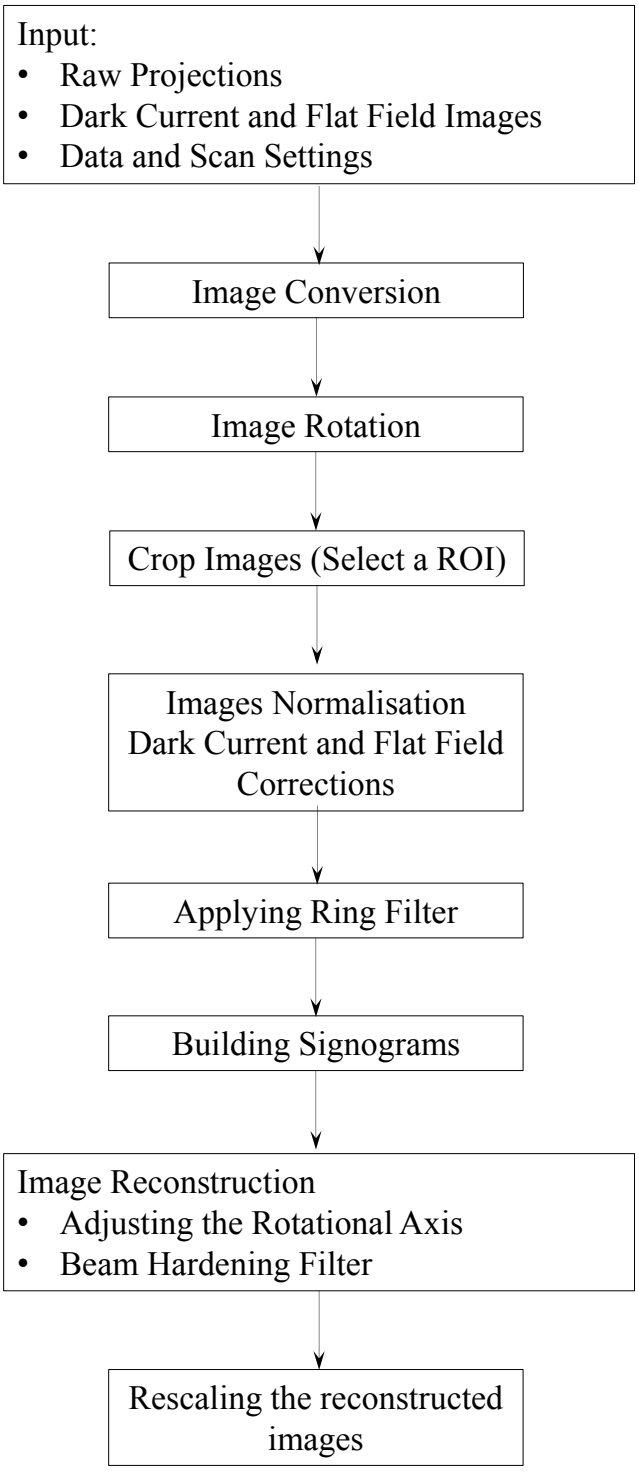

Figure A3: Image reconstruction workflow using Octopus (v.8.5-8.7) software.

Appendix B

Preliminary Experiment Workflow and Results

A preliminary experiment was performed, prior to the experiments presented in chapters 4 - 6, with the aim of (a) assessing the practicality of the designed experimental set-up and test procedures, (b) evaluating the quality of the outcome tomographic images, and (c) refining the test procedure including the injection flow rates, back pressure, etc. Figure B1 shows the test procedure of this preliminary experiment. It involved single flow rate drainage and imbibition steps at (q=100 µl/min).

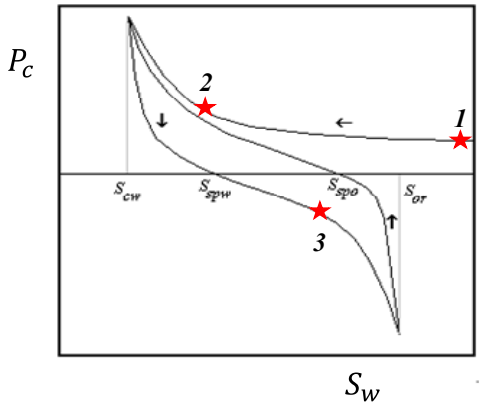

Figure B1: Test procedure for the core flood experiments (in terms of the appropriate capillary pressure describing the process). Red stars show the points of µCT scans.

The core plug used in this experiment was the same as the one used for the water-wet and oil-wet experiments discussed in the thesis. At each scanning point (shown on Figure B1 with red stars) two scans with different magnifications were collected. The lower magnification images scanned of the entire length of the core (44 mm) with voxel size of 27.1 µm, while the higher magnification images scanned only a central section of the cell (covering one third of the core length) with a voxel size of 11.9 µm.

The experiment started with scanning the dry plug twice in each magnification; these two data sets were then averaged to supress the measurement noise. The core was then vacuum saturated with brine (0.5 M KI), using considerably attenuating 0.5 M KI solution provided the chance to image the accessible porosity effectively. After the scans the KI solution was

flushed out of the cell by water; this provided a good contrast between the aqueous phase and the doped organic phase which was injected subsequently.

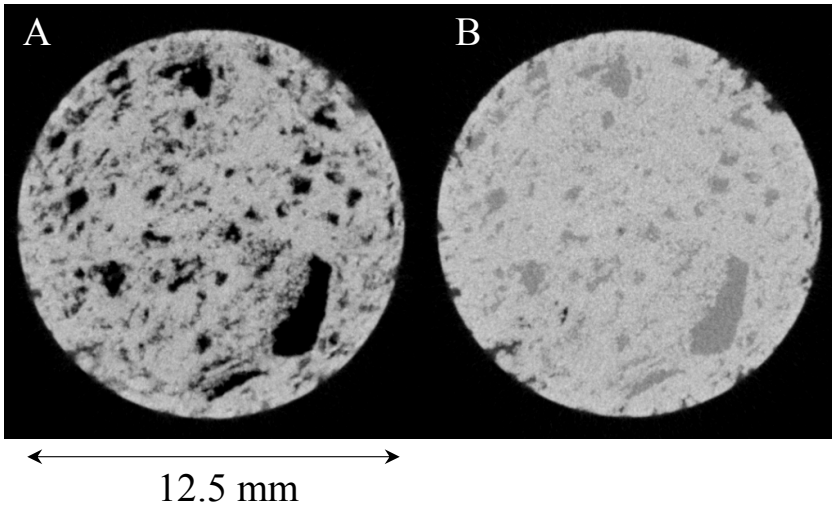

Figure B2: Example slice of the dry (A) and 0.5 M KI saturate (B) core plug.

Drainage and imbibition steps: A mineral oil mixture (50%v/v 1-iodo-decane in dodecane) was injected into the water saturated core (q=100 µl/min). The flow was stopped after injection of more than 10 pore volumes when no more water was produced. The cell was then locked off and scanned. Subsequently, more than 10 pore volumes of water was injected in the plug with q=100 µl/min until no more oil was produced. At this stage the cell was locked off and scanned.

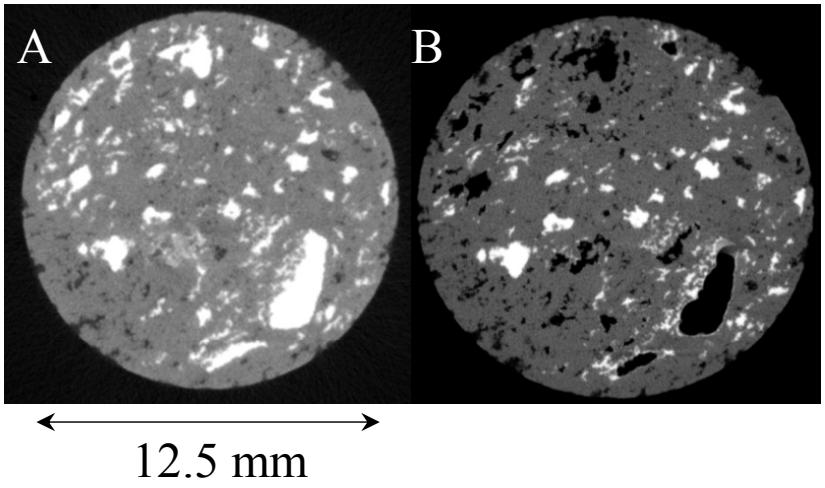

Figure B3: Example slice of the core plug after (A) Drainage and (B) Imbibition steps. White: oil, Black: Water (or air) and Grey: rock.

This experiment was the first attempt to image fluid phases in a porous carbonate rock using the Edinburgh University ECOSSE CT instrument. These tests were essential to optimise the experimental setup, fluid labelling and image quality for studies of fluid distributions in highly attenuating carbonate rocks.

Analysing the acquired images showed both oil and water phases saturated a range of pore sizes from small pores to larger ones. Further, both oil and water films were captured to be present in the core plug. This suggested that the core was of mixed wet nature, i.e. some parts of the core were oil-wet whereas other parts were water-wet. However, another possibility was that some air was trapped in the system. If that was the case then the black phase in the CT slices might correspond to both water and air phases. In the presence of air the wettability of the core plug could not be established only based on these images.

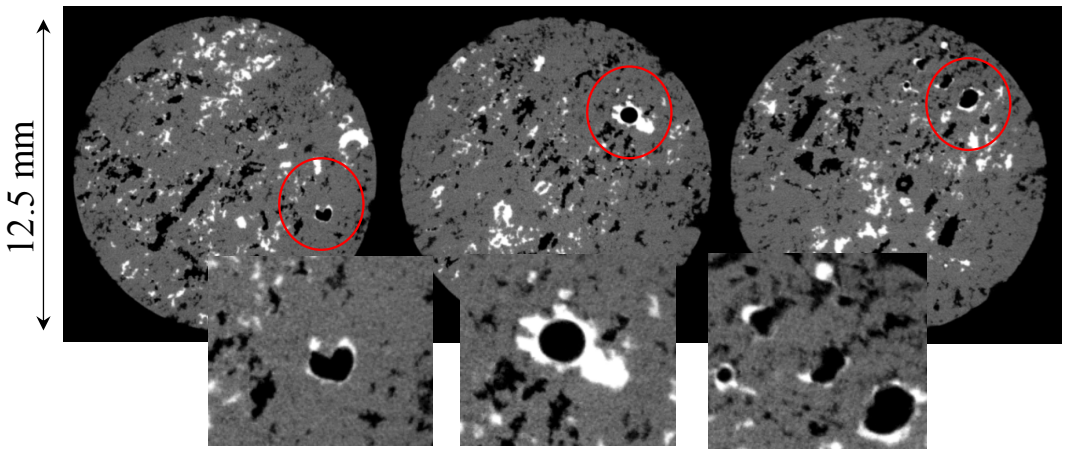

Figure B4: Oil films were established in some pores. The black phase may be air or water. White: oil and Grey: rock.

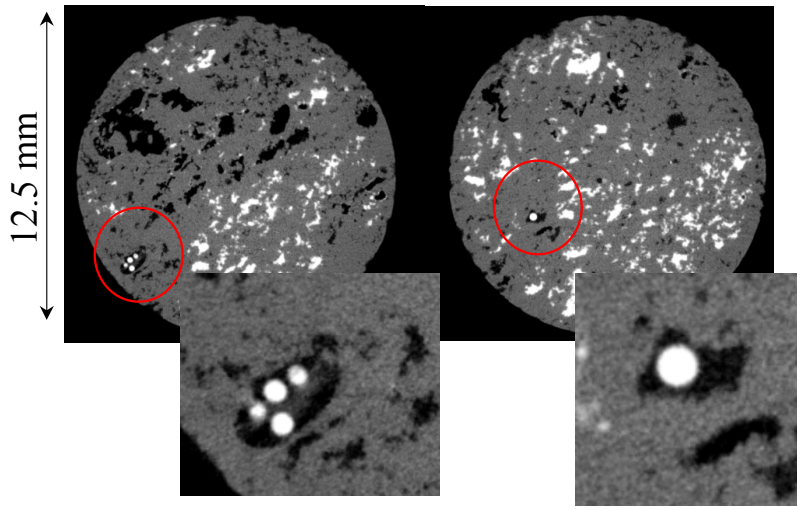

Figure B5: Water films (black) surrounding oil droplets. White: oil and Grey: rock.

To tackle the problem of having a three phase (air/oil/water) system a further step was introduced to the test procedure. For all experiments presented in the thesis the aqueous phases were Helium sparged to remove the soluble gas. This, along with vacuum saturating the core plug in the beginning of the experiment, has proven to successfully avoid air trapping in the pore structure.

Appendix C

Application of Radon Transform in CT Image Reconstruction

In what follows, a short review of the mathematical equations involved in reconstruction of 3D images from a set of 2D projections is presented (Hsieh, 2009). A straight line in Cartesian coordinates could be described either by its slope and intercept or by its normal representation (in polar coordinates) as shown in Figure C1:

$$x\cos\theta + y\sin\theta = \rho \tag{C1}$$

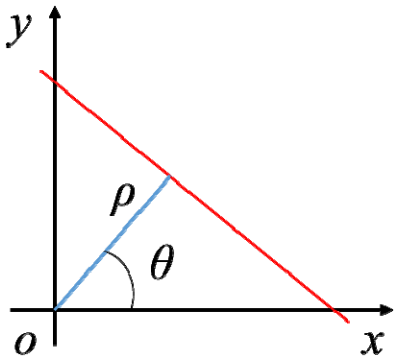

Figure C1: Two possible representation of a straight line

A parallel ray beam is composed of a series of such straight lines. Each arbitrary point on the projection axis is the ray sum along the beam line. If we denote the object by *f(x , y)* the ray sum is defined as a line integral as follows:

$$g(\rho_t,\theta_k) = \iint_{-\infty}^{+\infty} f(x,y)\,\delta(x\cos\theta_k + y\sin\theta_k - \rho_t)dxdy \tag{C2}$$

Where is δ the impulse function defined as:

$$\delta(t)=\begin{cases}\infty & if\ t=0\\ 0 & otherwise\end{cases} \tag{C3}$$

Having the impulse function, the argument of the double integral is equal to zero except for the points located on the line: $x\cos\theta_k + y\sin\theta_k = \rho_j$. Generalizing the eq. C2 for all values of ρ, θ will give:

$$g(\rho,\theta) = \iint_{-\infty}^{+\infty} f(x,y)\,\delta(x\cos\theta + y\sin\theta - \rho)\,dx\,dy \qquad \text{(C4)}$$

Eq. B4 which gives the line integral of *f(x , y)* is called its "Radon Transform". The radon transform could be displayed as an image with ρ and θ as the coordinates, this graphs is called "sinogram". In summary, the data collected during scanning of an object is the radon transformation of the object function. Consequently to reconstruct the image of the object an inverse radon transformation should be applied.

Appendix D

List of Fittings and Fixtures Used in the Experimental Setup

Most parts can be ordered online from: (https://www.idex-hs.com/)

Table D1: List of fittings and fixtures used in the experimental setup.

1528 - Tefzel® (ETFE) Tubing Natural 1/16" OD, .030" ID, 5ft	 https://www.idex-hs.com/fluidic-connections/tefzelr-etfe-tubing-natural-1-16-od-x-030-id-x-5ft.html
P-782 - Shut-Off Valve Tefzel® (ETFE) with 1/16" Fittings	 https://www.idex-hs.com/valves/flow-regulating-valves/shut-off-valves/shut-off-valve-tefzelr-etfe-with-1-16-fittings.html#tab-2
XP-235X - Flangeless Fitting Short, PEEK, 1/4-28 Flat-Bottom for 1/16" OD	 https://www.idex-hs.com/flangeless-fitting-short-peek-1-4-28-flat-bottom-for-1-16-od-cp.html?optionvalue=4421
P-786 - BPR Assembly 75 psi - Biocompatible	 https://www.idex-hs.com/valves/back-pressure-regulators/bpr-assembly-75-psi-biocompatible.html

P-200X - Flangeless Ferrule Tefzel® (ETFE), 1/4-28 Flat-Bottom, for 1/16" OD Blue-10 Pack	 https://www.idex-hs.com/fluidic-connections/flangeless-ferrule-tefzelr-etfe-1-4-28-flat-bottom-for-1-16-od-blue-10-pack.html
P-632 - Tee Asy Tefzel 1/16 .020 thru	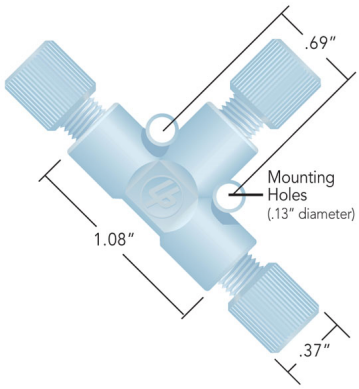 http://chromatography.hplcsupply.com/item/1-4-28-lc-fluid-transfer-fitting-connections/tees-and-crosses/p-632
P-710 - Union Tefzel® (ETFE) w/.030 thru hole	 https://www.idex-hs.com/fluidic-connections/connectors-1/low-pressure-multiport-connectors/union-assemblies/union-tefzelr-etfe-w-030-thru-hole.html
P-309 - Plug - Delrin®, 1/4-28 Flat-Bottom	 https://www.idex-hs.com/fluidic-connections/fittings/plugs-caps/plug-delrinr-1-4-28-flat-bottom.html

A-327 - Plastic Tubing Cutter	 https://www.idex-hs.com/fluidic-connections/tubing/tools/plastic-tubing-cutter.html
Mini fraction collector – Retriever® 500	 http://www.isco.com/products/products3.asp?PL=101603030

Appendix E

Crude Oil Characteristics

This section outlines the characteristics of the anonymous crude oil that was used in this study for wettability alteration. Table E1 lists the heavy fraction characteristics and Table E2 lists the heavy fraction composition.

Table E1: Heavy fraction characteristics of the anonymous crude oil that was used in this study for wettability alteration.

Wax content	2.5 – 5%
Wax appearance temperature (WAT)	88 – 90° F
Dead oil viscosity at 80 °F	12 – 18 cP
Asphaltene content	3 – 6 %
Total Acid Number (TAN)	1.5-3.0 %

Table E2: Heavy fraction composition of the anonymous crude oil that was used in this study for wettability alteration.

C_{16}	17.72
C_{17}	12.14
C_{18}	8.95
C_{19}	10.13
C_{20}	8.16
C_{21}	5.71
C_{22}	5.58
C_{23}	3.52
C_{24}	3.65
C_{25}	3.17
C_{26}	2.8
C_{27}	1.98
C_{28}	2.10
C_{29}	2.10
C_{30}	1.28
C_{31}	1.18
C_{32}	1.51
C_{33}	0.94
C_{34}	1.29
C_{35}	1.00
C_{36}	0.60
C_{37}	0.54
C_{38}	0.39
C_{39}	0.44
C_{40}	0.39
C_{41}	0.29
C_{42}	0.37
C_{43}	0.27
C_{44+}	0.00

References

HSIEH, J. Computed tomography: principles, design, artifacts, and recent advances. 2009. SPIE Bellingham, WA.